TURKISH JOURNAL OF SCIENCE & TECHNOLOGY

TURKISH JOURNAL OF SCIENCE AND TECHNOLOGY (TJST)

Year: 2022   **Vol: 17**   **Number: 1**

ADVISORY BOARD

Fırat University Turkish Journal of Science & Technology (TJST)
17-1, 2022

CONTENTS / İÇİNDEKİLER

Control Based on Feedback Linearization of a Mobile Manipulator Robot for Trajectory Tracking

Samir IKNI[1*], Abdelyazid ACHOUR[2]

[1] Laboratory of Industrial Technology and information (LTII), Faculty of Technology, University of Bejaia, Algeria
[2] Laboratory of Industrial Technology and information (LTII), Faculty of Technology, University of Bejaia, Algeria
[*1] samir.ikni@univ-bejaia.dz, [2] abdelyazid.achour@univ-bejaia.dz

Abstract: The use of robotic systems has now become almost necessary in various fields. Of which, the realization of any hard or dangerous place requiring an implication of manipulation and locomotion, is necessarily entrusted to a mobile manipulator. In this work, we present a control approach that ensures the stability of the system, based on feedback linearisation. The mobile platform is controlled in such a way that it always brings the manipulator's terminal organ to the desired position. The control of the platform depends on the information of the measured joint positions of the manipulator to ensure the planning of its own movement. It is shown that the considered strategy solves the problem ensuring the closed-loop stability of the system, thus allowing the convergence of the tracking errors. The performance of the approach is validated by simulation tests, showing an acceptable performance.

Key words: Mobile manipulator, Control stability, Great Precision, feedback linearization control.

Yörünge Takibi için bir Mobil Manipülatör Robotunun Geri Besleme Doğrusallaştırmasına Dayalı Kontrol

Öz: Robotik sistemlerin kullanımı artık çeşitli alanlarda neredeyse gerekli hale gelmiştir. Bunlardan, manipülasyon ve hareketin bir imasını gerektiren herhangi bir sert veya tehlikeli yerin gerçekleştirilmesi, zorunlu olarak bir mobil manipülatöre emanet edilmiştir. Bu çalışmada, geri beslemeli doğrusallaştırmaya dayalı olarak sistemin kararlılığını sağlayan bir kontrol yaklaşımı sunuyoruz. Mobil platform, manipülatörün terminal organını her zaman istenen konuma getirecek şekilde kontrol edilir. Platformun kontrolü, kendi hareketinin planlanmasını sağlamak için manipülatörün ölçülen eklem pozisyonlarının bilgisine bağlıdır. Ele alınan stratejinin sistemin kapalı döngü kararlılığını sağlayarak sorunu çözdüğü ve böylece izleme hatalarının yakınsamasına izin verdiği gösterilmiştir. Yaklaşımın performansı, kabul edilebilir bir performans gösteren simülasyon testleri ile doğrulanır.

Anahtar kelimeler: Mobil manipülatör, Kontrol kararlılığı, Büyük Hassasiyet, geri besleme doğrusallaştırma kontrolü.

1. Introduction

Advances in technology have shaped modern robotics to the design of more complex system for handling tasks can be extremely complicated. This complication that can manifest itself to a single robotic system that will be composed of many basic systems, such as it can manifest itself by a robotic system trained to perform tasks primarily related to handling [1, 2]. Nowadays the most common term is the mobile manipulator, which refers to robot systems formed from a robotic arm mounted on a mobile platform. These systems combine on the one hand the advantages of mobile platforms and robotic arms, and on the other hand ensure the reduction of their disadvantages. For example, the mobile platform offers the manipulator unlimited working space. The additional degrees of freedom of the mobile platform also provide the user with more choices, whereas an arm offers several operational features. Although it appeared very early in the history of robotics [3], this concept has been mainly studied for less than ten years [4]. Most of the publications inherit the problems related to robotic weapons and deal with the state of the art, such as control [4-6], trajectory optimization or operational trajectory tracking [7, 8]. Despite the wide variety of problems to be solved and the corresponding publications [9], very little effort has been made on modeling. When the mobile manipulator has a holonomic platform, the arm modeling can be directly applied [9, 10]. In the case of a wheeled mobile platform, the non-slip rolling of the wheels on the ground implies a different modeling. The mobile platform cannot move instantaneously in an arbitrary direction, because of this constraint [9-14]. It is then said to be non-holonomic and it is necessary to consider the specific properties of mobile platforms [15]. The prerequisites to implement a good total system control often involve the study of the

---

kinematics and dynamics of the mobile manipulator. Our study was initially justified by the generation of trajectories for a mobile manipulator in order to perform a given task [16], for example painting a surface or simply sweeping it. We have based our work on a study and a comparative analysis between works already done in the field, which considered simple structures of mobile manipulators to deal with trajectory tracking problems [17, 18]. And, other works, which consider such a complex structure: the flexible manipulators [19] and the omnidirectional mobile robot [20], using the technique of the calculated torque was considered to solve the problems of regulation and tracking of trajectory.

The contribution of this work is manifested in the application of a simple method of torque control calculated in the task space is suggested for the tracking control of a mobile manipulator considered to a complex structure. And finally, the effectiveness of the proposed system is evaluated through simulation by the MATLAB software of mobile manipulator robot.

2. Description of the mobile robot manipulator

The mobile manipulators can be built according to Platform, which differs by the mechanism from training employed. Mobile platforms most usually available to use a differential training or a training similar to a car.

A robot of the type unicycle east actuates by two independent wheels, it has possibly insane wheels to ensure its stability. Its centre of rotation is located on the axis connecting the two driving wheels. It is a robot non-holonomic; indeed, it is impossible to move it in a direction perpendicular to the wheels of locomotion [13, 17]. Its order can be very simple; it is indeed rather easy to move it of a point to another by a succession of simple rotations and straight lines.

3. Modeling of a mobile manipulator

The system to be considered is a mobile manipulator supported by two independently driven wheels with a common fixed axis to the platform and two passive self-aligning wheels. The wheeled platform is modeled as a non-nolonomic system in which slip is neglected due to idling [7, 17]. Therefore, the wheeled platform consists of three degrees of freedom that is reduced to two degrees of freedom due to the non-slip condition. On these assumptions that the kinematic model of robot is developed, the details of the development are given in section 3.1.
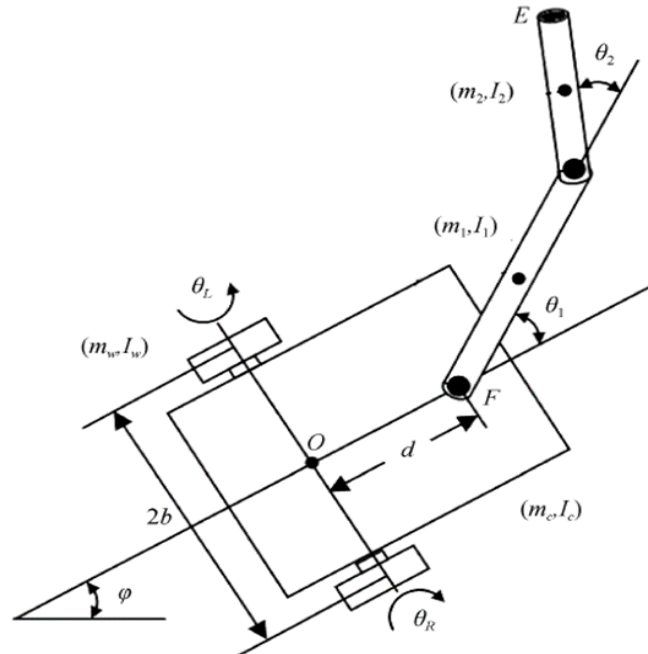
Figure 1. Mobile system of handling [14]

3.1. Kinematic modelling

Let us consider the mobile system of handling of Figure 1. For the mobile platform, the kinematic equation linear velocity at point F according to the speeds of wheel is given in the Equation 1 [14, 17]:

$$\begin{pmatrix} \dot{x}_F \\ \dot{y}_F \end{pmatrix} = \left(\frac{r}{2b}\right) \begin{pmatrix} (bC_0 + dS_0) & (bC_0 - dS_0) \\ (bC_0 - dS_0) & (bC_0 + dS_0) \end{pmatrix} \begin{pmatrix} \dot{\theta}_R \\ \dot{\theta}_L \end{pmatrix} \tag{1}$$

Where θ_R and θ_L are the angular velocities of the right-hand side and left, respectively. And
$S_0 = \sin(\varphi), C_0 = \cos(\varphi)$. The linear velocity of the final effector   is found while basing on the fact that its design speed is known and given by Equation 1. The speed of the final effector is written like:

$$\begin{pmatrix} \dot{x}_E \\ \dot{y}_E \end{pmatrix} = \begin{pmatrix} \dot{x}_F \\ \dot{y}_F \end{pmatrix} + \begin{pmatrix} C_0 & -S_0 \\ S_0 & C_0 \end{pmatrix} \begin{pmatrix} J_{11} & J_{12} \\ J_{21} & J_{22} \end{pmatrix} \begin{pmatrix} \dot{\theta}_1 + & \dot{\varphi} \\ & \dot{\theta}_2 \end{pmatrix} \tag{2}$$

Or Jij (i, j=1, 2) are elements of the fixed base Jacobien of the manipulator used, given by:
$J_{11} = -L_1 S_1 - L_2 S_{12}, \ J_{12} = - L_2 S_{12} , J_{21} = L_1 C_1 - L_2 C_{12} \ and \ J_{22} = L_2 C_{12}$
θ_1 , θ_2: are the joint variables of the manipulator, with notations: $S_i = \sin(\theta_i) , C_i = \cos(\theta_i)$,
$S_{ij} = \sin(\theta_i + \theta_j), \ C_{ij} = \cos(\theta_i + \theta_j)$.
While combining Equation 1 and Equation 2, the differential kinematics of the mobile manipulator is obtained as follows:

$$\begin{pmatrix} \dot{x}_E \\ \dot{y}_E \\ \dot{x}_F \\ \dot{y}_F \end{pmatrix} = \begin{pmatrix} C_0 & -S_0 & 0 & 0 \\ S_0 & C_0 & 0 & 0 \\ 0 & 0 & C_0 & -S_0 \\ 0 & 0 & S_0 & C_0 \end{pmatrix} \begin{pmatrix} \left(\frac{r}{2}\right) - \left(\frac{r}{2b}\right)J_{11} & \left(\frac{r}{2}\right) + \left(\frac{r}{2b}\right)J_{11} & J_{11} & J_{12} \\ -\left(\frac{r}{2b}\right)(d + J_{21}) & \left(\frac{r}{2b}\right)(d + J_{21}) & J_{21} & J_{22} \\ \frac{r}{2} & \frac{r}{2} & 0 & 0 \\ -\left(\frac{r}{2b}\right)d & \left(\frac{r}{2b}\right)d & 0 & 0 \end{pmatrix} \begin{pmatrix} \dot{\theta}_R \\ \dot{\theta}_L \\ \dot{\theta}_1 \\ \dot{\theta}_2 \end{pmatrix} \tag{3}$$

Who can be expressed in the following form:

$$\dot{x} = J v \tag{4}$$

With: $\dot{v}(t) = [\dot{\theta}_r \dot{\theta}_l \dot{\theta}_1 \dot{\theta}_2]^T$, by derivation Equation 4, we obtains:

$$\ddot{x} = \dot{J} v + J \dot{v} \tag{5}$$

This equation will be used in Equation 8, to make the link between the acceleration, the position and the motor torque of the robot.

4. Dynamic modeling

The dynamic model of the system, is based on the determination of the relationship between the torque and the speed of the robot. In this section the details to obtain this relationship are given.
The dynamics of a mobile manipulator subjected to constraints non-holonomic can be obtained by using the Lagrangian one in the following form, [6], [17, 18]:

$$M(q)\ddot{q} + C(q, \dot{q}) = E(q)\tau - A^T(q)\gamma \tag{6}$$

The constraints non-holonomic written in the form of: $A(q)\dot{q} = 0$, with $q = [x_c y_c \varphi \theta_r \theta_l \theta_1 \theta_2]^T \in R^n$, is the generalized coordinates. M (q)$\in R^{nxn}$ is the matrix of inertia of the system. $C(q, \dot{q}) \in R^{nx1}, A(q) \in R^{mxn}$ are vectors centrifugal forces and Coriolis, respectively. $A(q) \in R^{mxn}$ is matrix of the constraints.
In order to eliminate the force from constraint $\gamma, S^T(q)A^T(q) = 0$. We can find the vector of entry speed
$\dot{v}(t) = [\dot{\theta}_r \dot{\theta}_l \dot{\theta}_1 \dot{\theta}_2]^T$, for all $\dot{q}$ given in the following equation:
$$\dot{q} = S(q) \dot{v}(t) \tag{7}$$

$$\text{With: } s(q) = \begin{bmatrix} \frac{r(bC_0+dS_0)}{2b} & \frac{r(bC_0-dS_0)}{2b} & 0 & 0 \\ \frac{r(bS_0-dC_0)}{2b} & \frac{r(bS_0+dC_0)}{2b} & 0 & 0 \\ \frac{r}{2b} & \frac{-r}{2b} & 0 & 0 \\ 0 & 0 & 1 & 0 \\ 0 & 0 & 0 & 1 \end{bmatrix}$$

Differentiating Equation 7, substituting the expression for $\ddot{q}$ into Equation 6 and premultiplying by S^T, we get the Equation 8.

$$S^T(M(S\ddot{v}(t) + \dot{S}\dot{v}(t)) + C) = S^T\tau \tag{8}$$

Which can be reduced as follows:

$$\bar{M}\ddot{v} + \bar{C} = \bar{\tau} \tag{9}$$

Where $\bar{M} = S^T M S, \bar{C} = S^T(M\dot{S}\dot{v} + C), \bar{\tau} = S^T\tau$,
Since S is non-singular, $\bar{M}$ is always symmetric and positive definite. Considering Equation 4, the Equation 9, can be expressed as:

$$\bar{M}\ddot{x} + \bar{C} = J^{-T}\tau \tag{10}$$

This model of Equation 10, will be used in the trajectory tracking, which is explained in section 4.1.
The controller structure is shown in Figure 2.
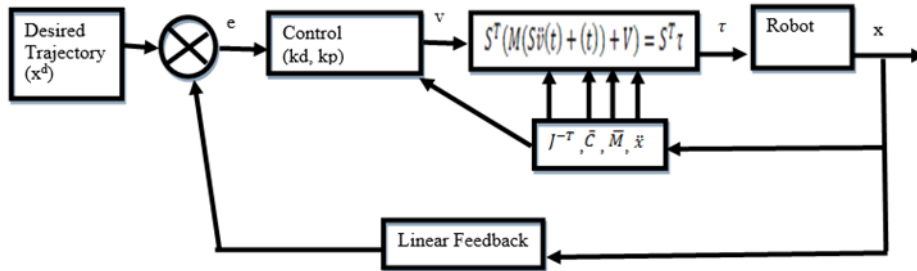
Figure 2. Modeling and control of a mobile manipulator.

4.1 Path Tracking

The path tracking is based on a control that minimizes the error between the robot position and the desired position, details of this control are given below:
Suppose that the desired trajectory is described by $\ddot{x}_d$, $\dot{x}_d$ and x_d, and since the general form of a mechanical system is given by Equation 10, its control is as follows:

$$J^T(\bar{M}\ddot{x} + \bar{C}) = \tau \tag{11}$$

Where auxiliary accelerations are given by:

$$\ddot{x} = \ddot{x}_d + k_d(\dot{x}_d - \dot{x}) + k_p(x_d - x) \tag{12}$$

Where e $= x_d - x$ represents the tracking error of the system. k_p and k_d are respectively the proportional and derivatives gain matrices, which is also considered to be diagonal positive definite matrices. Substituting the dynamic model in the operational space of the mobile manipulator given by Equation 6, in the control law given by Equation 11. The result given in Equation 13.

$$\bar{M}(\ddot{e} + k_v\dot{e} + k_p e) = 0 \tag{13}$$

Where $\bar{M} = S^T M S$ is invertible, the stability of the error (Equation 13), depends on the stability given in Equation 14:

$$\ddot{e} + k_v\dot{e} + k_p e = 0 \tag{14}$$

It is clear that for e = 0 is an equilibrium point for the system illustrated in Equation 14 and let us consider the candidate Lyapunov function of the quadratic type of the following form,

$$V(q) = \frac{1}{2}\dot{e}^T\dot{e} + \frac{1}{2}e(k_p + \gamma k_d)e + \gamma\dot{e}^T\dot{e} \tag{15}$$

In order to determine the stability of the closed loop system (Equation 14), let us now consider the time derivative of the function (Equation 15). The developments are illustrated in Equations (16) - (21).

$$\dot{V}(q) = \dot{e}^T\ddot{e} + \dot{e}^T(k_p + \gamma k_d)e + \gamma\dot{e}^T\ddot{e} \tag{16}$$

with $: \ddot{e} = -k_p e - k_d\dot{e}$ \hfill (17)

$$\dot{V}(q) = \dot{e}^T(-k_p e - k_d\dot{e}) + \dot{e}^T(k_p + \gamma k_d)e + \gamma\dot{e}^T(-k_p e - k_d)\dot{e} \tag{18}$$

$$= -\dot{e}^T k_p e - \dot{e}^T k_d\dot{e} + \dot{e}^T k_p e + \dot{e}^T\gamma k_d e - \gamma\dot{e}^T k_p e - \gamma\dot{e}^T k_d\dot{e} \tag{19}$$

$$= -\dot{e}^T k_d\dot{e} + \dot{e}^T\gamma k_d e - \gamma\dot{e}^T k_p e - \gamma\dot{e}^T k_d\dot{e} \tag{20}$$

$$\dot{V}(q) = -\dot{e}^T k_d(1 + \gamma)\dot{e} - \dot{e}^T\gamma(k_p - k_d)e \tag{21}$$

From Equations 21, $\dot{V}(q)$, is negative, we conclude that the closed-loop asymptotic stability indicate results for a sufficiently small epsilon(γ).

5. Results of simulation

To test the performance of the proposed study, the reference trajectory used is as follows:
$x^1_{ef}(t) = 1 - \exp(-4t)$ (First simultion case) and forme $x^2_{ef}(t) = 3*\sin(t)^2 + 2*\cos(t)^2$ (second simulation case)

The main results of the simulation are given in the figures below.
        The mobile manipulator robot moves from the start point to an end point (Figure 3), while following a desired trajectory of the end effector in the desired space, delimited by the small brown cycles. Nevertheless, it can be seen that there is some instability in the tracking, due to the non-holonomic constraints, which require the calculation of the steering angle at all times, whose manipulability index is slightly lower than the desired (maximum) value which should be equal to 1; in our case, it is stable around 0.748 (Figure 4 and 10) The linearvelocity of the robot is given in figure 9 and 10 , the speed starts with an acceleration phase and then remains at a constant value, then in the approach phase by a deceleration until the arrival, this speed control is directly linked to the calculation of the motor torque of the robot that we have developed.Figures 7 and 8 illustrate that the moving platform brings the end-effector of the manipulator to the desired position. Note that the movement of the platform is not planned.
 The control of the platform depends on the measured end-effector position information. The negative value of the velocities indicates that the moving platform moved backwards for a short period of time at the very beginning in order to reach the required heading angle. Therefore, the exposed backwards movement is not explicitly planned, which shows the performance of the developed control strategy.

- **First simulation case**

Desired trajectory is of form**:** $x^1_{ef}(t) = 1 - \exp(-4t)$
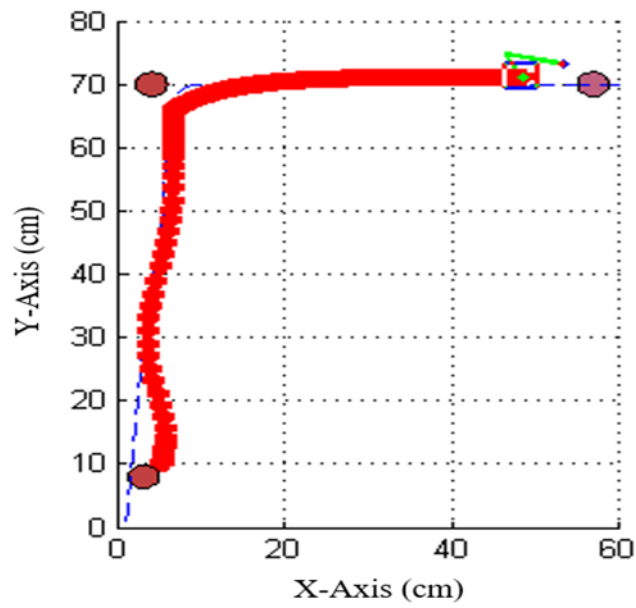
Figure 3. Robot trajectory tracking by the robot.
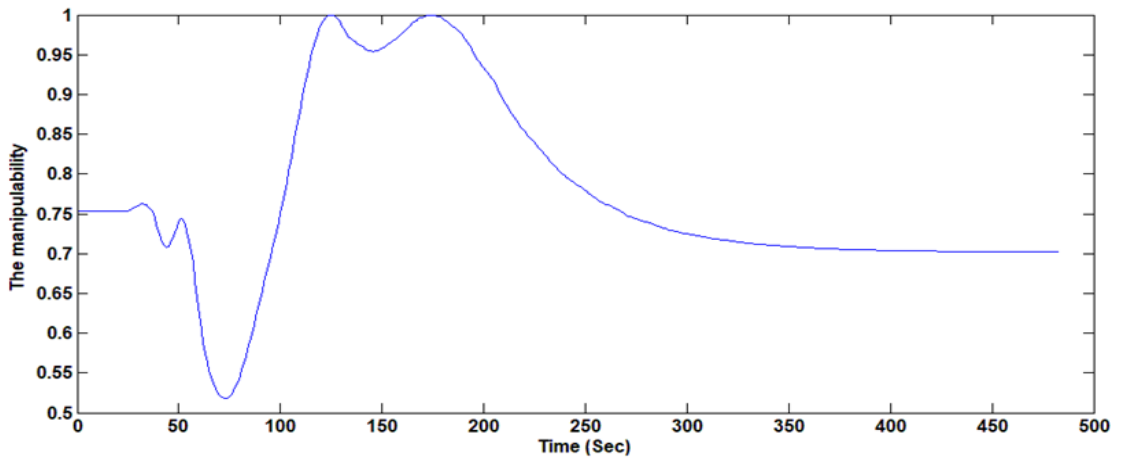
Figure 4. The manipulability.
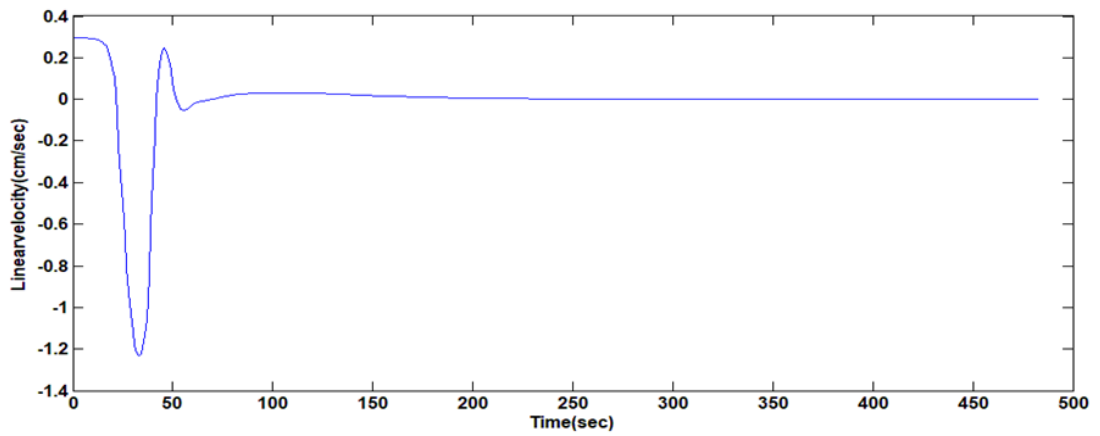
Figure 5. The linearvelocity.
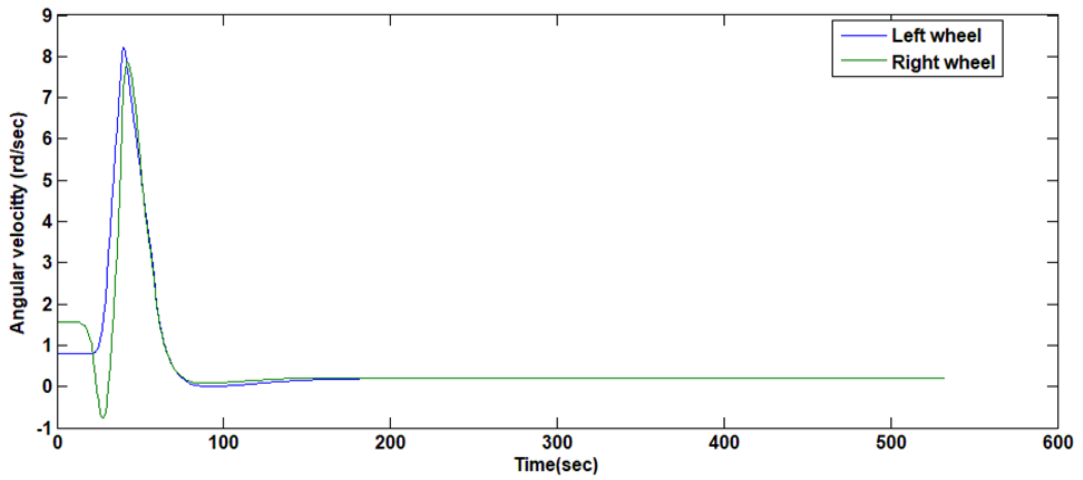
Figure 6. The angular velocity of wheels.

- **Second simulation case**

Desired trajectory is of form**:** $x^2_{ef}(t) = 3*\sin(t)^2 + 2*\cos(t)^2$
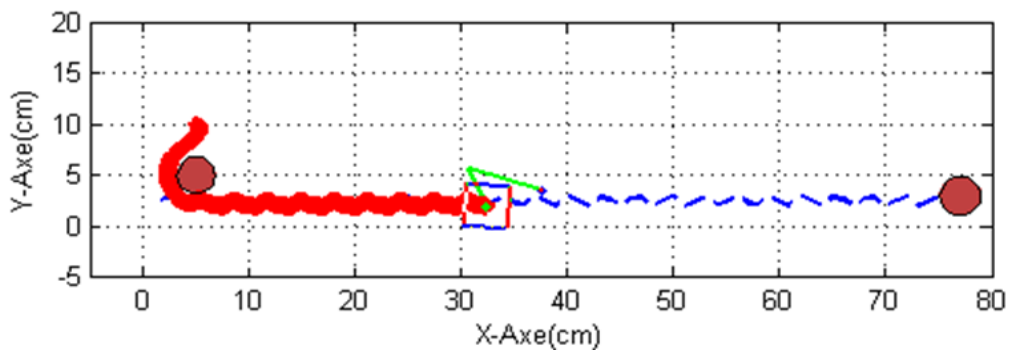
Figure 7. Robot trajectory tracking by the robot.
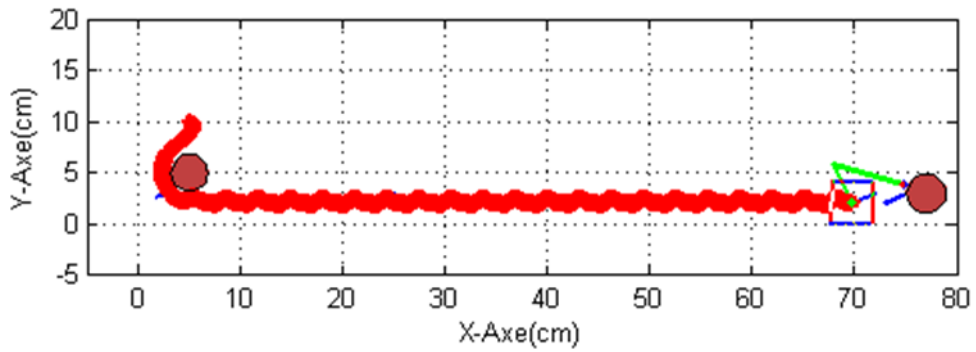
Figure 8. The final position of the robot.

7
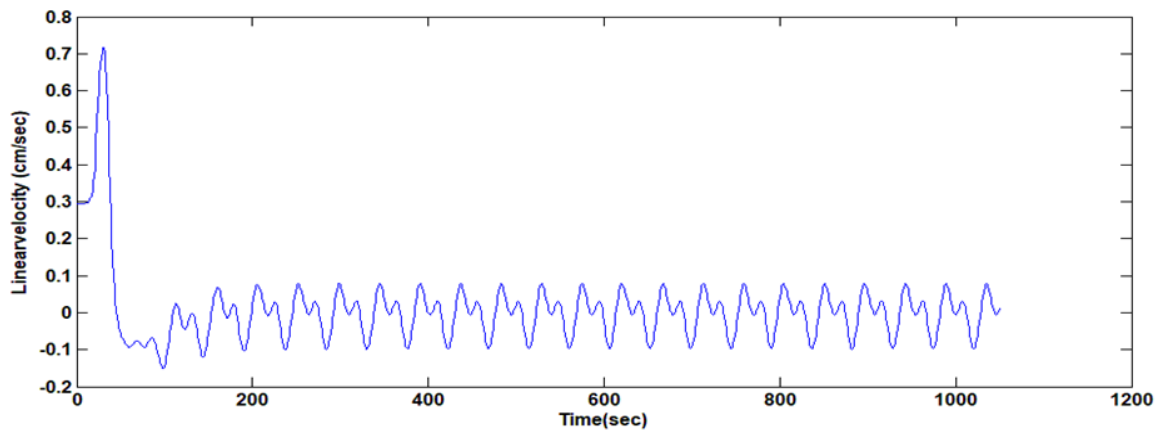
Figure 9 . Linearvolocity.
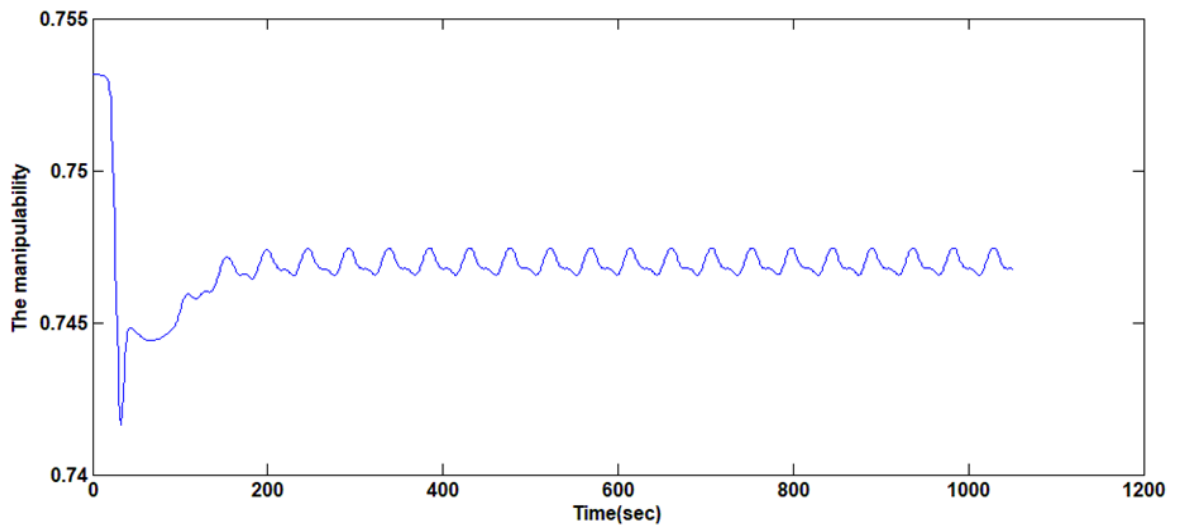
Figure 10. The manipulability.
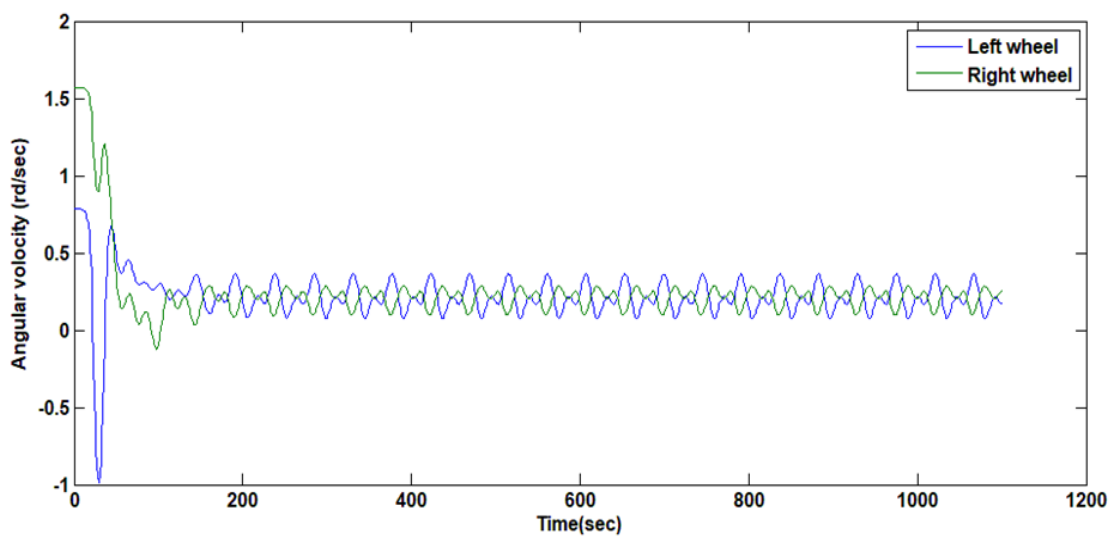
Figure 11 . Angular volocity of de wheels.

7. Conclusion

This work, focused on path following and control of the mobile manipulator, using a differential drive system as an example. The system platform was equipped with two link manipulators. In order to solve the problem of following the trajectory of the system subjected to non-holonomic constraints, we considered the control based on a dynamic model of a mobile manipulator. To solve the problem in the task space, the well-known computer torque control strategy, commonly used in the field of manipulator robots, has been considered. The stability of the entire closed loop system has been proven. The simulation results show that mobile manipulators can follow the reference path with great proximity, demonstrating the efficiency of the proposed calculated torque controller. Nevertheless, need to use the more robust PD-flou controller, Neuronal, passive, in order to better improve the performance of any structure (robot and its control).

References

[1] David DeVon et Timothy Bretl, "Kinematic and Dynamic Control of a Wheeled Mobile Robot", Proceedings of the 2007 IEEE/RSJ International Conference on Intelligent Robots and Systems San Diego, CA, USA, Oct 29 - Nov 2, 2007.

[2] F. Pin, and J.C. Culioli, "Optimal Positioning of Combined Mobile Platform-Manipulator Systems for Material Handling Tasks", Journal of Intelligent & Robotic Systems, Vol. 6, 1992, pp. 165-182.

[3] Dong Hun Shin and Kyung Hoon Park, "Velocity kinematic modeling for wheeled mobile robot", IEEE International Conference on Robotics and Automation, Proceedings 2001 ICRA Volume 4; 21-26 May 2001.

[4] W. F. Carriker, P. K. Khosla, and B.H. Krogh, "Path Planning for Mobile Manipulators for Multiple Tasks Execution", IEEE Transactions on Robotics and Automation, Vol. 7, No. 3, 1991, pp. 403-408.

[5] B. Bayle, J.-Y. Fourquet , et M. Renaud. « Génération des mouvements des manipulateurs mobiles : état de l'Art et perspectives ». JESA. Vol. 35. No. 6.pp. 809-845, 2001.

[6] Yoshio Yarnarnoto. Coordinated Control of a Mobile Manipulator. GRASP Laboratory Department of Mechanical Engineering and Applied Mechanics School of Engineering and Applied Science University of Pennsylvania, march 3, 1994.

[7] N. Hootsmanns , S. Dubowsky. The motion control of manipulators on mobile vehicles. In Proceedings of IEEE International Conference on Robotics and Automatics, IEEE, Sacramento, USA, vol. 3, pp. 2336{2341, 1991.

[8] E. Padopoulos, J. Poulakakis. Planning and model-based control for mobile manipulators. In Proceedings of IEEE/RSJ International Conference on Intelligent Robots and Systems, IEEE, Takamatsu, J

[9] Sarkar N, Yun X. and Kumar V., "Control of Mechanical Systems with Rolling Constraints: Application to Dynamic Control of Mobile Robots,"Int. J. Robotics Research, Vol. 13, No. 1, February 1994, pp. 55-69.apan, 2000.

[10] G. White. Simultaneous Motion and Interaction Force Control of a Nonholonomic Mobile Manipulator, Ph. D. dissertation, University of New York at Bu®alo, USA, 2006.

[11] Y. Guo , P. Y. Woo. Adaptive fuzzy sliding mode control for robotic manipulators. In Proceedings of the 42nd IEEE Conference on Decision and Control, IEEE, Maui, USA, vol. 3, pp. 2174–2179, 2003.

[12] A. Petitti, A. Franchi, D. Di Paola, and A. Rizzo, "Decentralized motion control for cooperative manipulation with a team of networked mobile manipulators," in 2016 IEEE International Conference on Robotics and Automation (ICRA). IEEE, May 2016, pp. 441–446.

[13] T. Lee, "Robust adaptive attitude tracking on SO (3) with an application to a quadrotor uav ," IEEE Transactions on Control Systems Technology, vol. 21, no. 5, pp. 1924–1930, 2013.

[14] Y.-H. Liu and S. Arimoto, "Decentralized Adaptive and Non-adaptive Position/Force Controllers for Redundant Manipulators in Cooperation," The International Journal of Robotics Research, vol. 17, no. 3,pp. 232–247, Mar 1998.

[15] G Dai, Y Liu (2016) Coordination distribuée et contrôle de coopération pour les manipulateurs mobiles en réseau. Transactions IEEE sur l'électronique industrielle 64: 5065-5074.

[16] N Chen, F Song, G Li, X Sun, C Ai (2013) Un contrôle de recul en mode glissant adaptif pour manipulateur mobile avec des contraintes non holonomiques. Commun Nonlinear Sci Numer Simulat 18: 2885-2899.

[17]   J Wen, D Bayard (1998) Nouvelle classe de lois de contrôle pour les manipulateurs robotiques. partie 1. cas non adaptatif. Int J Control 47: 1361-1385.

[18] Asama, H., Sato, M., Bongoni, L., Kaetsu, H., Matsumoto, A., and Endo, I.: 1995, Development of an omnidirectional mobile robot with 3 DOF decoupling drive mechanism, in: Proc. of 1995 IEEE Internat. Conf. on Robotics and Automation, Vol. 2, pp. 1925–1930.

[19] P. Ioannou, "Decentralized adaptive control of interconnected systems," IEEE Transactions on Automatic Control, vol. 31, no. 4, pp.

[20] C. Ott, A. Albu-Schaffer, A. Kugi, S. Stramigioli, and G. Hirzinger, " "A Passivity Based Cartesian Impedance Controller for Flexible Joint Robots - Part I: Torque Feedback and Gravity Compensation," in Proc. of the 2004 IEEE International Conference on Robotics and Automation, April 2004, pp. 2659–2665.

The Effect of Imide Substituents on the Excited State Properties of Perylene Diimide Derivatives

Erkan AKSOY[123]*, Andrew DANOS[2], Chunyong LI[2], Andrew P. MONKMAN[2], Canan VARLIKLI[3]

[1]Solar Energy Institute, Ege University, 35100 Izmir, Turkey

[2]Department of Physics, Durham University, Durham DH1 3LE, U.K.

[3]Department of Photonics, Izmir Institute of Technology, 35430 Urla, Izmir, Turkey

*[123]erkanaksoy@iyte.edu.tr, [2]andrew.danos@durham.ac.uk, [2]chunyong.li@durham.ac.uk,

[2]a.p.monkman@durham.ac.uk, [3]cananvarlikli@iyte.edu.tr

Abstract: Solid state optical properties of fluorescent materials are important for many photonic devices such as organic light emitting diodes, frequency down-converters or luminescent solar concentrators. Perylene diimides (PDIs) represent one of the most popular organic semiconductors which find application in such photonic device applications. In this study, photophysical properties of two dibrominated PDI (DiBrPDIs), one of which contains a branched alkyl chain (2-ethylhexyl, 2-EH) and the other with an aromatic substituent (diisopropylphenyl, DIA) at the imide positions are comparatively studied. We report their absorption and photoluminescence, lifetime and photoluminescence quantum yield (PLQY), as well as photoinduced absorption properties (PIA) examined by fs-transient absorption spectroscopy. Having the same π conjugated system, DiBrPDI-DIA and DiBrPDI-2EH exhibited identical absorption and photoluminescence (PL) spectra in chloroform (λ_{abs}:527 nm and λ_{PL}:552 nm). However, in film phase, DiBrPDI-DIA ($\lambda_{PL\text{-}DIA}$:596 nm; PLQY:73.4%) presented a shorter PL wavelength with a higher PLQY than that of DiBrPDI-2EH ($\lambda_{PL\text{-}2EH}$:649 nm; PLQY:36.7%). Bond lengths and core bending angles of PDI derivatives were calculated using Chem3D pro software. It was determined that the 2,6-diisopropylphenyl group in DiBrPDI(DIA) extends a distance of about 6.8 Å out from the imide positions, providing more effective steric protection from aggregation than the smaller 2EH group.

Key words: Solid state fluorescence, perylene diimide, fs-transient absorption spectroscopy, steric shielding.

Perilen Diimid Türevlerinin Uyarılmış Hal Özelliklerine İmid İkamelerinin Etkisi

Öz: Fluoresant malzemelerin katı hal optik özellikleri organik ışık yayan diyotlar, frekans dönüştürücü veya ışıyan güneş yoğunlaştırıcıları gibi birçok optik ve elektronik fotonik aygıtlar için önemlidir. Perilen diimidler (PDIs) bu tür fotonik aygıt uygulamalarında yer bulan en popüler organik yarı iletkenlerden birini temsil etmektedir. Bu çalışmada, biri dallı alkil zinciri (2-etilheksil, 2-EH) diğeri aromatik (diizopropilfenil, DIA) yer değiştirebilen grup içeren iki dibromlu PDI'nin (DiBrPDIs) fotofiziksel özellikleri karşılaştırmalı olarak incelenmiştir. Biz bunların soğurma ve fotolüminesans (PL), yaşam ömürü ve fotolüminesans kuantum veriminin (PLQY) ile fs-geçici absorpsiyon spektroskopisiyle incelenen foto-indüklenmiş absorpsiyon özelliklerini (PIA) rapor ediyoruz. Aynı π konjuge sistemine sahip olan DiBrPDI-DIA ve DiBrPDI-2EH, kloroformda (λ_{abs}:527 nm ve λ_{PL}:552 nm) özdeş soğurma ve PL davranışlarına sahiptir. Ancak, aynı koşullarda hazırlanan filmlerde DiBrPDI-DIA ($\lambda_{PL\text{-}DIA}$:596 nm; PLQY:73.4%), DiBrPDI-2EH'den ($\lambda_{PL\text{-}2EH}$:649 nm; PLQY:36.7%) daha yüksek bir PLQY ile daha kısa dalgaboyunda bir PL spektruma sahiptir. Chem3D pro yazılımı kullanılarak PDI türevlerin bağ uzunlukları ve körfez bükülme açıları hesaplanmıştır. DiBrPDI(DIA)'daki 2,6-diizopropilfenil grubunun imid konumlarından yaklaşık 6.8 Å'lık bir mesafeyi uzattığı ve yığılmaya karşı daha küçük 2EH grubuna göre daha etkili sterik koruma sağladığı belirlenmiştir.

Anahtar kelimeler: Katı hal fluoresans, perilen diimid, fs-geçici soğurma spektroskopisi, sterik koruyucu.

1. Introduction:

Solid state optical properties of singlet emitters are important for numerous photonic technologies due to their fast fluorescence radiative response to excitation and high photoluminescence quantum yields (PLQYs) [1–7]. Perylene diimide derivatives (PDIs) from the rylen family [8,9] (Figure 1) are one of the high performance fluorophore groups, possessing an extended π conjugation system with 2 naphthalene units substituted from the peri positions that support customisability for many photonic applications. Their excellent semiconductor properties are adjustable for specific desired application by chemical modifications of the peri or ortho positions

[9–11] (Figure 1), targeting material properties such as fluorescence wavelengths, highest occupied molecular orbital - lowest unoccupied molecular orbital (HOMO-LUMO) energy levels, and reduction potentials. The resulting materials find extensive use in organic light emitting diode (OLED) or organic solar cells (OSC) applications, with particularly valuable properties including their high emission efficiency (PLQY $\geq$ 90%), effective absorption of visible light ($\varepsilon \geq 10^4$ $M^{-1}cm^{-1}$), strong n type characteristic, high electron affinity and mobility, and high optical electronic and thermal stability [10,12–17].

In some photonic technologies (OLED, downconverters or fluorescence solar concentrators) which require the use of fluorescence, planar PDI structures make them susceptible to dimer formation and aggregation caused quenching (ACQ). Thus, they can lose almost all of their PLQY in film [14], limiting their successful use in these technologies. Different approaches have been reported to minimize the film phase ACQ of polycyclicaromatic compounds such as those containing the perylene or pyrene core [18,19]. One of them is direct chemical modification [14,20,21], while dispersal in an optical host material with low doping rates of emitter can also avoid ACQ [10,22]. As high concentrations are often required in applications though, the more commonly used method to reduce the aggregation of PDIs is by connecting steric groups from imide or bay positions [14,20,23–25]. Although structures attached from the imide group do not participate in π conjugation system of PDI, electron donating groups (containing amine or carbazole) can interact with the PDI core in photoinduced electron transfer processes and quench PDIs' PL by directly, affecting their photophysical properties [26,27]. Therefore, groups to be attached from imide positions should be carefully selected according to their potential applications.
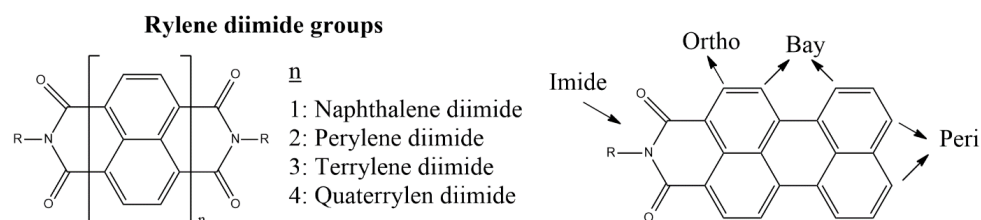
Figure 1. Some of the Rylen family members (left), and positions of Perylene for chemical modification (right).

In this work, film and solution phase photophysical properties of isomeric mixtures of 1,7 (~%83) and 1,6 (~%17) -dibromo perylene diimides [(N,N′-bis(2-ethylhexyl)-1,7(6)-dibromoperylene-3,4,9,10-tetracarboxylic diimide (DiBrPDI-2EH) and N,N′-bis(2,6-diisopropylphenyl)-1,7(6)-dibromoperylene-3,4,9,10-tetracarboxylic diimide (DiBrPDI-DIA), (shown in Figure 2)] were investigated. Bay-unsubstituted N,N′-bis(2-ethylhexyl)-perylene-3,4,9,10-tetracarboxylic diimide (PDIref) was also used as a reference for comparison with the compounds subject to this study. DiBrPDIs exhibiting the same absorption and PL in the solution phase exhibited different PL in the film phase, due to the different steric bulk of their imide groups. PLQY measurements and computer simulations of the molecular geometries demonstrate that the DIA substituents provide superior steric protection of the PDI core from ACQ, leading to the improved film phase properties of the DiBrPDI-DIA material. The Br bay-substituents are also found to assist in preventing aggregation compared to PDIref, disrupting π-π stacking interactions by twisting the otherwise planar PDI core.

2. Experimental

2.1. Materials and instruments:

Host polymer Zeonex 480-R and 2,6-diisopropylaniline were purchased from Zeon corporation and Acros Organics, respectively. Ethanol (absolute), hydrochloric acid, bromine, iodine, hexane, chloroform (CHCl$_3$), toluene, dichloromethane, N,N-dimethylformamide, acetic acid, 1-methyl-2-pyrrolidinone, silica gel (0.040–0.063 mm) were obtained from Sigma-Aldrich and perylene-3,4,9,10-tetracarboxylic dianhydride (PTCDA) was purchased from Fluka. Synthetic details of N,N′-bis(2-ethylhexyl)-perylene-3,4,9,10-tetracarboxylic diimide (PDIref), N,N′-bis(2-ethylhexyl)-1,7(6)-dibromoperylene-3,4,9,10-tetracarboxylic diimide (DiBrPDI-2EH) and N,N′-bis(2,6-diisopropylphenyl)-1,7(6)-dibromoperylene-3,4,9,10-tetracarboxylic diimide (DiBrPDI-DIA) (Figure 2) used in this study were previously reported [4,10,28].

Erkan AKSOY, Andrew DANOS, Chunyong LI, Andrew P. MONKMAN, Canan VARLIKLI

Analytik Jena S 600 UV-Vis and Edinburgh Instruments FLS920P spectrophotometers were used for absorption, photoluminescence (PL), photoluminescence quantum yield (PLQY) and emission lifetime (τ) measurements (time-correlated single photon counting-TCSPC). EPL-470 model (λ_{ext}; 472.4 nm, Pulse width: 86.9 ps) laser and an integrating sphere were utilized for lifetime (ns) and absolute PLQY measurements (λ_{ext}: 492 nm), respectively.

Excited state properties of DiBrPDIs were examined by fs-TAS in 480-800 nm range. The first part of the 1030 nm output from the fs amplifier PHAROS was used as the pump for the excitation (It was used to generate 343 nm via the third harmonic generation.). The second part of the 1030 nm output was focused on a 2 mm sapphire plate to create a continuum of white light, which was used as a probe to observe the excited state behaviour of DiBrPDIs.
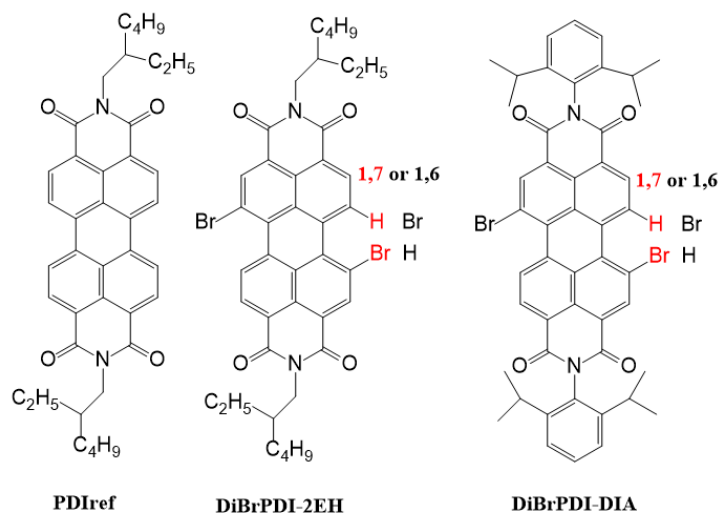
Figure 2. Molecular structure of PDIref, 1,7 (or 6) DiBrPDI(2EH) and DiBrPDI(DIA).

2.2. Preparation of neat and drop cast films

Neat films of DiBrPDIs were prepared on cleaned microscope slides by spin coating at 1500 rpm for 60 s of their solutions with the concentration of 5 mg/mL CHCl$_3$. Drop casted polymer film preparations of DiBrPDIs were started by introducing the perylene derivatives in 100 mg/mL Zeonex solution (in toluene) at different doping ratios (x: 0.25, 0.5. 1, 2, 3 and 5 wt.%) and stiring for 2 hs. Then, prepared DiBrPDIs-Zeonex solutions were drop casted on microscope slides and were dried for 30 min at 60°C.

3. Results and Discussions:

3.1 Steady state Absorption and PL properties of DiBrPDIs:

The absorption and PL spectra of PDIref, DiBrPDI-2EH and DiBrPDI-DIA (1.0 x 10^{-6} M in CHCl$_3$) and PL spectrum of neat films are given in Figure 3a-b. PDIref presented maximum absorption wavelength (λ_{abs}^{max}) and maximum PL wavelength (λ_{PL}^{max}) values of 526 nm and 532 nm, respectively. Although the λ_{abs}^{max} values of DiBrPDI-2EH and DiBrPDI-DIA are almost the same with PDIref, the Stokes shifts determined with these derivatives increased to 25 nm. This difference is attributed to the inductively electron donating property of the halogenic group (-Br) present at the bay positions of DiBrPDI-2EH and DiBrPDI-DIA as the N-substituents of PDIref and DiBrPDI-2EH are the same. Indeed, it is elsewhere reported that different alkyl chain or simple phenyl ring substituents (like 2EH and DIA) at the imide position have minimal effect on the properties of PDIs in dilute solution [29,30]. This contrasts strongly with the quenching effects via photoinduced electron transfer observed when using amine group-containing substituents [26,27].

13

Since DiBrPDI-2EH and DiBrPDI-DIA have the same π conjugation system, they present identical absorption and PL in solution phase. Their λ_{abs}^{max} and λ_{PL}^{max} are 527 and 552 nm, respectively. Despite all these similarities, the diisopropyl groups of DIA were found to prevent the π-π interaction of PDI cores more than 2EH based groups. Indeed, the DiBrPDI-DIA group displayed less evidence of aggregate formation and retained a higher energy PL than the DiBrPDI-2EH in neat film (Figure 3b). The λ_{PLmax}^{Film} of PDIref, DiBrPDI-DIA and DiBrPDI-2EH are 638, 596 and 649 nm, respectively. The PL peak of DiBrPDI-DIA in the film phase, which corresponds to the 2nd peak of the PL curve of its in the solution, suggests both excimer-dimer behaviour and significant self-reabsorption of the emitted light (dilute solution absorbance and emission spectra have some overlap). Both materials showed more evidence of aggregate PL at longer wavelengths (649 nm 2EH peak, 700 nm DIA peak) [14]. Also, the difference in their PL spectra of thin films is consistent with photographs of the pure material under UV light. DIA displayed higher energy 'orange-red PL', while 2EH displayed lower energy 'red PL' directly (Figure 3c). PDIref, on the other hand, exhibited a lower energy and broadened PL spectrum in film phase (Figure 3-a) due to the aggregation at lower energy states [14].
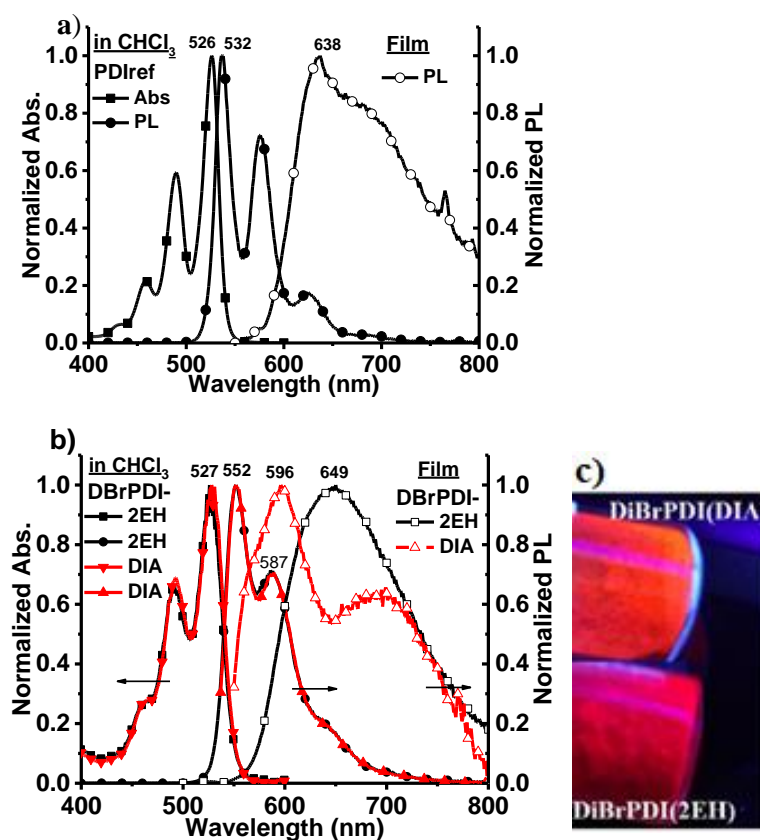
Figure 3. Absorption and PL spectrums of a) PDIref and b) DiBrPDI-2EH, DiBrPDI-DIA in dilute chloroform and neat films and c) image of orange-red (DiBrPDI-DIA) and red (DiBrPDI-2EH) powders fluorescence under UV light excition.

PDIref is well known to undergo aggregation (also named PDIref in this referenced study, [14]), and was qualitatively compared to the DiBrPDI derivatives doped with different wt.% in Zeonex (optically transparent) host material under UV light (Figure 4). Even in the 0.25% doped film of PDIref, it was found that the green-yellow PL of its monomer [PDIref PL - [13,14] was quenched (low intensity) and the PL color shifted predominantly to red-wavelength after 1% doping concentrations. DiBrPDI-2EH exhibited a fairly high PL at 1% doping rate due to sterically shielding bromines compared to planar PDIref. DiBrPDI-DIA containing both bromine and DIA was more successful at preventing aggregation and exhibited remarkably stronger PL up to 5% doping concentration. In addition to these photographs demonstrating relative PLQY under UV light excitation,

quantitative measurement of the absolute PLQY of the 5% doped DiBrPDI-2EH and DiBrPDI-DIA films are found to be 36.7% and 73.4%, respectively. The resulting PLQYs combined with the observed relative emission brightness in the photographs, reveal the different aggregation tendencies of the films (Figure 4).
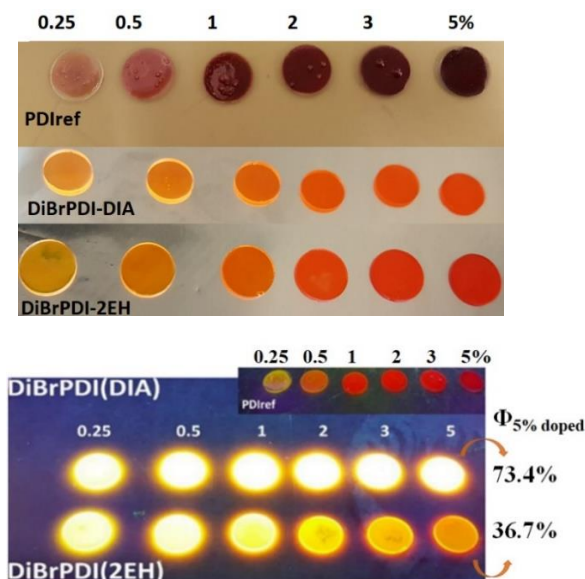
Figure 4. Images of PDIref, DiBrPDI-DIA and DiBrPDI-2EH films (in Zeonex host material with different wt.%s) under day light (upper) and UV light (lower) excitation.

PL spectra and lifetime decay of drop casted films (5 wt.%) are given in Figure 5. DiBrPDI-DIA and DiBrPDI-2EH exhibited λ_{PL}^{max} at 592 and 630 nm, respectively. In addition, average lifetime of DiBrPDI-2EH and –DIA were found to be 8.54 and 6.03 ns (Table 1), respectively. As described above (images of films in Figure 4), DiBrPDI-DIA exhibited higher energy PL (592 nm, 2.09 eV) with higher PLQY than that of DiBrPDI-2EH (630 nm, 1.96 eV) and a faster lifetime, due to its lower aggregation tendency [14].
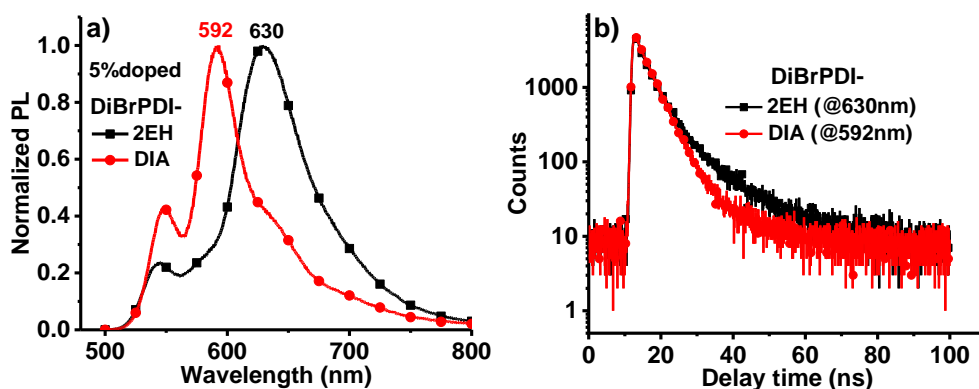
Figure 5. a) Emission spectra and b) PL lifetime (ns) decays of DiBrPDI-2EH and DiBrPDI-DIA films (5 wt. % doped in zeonex).

Table 1. Average lifetime value (τ) of DiBrPDIs at film phase (%5 doped in zeonex).

DiBrPDI-	τ_1 (ns)	%	τ_2 (ns)	%	τ_3 (ns)	%	τ average (ns)
2EH	1.57	8.84	4.16	69.39	13.26	21.77	8.54
DIA	3.87	95.36	16.48	4.64	-	-	6.03

3.2. 3-D study of steric shielding

In order to better explain the aggregation reducing effects of bromine and imide groups, a computational 3D study of brominated and unbrominated (-H) 2EH and DIA were carried out by using MM2 (molecular mechanics method) energy minimization in Chem3D Pro 12.0 software [10] (Table 2). In the accessible lowest-energy conformer, the DIA group occupies a volume that extends 6.8 Å perpendicular to the PDI core plane. In 2EH, this distance is only 6.0 Å. However, flexible 2EH group (alkyl group) can also rotate freely around the PDI plane, while rigid DIA groups cannot because of the presence of carbonyl groups. This causes the triisopropyl groups to stay perpendicular to the plane, providing better shielding from dimer interactions in the concentrated films.
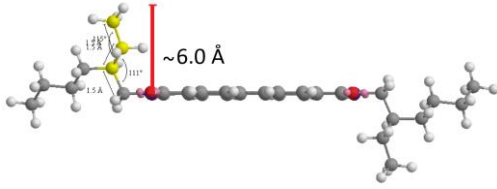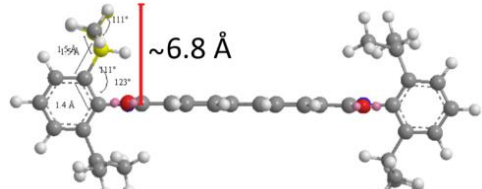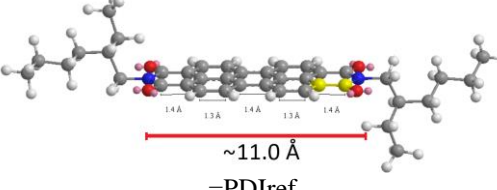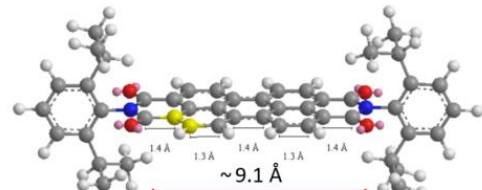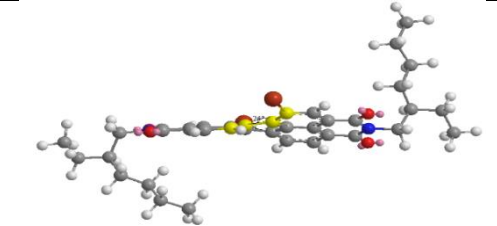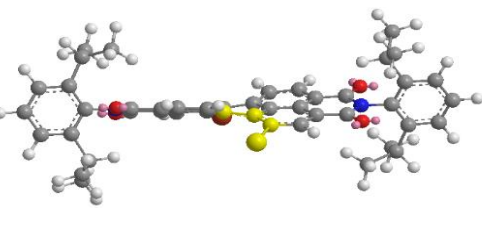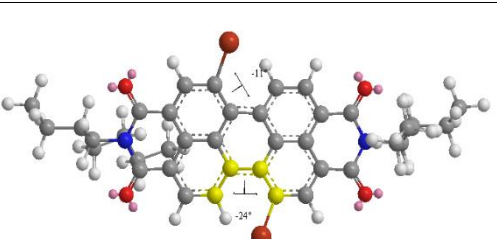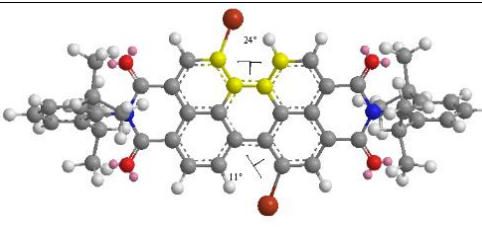
In addition to the N-substitution effect, it was observed that the PDI core twisting angle changed due to the binding of bromine atoms compared to the flat core of unsubstituted PDI. The change in core angle is also consistent with XRD results for the isolated crystal of dibromoPDI from a previously reported study [31]. This effect also caused a steric shielding among PDIs, with the twist frustrating close packing interactions. This is why the DiBr2PDI-2EH material displays better resistance to ACQ than PDIref, despite possessing the same imide group. DiBrPDI-DIA exhibited yet superior PLQY even at doping as high as 5% in films, as it has shielding due to both imide and bay groups, which provide rigid steric protection in contrast to the 2EH group.

3.3. Femtosecond Transient Absorption Properties (fs-TAS) of DiBrPDIs

Excited state properties of DiBrPDI-2EH and -DIA at 1.0×10^{-4} M and 1.0×10^{-3} M in CHCl$_3$, which exhibit similar behaviour at dilute concentrations (1.0×10^{-6} M, Figure 3b), were investigated. More detailed information about the pump–probe fs-TAS technique is detailed in previously reported study [14].

The TAS spectra of DiBrPDI-2EH and -DIA at different delayed time from 20 ps to 5.8 ns are summarized in Figure 6. Both DiBrPDIs exhibited only singlet state transitions at 1.0×10^{-4} M and 1.0×10^{-3} M. In summary, the DiBrPDIs showed overlap of both ground-state bleach (GSB) and stimulated emission (SE) signals at 529 nm (for -2EH), 532 nm (for -DIA), and also SE of fluorescence $S_{0-1'}$ at 575 nm (for -2EH) and 579 nm (for -DIA) at 1.0×10^{-4} M. Two intense PIA peaks, which were similar to each other, of DiBrPDI-2EH and -DIA were observed at 734 and 741 nm at 1.0×10^{-4} M, respectively. They exhibited similar features in the PIA regions (probably S1 to S2 or S3) as well as in the steady state features. Also, the PIA lifetimes of -2EH and -DIA were 4.3 and 4.6 ns, respectively (Table 3), in reasonable agreement with emission lifetimes in zeonex. These values are also similar to PDI derivatives reported with monomer structure [10,14,25]. At 1.0×10^{-3} M of DiBrPDIs, both PDIs' GSB-SE first overlap peaks shifted to a few nm longer wavelengths because of highly absorption of white light continuum of probe by DiBrPDIs [14] while the SE peaks did not change. No new peaks belonging to intersystem crossing transitions (which would otherwise reveal the presence of triplet states) were observed. It was observed that both DiBrPDIs were resistant to excimer-dimer at 1.0×10^{-3} M with no excessive increase in any PIA lifetime and no change observed at the SE peaks. The PIA lifetimes of DiBrPDI-2EH and -DIA were 5.0 and 4.8 ns, respectively (Figure 7 and Table 3), with larger values at these higher concentrations indicative of the formation of some excimer or dimer states [14].

Table 2. 3D study of brominated and unbrominated PDI-2EH and PDI-DIA.

Bay group.	PDI-2EH	PDI-DIA
-H	 ~6.0 Å =PDIref	 ~6.8 Å
-H	 ~11.0 Å =PDIref	 ~9.1 Å
DiBr		
DiBr		

Figure 6. TAS curves of DiBrPDI-2EH and DiBrPDI -DIA at 1.0 x 10^{-4} and 1.0 x 10^{-3} M concentrations in CHCl$_3$.

Table 3. Average lifetimes (ns, weighted average of mono or biexponential fit) for PIA peaks of DiBrPDIs at 1.0 x 10^{-4} and 1.0 x 10^{-3} M concentrations.

	DiBrPDI-2EH		DiBrPDI-DIA	
Concentration	1.0 x 10^{-4} M	1.0 x [10^{-3}] M	1.0 x 10^{-4} M	1.0 x 10^{-3} M
PIA (λ_{PIA}^{max}) Lifetime (ns)	4.3 ± 0.05	5.0 ± 0.01	4.6 ± 0.01	4.8 ± 0.09

18

Erkan AKSOY, Andrew DANOS, Chunyong LI, Andrew P. MONKMAN, Canan VARLIKLI

Figure 7. PIA peak decays of DiBrPDIs at 1.0 x 10^{-4} and 1.0 x 10^{-3} M concentrations in $CHCl_3$.

4. Conclusion

Unshielded planar PDIs often do not exhibit adequate photophysical properties in the film phase because of ACQ limiting many photonic applications. Especially in down-conversion studies, low rates of doping of PDIs must be made into an optical-resin in order to preserve the PLQYs of PDIs in the film phase. In this study, films and solutions of reference PDI and sterically shielded DiBrPDI derivatives with different steric imide groups were produced and compared. While both dibromoPDI derivatives exhibited very high luminescence compared to the reference at 0.25 and 5 % wt doped, DiBrPDI-DIA was able to exhibit very high PLQY even at a very high doping rate of 5 % due to the superior space filling steric protection of the DIA group. This structural property was confirmed by chemical computations. In this way, target white light downconverters may in future be produced by coating a single or several times instead of repeatedly coating from low concentrations [22], alongside enabling many other photonic applications of these materials.

Acknowledgment

References

[1]   M. Mosca, F. Caruso, L. Zambito, R. Macaluso, C. Cali, E. Feltin, Hybrid LEDs pave way to new lighting applications, Photonics Spectra. 47 (2013) 60–64.

[2]   M. Mosca, F. Caruso, L. Zambito, B. Seminara, R. Macaluso, C. Calì, et al., Warm white LED light by frequency down-conversion of mixed yellow and red Lumogen, in: Integr. Photonics Mater. Devices, Appl. II, 2013: p. 87670L. doi:10.1117/12.2017274.

[3]   F. Caruso, M. Mosca, R. MacAluso, E. Feltin, C. Calì, Generation of white LED light by frequency downconversion using perylene-based dye, Electron. Lett. 48 (2012) 1417–1419. doi:10.1049/el.2012.3084.

[4]   E. Aksoy, N. Demir, C. Varlikli, White LED light production using dibromoperylene derivatives in down conversion of energy, in: Can. J. Phys., 2018: pp. 734–739. doi:10.1139/cjp-2017-0752.

[5]   F. Galeotti, W. Mróz, M. Catellani, B. Kutrzeba-Kotowska, E. Kozma, Tailorable perylene-loaded fluorescent nanostructures: A multifaceted approach enabling their application in white hybrid LEDs, J. Mater. Chem. C. 4 (2016) 5407–5415. doi:10.1039/c6tc00486e.

[6]   S. a. Ruetten, J.K. Thomas, Fluorescence and triplet quantum yields of arenes on surfaces, J. Phys. Chem. B. 102 (1998) 598–606. doi:10.1021/jp972934o.

[7]   M. Mosca, R. Macaluso, I. Crupi, Hybrid Inorganic-Organic White Light Emitting Diodes, Polym. Light. Devices Displays. (2020) 197–262. doi:10.1002/9781119654643.ch8.

[8]   H. Langhals, Cyclic carboxylic imide structures as structure elements of high stability. Novel developments in perylene dye chemistry, Heterocycles. 40 (1995) 477–500. doi:10.3987/REV-94-SR2.

[9]   L. Chen, C. Li, K. Müllen, Beyond perylene diimides: Synthesis, assembly and function of higher rylene chromophores, J. Mater. Chem. C. 2 (2014) 1938–1956. doi:10.1039/c3tc32315c.

[10]   T. Guner, E. Aksoy, M.M. Demir, C. Varlikli, Perylene-embedded electrospun PS fibers for white light generation, Dye. Pigment. 160 (2019) 501–508. doi:10.1016/j.dyepig.2018.08.040.

[11]   C. Li, H. Wonneberger, Perylene imides for organic photovoltaics: Yesterday, today, and tomorrow, Adv. Mater. 24 (2012) 613–636. doi:10.1002/adma.201104447.

[12]   F. Würthner, C.R. Saha-Möller, B. Fimmel, S. Ogi, P. Leowanawat, D. Schmidt, Perylene Bisimide Dye Assemblies as Archetype Functional Supramolecular Materials, Chem. Rev. 116 (2016) 962–1052. doi:10.1021/acs.chemrev.5b00188.

[13]   V. Bozkus, E. Aksoy, C. Varlikli, Perylene based solution processed single layer woled with adjustable CCT and CRI, Electron. 10 (2021) 1–12. doi:10.3390/electronics10060725.

[14]   E. Aksoy, A. Danos, C. Li, A.P. Monkman, C. Varlikli, Silylethynyl Substitution for Preventing Aggregate Formation in Perylene Diimides, J. Phys. Chem. C. 125 (2021) 13041–13049. doi:10.1021/acs.jpcc.1c03131.

[15]   M. Kus, Ö. Hakli, C. Zafer, C. Varlikli, S. Demic, S. Özçelik, et al., Optical and electrochemical properties of polyether derivatives of perylenediimides adsorbed on nanocrystalline metal oxide films, Org. Electron. 9 (2008) 757–766. doi:10.1016/j.orgel.2008.05.009.

[16]   C. Karapire, M. Kus, G. Turkmen, C.C. Trevithick-Sutton, C.S. Foote, S. Icli, Photooxidation studies with perylenediimides in solution, PVC and sol-gel thin films under concentrated sun light, Sol. Energy. 78 (2005) 5–17. doi:10.1016/j.solener.2004.07.003.

[17]   C. Karapire, C. Zafer, S. Içli, Studies on photophysical and electrochemical properties of synthesized hydroxy perylenediimides in nanostructured titania thin films, Synth. Met. 145 (2004) 51–60. doi:10.1016/j.synthmet.2004.04.016.

[18]   J. Li, S. Yuan, J.S. Qin, L. Huang, R. Bose, J. Pang, et al., Fluorescence Enhancement in the Solid State by Isolating Perylene Fluorophores in Metal-Organic Frameworks, ACS Appl. Mater. Interfaces. 12 (2020) 26727–26732. doi:10.1021/acsami.0c05512.

[19]   Y. Zhang, B. He, J. Liu, S. Hu, L. Pan, Z. Zhao, et al., Aggregation-induced emission and the working mechanism of 1-benzoyl and 1-benzyl pyrene derivatives, Phys. Chem. Chem. Phys. 20 (2018) 9922–9929. doi:10.1039/c8cp00260f.

[20]   M. Stolte, T. Schembri, J. Süß, D. Schmidt, A.M. Krause, M.O. Vysotsky, et al., 1-Mono- And 1,7-Disubstituted Perylene Bisimide Dyes with Voluminous Groups at Bay Positions- And Search for Highly Effective Solid-State Fluorescence Materials, Chem. Mater. 32 (2020) 6222–6236. doi:10.1021/acs.chemmater.0c02115.

[21]   S.K. Mohan Nalluri, J. Zhou, T. Cheng, Z. Liu, M.T. Nguyen, T. Chen, et al., Discrete Dimers of Redox-Active and Fluorescent Perylene Diimide-Based Rigid Isosceles Triangles in the Solid State, J. Am. Chem. Soc. 141 (2019) 1290–1303. doi:10.1021/jacs.8b11201.

[22]   E. Aksoy, A. Danos, C. Varlikli, A.P. Monkman, Navigating CIE Space for Efficient TADF Downconversion WOLEDs, Dye. Pigment. 183 (2020) 108707. doi:10.1016/j.dyepig.2020.108707.

[23]   D. Schmidt, M. Stolte, S. Jasmin, A. Liess, V. Stepanenko, F. Würthner, Protein-like Enwrapped Perylene Bisimide Chromophore as a Bright Microcrystalline Emitter Material, Angew. Chemie - Int. Ed. 58 (2019) 13385–13389. doi:10.1002/anie.201907618.

Erkan AKSOY, Andrew DANOS, Chunyong LI, Andrew P. MONKMAN, Canan VARLIKLI

[24] B. Zhang, H. Soleimaninejad, D.J. Jones, J.M. White, K.P. Ghiggino, T. a. Smith, et al., Highly fluorescent molecularly insulated perylene diimides: Effect of concentration on photophysical properties, Chem. Mater. 29 (2017) 8395–8403. doi:10.1021/acs.chemmater.7b02968.

[25] R. Muñoz-Mármol, P.G. Boj, J.M. Villalvilla, J. a. Quintana, N. Zink-Lorre, Á. Sastre-Santos, et al., Effect of Substituents at Imide Positions on the Laser Performance of 1,7-Bay-Substituted Perylenediimide Dyes, J. Phys. Chem. C. (2021). doi:10.1021/acs.jpcc.1c00833.

[26] F. Kong, M. Lin, T. Qiu, The effect of imide substituents on the optical properties of perylene diimide derivatives, Luminescence. 33 (2018) 1209–1216. doi:10.1002/bio.3537.

[27] Q.U. Khan, G. Tian, L. Bao, S. Qi, D. Wu, Highly uniform supramolecular nano-films derived from carbazole-containing perylene diimide: Via surface-supported self-assembly and their electrically bistable memory behavior, New J. Chem. 42 (2018) 11506–11515. doi:10.1039/c8nj01380b.

[28] S. Chen, Y. Liu, W. Qiu, X. Sun, Y. Ma, D. Zhu, Oligothiophene-functionalized perylene bisimide system: Synthesis, characterization, and electrochemical polymerization properties, Chem. Mater. 17 (2005) 2208–2215. doi:10.1021/cm048642z.

[29] B. Jancy, S.K. Asha, Hydrogen-bonding-induced conformational change from J to H aggregate in novel highly fluorescent liquid-crystalline perylenebisimides, Chem. Mater. 20 (2008) 169–181. doi:10.1021/cm702497y.

[30] G. Paramaguru, N. Nagarajan, R. Renganathan, Effect of number of anchoring groups on binding ability of perylene diimides with SnO2 and TiO2 nanoparticles: A spectroscopic approach, J. Mol. Struct. 1038 (2013) 235–241. doi:10.1016/j.molstruc.2013.01.050.

[31] P. Rajasingh, R. Cohen, E. Shirman, L.J.W. Shimon, B. Rybtchinski, Selective bromination of perylene diimides under mild conditions, J. Org. Chem. 72 (2007) 5973–5979. doi:10.1021/jo070367n.

Comparison Photon Exposure and Energy Absorption Buildup Factors of CR-39 and Trivex Optical Lenses

Sevim BİLİCİ[1*], Ahmet BİLİCİ[2], Fatih KÜLAHCI[3]

[1] Department of Opticianry, Vocational School of Health Services, Bandirma Onyedi Eylul University, Balıkesir, Turkey
[2] Department of Medical Imaging Techniques, Vocational School of Health Services, Bandirma Onyedi Eylul University, Balıkesir, Turkey
[3] Department of Physics, Faculty of Science, Fırat University, Elazig, Turkey
[*1] sbilici@bandirma.edu.tr, [2] abilici@bandirma.edu.tr, [3] fatihkulahci@firat.edu.tr

Abstract: In the present study, Energy Absorption Buildup Factor (EABF) and Exposure Buildup Factors (EBF) of the CR-39 and Trivex optical lenses are calculated by using the Geometric Progression (GP) fitting method based on ANSI/ANS-6.4.3 database. The study analyses comprehensively for different penetration depths within the energy range of 0.015 - 15 MeV up to 40 mfp. The buildup factors are calculated in the examined materials depending on the photon energy that arrives, the penetration depths, and the chemical composition of the material reach at maximum values in the energy region where inconsistent scattering interaction probabilities are intensive. The results show that the CR-39 optical lens had better radiation shielding performance. The suitability of the results is compared with the powerful software tools (EPICS2017 and Phy-X/PSD), which are preferred frequently in the literature to calculate radiation shielding parameters. It is found that the relative changes between the EPICS2017 and Phy-X/PSD software compared with the results of this study are about 8% and 9% for the CR-39 and Trivex optical lens, respectively. This indicates that the results from the study are in good agreement.

Key words: CR-39, Trivex Optical lenses, Buildup factors, EPICS2017 Library, Phy-X/PSD Software.

CR-39 ve Trivex Optik Lenslerinin Foton Maruz Kalma ve Enerji Soğurma Buildup Faktörlerinin Karşılaştırılması

Öz: Bu çalışmada CR-39 ve Trivex optik lenslerinin enerji absorpsiyon buildup faktörü (EABF) ve maruz kalma buildup faktörleri (EBF), geometrik ilerleme (GP) uydurma yöntemi kullanılarak ve ANSI/ANS-6.4.3 veri tabanı dikkate alınarak hesaplanmıştır. Çalışma 0.015 ila 15 MeV enerji aralığında ve 40 mfp'ye kadar farklı penetrasyon derinliği için kapsamlı bir şekilde analiz edilmiştir. İncelenen materyallerde hesaplanılan her iki buildup faktörünün gelen fotonun enerjisine, penetrasyon derinliklerine ve materyalin kimyasal bileşimine bağımlılık gösterdiği ve tutarsız saçılma etkileşim olasılıklarının baskın olduğu enerji bölgesinde maksimum değerlerine ulaştığı bulundu. Sonuçlar, CR-39 optik lensinin daha iyi radyasyon koruma performansına sahip olduğunu gösterdi. Sonuçların uygunluğu radyasyon koruyucu parametrelerin hesaplanmasında literatürde sıklıkla tercih edilen EPICS2017 ve Phy-X/PSD güçlü yazılım araçları ile karşılaştırıldı. EPICS2017 ve Phy-X/PSD yazılımları ile bu çalışmadan elde edilen sonuçlar arasında nispi değişikliklerin CR-39 ve Trivex Optik lensi için sırasıyla %8, %9 olduğu bulundu. Bu, çalışmadan elde edilen sonuçların iyi bir uyum gösterdiğini belirtmektedir.

Anahtar kelimeler: CR-39, Trivex Optik lensleri, Buildup Faktörü, EPICS2017 Kütüphanesi, Phy-X/PSD Yazılımı.

1. Introduction

CR-39 is a type of plastic in which the optical, mechanical, and physical features of glass are combined. It is used widely in the optical industry with chemical structure and composition for, processing and coatings and it has structure lighter than mineral glasses. CR-39 Resin (Columbia Resin) developed by Pittsburgh Plate Glass Company (PPG) is known also as Allyl Diglycol Carbonate (ADC). The lenses made from CR-39 polymer are resistant against scratches, heat, and household chemicals [1–3]. In addition to their optical use in eyeglass lenses, they are also used in detectors and glass-reinforced fuel tanks for fighter planes to detect radioactive particles such as alpha and protons. The PPG focused on Trivex optical lens is lighter material, in 2001. This lens has excellent impact resistance, and is preferred highly in the optical industry. Trivex lenses are polyurethane, and have optical quality, light weight, and safety features. They are named based on these features [3]. They are also lighter than the CR-39 optical lens [3,4].

---

[*] Corresponding author: sbilici@bandirma.edu.tr. ORCID Number of authors: [1] 0000-0002-7694-5081, [2] 0000-0002-3192-456X, [3] 0000-0001-6566-4308

The uses of these lenses are preferred in the optical industry, and especially they increase in eyeglasses, with their importance even more. For this reason, it is important to determine the radiation shielding features of optical lenses.The radiation shielding features differ according to the type of the optical lens used. The World Health Organization (WHO) issued an urgent international public health warning as Public Health Emergency of International Concern (PHEIC) on January 30, 2020, which included recommendations for the use of goggles or face shields to protect against eye contamination of CoV [5]. There are some reports on its effect on the eye in the recent CoVid-19 pandemic [6,7].

The buildup factors for CR-39 and Trivex optical lenses were investigated in the present study by using gamma rays within 0.015-15 MeV energy range. These Gamma rays pass through a medium that interact with the atoms of the substance as a result of which some of them are absorbed or scattered, which creates fluorescence, pair production, and Bremsstrahlung secondary photons. The buildup factors stand for the contribution of secondary photons to the number of photons present at a specific point. It is also defined as the rate of the total amount of photons at a fixed point to the number of photons that arrive at that point without any interaction [8,9]. Buildup factors are evaluated in two classes, which are the Exposure Buildup Factor (EBF) and the Energy Absorption Buildup Factor (EABF). The quantity of interest in EBF is the exposure to incoming photons, and it is the amount of energy stored or absorbed in the material interacting with the photon in EABF [10]. In this study, the database is prepared by the American Nuclear Society (ANS) Standards Committee Work Group ANS-6.4.3 [11] and approved by the American National Standards Institute (ANSI) and then taken as the reference to calculate the buildup factors. The data include a compilation of the Geometric-Progression (G-P) fitting parameters for penetration depths of up to 40mfp (i.e. the mean free path) within the 0.015-15MeV energy range [8,12]. The G-P fitting formula by Harima (1983) and Harima et al. (1986, 1991) is used to determine the buildup factors that took into account multiple scattering. All the results obtained in this study are compared with powerful tools e.g. EPICS2017 [13] and Phy-X/PSD [14] that made radiation shielding parameters, and the results are found as compatible.

2. Materials and Methods

The chemical formula of CR-39 is $(C_{12}H_{18}O_7)_n$, where the elemental compositions of C, H and O contents are 52.6% wt, 6.6% wt and 40.8% wt, respectively. The chemical formula of Trivex is $(C_{11}H_{18}N_2)_n$, with the elemental compositions of C, H and N contents are 74.1% wt, 10.2% wt and 15.7% wt, respectively. Some other features of CR-39 and Trivex optical lenses are given in Table 1 [1,3,4,15–17].

Tablo 1. Some of the physical and optical parameters for lenses

Parameters	CR-39	Trivex
Refractive index (n)	1.49	1.53
Abbe number	58	43-45
Density (g cm^{-3})	1.32	1.11
Average molecular weight (g/mol)	274.26	178.27
Molar Volume (V_m), (cm^3/mol)	207.77	160.60

It is expected that the polymer structures of the lenses are used commonly in the optical industry, and they have good radiation protection potential. The Equivalent Atomic Number (Z_{eq}), G-P fitting parameters, and EBF and EABF values of the CR-39 and Trivex optical lenses are examined and calculated in this study within the photon energy range of 0.015-15 MeV up to 40 mean free path (mfp) penetration depth. The EBF and EABF values are evaluated by the G-P Fitting method, which is a very convenient and precise approach in calculating EBF and EABF values. The mass attenuation coefficients (MAC) for CR-39 and Trivex optical lenses are obtained theoretically by using the XCOM Web Program [18], which provides convenience to the user with interface that is developed by NIST including a list to describe the material [19,20]. The MAC values of any element, compound or mixture can be assessed with this program for partial photon interactions such as atomic photoelectric effect, incoherent, coherent scattering, and pair production as well as for total photon interaction. MAC is an important parameter for description of how much incoming photon is absorbed, transmitted, and scattered when it interacts with the matter [21]. The amount of photon that is transmitted from a material is calculated by the Beer-Lambert $I = I_0 e^{-\mu x}$ law, which links the absorption of light in optics to the features of the material through which it passes [22–25]. Here I_o is the intensity of the incoming photon, I is the intensity of the transmitted photon, x is the thickness, and μ is the MAC value. Basically, this law applies under three conditions, which are monochromatic beam, thin absorber material, and narrow beam geometry. If one of the conditions is not met, then the law loses

its validity. In such a case, it is changed as the Beer-Lambert $I = BI_0 e^{-\mu x}$, Law where B (E, x) is the buildup factor [9,21,26]. The photon buildup factor represents the amount of the secondary photons that are included in the total photon number at a specified point [9]. By using the G-P method with ANSI/ANS-6.4.3 database, the buildup factors take place in three steps after determining the equivalent atomic number (Z_{eq}), G-P fitting coefficients, and EBF/EABF values.

2.1. Computation of the equivalent atomic number (Z_{eq})

The MAC values are obtained for the selected CR-39 and Trivex lenses in the 0.015-15 MeV energy range by using the XCOM program. The Z_{eq} values are determined with the logarithmic interpolation method given in the following equation by using the ratio between the Compton partial mass attenuation coefficient (μ_m)$_{Compton}$ and the total mass attenuation coefficients (μ_m)$_{total}$ [27–30]. Z_{eq} is a parameter dependent on the energy of the incoming photon describing the features of a material in terms of equivalent elements in scattering interactions [14,31]. Basically, the accumulation of photons consists of multiple scattering resulting from the Compton scattering process. For this reason, the determination of Z_{eq} is based frequently on the (μ_m)$_{Compton}$ calculation [30].

$$Z_{eq} = \frac{Z_1 \left(\log R_2 - \log R \right) + Z_2 \left(\log R - \log R_1 \right)}{\log R_2 - \log R_1} \tag{1}$$

Here R's are the (μ_m)$_{Compton}$/(μ_m)$_{total}$ ratio. Z_1 and Z_2 refer to the atomic numbers of the elements corresponding to the ratios of R_1 and R_2, respectively.

2.2. Computation of the G-P fitting coefficients

The geometric-progression (G-P) fitting formula by Harima (1983) [29] and Harima et al (1986, 1991) [32,33] has been used widely to calculate the buildup factors (EABF and EBF) for a wide variety of materials [34]. G-P fitting parameters for the elements are obtained from the database of the American Nuclear Society standard ANSI/ANS 6.4.3 [11]. The ANSI/ANS 6.4.3 standard database has compiled G-P fitting parameters and buildup factor data up to 40 mfp in the photon energy range of 0.015-15 MeV for 23 elements in addition to a compound (water) and two mixtures (air and concrete). Mfp (mean free path) is the path taken by the photon between two interactions. In this study, the Z_{eq} values are calculated for the CR-39 and Trivex optical lenses as in the previous step; the G-P fitting coefficients (a, b, c, d and X_k) are calculated according to the following expression.

$$P = \frac{P_1 \left(\log Z_2 - \log Z_{eq} \right) + P_2 \left(\log Z_{eq} - \log Z_1 \right)}{\log Z_2 - \log Z_1} \tag{2}$$

where the P's are the G-P fitting coefficients corresponding to the Z atomic numbers at the determined energy.

2.3. Computation of the buildup factors

EBF and EABF values are obtained from the following equations using the G-P fitting parameters for the CR-39 and Trivex optical lenses in the previous step [32]. The buildup factor is expressed as a function of mfp [30].

$$B(E,x) = 1 + (b-1) \times \begin{cases} \dfrac{K^x - 1}{K - 1} & K \neq 1 \\[2mm] x & K = 1 \end{cases} \tag{3}$$

$$K(E,x) = cx^a + d\, \frac{\tanh\left(x/X_k - 2 \right) - \tanh(-2)}{1 - \tanh(-2)} \quad \textit{for } x \leq 40\, mfp \tag{4}$$

Here, E is the photon energy, x is the mfp value, and a, b, c, d and X_k are the G-P fitting coefficients. The b coefficient corresponds to the buildup factor in 1 mfp. The parameter K (E, x) expresses the photon dose multiplier and the change in the shape of the spectrum at 1 mfp.

3. Results and Discussion

The buildup factors are calculated for the CR-39 and Trivex optical lenses using the procedure as described above. It is necessary to know the Z_{eq} and G-P fitting coefficients to calculate the buildup factors according to the G-P fitting method. The MAC values from the XCOM program are used in the photon energy range of 0.015-15 MeV to calculate the Z_{eq} values of the optical lenses that are considered in the study. The G-P fitting coefficients of these optical lenses are evaluated in the photon energy range of 0.015-15 MeV using the ANSI Database. Some results are given in Tables 2-5 for the examined optical lenses that. The dependency of the calculated buildup factors on Z_{eq}, incoming photon energy and mfp is discussed in the following parts. All the results of this study are compared with powerful software such as EPICS2017 and Phy-X/PSD. EPICS2017 calculates the photon attenuation and accumulation factors for the energy absorption and exposure. The data library is formed by interpolation of the relevant photon energies in the ENDF-6 [35] data format on IAEA-NDS website. Phy-X/PSD is an online software that is developed to calculate various radiation shielding parameters. The WinXCOM software is useful to generate the data library. The deviation percentages (Dev.%) between the buildup factors are obtained from the EPICS2017 and Phy-X/PSD software according to Equation 5, and some of the buildup factors are given in Tables 4 and 5. The maximum EBF deviations are between Phy-X/PSD and EPICS2017 software as 7.889 for CR-39 and 9.322 for Trivex. The maximum deviations are 4.230 for CR-39, 6.351 for Trivex for the EABF values, which indicates that the results are compatible.

$$Dev. = \left| \frac{\left(EBF \right)_{EPICS2017} - \left(EBF \right)_{XCOM}}{\left(EBF \right)_{XCOM}} \right| \times 100 \tag{5}$$

Tablo 2. G-P fitting parameters (exposure and absorption) calculated in this work for CR-39

Energy (MeV)	Z_{eq}	EBF					EABF				
		a	b	c	d	X_k	a	b	c	d	X_k
0.015	6.7447	0.1648	1.2729	0.4906	-0.0824	14.2911	0.1611	1.2738	0.4940	-0.0782	14.5319
0.02	6.7589	0.1178	1.6236	0.6199	-0.0578	15.4035	0.1207	1.6345	0.6150	-0.0593	15.2654
0.03	6.7702	0.0357	2.8229	0.9092	-0.0293	15.0661	0.0350	2.9259	0.9098	-0.0274	15.2930
0.04	6.7770	-0.0690	4.2368	1.3787	0.0271	13.6567	-0.0672	4.2241	1.3677	0.0251	13.8412
0.05	6.7815	-0.1244	5.4041	1.7374	0.0539	13.9562	-0.1214	5.0296	1.7240	0.0518	14.0599
0.06	6.7861	-0.1624	5.8791	2.0269	0.0746	13.8894	-0.1578	5.1888	1.9914	0.0708	13.9971
0.08	6.7939	-0.2005	5.7148	2.3614	0.0912	13.5291	-0.1894	4.9021	2.2699	0.0822	13.6942
0.1	6.7986	-0.2008	5.3312	2.4111	0.0871	14.3662	-0.1886	4.5921	2.3117	0.0786	14.5252
0.15	6.8023	-0.2152	4.0590	2.5292	0.0966	14.1348	-0.1912	3.7035	2.3325	0.0768	14.5800
0.2	6.8049	-0.2117	3.4714	2.4601	0.0919	13.6414	-0.1819	3.3289	2.2243	0.0760	14.7911
0.3	6.8112	-0.1856	3.0048	2.1921	0.0789	14.1872	-0.1687	2.8364	2.0662	0.0669	14.4223
0.4	6.8132	-0.1686	2.7329	2.0169	0.0707	13.8948	-0.1506	2.6271	1.8985	0.0606	14.3832
0.5	6.8140	-0.1509	2.5647	1.8677	0.0646	14.1585	-0.1379	2.4627	1.7841	0.0566	14.3938
0.6	6.8149	-0.1365	2.4408	1.7567	0.0577	13.9871	-0.1232	2.3745	1.6713	0.0492	14.3736
0.8	6.8148	-0.1157	2.2542	1.6017	0.0514	13.9916	-0.1055	2.2026	1.5460	0.0437	14.1934
1	6.8161	-0.0984	2.1401	1.4863	0.0444	13.9690	-0.0871	2.1011	1.4383	0.0364	14.6302
1.5	6.1870	-0.0669	2.0007	1.3029	0.0315	13.8816	-0.0599	1.9397	1.2748	0.0264	14.3027
2	6.1626	-0.0433	1.8960	1.1893	0.0200	14.0267	-0.0373	1.8420	1.1680	0.0148	14.4658
3	6.1560	-0.0140	1.7468	1.0584	0.0058	12.2964	-0.0113	1.7141	1.0508	0.0029	14.1578
4	6.1526	0.0040	1.6498	0.9865	-0.0074	24.0742	0.0037	1.6262	0.9888	-0.0028	13.0639

5	6.1516	0.0172	1.5730	0.9392	-0.0112	14.3983	0.0151	1.5641	0.9451	-0.0081	14.8325
6	6.1503	0.0266	1.5236	0.9071	-0.0155	14.0908	0.0281	1.5161	0.9039	-0.0181	13.1077
8	6.1475	0.0373	1.4376	0.8709	-0.0320	16.2444	0.0341	1.4295	0.8828	-0.0170	12.1088
10	6.1458	0.0414	1.3713	0.8577	-0.0211	12.5927	0.0398	1.3759	0.8604	-0.0221	14.3094
15	6.1449	0.0463	1.2752	0.8410	-0.0303	15.2397	0.0472	1.2812	0.8384	-0.0328	15.7840

Tablo 3. G-P fitting parameters (exposure and absorption) calculated in this work for Trivex

Energy (MeV)	Z_{eq}	EBF					EABF				
		a	b	c	d	X_k	a	b	c	d	X_k
0.015	5.8161	0.1379	1.4398	0.5616	-0.0677	14.4122	0.1435	1.4538	0.5490	-0.0725	14.5000
0.02	5.8315	0.0698	1.9858	0.7662	-0.0359	16.1229	0.0673	2.0145	0.7720	-0.0344	16.3288
0.03	5.8421	-0.0402	3.6807	1.2242	0.0147	13.0577	-0.0393	3.8743	1.2231	0.0139	12.8917
0.04	5.8453	-0.1373	5.4860	1.8151	0.0602	14.0005	-0.1353	5.1513	1.8033	0.0586	14.1345
0.05	5.8528	-0.1775	6.9258	2.1829	0.0769	14.3679	-0.1700	5.6279	2.1257	0.0714	14.5246
0.06	5.8564	-0.2046	7.4053	2.4571	0.0905	14.5334	-0.1905	5.4220	2.3387	0.0802	14.7032
0.08	5.8633	-0.2315	6.9387	2.7520	0.1014	14.4911	-0.2068	4.8291	2.5267	0.0835	14.8626
0.1	5.8643	-0.2401	6.1882	2.8500	0.1035	14.5727	-0.2112	4.2682	2.5798	0.0834	14.9422
0.15	5.8506	-0.2470	4.5611	2.8895	0.1073	14.2674	-0.2042	3.5238	2.4950	0.0765	15.2121
0.2	5.8712	-0.2381	3.7759	2.7568	0.1080	15.0281	-0.1951	3.1764	2.3653	0.0744	15.0837
0.3	5.8737	-0.2170	3.1521	2.4693	0.0980	14.3763	-0.1759	2.7888	2.1387	0.0697	14.9957
0.4	5.8752	-0.1978	2.8481	2.2436	0.0837	13.3713	-0.1544	2.6200	1.9354	0.0634	14.8063
0.5	5.8758	-0.1764	2.6618	2.0498	0.0823	14.0470	-0.1390	2.4534	1.8070	0.0618	15.9483
0.6	5.8764	-0.1559	2.5465	1.8831	0.0657	13.5971	-0.1198	2.3959	1.6680	0.0461	14.9729
0.8	5.8768	-0.1367	2.3180	1.7127	0.0669	13.7550	-0.1095	2.1968	1.5658	0.0464	14.0932
1	5.8764	-0.1127	2.1998	1.5579	0.0553	13.7519	-0.0934	2.0864	1.4631	0.0408	14.1655
1.5	5.2502	-0.0791	2.0563	1.3541	0.0433	13.7533	-0.0612	1.9388	1.2808	0.0275	14.3136
2	5.2328	-0.0483	1.9396	1.2075	0.0261	14.2773	-0.0407	1.8379	1.1757	0.0180	14.1990
3	5.2296	-0.0171	1.7777	1.0645	0.0095	12.5315	-0.0125	1.7160	1.0515	0.0047	13.2708
4	5.2250	0.0055	1.6759	0.9805	-0.0053	19.1483	0.0038	1.6281	0.9890	-0.0031	14.4484
5	5.2246	0.0177	1.5921	0.9351	-0.0101	14.9222	0.0162	1.5680	0.9437	-0.0092	14.1768
6	5.2246	0.0260	1.5363	0.9065	-0.0144	14.7317	0.0276	1.5264	0.9033	-0.0154	12.9421
8	5.2238	0.0357	1.4470	0.8683	-0.0237	14.8066	0.0404	1.4463	0.8625	-0.0212	11.3814
10	5.2236	0.0412	1.3811	0.8510	-0.0186	13.1120	0.0401	1.3871	0.8555	-0.0212	14.4388
15	5.2215	0.0475	1.2831	0.8340	-0.0256	14.2945	0.0470	1.2923	0.8353	-0.0279	14.5319

Tablo 4. Comparison of buildup factors from Phy-X/PSD, EPICS2017 and this work for CR-39

Energy (MeV)	EBF for 1 mfp			EBF for 5 mfp			EBF for 10 mfp			EBF for 40 mfp		
	Phy-X/ PSD	EPICS 2017	This work	Phy-X/ PSD	EPICS 2017	This work	Phy-X/ PSD	EPICS 2017	This work	Phy-X/ PSD	EPICS 2017	This work
0.015	1.2708	1.2705	1.2729	1.6691	1.6683	1.6744	1.9108	1.9096	1.9180	2.6201	2.6177	2.6317
0.1	5.3381	5.3365	5.3312	89.6972	89.5769	89.5267	551.7521	550.5560	548.7464	60337.2317	60070.6000	58189.1673

Energy (MeV)												
0.2	3.4601	3.4601	3.4714	51.5413	51.5400	51.9123	298.7471	298.7350	303.3430	19721.7098	19720.1000	21410.9834
1.5	2.0024	2.0025	2.0007	8.0396	8.0400	8.0266	18.4882	18.4891	18.4502	108.2787	108.2820	107.8566
3	1.7463	1.7464	1.7468	5.0025	5.0026	5.0040	9.3736	9.3738	9.3738	37.9086	37.9092	37.8260
15	1.2752	1.2752	1.2752	2.1397	2.1397	2.1395	3.0653	3.0653	3.0652	7.9250	7.9248	7.9268
Energy (MeV)	EABF for 1 mfp			EABF for 5 mfp			EABF for 10 mfp			EABF for 40 mfp		
0.015	1.4443	1.4442	1.4398	2.2362	2.2357	2.2196	2.7882	2.7875	2.7607	4.6767	4.6749	4.5985
0.1	6.1872	6.1882	6.1882	146.0108	146.0500	146.7632	1152.5615	1152.9800	1159.4548	208977.6072	209124.0000	204136.5642
0.2	3.7711	3.7711	3.7759	72.0774	72.0744	72.0285	502.3245	502.2900	501.0687	48246.3886	48240.4000	47726.6145
1.5	2.0578	2.0579	2.0563	8.7816	8.7823	8.7531	20.6700	20.6721	20.5497	126.1588	126.1770	123.8823
3	1.7769	1.7770	1.7777	5.1885	5.1890	5.1775	9.7418	9.7426	9.6777	39.0314	39.0337	37.6838
15	1.2836	1.2836	1.2831	2.1576	2.1577	2.1589	3.0696	3.0696	3.0790	7.7658	7.7657	7.9264

Tablo 5. Comparison of buildup factors from Phy-X/PSD, EPICS2017 and this work for Trivex

Energy (MeV)	EBF for 1 mfp			EBF for 5 mfp			EBF for 10 mfp			EBF for 40 mfp		
	Phy-X/ PSD	EPICS 2017	This work	Phy-X/ PSD	EPICS 2017	This work	Phy-X/ PSD	EPICS 2017	This work	Phy-X/ PSD	EPICS 2017	This work
0.015	1.4443	1.4442	1.4398	2.2362	2.2357	2.2196	2.7882	2.7875	2.7607	4.6767	4.6749	4.5985
0.1	6.1872	6.1882	6.1882	146.0108	146.0500	146.7632	1152.5615	1152.9800	1159.4548	208977.6072	209124.0000	204136.5642
0.2	3.7711	3.7711	3.7759	72.0774	72.0744	72.0285	502.3245	502.2900	501.0687	48246.3886	48240.4000	47726.6145
1.5	2.0578	2.0579	2.0563	8.7816	8.7823	8.7531	20.6700	20.6721	20.5497	126.1588	126.1770	123.8823
3	1.7769	1.7770	1.7777	5.1885	5.1890	5.1775	9.7418	9.7426	9.6777	39.0314	39.0337	37.6838
15	1.2836	1.2836	1.2831	2.1576	2.1577	2.1589	3.0696	3.0696	3.0790	7.7658	7.7657	7.9264
Energy (MeV)	EABF for 1 mfp			EABF for 5 mfp			EABF for 10 mfp			EABF for 40 mfp		
0.015	1.4584	1.4582	1.4538	2.2567	2.2563	2.2357	2.8122	2.8115	2.7706	4.7291	4.7272	4.5525
0.1	4.2714	4.2713	4.2682	78.8384	78.8426	78.8725	567.7329	567.8160	568.1815	97565.4832	97608.1000	97158.0623
0.2	3.1825	3.1825	3.1764	44.1534	44.1532	44.1546	263.0272	263.0240	263.2623	21207.7910	21206.9000	21144.1716
1.5	1.9366	1.9366	1.9388	7.4671	7.4671	7.4704	17.0071	17.0072	16.9911	101.1113	101.1130	100.5558
3	1.7150	1.7150	1.7160	4.8122	4.8122	4.8064	8.9519	8.9518	8.9104	35.7384	35.7372	34.8036
15	1.2921	1.2922	1.2923	2.1965	2.1966	2.1979	3.1442	3.1443	3.1482	7.8822	7.8822	7.9302

3.1. The depence of buildup factors on Z_{eq}

The Z_{eq} values for CR-39 and Trivex optical lenses are given in Tables 2, 3 and they indicate that Trivex had lower values than CR-39. Although Z_{eq} depends on the incoming photon energy it differed for all materials, because of the differences in the materials chemical structure. It is seen in Figure 2. (a-d) that the buildup factors depend on the chemical composition. The fact that the Trivex had higher buildup factor values than CR-39 may be associated with Trivex's lower Z-element polymer structure. The size of the accumulation factors and their dependence on Z_{eq} vary depending on the energy region in question. Although the Z_{eq} values for both optical lens materials had small values in the low and high energy regions, they have high values in the medium energy region, which can be explained by the dominance of the photon interaction process. Z_{eq} has the maximum value in the region dominated by Compton scattering as there is a strong dependence on Z_{eq} in this energy region. Low Z_{eq} values occur because of the dominance of photoelectric interactions in the low energy region and pair production interactions in the high energy region. It is seen from Figure 3 (a-d) that the buildup factors at 0.015 and 0.15 MeV are inversely proportional to Z_{eq} for all determined mfps. The buildup factors of the lens materials at 1.5 and 15 MeV are nearly constant for all mfps, which indicates that the buildup factors are independent of Z_{eq} and of the chemical structure of the material.

28

(a)   (b)
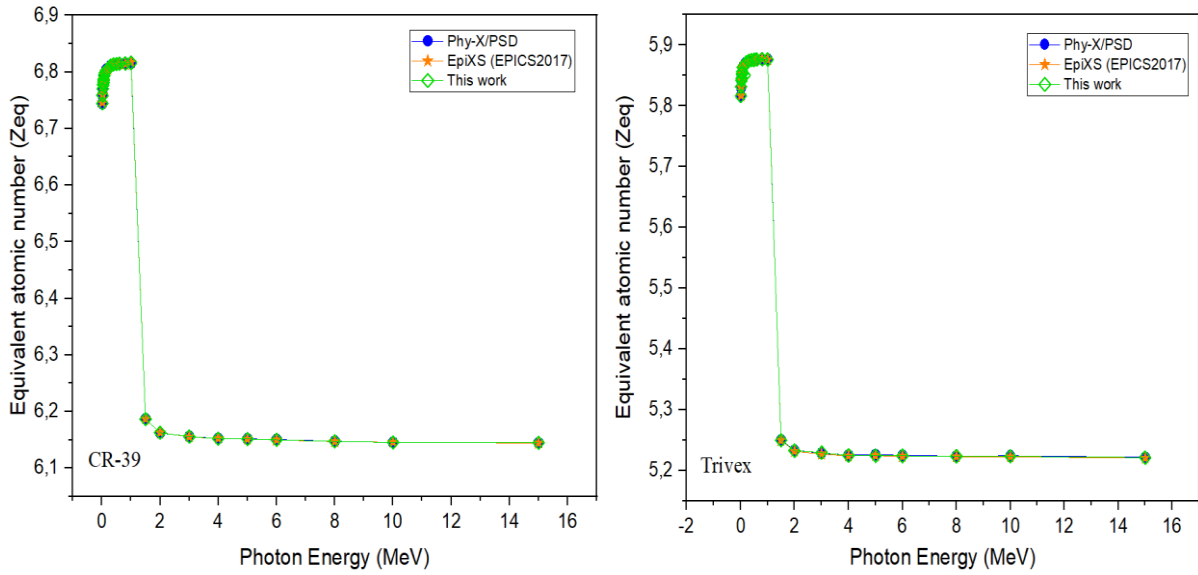
Figure 1. (a–b) Equivalent atomic numbers of the CR-39 and Trivex optical lenses with photon energy.

3.2. The depence of buildup factors on incident photon energy

It is seen that the EBF and EABF changes calculated for the CR-39 and Trivex optical lenses and given in Table 2 and 3 are similar. In the low energy range, photoelectric is dominant, and in the high energy range, the absorption of photons is more because the pair production is dominant. Thus, the lifetime of photons in optical materials is short. This is Figure 2. When (a-d) is examined, it can be explained as the reason for the formation of less buildup factor in low and high energy regions. In the intermediate energy region, since Compton scattering is dominant, only the energies of the photons change and their lifetimes in the material are longer. This causes more buildup factor in the material. Maximum buildup occurs in the intermediate energy range where scattering increases [9]. Maximum buildup factor values for CR-39 and Trivex optical lens materials were approximately 58189 and 204136, respectively. In the intermediate energy values where Compton scattering is dominant, the buildup factor values are independent of the chemical composition.

(a)   (b)
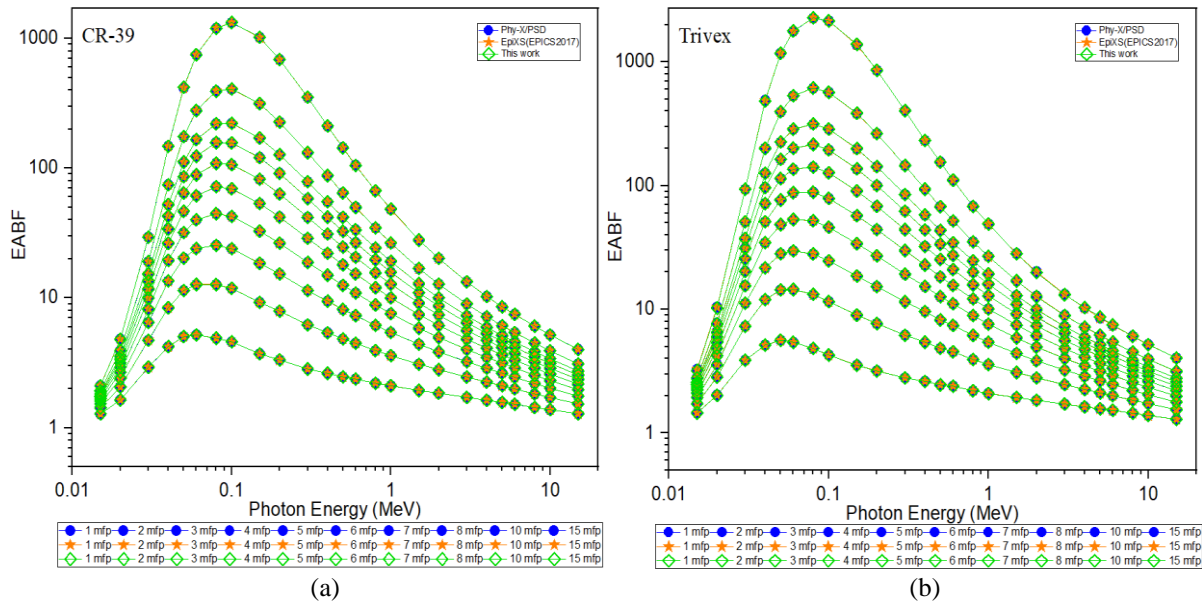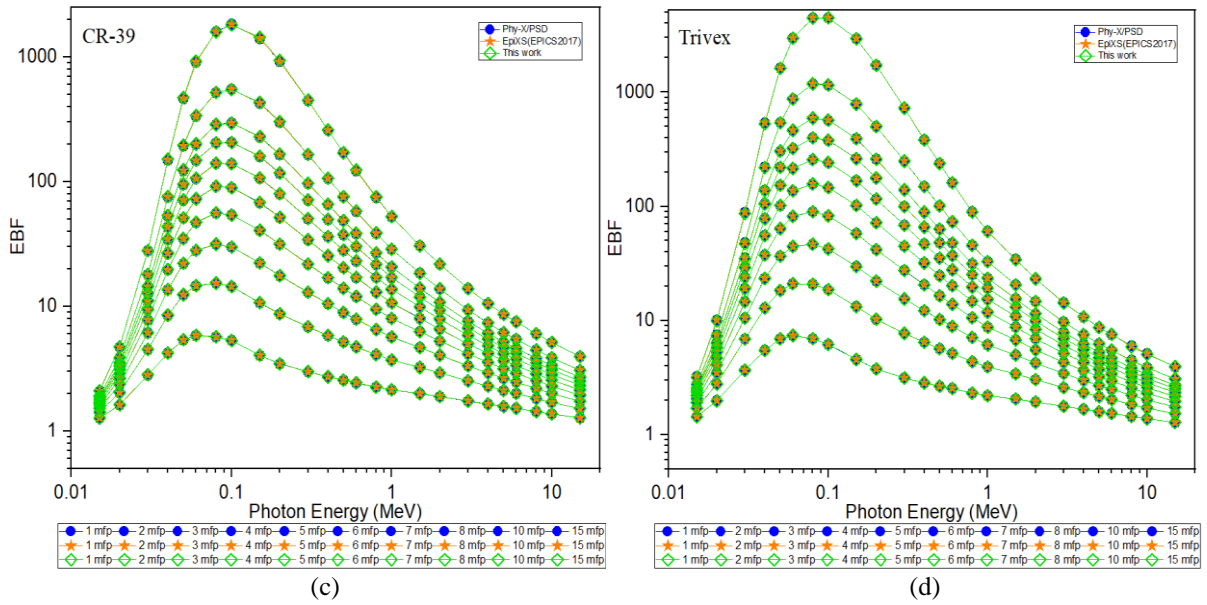
Figure 2. (a–d) The buildup factors in the energy region 0.015–15 MeV at the 1–15 mfp for CR-39 and Trivex optical lenses.

3.3. The depence of buildup factors on penetration depth

The variation of mfp for CR-39 and Trivex optical lenses at some specific photon energies such as 0.015, 0.15, 1.5 and 15 MeV is given in Figure 3 (a–d) and Figure 4 (a–d). In general, an increase in buildup factors is valid as increasing mfp values. This observation arises from the fact that the big mfp is proportional to the photon scattering. Maximum buildup factors for the optical materials study range are from 41833-58189 to 99626-204136 for CR-39 and Trivex, respectively. The buildup factor results reveal that the EBF effect should be considered at high penetration depths.

(a)

(b)

(c)

(d)
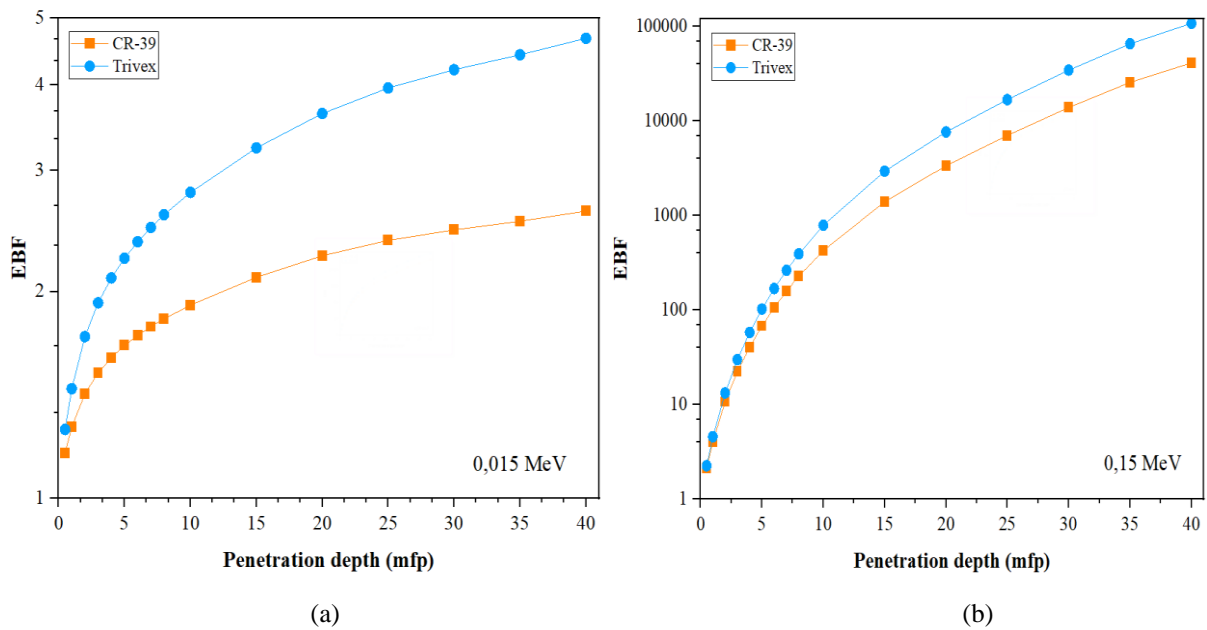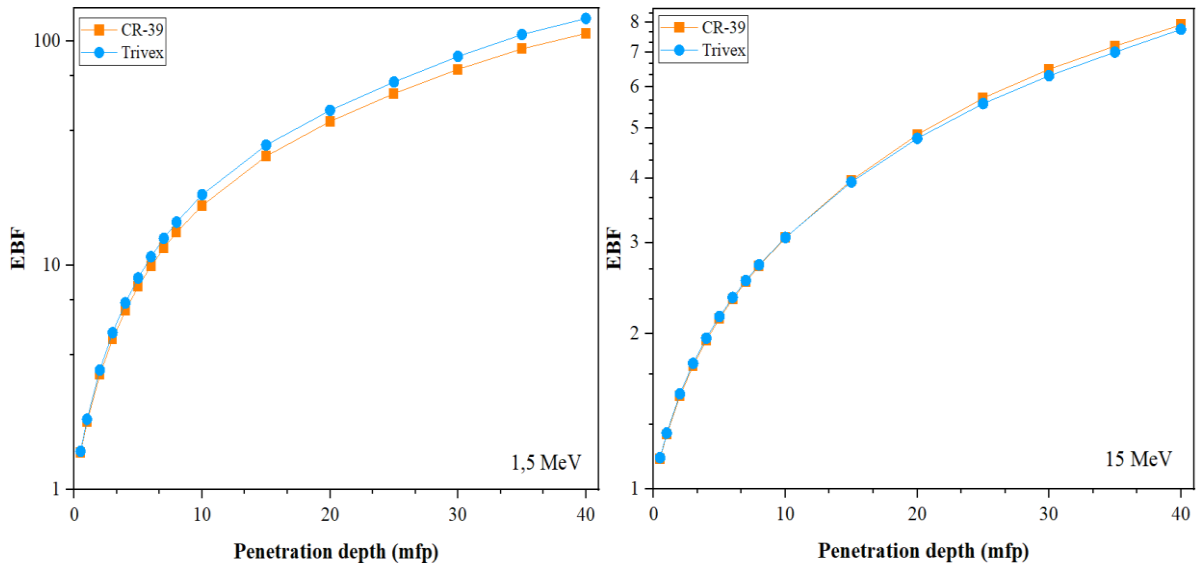
Figure 3. (a–d) The exposure buildup factors in the energies 0.015,0.15,1.5 and 15 MeV at the 1–40 mfp for CR-39 and Trivex optical lenses.

(a)

(b)

(c)

(d)
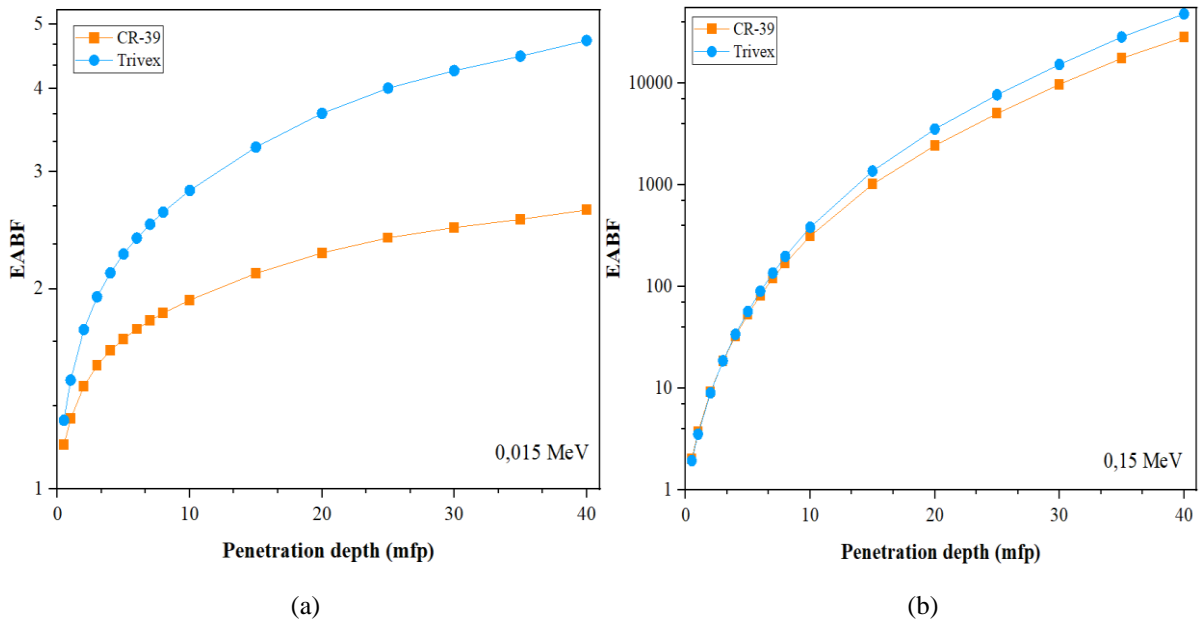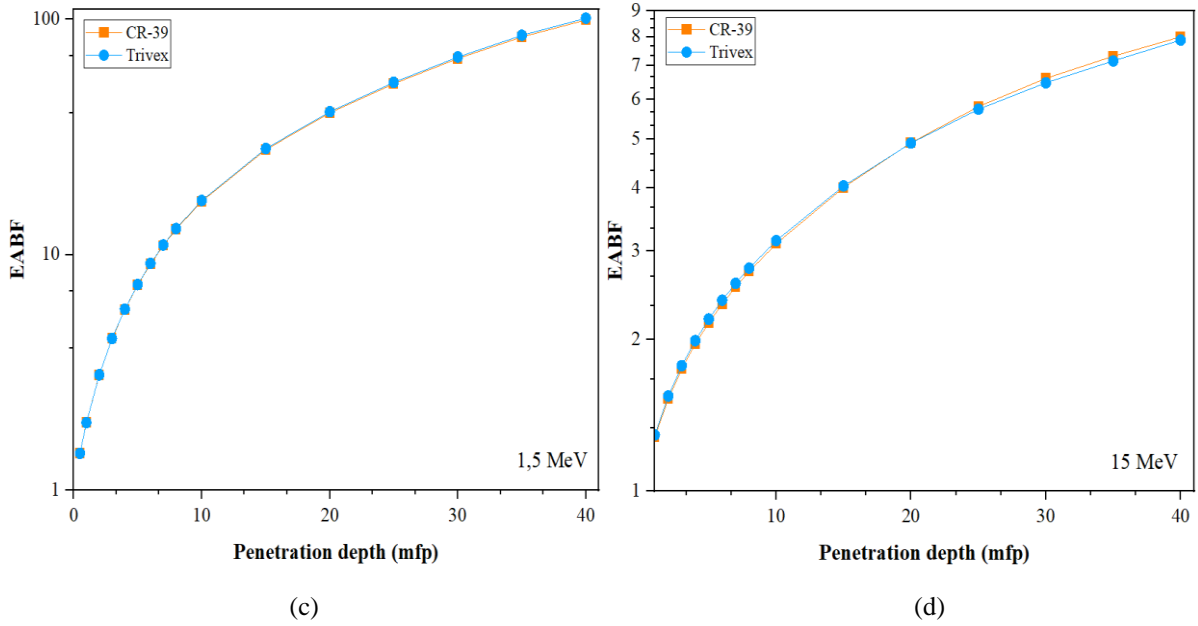
Figure 4. (a–d) The energy absorption buildup factors in the energies 0.015,0.15,1.5 and 15 MeV at the 1–40 mfp for CR-39 and Trivex optical lenses

The variation of the accumulation factors at 1 and 40 mfp for CR-39 and Trivex optical glasses is given in Figure 5 (a-d). It is seen that the maximum EABF values are 5.196-41833 and 5.627-99626, respectively for CR-39 and Trivex optical glasses at 1 and 40 mfp, and the maximum EBF values are 5.879-58189 and 7.405-204136, respectively. Furthermore, CR-39 had lower buildup values, which indicate that CR-39 had a greater absorption effect than scattering. Like the explanations given above, it is obvious that the accumulation effects are much higher in the intermediate energy region, where Compton scattering is dominant and tended to decrease in the high energy region at dominant pair production. The chemical composition of the investigated materials had no impact on the accumulation factor values in the high-energy region.

(a)

(b)

(c) (d)
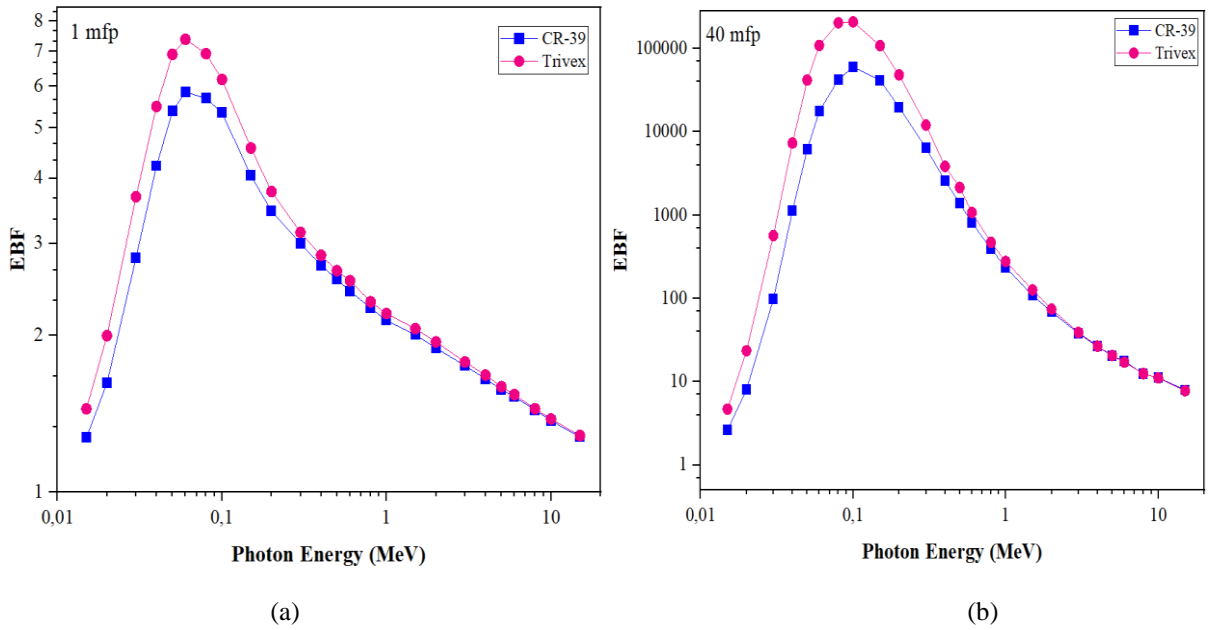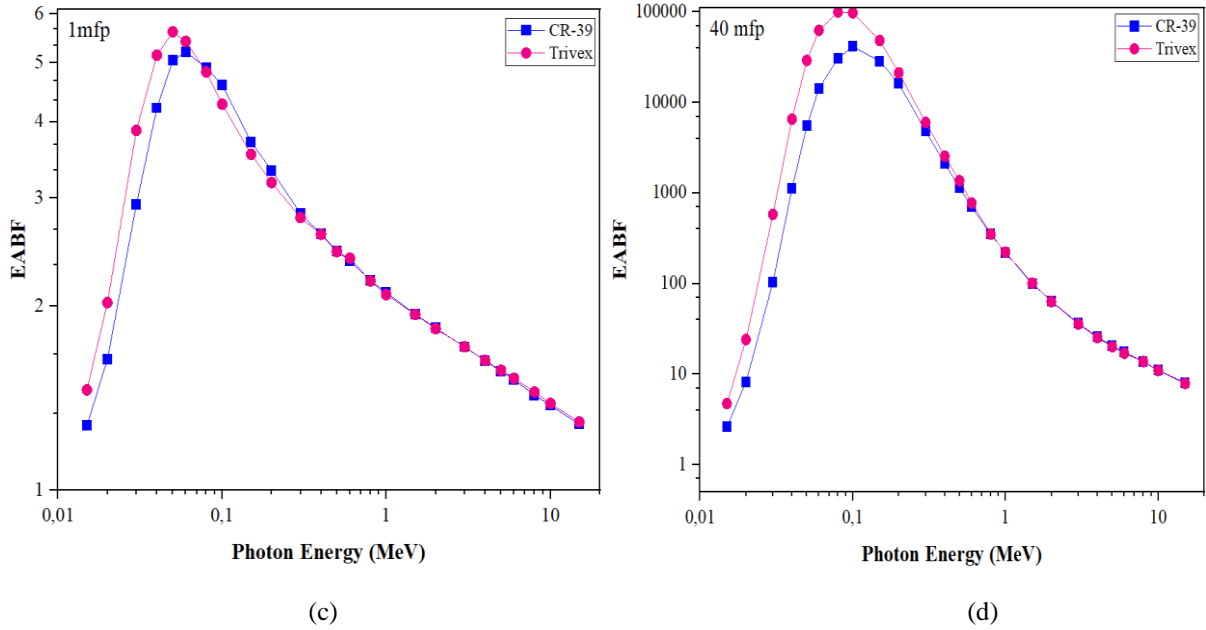
Figure 5. (a–d) The energy absorption buildup factors in the energy region 0.015–15 MeV at 1 and 40 mfp for CR-39 and Trivex optical lenses

4. Conclusion

In the present study, the compatibility of the results is analysed by the buildup factor values that are obtained from the XCOM and the EPICS2017 library and Phy-X/PSD software, which are frequently preferred in the literature to determine radiation shielding features. It is found that the relative changes between the EPICS2017 and Phy-X/PSD software and the results obtained in this study are 8% and 9%, respectively for the CR-39 and Trivex optical lens, which indicate good agreement. Buildup factors (EBF and EABF) are important and required for radiation shielding in healthcare physics, nuclear laboratories, and optics. Good radiation shielding performance of the materials requires that the buildup factor values are small. In this respect, it is seen that the radiation shielding performance of CR-39 had better shield features among the examined optical lens materials. This is also a result of the CR-39 with higher Z_{eq} values. Figure 2 (a-d) indicates that the changes against the photon energy and mfp values are similar. There is a significant difference between the values, because the energy absorbed in the material is taken into account in the interaction of the material with the photon in EABF, and the absorption in the air in EBF. Although there are similar variations in the graphs in terms of the dependence of the buildup factors on incoming photon energy, namely mfp and Z_{eq}, it is discussed in the text that different photon interaction events are intense in the low, moderate, and high-energy regions of the buildup factors. Especially, Figure 2 (a-d), presents that both buildup factors reach maximum values in the moderate-energy region, where Compton scattering is dominant, and hence, supports the occurrence of multiple scattering in this region. It is important to note that the buildup factor increases in the energy region that has the Compton Scattering, and photon absorption is higher in the energy regions where photoelectric and pair production are dominant, and this causes the buildup factor to have lower values. In addition, it was observed that the differences between increasing energy and buildup factor values in CR-39 and Trivex optical lenses decreased significantly at 1.5 MeV (Figure 3c and Figure 4c). This can be explained by the fact that the variation of the buildup factors with the depth of penetration in this energy region is independent of the chemical composition of the material. After 1.5 MeV, it was observed that the order of the buildup factor changed (Figure 3d and Figure 4d). This is a consequence of the reduced probability of multiple scattering at higher penetration depths and the increased probability of the absorption effect. Because the pair production event with an initial energy of 1.02 MeV becomes more dominant with increasing energy.

References

[1] Musikant S. Optical Materials, New York, Marcel Dekker, Inc, 1985.

[2] Şen F, Durdu B.G, Oduncuoğlu M, Efil K, Dinçer M, A Theoretical Investigation by DFT Method on CR – 39 Monomer that is a Plastic Polymer Commonly Used in the Manufacture of Eyeglass Lenses, Am. J. Opt. Photonics 2014; 2: 7–11.

[3] Alonso J, Gómez-Pedrero J.A, Quiroga J.A. Modern ophthalmic optics, New York, Cambridge University, 2019.

[4] Ralph Chou B, Dain S.J, Cheng B.B, Effect of ultraviolet exposure on impact resistance of ophthalmic lenses, Optom. Vis. Sci 2015; 92: 1154–1160.

[5] Organisation WH. Coronavirus disease 2019 (COVID-19) situation report 32, 2020 (Available:https://www.who.int/docs/default-source/coronaviruse/situation-reports/20200221-sitrep-32-covid-19.pdf/ 2020).

[6] Chandrinos A, Tzamouranis D.-D. The Pandemic of COVID-19 and the Use of Contact Lenses, Asian J. Res. Reports Ophthalmol 2020; 3: 24–30.

[7] Zeng W, Wang X, Li J, Yang Y, Qiu X, Song P, Xu J, Wei Y. Association of dailywear of eyeglasses with susceptibility to coronavirus disease 2019 infection, JAMA Ophthalmol 2020; 138: 1196–1199.

[8] Manohara S.R, Hanagodimath S.M, Gerward L. Energy absorption buildup factors for thermoluminescent dosimetric materials and their tissue equivalence, Radiat. Phys. Chem 2010; 79: 575–582.

[9] Sayyed M.I, AlZaatreh M.Y, Matori K.A, Sidek H.A.A, Zaid M.H.M. Comprehensive study on estimation of gamma-ray exposure buildup factors for smart polymers as a potent application in nuclear industries, Results Phys 2018; 9: 585–592.

[10] Kurudirek M, Sardari D, Khaledi N, Çakir C, Mann K.S. Investigation of X- and gamma ray photons buildup in some neutron shielding materials using GP fitting approximation, Ann. Nucl. Energy 2013; 53: 485–491.

[11] ANSI/ANS-6.4.3. Gamma Ray Attenuation Coefficient and Buildup Factors for Engineering Materials, American Nuclear Society La Grange Park, IL 1991.

[12] Şakar E. Determination of photon-shielding features and build-up factors of nickel–silver alloys, Radiat. Phys. Chem 2020; 172:108778.

[13] Hila F.C, Asuncion-astronomo A, Anne C, Dingle M, Federico J, Jecong M, Javier-hila A.M.V, Bryan M, Gili Z et al. EpiXS : A Windows-based program for photon attenuation , dosimetry and shielding based on EPICS2017 (ENDF / B-VIII) and EPDL97 (ENDF / B-VI.8). Radiat. Phys. Chem 2021; 182:109331.

[14] Şakar E, Özpolat Ö.F, Alım B, Sayyed M.I, Kurudirek M. Phy-X / PSD: Development of a user friendly online software for calculation of parameters relevant to radiation shielding and dosimetry. Radiat. Phys. Chem 2020; 166: 108496.

[15] Chou B.R, Hovis J.K. Effect of multiple antireflection coatings on impact resistance of Hoya Phoenix spectacle lenses, Clin. Exp. Optom 2006; 89: 86–89.

[16] Bhootra A.K. Ophthalmic Lenses, India, Jaypee Brothers Medical Publishers (P) Ltd, 2009.

[17] Fernando J, Domínguez R, Resistencia a los impactos : una mirada óptica, Cien. Tecnol. Salud. Vis. Ocul 2013; 11: 113–125.

[18] Gerward L, Guilbert N, Jensen K.B, Levring H. WinXCom - A program for calculating X-ray attenuation coefficients, Radiat. Phys. Chem 2004; 71: 653–654.

[19] Berger M.J, Hubbell J.H, Seltzer S.M, Chang J, Coursey J.S, Sukumar R, Zucker D.S, Olsen K. XCOM: Photon Cross Sections Database, NIST Standard Reference Database, NIST Stand. Ref. Database. 8 XGA 2010.

[20] Hila F.C, Amorsolo A. V, Javier-Hila A.M. V, Guillermo N.R.D. A simple spreadsheet program for calculating mass attenuation coefficients and shielding parameters based on EPICS2017 and EPDL97 photoatomic libraries, Radiat. Phys. Chem 2020; 177:109122.

[21] Oyeleke Olarinoye I. Photon Buildup Factors For Some Tissues and Phantom Materials For Penetration Depths Up To 100 Mfp, J. Nucl. Res. Dev 2017; 13.

[22] Kerur B.R. Thontadarya S.R, Hanumaiah B. A novel method for the determination of x-ray mass attenuation coefficients, Int. J. Radiat. Appl. Instrumentation. Part 1991; 42: 571–575.

[23] Heath DR. Optics and vision, Telecommunications Engineer's Reference Book, Elsevier, 1993.

[24] Gilmore G. Practical gamma-ray spectrometry, England, WILEY, 2008.

[25] Bass M. Handbook of Optics Volume III: Classical Optics, Vision Optics,X-ray Optics. 2nd ed. United States of America: McGraw-Hill, inc 2010.

[26] Yonphan S, Limkitjaroenporn P, Borisut P, Kothan S, Wongdamnern N, Alhuthali A.M.S, Sayyed M.I, Kaewkhao J. The photon interactions and build-up factor for gadolinium sodium borate glass: Theoretical and experimental approaches, Radiat. Phys. Chem 2021; 188.

[27] Sayyed M.I, Elmahroug Y, Elbashir B.O, Issa S.A.M, Gamma-ray shielding properties of zinc oxide soda lime silica glasses, J. Mater. Sci. Mater. Electron 2017; 28: 4064–4074.

[28] Stalin S, Gaikwad D.K, Al-Buriahi M.S, Srinivasu C, Ahmed S.A, Tekin H.O, Rahman S. Influence of Bi2O3/WO3 substitution on the optical, mechanical, chemical durability and gamma ray shielding properties of lithium-borate glasses, Ceram. Int 2021; 47: 5286–5299.

[29] Harima Y. Approximation of Gamma-Ray Buildup Factors By Modified Geometrical Progression., Nucl. Sci. Eng 1983; 83: 299–309.

[30] Alsaif N.A.M, Elmahroug Y, Alotaibi B.M, Alyousef H.A, Rekik N, Hussein A.W.M.A, Chand R, Farooq U. Calculating photon buildup factors in determining the γ-ray shielding effectiveness of some materials susceptible to be used for the conception of neutrons and γ-ray shielding, J. Mater. Res. Technol 2021; 11: 769–784.

[31] Kadri O, Alfuraih A. Photon energy absorption and exposure buildup factors for deep penetration in human tissues, Nucl. Sci. Tech 2019; . 30: 1–9.

[32] Harima Y, Sakamoto Y, Tanaka S, Kawai M. Validity of the Geometric-Progression Formula in Approximating Gamma-Ray Buildup Factors., Nucl. Sci. Eng 1986; 94:24–35.

[33] Harima Y, Tanaka S.I, Sakamoto Y, Hirayama H. Development of new gamma-ray buildup factor and application to shielding calculations, J. Nucl. Sci. Technol 1991; 28:74–84.

[34] Jarrah I, Radaideh M.I, Kozlowski T, Rizwan-uddin. Determination and validation of photon energy absorption buildup factor in human tissues using Monte Carlo simulation, Radiat. Phys. Chem 2019; 160: 15–25.

[35] Trkov A, Herman M, Brown D.A. ENDF-6 Formats Manual: Data Formats and Procedures for the Evaluated Nuclear Data Files, ENDF/B-VI and ENDF/B-VII, CSEWG Document ENDF-102, Report BNL-90365-2009 Rev. 2, Brookhaven National Laboratory, 2009.

Mobile Robot Indoor Localization Using Color-Coded Beacons and a Depth Camera

Mawj MOHAMMED BASHEER[1*], Mehmet ÇAVAŞ[2], Mohammed QASIM[3]

[1,2] Mechatronics Engineering, Technology Faculty, Firat University, Elazığ, Turkey
[3] Systems & Control Engineering, Electronics engineering Faculty, Ninevah University, Mosul, Iraq
[*1] eng.mawj.aljadirjy@gmail.com, [2] mcavas@firat.edu.tr, [3] mohammed.qasim@uoninevah.edu.iq

Abstract: This paper aims to design and implement an indoor localization method for mobile robots based on trilateration technique, Color Code signatures (CCs) as artificial passive beacons, and a depth camera. The artificial passive beacons are designed as three disks positioned one on top of the other's with different sizes and colors (primary colors only, RGB). The three disks share the same center. The designed beacons are placed on the ceiling to be visible from most locations within the room. The robot's model, controller, and localization method are implemented and evaluated inside the CoppeliaSim environment. The simulation results show that the CCs detecting algorithm enables the robot to discover the designed beacons, achieve an accurate localization and reach the target.

Keywords: Omnidirectional robot, localization, CoppeliaSim program, Trilateration.

Renk Kodlu İşaretler ve Derinlik Kamerası Kullanan Mobil Robot İç Mekan Lokalizasyonu

Öz: Bu makale, mobil robotlar için trilaterasyon tekniğine, yapay pasif işaretler olarak Renk Kodu imzalarına (CC'ler) ve bir derinlik kamerasına dayalı bir iç mekan lokalizasyon yöntemi tasarlamayı ve uygulamayı amaçlamaktadır. Yapay pasif işaretçiler, farklı boyut ve renklerde (yalnızca ana renkler, RGB) biri diğerinin üzerine yerleştirilmiş üç disk olarak tasarlanmıştır. Üç disk aynı merkezi paylaşır. Tasarlanan fenerler, oda içindeki çoğu yerden görülebilecek şekilde tavana yerleştirilmiştir. Robotun modeli, denetleyicisi ve yerelleştirme yöntemi CoppeliaSim ortamında uygulanır ve değerlendirilir. Simülasyon sonuçları, CC'lerin tespit algoritmasının robotun tasarlanan işaretleri keşfetmesini, doğru bir lokalizasyon elde etmesini ve hedefe ulaşmasını sağladığını göstermektedir.

Anahtar kelimeler: Omnidirectional robot, yerelleştirme, CoppeliaSim programı, Trilaterasyon.

1. Introduction

Robotics is an interdisciplinary field that consists of the integration of computer science, electronics, artificial intelligence, mechanics, and control. Mobile robots are the type of robots that can move around and are not fixed in a single physical location [1]. Many studies deal with mobile robots and how they can move to achieve their objectives in the real world without the need for humans. For the correct operation of mobile robots, several technological areas and fields should be noted and integrated to understand the fundaments such as the locomotion system and kinematics, perception system (sensors), localization system, and navigation system. All these systems must be followed by a control system in order to make the mobile robot achieves its action or task in an intelligible way [2]. Localization is considered one of the essential problems that mobile robots face. The best explanation of the localization term is "the ability of the mobile robot to recognize its location within the environment." In other words, the localization term refers to the position and orientation of a mobile robot within a specific location [3]. In order to solve the localization problem, there are different practical applications depending on passive or active beacons. Beacons make the optimal localization operation easy. Despite, the artificial beacons are necessary to achieve localization, the number of beacons that are placed in the environment is limited. For the previous reason, a localization algorithm for mobile robots is used with specific placement and number of beacons [9]. The trilateration method needs at least three beacons to be recognized at the same time, with the distance between them and the robot to work[10]. Since advanced robots are still highly expensive and can be damaged in the workspace, simulators are used to create virtual environments which have many advantages for robotics studies. The CoppeliaSim software is one of the most widely used simulators today, and it deserves special attention. This simulator is a scalable and flexible framework for creating 3D simulations in a short time. CoppeliaSim includes

---

[*] Corresponding author: eng.mawj.aljadirjy@gmail.com.ORCID Number of authors: [1] 0000-0003-1687-6835, [2] 0000-0002-0130-1644, [3] 0000-0003-2947-8887

a large number of examples, robot models, sensors, and actuators, which can be used to build a virtual environment and interact with it in real-time. To execute customized simulation experiments, new models can be built and added to the CoppeliaSim program [8]. for these reasons, the CoppeliaSim simulation platform has been used. Artificial landmarks are often installed at a predefined area of the robot's workspace. the robot needs sensors to detect or measure the angle and distance to these landmarks. Measuring distance is simple for many sensors, such as cameras or wireless devices [11].

Over the past years, a wide range of research has been explored, evaluated, and applied to mobile robots to overcome the problem of localization. Chunag, L. [4] utilized RFID (Radio-Frequency Identification) tags as artificial landmarks to perform a mobile robot's localization approach. The RFID tags have been set in a well-known area within the robot's workspace, and the robot's dual-antenna RFID reader has successfully communicated with them. A similar technique was used by Chunag, L. [4] and Gueaieb et al. [5], although they used a different strategy, placing the RFID tags on the ceiling. The main problem with this technology is that exterior items (metal objects or even humans) affect indoor RF propagation; it is extremely sensitive to these items, causing measurements to be changed. Various RFID tags also result in different behaviors. As a result, if this issue is not fixed, the pre-calibrated system may be rendered unusable. As a result, infrared technology has been used as beacons to lead the blind robot through an unfamiliar environment [5]. Huosheng Hu and Dongbing Gu [12] made a study on artificial landmarks and laser scanners for localization. With six identically sized landmarks in the environment, they utilized a 360° scanner laser with a range of 50m and a constant velocity of 2Hz. For successful detection at large distances, the landmarks were made from a single strip and pre-stored in the memory. These artificial landmarks can provide powerful signals back to the scanner. When the mobile robot moves on a non-smooth floor surface. It causes the laser scanner to vibrate, resulting in incorrect readings. The infrared beam-based mobile robot localization system was first presented in 1992. Mobile robot localization applications based on infrared technology are also widely utilized for mobile localization. Before looking at how to use this technology to locate a robot, it's necessary to understand that it's divided into two categories: active beacons and passive beacons. Active beacons are those that produce infrared signals, whilst passive beacons are those that act as reflectors [13]. Recently, in 2021 [6], the researchers used Landmarks Exploration Algorithm (LEA) for indoor localization, which operates in two stages. In the first stage, the artificial color-coded landmarks (passive cylindrical landmarks) are detected and their locations are stored. At the same time, an extended Kalman filter (EKF) is used to update the robot's state. In the second stage, a proximity sensor is utilized to calculate the distance to the detected CCLs and apply the trilateration method to localize the robot. In addition, they used the CoppeliaSim environment connected with Matlab for the simulation.

The contributions of this paper include: i) unlike other methods, the approach in this paper uses passive beacons of circular shapes, which do not require a power source and are easy to build and scale (more beacons can be generated by increasing the number of rings forming them), ii) one sensor (depth camera) is all that is required to accurately localize the robot in an indoor environment and iii) the effectiveness of the proposed localization method is verified using the realistic CoppeliaSim robot simulator.

This paper is organized as follows: Section 2 illustrates the robot design in CoppeliaSim. Section 3 derives the trilateration formula. Section 4 demonstrates the design and detection of the color-coded beacon. Section 5 shows the simulation results and briefly discusses them. Section 6 concludes the papers.

2. Kinematics Modelling of Three-Wheels Omnidirectional Robot in CoppeliaSim

The Omni-Wheels Robot building is done by adding two-cylinder shapes with a diameter of 0.14 m and thickness of 0.005 m as the base of the Omni-Wheels Robot. Three Omni-wheels with a diameter of 0.0352 m and 120 degrees between each wheel joint are attached to the base. The distance between the center of the robot and the center of each wheel is $l = 0.093$ m. The final model of the Omni-Wheels robot is shown in Figure 1.

Mawj MOHAMMED BASHEER[1*], Mehmet ÇAVAŞ[2], Mohammed QASIM[3]
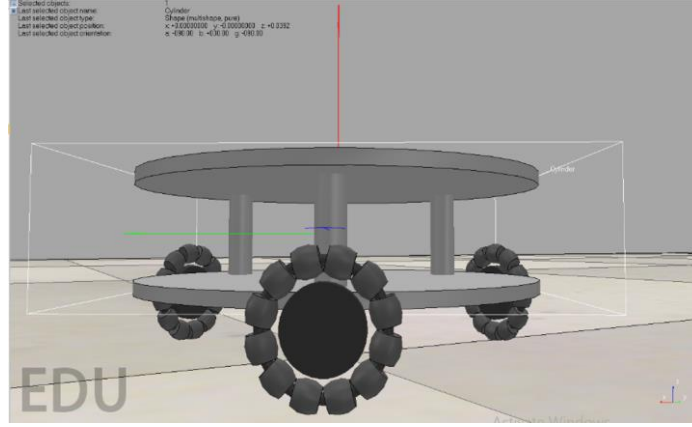
Figure 1. Omnidirectional Robot Model.

The desired angular velocities ($\omega_1, \omega_2, \omega_3$) of the robot wheels can be obtained by using the following equations:

$$\begin{bmatrix} \omega_1 \\ \omega_2 \\ \omega_3 \end{bmatrix} = \frac{1}{r} \begin{bmatrix} \frac{\sqrt{3}}{2} & -\frac{1}{2} & l \\ 0 & 1 & l \\ -\frac{\sqrt{3}}{2} & -\frac{1}{2} & l \end{bmatrix} \begin{bmatrix} \dot{X}_R \\ \dot{Y}_R \\ \dot{\theta} \end{bmatrix} \tag{1}$$

where r represents the radius of the wheels $\dot{X}_R, \dot{Y}_R$ and $\dot{\theta}$ represent the robot linear velocities along the robot X_R, Y_R axes and angular velocity around its Z_R axis respectively. The wheels' motors are then programmed to track the appropriate angular velocities using a low-level PI controller. The velocity equations are programmed by using Lua in CoppeliaSim's script.

3. Trilateration Technique

Basically, localization means that the robot has to determine its position and orientation in the environment[14]. The position will be estimated based on the concept of the trilateration method [7]. The trilateration technique can be clearly shown in Figure 2.
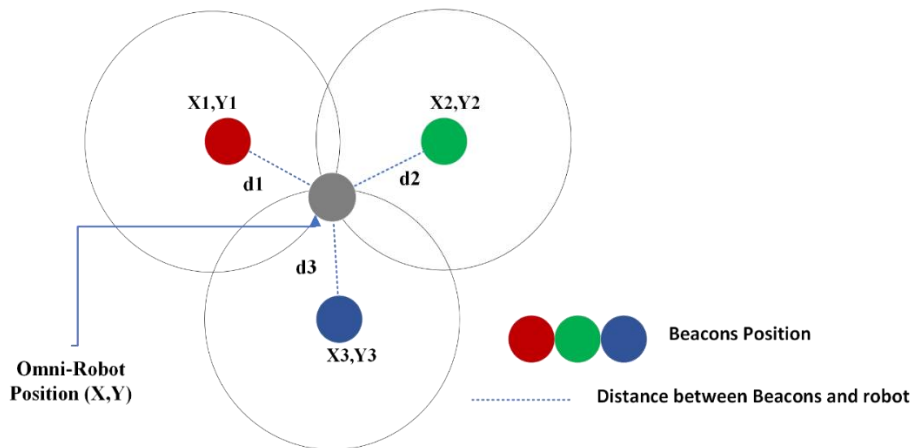
Figure 2. Trilateration technique.

39

Considering the basic formula for the general equation of a circle which is shown in equation (2)

$$d^2 = X^2 + Y^2 \qquad (2)$$

where d is the radius of the circle, the equations of three circles centered at points (X_1, Y_1), (X_2, Y_2) and (X_3, Y_3) can be formed as shown in equations (3), (4), and (5) respectively:

$$d_1^2 = (X - X_1)^2 + (Y - Y_1)^2 \qquad (3)$$

$$d_2^2 = (X - X_2)^2 + (Y - Y_2)^2 \qquad (4)$$

$$d_3^2 = (X - X_3)^2 + (Y - Y_3)^2 \qquad (5)$$

The distances d_1, d_2, and d_3 are known from the depth information of the camera. After the detection of the beacons, their coordinates (X_1, Y_1), (X_2, Y_2) and (X_3, Y_3) with respect to the global frame are known, which are set by the designer. Therefore, the two unknown variables (X, Y) which represents the point of intersection of the three circles and the robot current position can be determined by solving the equations (3), (4), and (5) as follows:
After subtracting equation (4) from (3) we obtain:

$$-2XX_1 + 2XX_2 + X_1{}^2 - X_2{}^2 - 2YY_1 + 2YY_2 + Y_1{}^2 - Y_2{}^2 = d_1^2 - d_2^2$$

$$X(-2X_1 + 2X_2) + Y(-2Y_1 + 2Y_2) = d_1^2 - d_2^2 - X_1{}^2 + X_2{}^2 - Y_1{}^2 + Y_2{}^2$$

Let: $A = -2X_1 + 2X_2$, $B = -2Y_1 + 2Y_2$ and $C = d_1^2 - d_2^2 - X_1{}^2 + X_2{}^2 - Y_1{}^2 + Y_2{}^2$

This yields a new equation:

$$AX + BY = C \qquad (6)$$

And by subtracting equation (5) from (4) the following equations are formed:

$$X(-2X_2 + 2X_3) + Y(-2Y_2 + 2Y_3) = d_2^2 - d_3^2 - X_2{}^2 + X_3{}^2 - Y_2{}^2 + Y_3{}^2$$

Where: $D = -2X_2 + 2X_3$, $E = -2Y_2 + 2Y_3$, $F = d_2^2 - d_3^2 - X_2{}^2 + X_3{}^2 - Y_2{}^2 + Y_3{}^2$

A new equation is formed:

$$DX + EY = F \qquad (7)$$

Then, by multiplying (6) with (E) and (7) with (B) the following equations have been obtained:

$$AEX + BEY = CE \qquad (8)$$

$$DBX + EBY = FB \qquad (9)$$

After subtracting (9) from (8) we obtain:

$$X = \frac{CE - FB}{AE - DB} \qquad (10)$$

by multiplying (6) with (D) and (7) with (A) we obtain:

$$ADX + BDY = CD \qquad (11)$$

$$DAX + EAY = FA \qquad (12)$$

After subtracting (12) from (11) we obtain:

$$Y = \frac{CD - FA}{DB - AE}$$

(13)

The equations (10) and (13) are simply implemented in CoppeliaSim.

4. Artificial Passive Beacon Design

Practically, the vision sensor depends on the color's signature to detect the object. In the design of the beacon, two or more colors' signature is placed together to form a color code signature (CCs). The design is based on the combination of three disks with distinct sizes and colors (red, green, and blue only). The disks are placed on top of each other and have the same center. As a result, twelve beacons can be generated. Table 1 shows three designed shapes of the beacon and its codes. These artificial passive beacons are placed on the ceiling and used for indoor localization.

Table 1. The designed shape of the beacon.

Color Tags	Color Codes	Beacons
Red-Green-Red	121	
Red-Green-Blue	123	
Red-Blue-Red	131	

The designed beacon is placed on the ceiling with specific arranging that helps the vision sensor to detect at least three beacons at the same time. Figure 3 illustrates the arrangement of the designed beacons on the ceiling.
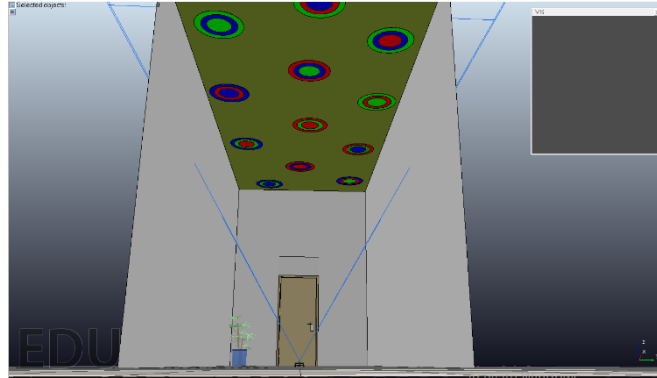
Figure 3. Beacons are set on the ceiling.

4.1. Color-coded beacon detection framework

The vision sensor in CoppeliaSim has built-in image processing filters. A combination of these filters is used to detect the designed tag. As shown in Figure 4, three filters with appropriate parameters are used to detect only the three primary colors (RGB) in the images and return binary images with ones in the pixels with red, green, and blue colors and zero otherwise. After that, three filters are used to segment the images returned from the first three filters. The goal of segmentation is to find the pixels with values of ones that are close to each other, Binary Large

Object (BLOB)[15]. These filters eliminate the BLOBs with small sizes and also return the coordinates of the center of each blob in the image coordinates in pixels. Each color code signature consists of three blobs of two or three different colors that have the same center coordinates in the image coordinates.

The detection of the CCs beacon is as follows: Frist, the distance between a blob center of a certain color and every other blob center of the same and different color is calculated using the distance formula between two points. If this distance is less than a certain threshold then the three blobs belong to the same beacon. The process is repeated until all tags are detected and recorded. Second, a color code is assigned to each beacon based on the sizes of the blobs with the assumption that red = 1, green = 2, and blue = 3, see Table 1.
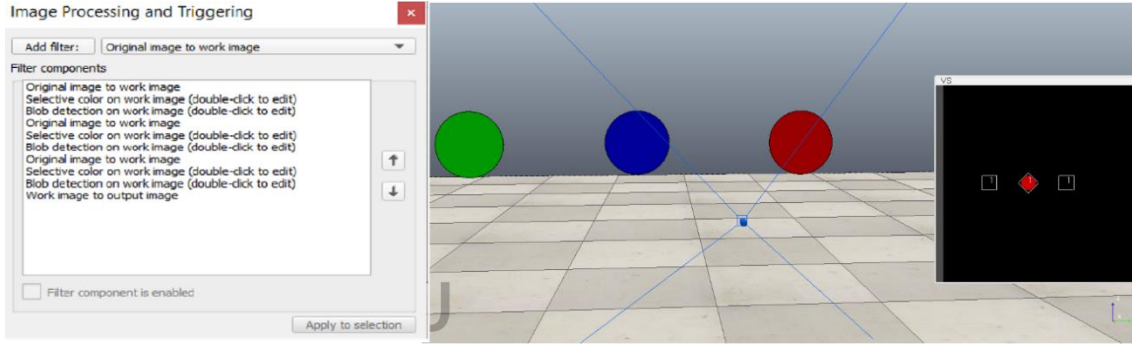
Figure 4. Blob detection of three colors (Red-Green-Blue).

5. Results and Discussion

The localization of the Omni-directional robot has been implemented using the simulation environment of CoppeliaSim which is controlled via scripts written in Lua language. Twelve circular objects with RGB color are used as beacons with a predefined position relative to the global frame. The scene in CoppeliaSim has a corridor with dimensions (3x8x4) in meters. The Omni-wheels robot designed in section (2) is used. The vision sensor is located on the top of the robot with a 60° FOV to detect at least three beacons at the same time. Two scenarios are considered to show the effectiveness of the proposed localization method.

The first scenario is shown in Figure 5. The robot is located at point **A,** and the target is located at pose ($x_t = -3$ m, $y_t = 1$ m, $\theta_T = -11.6°$). In the first stage, the robot at point **A** starts rotating using the following control law :

$$\dot{\theta} = k_{p\theta}(\theta - \theta_d) \tag{14}$$

where θ is the current robot orientation, $\theta_d = atan2(y_t - y_r, x_t - x_r)$, (y_r, x_r) and (y_t, x_t) is the Cartesian coordinates for the robot and target positions respectively and the controller parameter $k_{p\theta} > 0$. In the second stage, trilateration equations (10) and (13) are applied to obtain the robot's position relative to the global frame. The robot is then moved with a velocity $\dot{X}_R$ that is calculated according to the equation:

$$\dot{X}_R = K_P \, \rho \, \cos \alpha \tag{15}$$

where $\dot{X}_R$ is the desired speed of the robot (with the assumption of $\dot{Y}_R = 0$), and controller parameter $K_P > 0$, $\rho = \sqrt{(y_t - y_r)^2 + (x_t - x_r)^2}$ and $\alpha = 0$ due to the previous rotation by θ_d. Finally, the robot is rotated to achieve the desired orientation θ_T using the control law (14) with $\theta_T = \theta_d$ The results are shown in Table 2.

Mawj MOHAMMED BASHEER[1*], Mehmet ÇAVAŞ[2], Mohammed QASIM[3]
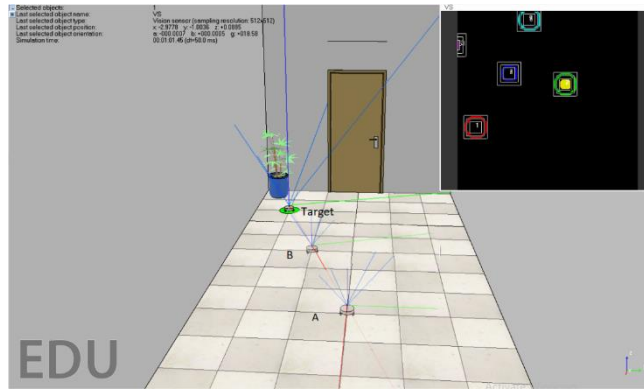
Figure 5. The first scenario of the robot localization.

Table 2. The result of scenario 1.

	X_{Actual} (m) (Robot)	X_{Tri} (m) (Robot)	Y_{Actual} (m) (Robot)	Y_{Tri} (m) (Robot)	Distance error (m)= Target position – Robot position
A	0	0.08	0	0.02	3.16
B	1.227	1.209	0.413	0.404	1.88
Target	3	2.95	1	0.99	0.05

Figure 6 shows that The Omni-Wheels robot starts rotating from its initial orientation until reaching θ_d with an execution time of 4 seconds.
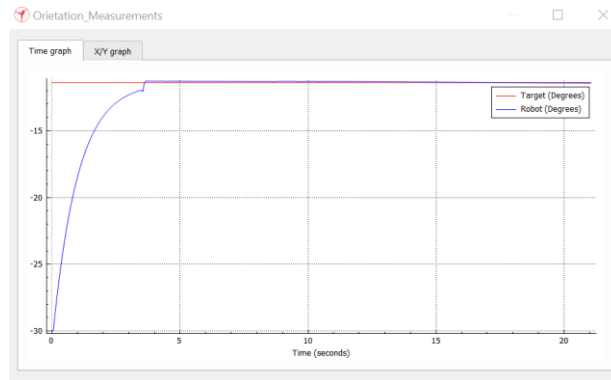
Figure 6. The orientation measurements.

Additionally, the (X, Y) coordinates of the robot from the initial position until reaching the target are shown in Figure 7. The graph shows that the robot coordinates do not change for the first 4 sec due to the rotation of the robot; after that, it can be seen that the robot (X, Y) coordinates change exponentially until reaching the target's coordinates.
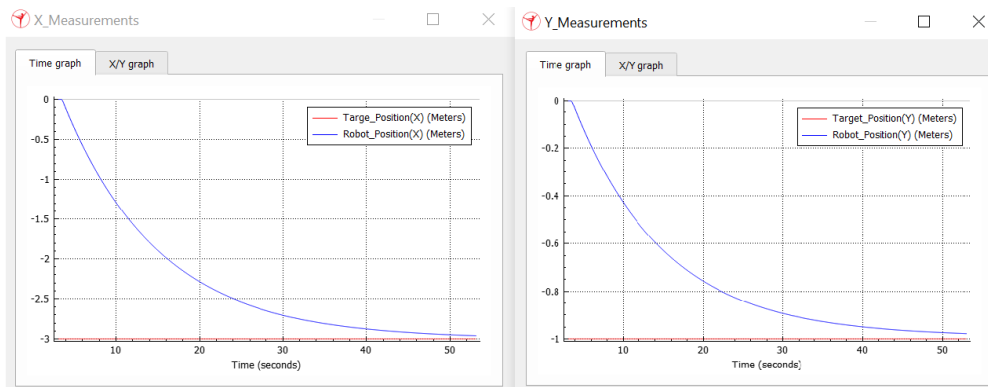
Figure 7. The Omni-wheels robot coordinates.

In the second scenario, as shown in Figure 8, the target is located at the pose ($x_t = 2$ m, $y_t = 1$ m, $\theta_T = 176°$). The robot starts rotating at point **A** and then the steps of the first scenario are repeated. The robot reaches the target as demonstrated in Table 3.
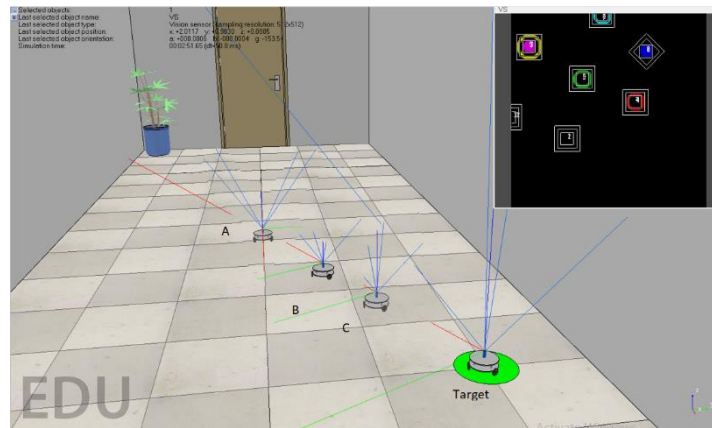
Figure 8. The second scenario of the robot localization.

Table 3. The result of scenario 2.

	X_{Actua}(m) (Robot)	X_{Tri}(m) (Robot)	Y_{Actual}(m) (Robot)	Y_{Tri}(m) (Robot)	Distance error (m)= Target position – Robot position
A	0	0.039	0	0.019	2.192
B	0.693	0.673	0.339	0.329	1.487
C	1.295	1.288	0.637	0.633	0.801
Target	2	1.991	1	0.978	0.023

Figure 9 shows that The Omni-Wheels robot starts rotating from its initial orientation until reaching θ_d with an execution time of 5 seconds.

Mawj MOHAMMED BASHEER[1*], Mehmet ÇAVAŞ[2], Mohammed QASIM[3]
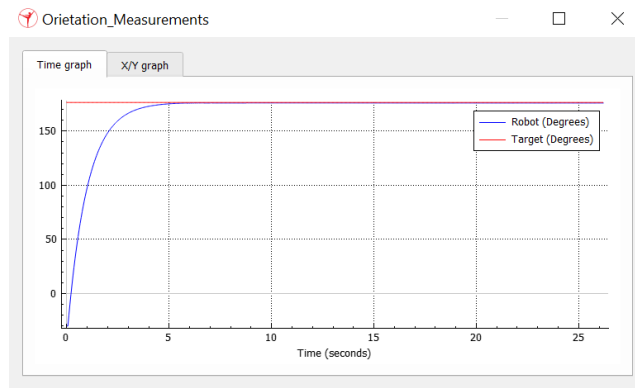
Figure 9. The orientation measurements.

Additionally, the (X, Y) coordinates of the robot from the initial position until reaching the target are shown in Figure 10. The graph shows that the robot coordinates do not change for the first 5 seconds due to the rotation of the robot; after this time, it can be seen that the robot (X, Y) coordinates change exponentially until reaching the target's coordinates.
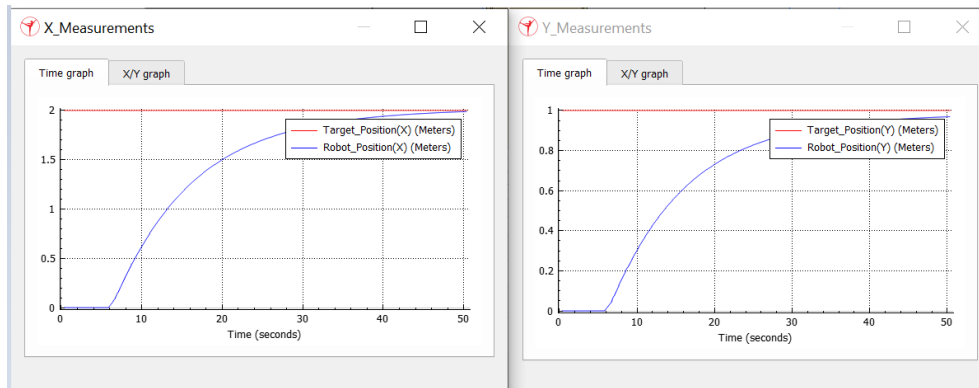
Figure 10. The Omni-wheels robot coordinates.

6. Conclusion

In this paper, the indoor localization of the Omni-wheels robot was simulated using the CoppeliaSim robot simulator. The indoor localization of the robot was achieved by applying the trilateration method. This method depends on identifying color-coded beacons to obtain their position with respect to the global frame and calculating the distances between each beacon and the robot. These beacons have been designed in circular shapes so that the detection of them can be done easily from any robot orientation. Two scenarios were examined to prove the capability of the proposed method for robot indoor localization. In both scenarios, the simulation results show that the robot rotates around itself to achieve the desired angle, then moves towards the target pose. The designed CCs beacons have enabled the Omni-wheels robot to estimate its position and reach the desired target.

References

[1] Fabregas, E., Farias, G., Peralta, E., Vargas, H. & Dormido, S. Teaching control in mobile robotics with V-REP and a Khepera IV library. In 2016 IEEE conference on control applications.2016. IEEE. pp.821-826.

[2] Francisco R., Francisco V. and Carlos L.A.,. A review of mobile robots: Concepts, methods, theoretical framework, and applications. International Journal of Advanced Robotic Systems.2019. 16(2).1-22

[3] Pablo, C., Miguel, V., David, C., Luis, M. and Manuel, B., Indoor Robot Positioning using an Enhanced Trilateration Algorithm. Engineering and Industrial Development Center (CIDESI).2016. 13(3).1-8

[4] Chuang, L. Object localisation strategy for a mobile robot using RFID.2012. 1(1). 5.

[5] Gueaieb, W., and Miah, M.S. An intelligent mobile robot navigation technique using RFID technology. IEEE Transactions on Instrumentation and Measurement.2008. 57(9), pp. 1908-1917.

[6] Mohanad, N. N., Mohammed, Q., and Omar, Y. I. Landmarks exploration algorithm for mobile robot indoor localization using vision sensor. Journal of Engineering Science and Technology. 2021. 16(4). pp. 3165 – 3184.

[7] Ladd, A.M., Bekris, K.E., Rudys, A.P., Wallach, D.S. and Kavraki, L.E. On the feasibility of using wireless ethernet for indoor localisation. IEEE Transactions on Robotics and Automation.2004. 20(3), pp. 555-559.

[8] Felipe, P. C., Joao, A. F., and Andre S. O. Integrating mobile robot navigation control, visual object detection and manipulation using ROS and V-REP. Conference: Congresso Brasileiro de Inteligência Computacional.2020.134(10).5.

[9] Bittel, O. and Blaich, M. Mobile robot localisation using beacons and the Kalman filter technique for the Eurobot competition. International Conference on Research and Education in Robotics. Springer.2011.pp. 55-67.

[10] Huosheng, H., and Dongbing, G. Landmark-based navigation of industrial mobile robots. Industrial Robot- an International Journal.2000.27 (6). pp. 458-467.

[11] Bekris, K.E., Argyros, A.A. and Kavraki, L.E. Angle-based methods for mobile robot navigation: Reaching the entire plane, Robotics and Automation. IEEE International Conference on 2004, pp. 2373-2378.

[12] Huosheng, H., and Dongbing, G. Landmark-based navigation of industrial mobile robots. Industrial Robot: An International Journal.2000. 27(6), pp. 458-467.

[13] Kostomins, A., and Osadcuks, V. Infrared active beacon application evaluation for mobile robot localisation in agriculture. Engineering for Rural Development (Latvia).2014.pp. 373-378.

[14] Hugh, D.,W.Where am I? A tutorial on mobile vehicle localization. Industrial Robot: An International Journal.1994, 21(2). pp. 11-16.

[15] Alexander, B., Rainer, H., and Kenneth, B.K. Hardware Acceleration of BLOB Detection for Image Processing.Third International Conference on Advances in Circuits, Electronics and Micro-electronics.IEEE.2010.pp 28-33.

Fault Detection from Images of Railroad Lines Using the Deep Learning Model Built with the Tensorflow Library

Abdullah ŞENER[1]*, Burhan ERGEN[2], Mesut TOĞAÇAR[3]
[1]Department of Computer Technologies, Genc Vocational School, Bingol University, Bingol, Turkey
[2]Department of Computer Engineering, Faculty of Engineering, Firat University, Elazig, Turkey
[3]Department of Computer Technology, Vocational School of Technical Sciences, Fırat University Elazig, Turkey
[*1] asener@bingol.edu.tr, [2]bergen@firat.edu.tr,[3]mtogacar@firat.edu.tr

Abstract: A means of transportation is the way in which an object, person, or service is transported from one place to another. Rail transportation occupies an important place in terms of cost and reliability. Most train accidents are caused by faults in railroad tracks. Detecting faults in railroad tracks is a difficult and time-consuming process compared to conventional methods. In this study, an artificial intelligence based model is proposed that can detect faults in railroad tracks. The dataset used in the study consists of defective and non-defective railroad images. The proposed model consists of foldable neural networks developed using the Tensorflow library. Softmax method was used as a classifier. An overall accuracy of 92.21% was achieved in the experiment.

Key words: Decision support systems, Deep learning, Rail fault detection, Artificial intelligence.

Tensorflow Kütüphanesi Kullanılarak Oluşturulan Derin Öğrenme Modeli ile Demiryolu Hattı Görüntülerinden Arıza Tespitinin Gerçekleştirilmesi

Öz: Ulaşım aracı, bir nesnenin, bireyin veya hizmetin bir yerden başka bir yere aktarılmasını sağlayan vasıtadır. Demiryolu ulaşımı maliyet ve güvenirlilik açısından önemli bir yere sahiptir. Tren kazaların çoğu demiryolu raylarında meydana gelen arızalardan kaynaklanmaktadır. Demiryolu hatlarındaki arızaların tespiti geleneksel yöntemlere göre zor ve zaman alıcı bir süreçtir. Bu çalışmada demiryolu hatlarında meydana gelen arızaların tespitini gerçekleştirebilen yapay zekâ tabanlı bir model önerilmiştir. Çalışmada kullanılan veri kümesi arızalı ve arızalı olmayan ray görüntülerinden oluşmaktadır. Önerilen model Tensorflow Kütüphanesi kullanılarak tasarlanmış evrişimsel sinir ağlarından oluşmaktadır. Sınıflandırıcı olarak Softmax yöntemi kullanılmıştır. Gerçekleştirilen deneyde %92,21 genel doğruluk başarısı elde edilmiştir.

Anahtar kelimeler: Karar destek sistemleri, Derin öğrenme, Ray arıza tespiti, Yapay zekâ.

1. Introduction

Road transport is the preferred mode of transport compared to sea and air transport [1]. The transportation sector directly affects factors such as the transportation of people and goods, the national and international economy, the construction and development of residential areas, and the functioning and order of other sectors. Developments in the transportation sector will also have a positive impact on the country's economy. Rail transport occupies an important place in road transport. Compared to Turkey, rail transport enjoys more attention in European countries. In our country, the share of passengers using railroads annually is about 1.1%, depending on the type of transport, while the share of freight transport is 4.6% [2].

Most accidents that occur in rail transportation are due to undetected defects in the tracks [3]. It is important to control reliability by considering rail transportation, scheduling, and economics [4]. Detecting faults in railroad tracks is a costly and time-consuming task. Traditionally, fault detection has been performed by humans. Recently, artificial intelligence-based technological infrastructure systems have come to the forefront to maximize fault detection, reduce costs, and increase safety levels. With artificial intelligence, it is possible to quickly detect faults on railroad tracks [5], [6]. Recently, many artificial intelligence-based studies have been conducted to detect faults on railroad tracks. Some of these studies are:

Ya-Wen Lin et al. examined railroad link images and detected errors using their proposed Deep Learning model. They created the dataset from the data captured by the GoPro device. Ya-Wen Lin et al. trained the dataset with the Yolo-V3 model and then performed the fault detection with test images. Ya-Wen Lin et al. achieved a success rate of 89% considering the precision metric in their studies. [7]. Yang et al. found that they could use their proposed approach to proactively maintain faults that may occur on railroad lines.

*Corresponding author: asener@bingol.edu.tr. ORCID Number of authors: [1]0000-0002-8927-5638, [2]0000-0003-3244-2615, [3]0000-0002-8264-3899

They used the ResNet model and fully foldable networks in their proposed approach. The analysis was performed to detect the connection points and faults on the railroad lines. Yang et al. used two data sets in their study. As a result of the analysis, they achieved success in the range of 74% to 91% considering the f-score metrics. [8]. Hovad et al. used the Yolo-V3 model in experimental analyzes to detect defects by examining images of railroad track fasteners. Considering the f-score criterion for detecting defective surfaces in the data set, they achieved a success rate of 84% [9]. Sysyn et al. used image preprocessing and principal component analysis (TBA) methods together to perform a contact fatigue analysis of railroad rails. Sysyn et al. processed the images morphologically and then performed efficient feature selection among the features obtained from the images using the PCA method. They showed that they could obtain accurate predictions of up to 11 meters in the surface images in the regression processes they performed with the surface crack images. [10]. Rajagopa et al. used artificial intelligence approaches to detect defects and cracks in railroad lines. Rajagopa et al. used the gray leveling matrix (GLCM) and local binary patterns (LBP) as a preprocessing step and classified the obtained features using the neural network model they developed. They achieved an overall accuracy of 94.9% in detecting defects in railroad lines. [11].

In this paper, an artificial intelligence-based deep network model is developed that can detect faulty rails on railroad tracks. In order to achieve successful results in the experimental analysis, a new convolutional neural network (ESA) model was created by testing all neural network layers of the Tensorflow library. The summary of the other parts of the paper is as follows: Information about the material and the proposed approach can be found in Chapter 2, and information about the analysis of the experiments, the preferred parameters, and the hardware information are described in Chapter 3. Information about the comparison of the study, the advantages and disadvantages of the scientific research and the results are given in Chapters 4 and 5.

2. Method

This section provides detailed information about the data set used for the experimental analysis of the study and the proposed approach.

2.1. Dataset

The dataset consists of railroad images forming the railroad lines. The dataset is public and consists of two classes. The classes consist of defective and non-defective categories. The resolution of each image is not fixed and the resolution ratio is generally of good quality. The image depth is 24 bits and the file extensions are JPG. In the defective class include loose nuts, missing parts, missing fasteners, gaps in connection points, etc. Defects. Figure 1 shows an example subset of images in the dataset. 191 of the dataset consist of defective images that occur on railroad tracks, and 192 consist of non-defective images of rails. In total, there are 383 images. [12]. In the dataset of this study, the data reserved for training, testing, and validation were combined into a single folder. Then, 80% of the dataset was randomly assigned as training data and 20% as test data for analysis. To validate the accuracy of the analysis result, the proposed approach was trained several times with the dataset and average accuracy was obtained.

Figure 1. Dataset classes and sample images;
a) Non-defective images, b) Defective images

2.2. Designed ESA Model

ESA models can be designed by software developers using open source codes to perform operations such as regression, classification, species detection, abnormal region detection, and segmentation. Open source ESA models are developed using various software languages (Python, MATLAB, R, Shell, etc.). [13]. Common layers used in ESA models are convolutional layers, pooling layers, and fully connected (dense) layers. The convolution layer allows the input image to be convolved by circulating it with the preferred filter parameter. In this way, filter activation maps are created, which are circulated in each region. The activation maps are used to determine the feature values of each region in the input data. [14]. Thanks to the pooling layer, the ESA model is guided through a simpler training process. With the pooling layer, the size of the input data is reduced. In general, pooling layers are used after convolution layers. [15]. The convolutional layer pooling layer can also be used continuously across multiple layers. The dense/fully linked layer is used as the last layer of the ESA model. The dense layer collects the features obtained from the previous layers in the form of a single row. To perform the classification/regression function, which is the next step, it prepares the formation of probability values for each input data [16].

During training of the ESA model, parameters such as normalization and dropout can also be used to prevent overlearning of the model. In addition, activation functions (ReLU, Sigmoid, tanh, etc.) are used to activate not all features obtained from the layers, but the features that have a certain threshold value. While the activation features facilitate the training of the model, they also contribute to the overall performance of the model [17].

Softmax method can be used as an activation function between layers of ESA models and is generally preferred to perform the classification function after the dense layer of models. Softmax processes the input features obtained from the dense layer and determines probability scores between 0 and 1 according to the class types. In a final processing step, Softmax assigns the input data to the class type with the highest score [18].

The proposed approach was developed using the Tensorflow library and the input size was set to 300×300 pixels. The proposed approach includes convolutional layers, pooling layers, density layers and features. Softmax method was used for image classification. In composing the model, the ADAM optimization method was preferred. Detailed information about the layers and functions used in the proposed approach can be found in Table 1.

Table 1. Designed ESA model

Layer/Function	Number of Input Channels	Step Size/Value
Input	-	300×300
Convolutional	256	3×3/150×150
ReLU	-	-
Maximum Pooling	-	3×3
Convolutional	128	3×3/150×150
Normalization	-	-
ReLU	-	-
Average Pooling	-	2×2
. . .		
Convolutional	64	3×3/38×38
Normalization	-	-
ReLU	-	-
Average Pooling	-	2×2
Dilution	-	0,2
Convolutional	32	3×3/19×19
Normalization	-	-
ReLU	-	-

Average Pooling	-	2×2
Dilution	-	0,25
Convolutional	16	3×3/10×10
ReLU	-	-
Average Pooling	-	2×2
Dilution	-	0,25
Dense	-	-
Softmax	Output=2 (defective / non-defective)	

3. Findings

The Jupyter Notebook interface was used for the experimental analysis of this study and the proposed approach was created using the Google Collaboratory server. Hardware information of the computer used in the study NVIDIA GeForce® RTX™ 3060 6GB graphics card, 11th generation Intel® Core™ i7 2.3GHz (24M cache, up to 4.6GHz, 8 cores) processor and 16GB memory. The Python programming language was used in the development of this approach. The most important reason why Google Colab servers are preferred is the ability to use Tensor Processing Unit (TPU). TPUs are capable of processing faster than the graphics processing unit (GPU) [19]. In performing the analysis, the TPU unit was preferred instead of the GPU. The value of the mini-batch parameter, which allows the model to process the images simultaneously, was set to 4. [20]. The number of cycles (epoch) 32 was preferred for training the dataset. Also, the early stop parameter was used to prevent overfitting during model compilation [21]. The complexity matrix and metrics were used to measure the analysis of the proposed approach. The formulas given between equation 1 and equation 4 were used to calculate the metrics. True (T), false (F), positive (P), and negative (N) variables were used in the formulas. [22], [23]. In addition, the Matthews correlation coefficient was preferred to compare the results of the analysis. Equation 5 was used to calculate Matthews [24].

$$\text{Sensitivity} = \frac{TP}{TP+FN} \tag{1}$$

$$\text{Specificity} = \frac{TN}{TN+FP} \tag{2}$$

$$\text{F-score} = \frac{2 \times TP}{2 \times TP+FP+FN} \tag{3}$$

$$\text{Accuracy} = \frac{TP+TN}{TP+TN+FP+FN} \tag{4}$$

$$\text{Matthews} = \frac{(TP \times TN - FP \times FN)}{\sqrt{((TP+FP) \times (TP+FN) \times (TN+FP) \times (TN+FN))}} \tag{5}$$

In the experimental analysis, 80% of the dataset was trained using the proposed approach as training data. 20% of the dataset was used as test data. The training time of the model was 5671 seconds. The graphs of the overall accuracy of the training and test data are shown in Figure 2
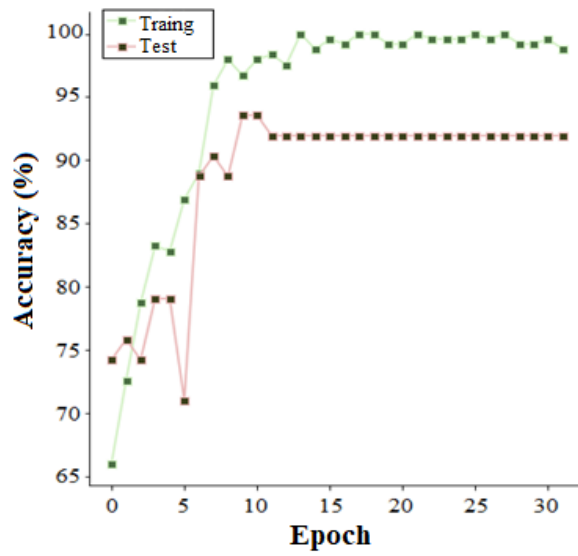
Figure 2. Training-test accuracy graph of the proposed approach
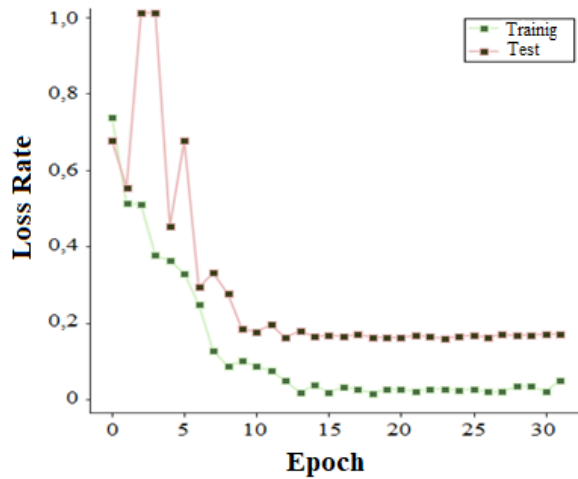
Figure 3. The training-test loss graph of the proposed approach

The result of the experimental analysis was an overall accuracy of 92.21%. The complexity matrix used to calculate the measurement metrics is shown in Figure 4. The analysis results of the measurement metrics are shown in Table 2.

Figure 4. The complexity matrix obtained as a result of the experimental analysis

Table 2. Experimental analysis results (%)

Dataset Types	Sensitivity	Specificity	F-score	Accuracy	Matthews
Defective & Non defective	95,12	88,89	92,86	92,21	84,41

4. Discussion

The study proposed an artificial intelligence-based ESA model to prevent train accidents. The fact that this study is designed with open source codes and end-to-end makes the original aspect of the study. In the proposed approach, the analyzes were performed using TPU, which resulted in an increase in performance speed and time saving. Moreover, the advantage of the proposed approach is that it provides a decision support system that avoids wasting time in error detection and provides instantaneous results for multiple images. The disadvantages of this study are that no preprocessing steps are applied to the input images, the number of images in the dataset is small, and the hardware features are only used for a limited time (limit of free use of Google Colab, etc.). The analyzes of this study were compared with similar studies in the literature and the results of the analysis are shown in Table 3.

Table 3. Comparison of this study with similar studies in the literatüre

Article	Year	Model	Accuracy (%)
Ya-Wen Lin vd. [7]	2019	Yolo-V3	89
Hovad vd. [9]	2021	Yolo-V3	84
Rajagopa vd. [11]	2018	GLCM, LBP, ESA	94,9
This study	2022	Designed ESA	92,21

Ya-Wen Lin et al. and Hovad et al. used the Yolo-V3 model in their work. It was found that the Yolo-V3 model used in both studies limited success. Preprocessing steps (image enhancement techniques, feature extraction methods, etc.) could be preferred to increase the success of the analysis results. Indeed, Rajagopa et al. observed that they were able to increase the overall success thanks to the preprocessing steps (GLCM, LBP) they used in their studies.

5. Conclusion

Troubleshooting railroad lines is a difficult and time-consuming process. Troubleshooting with conventional methods prolongs this process. With models based on artificial intelligence, the detection of defective rails on railroad lines can be easier and faster than with conventional methods. Defects that occur on rails account for the largest share of train accidents. To prevent train accidents, an artificial intelligence-based ESA model is proposed in this study. In the study of the analysis results obtained by the proposed approach, the success in sensitivity was 95.12%, in specificity 88.89%, in f-score 92.86% and in Matthews 84.41%. The approach proposed in the next study is developed using preprocessing steps (noise removal, segmentation, resolution enhancement techniques). The features obtained from the developed ESA model are transferred to the classification process using feature selection techniques. Thus, they contribute to the performance of the model. Moreover, the analysis of the ESA model to be developed is performed using freely available datasets.

References

[1] G. Sarang, "Replacement Of Stabilizers By Recycling Plastic In Asphalt Concrete," in Use of Recycled Plastics in Eco-efficient Concrete, Elsevier, 2019, pp. 307–325.

[2] T. Deniz, "Türkiye'de Ulaşım Sektöründe Yaşanan Değişimler Ve Mevcut Durum," Doğu Coğrafya Derg., vol. 21, no. 36, p. 135, Aug. 2016.

[3] A. Welankiwar, S. Sherekar, A. P. Bhagat, and P. A. Khodke, "Fault Detection in Railway Tracks Using Artificial Neural Networks," in 2018 International Conference on Research in Intelligent and Computing in Engineering (RICE), 2018, pp. 1–5.

[4] A. James et al., "TrackNet - A Deep Learning Based Fault Detection for Railway Track Inspection," in 2018 International Conference on Intelligent Rail Transportation (ICIRT), 2018, pp. 1–5.

[5] R. Shafique et al., "A Novel Approach to Railway Track Faults Detection Using Acoustic Analysis," Sensors, vol. 21, no. 18, p. 6221, Sep. 2021.

[6] X. Wei, Z. Yang, Y. Liu, D. Wei, L. Jia, and Y. Li, "Railway Track Fastener Defect Detection Based on Image Processing and Deep Learning Techniques: A Comparative Study," Eng. Appl. Artif. Intell., vol. 80, pp. 66–81, 2019.

[7] Y.-W. Lin, C.-C. Hsieh, W.-H. Huang, S.-L. Hsieh, and W.-H. Hung, "Railway Track Fasteners Fault Detection using Deep Learning," in 2019 IEEE Eurasia Conference on IOT, Communication and Engineering (ECICE), 2019, pp. 187–190.

[8] C. Yang, Y. Sun, C. Ladubec, and Y. Liu, "Developing Machine Learning-Based Models for Railway Inspection," Appl. Sci., vol. 11, no. 1, p. 13, Dec. 2020.

[9] E. Hovad et al., "Deep Learning for Automatic Railway Maintenance," 2021, pp. 207–228.

[10] M. Sysyn, U. Gerber, O. Nabochenko, D. Gruen, and F. Kluge, "Prediction of Rail Contact Fatigue on Crossings Using Image Processing and Machine Learning Methods," Urban Rail Transit, vol. 5, no. 2, pp. 123–132, 2019.

[11] M. Rajagopal, M. Balasubramanian, S. Palanivel, "An Efficient Framework to Detect Cracks in Rail Tracks Using Neural Network Classifier," Computacion y Sistemas, vol. 22, no. 3, pp. 943–952, 2018.

[12] S. I. Eunus, "Railway Track Fault Detection," Kaggle, 2021. [Online]. Available: https://www.kaggle.com/salmaneunus/railway-track-fault-detection. [Accessed: 28-Nov-2021].

[13] H. Selçuk, T. Ç. Akıncı, and Ş. S. Şeker, "Derin Evrişimli Sinir Ağı Modellerinin Açık Kaynak Kodlu Yazılım Platformlarında Tasarımının Değerlendirilmesi," İstanbul Sabahattin Zaim Üniversitesi Fen Bilim. Enstitüsü Derg., Apr. 2021.

[14] T.-C. Lu, "CNN Convolutional Layer Optimisation Based On Quantum Evolutionary Algorithm," Conn. Sci., vol. 33, no. 3, pp. 482–494, Jul. 2021.

[15] C. F. G. dos Santos, T. P. Moreira, D. Colombo, and J. P. Papa, "Does Removing Pooling Layers from Convolutional Neural Networks Improve Results?," SN Comput. Sci., vol. 1, no. 5, p. 275, Sep. 2020.

[16] P. Sperl, C.-Y. Kao, P. Chen, X. Lei, and K. Böttinger, "DLA: Dense-Layer-Analysis for Adversarial Example Detection," in 2020 IEEE European Symposium on Security and Privacy (EuroS&P), 2020, pp. 198–215.

[17] C. Garbin, X. Zhu, and O. Marques, "Dropout vs. Batch Normalization: An Empirical Study of Their Impact to Deep Learning," Multimed. Tools Appl., vol. 79, no. 19, pp. 12777–12815, 2020.

[18] S. Maharjan, A. Alsadoon, P. W. C. Prasad, T. Al-Dalain, and O. H. Alsadoon, "A novel enhanced softmax loss function for brain tumour detection using deep learning," J. Neurosci. Methods, vol. 330, p. 108520, 2020.

[19] N. P. Jouppi et al., "In-Datacenter Performance Analysis Of A Tensor Processing Unit," in 2017 ACM/IEEE 44th Annual International Symposium on Computer Architecture (ISCA), 2017, pp. 1–12.

[20] S. Khirirat, H. R. Feyzmahdavian, and M. Johansson, "Mini-Batch Gradient Descent: Faster Convergence Under Data Sparsity," in 2017 IEEE 56th Annual Conference on Decision and Control (CDC), 2017, pp. 2880–2887.

[21] X. Ying, "An Overview Of Overfitting And Its Solutions," J. Phys. Conf. Ser., vol. 1168, p. 022022, Feb. 2019.

[22] Z. Cömert, "Fusing Fine-Tuned Deep Features For Recognizing Different Tympanic Membranes," Biocybern. Biomed. Eng., vol. 40, no. 1, pp. 40–51, Jan. 2020.

[23] E. Başaran, Z. Cömert, A. Şengür, Ü. Budak, Y. Çelik, and M. Toğaçar, "Chronic Tympanic Membrane Diagnosis based on Deep Convolutional Neural Network," in 2019 4th International Conference on Computer Science and Engineering (UBMK), 2019, pp. 1–4.

[24] S. Boughorbel, F. Jarray, and M. El-Anbari, "Optimal Classifier For Imbalanced Data Using Matthews Correlation Coefficient Metric," PLoS One, vol. 12, no. 6, p. e0177678, Jun. 2017.

Investigation of an Outer Rotor In-Wheel Switched Reluctance Motor for Electric Vehicles by Finite Element Method

Zeki OMAÇ[1*]

[1] Department of Electrical and Electronics Engineering, Faculty of Engineering, Munzur University, Tunceli, Turkey
[*1] zomac@munzur.edu.tr

Abstract: The demand of fossil fuel vehicles has decreased due to carbon emissions. Recently, electric vehicles (EV) with electric motor propulsion have got attention due to their zero carbon emissions and high efficiency. In this study, an outer rotor in-wheel switched reluctance motor (IWSRM) with 18 poles on the stator and 24 poles on the rotor, designed for the propulsion of electric vehicles, is investigated in two-dimensional Finite Element Method (FEM). The magnetic field distributions of IWSRM for different rotor positions at nominal current are obtained. Then, the torque and phase inductance are calculated. As a result, the designed outer rotor IWSRM provided low torque ripple.

Key words: In-Wheel Switched Reluctance Motor, Finite Element Method, Electric Vehicle.

Elektrikli Araçlar için Rotoru Dışta Tekerlek İçi bir Anahtarlamalı Relüktans Motorun Sonlu Elemanlar Yönteminde İncelenmesi

Öz: Karbon salınımları nedeniyle fosil yakıtlı araçlara ilgi azalmaktadır. Sıfır karbon salınımları ve yüksek verimleri nedeniyle son zamanlarda elektrik motoru tahrikli araçlar gündeme gelmiştir. Bu çalışmada, elektrikli araçların tahriki için tasarlanmış, statorunda 18 kutup ve rotorunda 24 kutup olan rotoru dışta tekerlek içi bir anahtarlamalı relüktans motor (TARM), iki boyutlu Sonlu Elemanlar Yönteminde (SEY) incelenmiştir. Nominal akımda farklı rotor konumları için TARM'ın alan dağılımları elde edilmiş, ürettiği nominal moment hesaplanmış ve endüktans eğrisi çıkarılmıştır. SEY analiz sonucunda, incelenen TARM'de düşük moment dalgalanması elde edilmiştir.

Anahtar kelimeler: Tekerlek İçi Anahtarlamalı Relüktans Motor, Sonlu Elemanlar Yöntemi, Elektrikli Araç.

1. Introduction

Recently, interest regarding electric vehicles has raised because of their higher efficiency, zero carbon emission, noiseless operation and low cost compared to internal combustion engines [1-2]. In addition, electric vehicles with in-wheel electric motors do not need gears and transmission parts, which gives these vehicles an additional advantage.

In electric vehicles, permanent magnet synchronous motor (PMSM), induction motor (IM) and switched reluctance motor (SRM) are used as propulsion motors [3-4]. These motors have some advantages and disadvantages in terms of cost, losses, and efficiency. Although the PMSM is a highly efficient motor, it is the most expensive electric motor due to the magnets used in its rotor. However, these magnets are not used in the IM and SRM, so the cost of the IM and SRM are lower than PMSM. Compared to SRM, which does not have winding on the rotor, the losses in IM are high due to the conductors in the rotor. Therefore, SRM is a motor with the lowest cost with its simple and rugged motor structure, invulnerability to harsh operating conditions, robust rotor, low maintenance cost and decreased losses. In addition, SRMs have salient pole structure in stator and rotor facilitating the cooling of the heat generated due to losses [5-12].

To generate larger torque values, the SRM is operated at high magnetic saturation. Therefore, the nonlinear magnetization curve of the iron sheet used in the stator and rotor should be considered when the magnetic field distribution of the SRM is obtained. It is easier to assemble the outer rotor in-wheel switched reluctance motor (IWSRM) to the wheel rim, and then the torque produced is greater than the conventional SRM [6]. For solving these magnetic problems, FEM, a computer-aided numerical method, is a suitable method.

In the SRM for a continuous rotational motion, the current flows through the phases sequentially. In other words, the torque produced by the SRM is equal to the sum of the torques sequentially produced by the phases. The torque produced by a phase at constant current is a curve varying from zero to maximum depending on the

---
[*] Corresponding author: zomac@munzur.edu.tr. ORCID Number of authors: [1] 0000-0002-9339-8243

position. This causes a ripple in the total torque produced. The torque ripple causes acoustic noises in SRM [13-18].

In the literature, different IWSRM models designed for electric vehicles have been emphasized. In [2], a IWSRM model with double teeth per pole on a 6/16 pole stator is examined. In [5], the design of an 18/12 pole IWSRM is best done using a Pareto-based multi-objective differential evolution algorithm. In [7], a new 18/12 pole IWSRM for electric vehicle is designed, FEM analysis and control are performed. In [9], an 8/6 pole IWSRM is designed using multi-objective optimization.

In this study, the magnetic field distribution, torque, and inductance variations of outer rotor IWSRM are calculated from two-dimensional FEM for electric vehicles.

2. Outer Rotor in Wheel Switched Reluctance Motor

Unlike the conventional SRM motor structure, the rotor is outside, and the stator is inside in an outer rotor in wheel SRM. The cross-sectional view of the 18/24-pole IWSRM is shown in Figure 1. In addition, stator and rotor outer diameters and other pole length dimensions are shown in Figure 2. Furthermore, all other motor dimensions are given in Table 1.
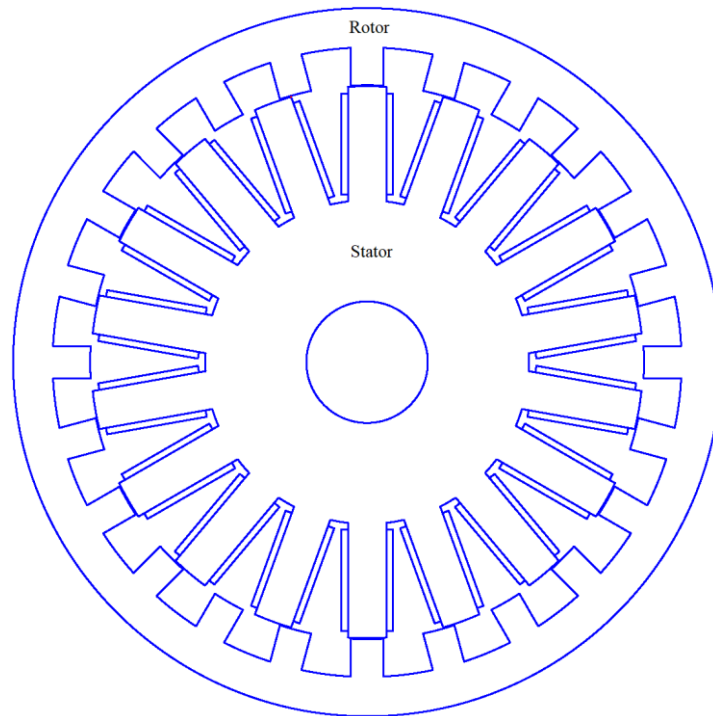
Figure 1. The cross-sectional view of outer rotor IWSRM.

For constant current, the torque produced in one phase of the SRM can be calculated from the equation (1) [12].

$$T_e = \frac{\partial W_m}{\partial \theta} \tag{1}$$

Where, T_e, W_m and θ denote electromagnetic torque, co-energy, and rotor position, respectively. The total torque produced in SRM is equal to the sum of the torques produced by the individual phases. The total torque for a three-phase SRM can be written as in equation (2).

$$T_t = T_a(\theta, i_a) + T_b(\theta, i_b) + T_c(\theta, i_c) \tag{2}$$

Here, T_t the total torque, T_a, T_b and T_c represent the torque produced in phases a, b, and c, respectively.
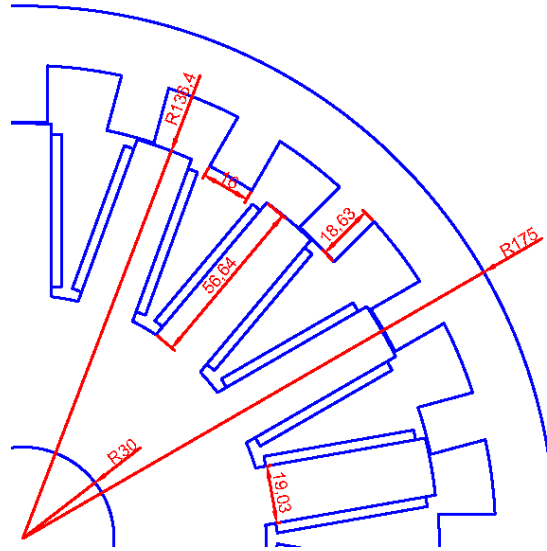
Figure 2. The representation of some dimensions of IWSRM on a quarter view.

Table 1. Parameters of outer rotor in-wheel switched reluctance motor.

Parameter	Value
Number of stator poles (N_s)	18
Number of rotor poles (N_r)	24
Rotor outer diameter (mm)	350
Stator outer diameter (mm)	273.8
Package length (mm)	55
Air gap (mm)	0.5
Shaft diameter (mm)	60
Stator pole arc (degree)	8
Rotor pole arc (degree)	7
Stator pole width (mm)	19.03
Rotor pole width (mm)	16
Stator pole height (mm)	56.64
Rotor pole height (mm)	18.63

3. Finite Element Method Analysis of Outer Rotor IWSRM and Results

In the Finite Element Method, the geometry of outer rotor IWSRM, stator, rotor and air gap are divided into small triangular elements, as shown in Figure 3 [17]. To minimize the amount of error and to calculate accurate results, the air gap region between the stator and the rotor, where there is a large change in magnetic parameters, is divided into smaller triangular elements in as four layers as shown in Figure 4. The air region outside the IWSRM is meshed with larger triangular elements. A zero-vector potential is defined at the boundary of the region of solution. A current density of J=21161876 A/m^2 is applied to the windings on six poles forming a phase for a nominal current of 75 A. Steel 1008 sheet is chosen for the stator and rotor iron sheets.

The rotor position is rotated one degree from the aligned to the unaligned position, and the magnetic field distribution for the IWSRM is obtained for each rotor position, and the produced torque and phase inductance are calculated for a single phase. The air gap magnetic field distribution is given in Figure 5 for the rotor position θ=5°. The magnetic field distributions obtained from the two-dimensional FEM are shown in Figure 6 (a) and (b) for rotor positions θ=0° and θ=5°, respectively. The graph of the torque produced in one phase depending on the rotor position at the nominal current is shown in Figure 7 and the graph of inductance is shown in Figure 8.
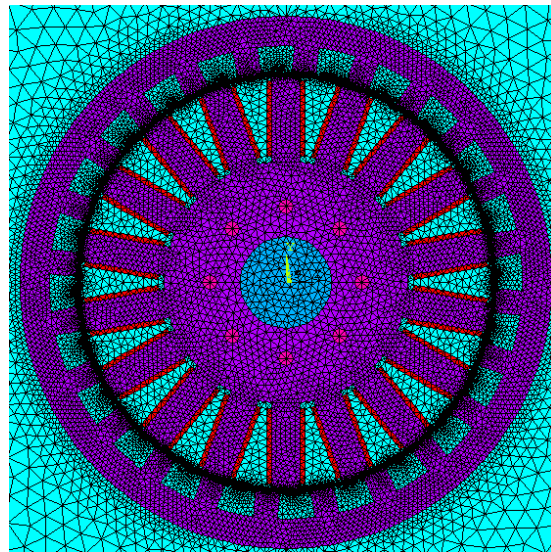
Figure 3. The meshed of outer rotor IWSRM.
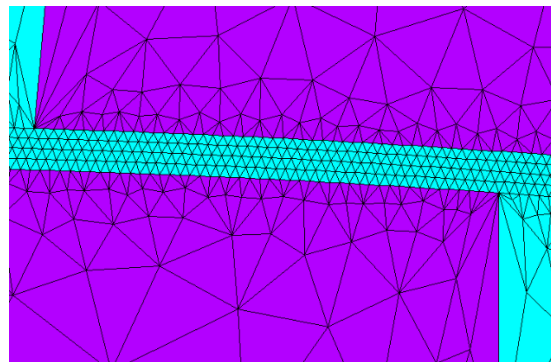
Figure 4. The meshed of air gap between stator and rotor in outer rotor IWSRM.
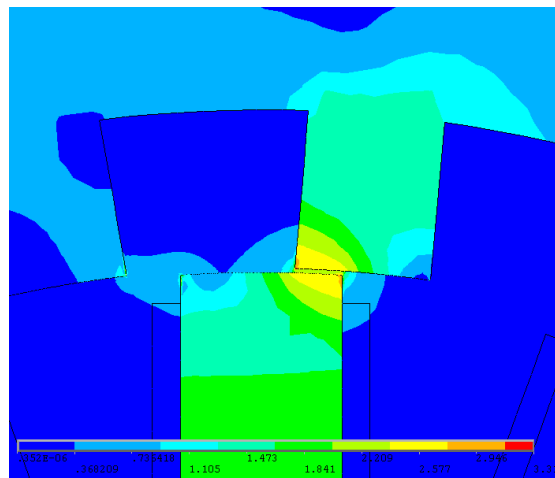
Figure 5. The magnetic field distribution in air gap region for θ=5° rotor position.
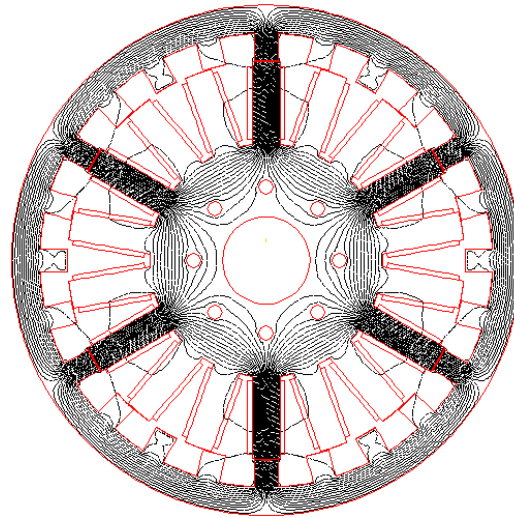
(a)
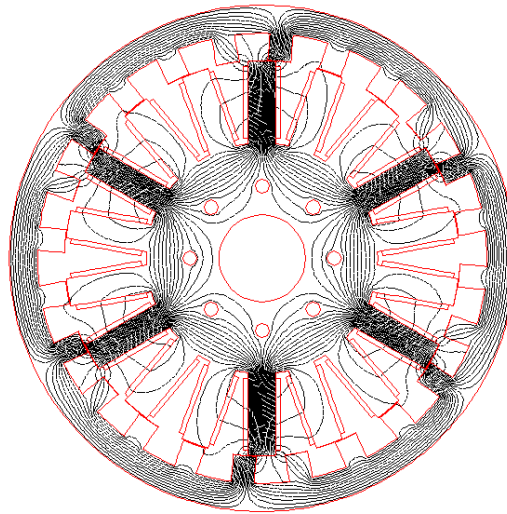
(b)

Figure 6. Magnetic field distributions for different rotor positions (a) θ=0°, (b) θ=5°.

Figure 7. The graph of the torque generated by a phase at the nominal current depending on the rotor position.
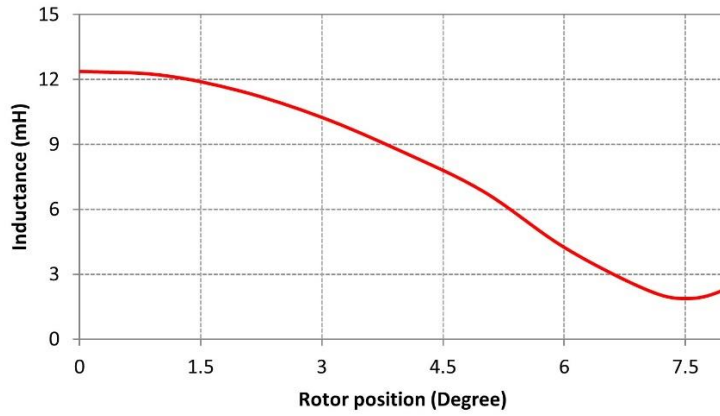
Figure 8. The graph of a phase inductance with respect to the rotor position.
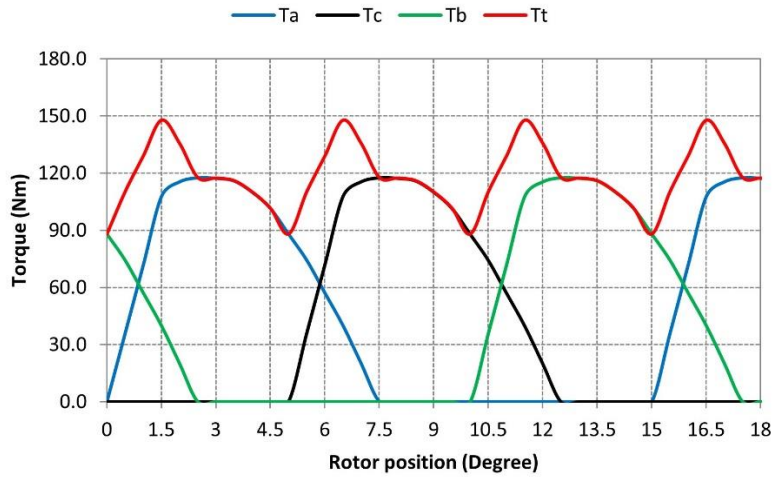
Figure 9. The graph of phase torques and total torque with respect to the rotor position at the nominal current.
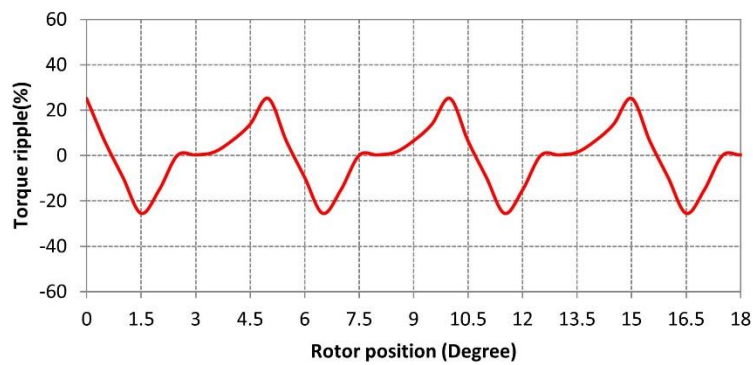
Figure 10. The graph of torque ripple with respect to the rotor position at the nominal current.

In outer rotor IWSRM, the torques separately produced by phases a, b and c depending on the rotor position at the nominal current, and the total torque produced are displayed in Figure 9. In addition, the percentage ripple in the total torque is given in figure 10.

In designing of outer rotor IWSRM models, the low torque ripple is desired for smooth speed response. For example, in the SRM model with 18 poles on the stator and 12 poles on the rotor, designed for hybrid electric vehicles in a study [10], the torque ripple varies between ±36% for square wave current. In this study, the investigated the outer rotor IWSRM model with the 18/24 poles, the torque ripple is ±25% for square wave current. Therefore, the investigated the outer rotor IWSRM model has ±11% lower torque ripple than the 18/12 pole SRM model in [10]. Radial forces cause acoustic noises in the outer rotor IWSRM. Another source of acoustic noise is torque ripple. When torque ripple is reduced, the acoustic noise will be lower at the same rate due to the torque ripple.

4. Mathematical Model of Outer Rotor IWSRM and Simulation Results

If the mutual inductance between phases is neglected, the voltage can be written for a phase of the outer rotor IWSRM in equation (3) [12-13].

$$v = iR + \frac{d\psi(\theta, i)}{dt} \tag{3}$$

Where v is the phase voltage, R is the phase resistance, i is the phase current, ψ is the magnetic flux and θ is the rotor position. If the relation $\psi = iL$ is used for the magnetic flux, the voltage of a phase becomes as equation (4).

$$v = iR + L(\theta, i)\frac{di}{dt} + i\omega_m \frac{dL(\theta, i)}{d\theta} \tag{4}$$

Where ω_m is the rotor angular velocity and L is the phase inductance. The torque induced in the rotor can be calculated from equation (5).

$$T_e = \frac{1}{2}i^2 \frac{dL(\theta, i)}{d\theta} \tag{5}$$

Where T_e is the torque induced in the rotor. The mechanical motion equation of the outer rotor IWSRM is given in equation (6).

$$T_e = J\frac{d\omega_m}{d\theta} + B\omega_m + T_L \tag{6}$$

Where, J is the moment of inertia, B is the friction coefficient and T_L is the load torque.
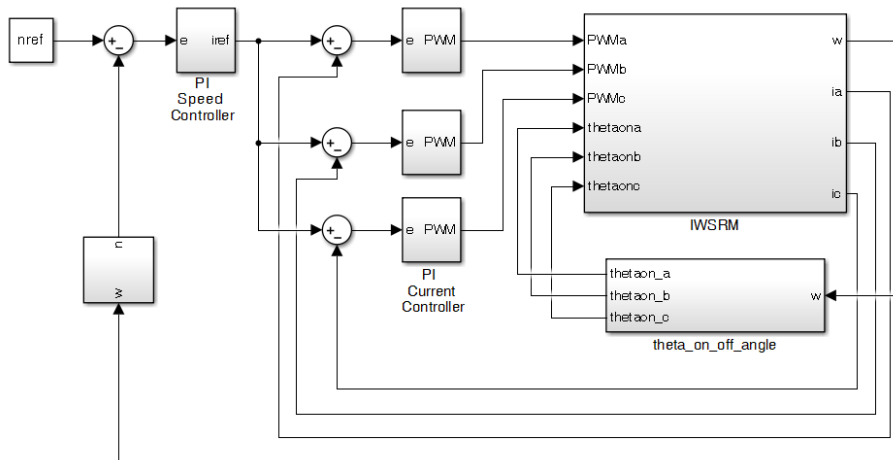
Figure 11. Matlab/Simulink model of the outer rotor IWSRM.

The dynamic model of the outer rotor IWSRM prepared in Matlab Simulink software is shown in Figure 11. The simulation model parameters and values of the outer rotor IWSRM are given in Table 2. The simulation results of the outer rotor IWSRM are given in Figure 12 for speed, torque, and phase currents under T_L=80 Nm load torque at n=200 rpm reference speed. Proportional integral (PI) controller is used for speed and current control of the outer rotor IWSRM. When the speed graph is examined, the outer rotor IWSRM rotor speed reaches the reference speed in a short time and catches the steady state with a small oscillation. When the outer rotor IWSRM is started, the phase currents take large values. After the outer rotor IWSRM is started, phase currents decrease to normal values. Likewise, the torque ripple produced in the rotor during starting is high. When the rotor speed reaches the reference speed, the torque graph becomes smooth.

(a)

(b)

(c)
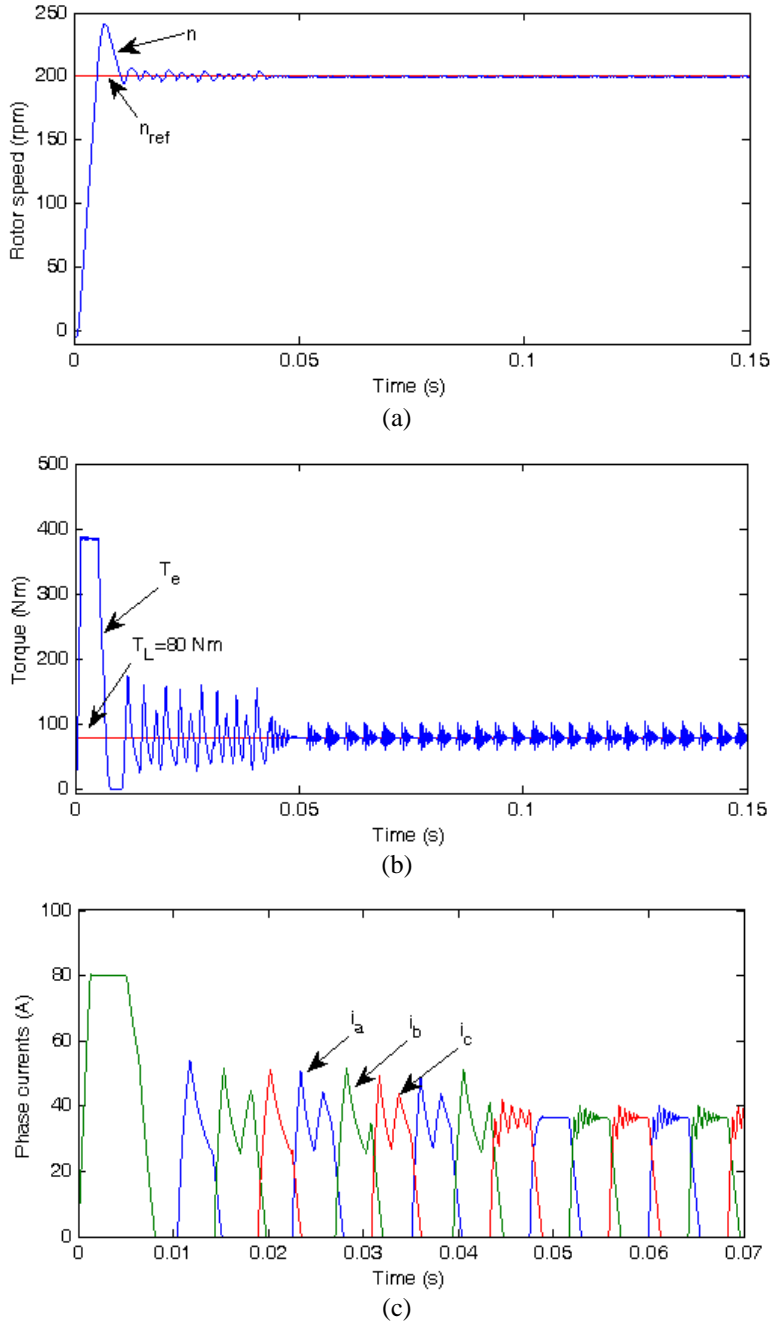
Figure 12. Simulation results for n_{ref}=200 rpm reference speed, and T_L=80 Nm load torque (a) Rotor speed, (b) Torque, (c) Phase currents.

Table 2. Simulation parameters of the outer rotor IWSRM.

Parameter	Value
DC bus voltage	300 V
A phase resistance (R)	0.5 Ω
Friction factor (B)	0.0055 Nm/(rad/s)
Inertia of rotor (J)	0.0593 Kg.m^2
Proportional coefficient (K_p)	30
Integral coefficient (K_i)	0.5
Load torque (T_L)	80 Nm

5. Conclusion

In this study, outer rotor in wheel switched reluctance motor with 18 poles in its stator and 24 poles in its rotor designed for electric vehicles is investigated using FEM under nonlinear magnetic conditions. In outer rotor IWSRM, a phase is formed by simultaneously exciting the windings on six opposite poles in the stator. Thus, the outer rotor IWSRM converter is simpler and produces larger torques by using fewer solid-state switches. At the nominal current, the magnetic field distribution of the outer rotor IWSRM is obtained by rotating the rotor at an angle of each one degree. In addition, a phase inductance, torque, and total torque are calculated at the nominal current. As a result, low torque ripple is obtained in the investigated model of outer rotor IWSRM.

References

[1]   Yang Z, Shang F, Brown I P, and Krishnamurthy M. Comparative study of interior permanent magnet, induction, and switched reluctance motor drives for EV and HEV applications. IEEE Trans Transp Electrific 2015; **1**(3): 245-254.

[2]   Zhu J, Cheng K W E, Xue X, and Zou Y. Design of a new enhanced torque in-wheel switched reluctance motor with divided teeth for electric vehicles. IEEE Trans Magn 2017; 53(11).

[3]   Gong C, Li S, Habetler T, and Zhou P. Acoustic modeling and prediction of ultrahigh-speed switched reluctance machines based on multiphysics finite element analysis. IEEE Trans Ind Appl 2021; 57(1):198- 207.

[4]   Chiba A, Kiyota K, Hoshi N, Takemoto M, and Ogasawara S. Development of a rare-earth-free SR motor with high torque density for hybrid vehicles. IEEE Trans Energy Convers 2015; 30(1): 175-182.

[5]   Öksüztepe E. In-wheel switched reluctance motor design for electric vehicles by using pareto based multi objective differential evolution algorithm. IEEE Transs Vehic Technol 2017; 66(6): 4706-4715.

[6]   Rallabandi V, Han P, Wu J, Cramer A M, Ionel D M, and Zhou P, Design optimization and comparison of direct-drive outer-rotor SRMs based on fast current profile estimation and transient FEA. IEEE Trans Ind Appl 2021; 57(1): 236-245.

[7]   Omaç Z, Polat M, Öksüztepe E, Yıldırım M, Yakut O, Eren H, Kaya M, and Kürüm H. Design, analysis, and control of in-wheel switched reluctance motor for electric vehicles. Elec Eng 2018;100: 865–876.

[8]   Yildirim M, Polat M, Öksüztepe E, Omaç Z, Yakut O, Eren H, Kaya M, Kürüm H. Designing in-wheel switched reluctance motor for electric vehicles 2014; IEEE PEMC'14: 793-798.

[9]   Xue X D, Cheng K W E, Ng T W, and Cheung N C. Multi-objective optimization design of in-wheel switched reluctance motors in electric vehicles. IEEE Trans Ind Electron 2010; **57**(9): 2980-2987.

[10] Furqani J, Wiguna C A, Chiba A, Gundogmus O, Sozer Y, and Purwadi A. Experimental verification of acoustic noise and radial force sum variation in switched reluctance motor. IEEE Trans Ind Appl 2021; **57**(1): 2481- 2493.

[11] Kiyota K, Kakishima T, Chiba A, Rahman M A. Cylindrical rotor design for acoustic noise and windage loss reduction in switched reluctance motor for HEV applications. IEEE Trans Ind Appl 2016; **52**(1): 154-162.

[12] Desai P C, Krishnamurthy M, Schofield N, Emadi A. Novel switched reluctance machine configuration with higher number of rotor poles than stator poles: concept to implementation. IEEE Trans Ind Electron 2010; **57**(2): 649-659.

[13] Omaç Z. Fuzzy-logic-based robust speed control of switched reluctance motor for low and high speeds. Turk J Elec Eng & Comp Sci 2019; 27(1): 316–329.

[14] Omaç Z, Polat M, Kaya M, Öksüztepe E, Eren H, Yıldırım M, Kürüm H. New trends in electrical vehicle powertrains, Outer rotor srm design for electric vehicle without reducer via speed-up evolutionary algorithm. UK: IntechOpen, 2018. pp.129-151.

[15] Omaç Z, Cevahir C. Control of switched reluctance generator in wind power system application for variable speeds. Ain Shams Eng J 2021; **12**: 2665-2672.

[16] Omaç Z. Design and analysis of a water pumping system with photovoltaic source and switched reluctance motor. Balkan J of Elec & Comp Eng 2019; **7**(3): 355-361.

[17] Omaç Z, Kürüm H, and Selçuk A H. Design, analysis and control of a switched reluctance motor having 18/12 poles. Fırat Uni Sci & Eng J 2007; **3**(19) 339-346.

[18] Omaç Z, Kürüm H, and Selçuk A H. Digital current control of switched reluctance motor. Inter J Elec & Power Eng 2011; 5:54-61.

MUSIC Based Microwave Imaging of Nonlinear Point-Like Scatterers

Cüneyt UTKU[1*]

[1] Informatics and Information Security Research Center, Scientific and Technological Research Council of Turkey,
Kocaeli, Turkey
[*1] cuneyt.utku@tubitak.gov.tr

Abstract: Narrowband localization of point-like nonlinear scatterers in a homogeneous background medium is investigated. A theoretical framework is provided based on Multiple Signal Classification (MUSIC) imaging, formerly developed for time-reversal imaging of point-like targets in cluttered environment. Numerical simulations are provided to assist in understanding the relations between various aspects of the imaging method. Numerical evidence shows that for the same signal to noise ratio, higher order harmonics (second and third harmonics) resulting from nonlinear scattering, have better imaging resolutions compared to the fundamental harmonic corresponding to linear scattering.

Key words: Harmonic radar, nonlinear target, microwave imaging, MUSIC.

Lineer Olmayan Noktasalımsı Saçıcıların MUSIC Tabanlı Mikrodalga Görüntülemesi

Öz: Homojen ortamda lineer olmayan noktasalımsı saçıcıların darbant lokalizasyonu incelenmiştir. Noktasalımsı hedeflerin parazit yankılı ortamda zaman evirme (time reversal) görüntülenmesi için daha önce geliştirilmiş olan Multiple Signal Classification (MUSIC) görüntülemesine dayalı teorik çerçeve sunulmuştur. Görüntüleme metodunun muhtelif yönleri arasındaki ilişkilerin anlaşılması için sayısal benzetimler verilmiştir. Sayısal sonuçlar, aynı sinyal-gürültü oranı için lineer olmayan saçılmadan kaynaklanan yüksek mertebeden harmoniklerin (ikinci ve üçüncü harmonikler), lineer saçılmaya tekabul eden temel harmoniğe nisbetle daha iyi görüntüleme çözünürlüğüne sahip olduklarını göstermektedir.

Anahtar kelimeler: Harmonik radar, lineer olmayan hedef, mikrodalga görüntüleme, MUSIC.

1. Introduction

Harmonic radars have received considerable attention in recent years mainly due to their inherent clutter rejecting nature. Harmonic radars using passive transponders/tags have been proposed for diverse applications such as tracking [1,2], monitoring of vital signs [3], search and rescue of people under distress [4,5] and in standoff measurement of temperature [6]. Recent advances on harmonic tag applications can be found in [7]. Another very important application of harmonic radars is the detection of concealed electronics [8,9]. Most of the above applications require localization of these harmonic generating tags or devices. Two imaging based localization strategies of nonlinear targets have been proposed in the past. Both are broadband systems operating in stepped frequency mode. The first system based on synthetic aperture radar (SAR) processing was proposed for two-dimensional localization of stationary nonlinear scatterers [10]. With later improvements the system was modified to locate and also estimate the speed of moving nonlinear scatterers [11]. The second proposed system is based on Robust Capon Beamforming with frequency smoothing and has improved imaging quality compared the former SAR based system for stationary targets [12].

In contrast to the aforementioned imaging methods, this study focuses on narrowband and near field imaging of point-like nonlinear targets/scatterers embedded in a homogeneous background medium. A MUSIC based imaging method, which was originally proposed [13-15] as an alternative to conventional time-reversal imaging, is adopted here. The time reversal matrix can be decomposed into a product of the multistatic response matrix/transfer matrix (corresponding to a set linear targets and an associated transmit/receive array configuration) and its Hermitian [16]. With this decomposition, Lev-Ari and Devaney [13], Devaney [14] and Devaney et al [15] used the MUSIC framework to classify the singular system of the multistatic response matrix into its signal and

---

noise subspaces and exploited the orthogonality of these subspaces to define a pseudo-spectrum that peaked at the target locations. In this study, the multistatic response matrix, originally defined for linear scatterers, is generalized for nonlinear scatterers to a set of multistatic response matrices and the MUSIC framework is similarly applied to this new set of multistatic response matrices to image point-like nonlinear scatterers.

In the next section, the signal model for EM fields measured by an array of antenna elements is discussed, followed by adaptation of the signal model to MUSIC based imaging. Numerical simulations are presented, investigating important aspects of the MUSIC based imaging. A summary of the findings along with short discussions is provided in the conclusion.

2. The Signal Model and MUSIC Imaging

Consider a collection of M nonlinear point-like scatterers embedded in a homogeneous background medium with relative permittivity ε_{rb}. We are interested in estimating the location of these scatterers by probing the collection with time harmonic EM waves at frequency f (a time dependence of $\exp\{-i\omega t\}$ is assumed where $\omega = 2\pi f$) using a distributed system of N antennas operating both in transmit and receive modes i.e. transmitters and receivers are collocated. In this study, it is assumed that $M \leq N$ and multiple scattering between scatterers is assumed to be negligible so that the results are valid to first order of scattering. Moreover, the problem is treated in two dimensions for simplicity. The two-dimensional treatment is not a restriction, however, and generalization of the following mathematical development to three dimensions is possible with some rigour. The problem geometry is depicted in Figure 1 where the point-like scatterers correspond to infinite length lines aligned with z-axis, having nonlinear scattering characteristics. Similarly, the system of RX/TX antennas is a uniform linear array of line sources aligned with z-axis. The array axis runs parallel to the x-axis and is located in the region $y < 0$. Array length is given by $\mathcal{L} = Nd$ where N is the number of array elements and d is the array inter-element spacing. The region of interest (ROI) is the region subject to imaging and is conservatively selected between $[-\mathcal{L}/2, \mathcal{L}/2]$ in the x-direction and between $[0, \mathcal{L}/2]$ in the y-direction. Also shown in the figure is a grid comprising the actual pixels of the image. The grid spacings are Δ_x and Δ_y along the x- and y-axis, respectively. These spacings do not necessarily correspond to the imaging resolution to be discussed later. In two dimensions, the problem can be treated with scalar formalism, so for the geometry considered here, the electric field normal to the xy-plane is sufficient to completely determine the problem. Let the scalar quantity $E(\boldsymbol{x}_r, \boldsymbol{x}_t)$ denote the electric field along z-axis, received by the antenna at $\boldsymbol{x}_r \in \{\boldsymbol{x}_1, \cdots, \boldsymbol{x}_N\}$ when the antenna (line source) at $\boldsymbol{x}_t \in \{\boldsymbol{x}_1, \cdots, \boldsymbol{x}_N\}$ is in transmission. This field can be expressed as the sum of all the harmonics generated by nonlinearity [9, 19] (the DC component is suppressed):

$$E(\boldsymbol{x}_r, \boldsymbol{x}_t, t) = \sum_{n=1}^{\infty} E^{(n)}(\boldsymbol{x}_r, \boldsymbol{x}_t) e^{-in\omega t} \tag{1}$$

where

$$E^{(n)}(\boldsymbol{x}_r, \boldsymbol{x}_t) \approx \sum_{m=1}^{M} \alpha_m^{(n)} G(\boldsymbol{x}_r, \boldsymbol{x}_m, n\omega) G^n(\boldsymbol{x}_m, \boldsymbol{x}_t, \omega) b^n \tag{2}$$

is the electric field (z-axis) corresponding to the n'th harmonic scattered by M nonlinear particles, $\alpha_m^{(n)}$ is a nonlinearity coefficient for the m'th particle corresponding to the n'th harmonic, b is the amplitude of the time harmonic signal transmitted by the antenna (line source) and $G(\boldsymbol{x}, \boldsymbol{x}', \omega)$ is the two dimensional Green's function for a line source at $\boldsymbol{x}'$ and observation point at $\boldsymbol{x}$. The Green' function is given by $G(\boldsymbol{x}, \boldsymbol{x}', \omega) = (i/4)H_0^{(1)}(|\boldsymbol{x} - \boldsymbol{x}'| \omega \sqrt{\varepsilon_{rb}}/c)$ where $H_0^{(1)}(\cdot)$ is the Hankel function of the first kind and zero order. In deriving
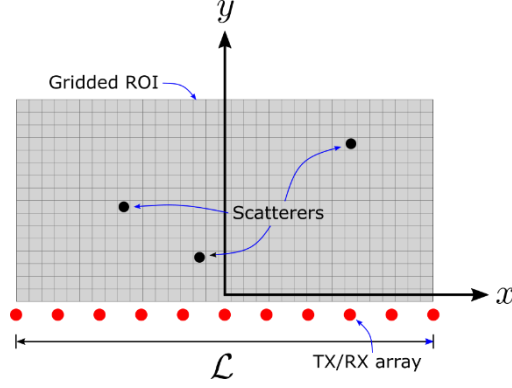
Figure 1. Geometry for imaging of point-like nonlinear scatterers. Red dots indicate the array of length $\mathcal{L}$.

Equation 2, it is reasonably assumed that $Q_m^{2(q+1)} \ll Q_m^{2q}$ and $Q_m^{2(q+1)+1} \ll Q_m^{2q+1}$ for $\forall\, q \in \mathbb{N}$ where $Q_m^n = \left| \alpha_m^{(n)} G^n(\boldsymbol{x}_m, \boldsymbol{x}_t, \omega) b^n \right|$. We restate that the effect of multiple scattering between scatterers is neglected so that Equation 2 is correct to first order of scattering.

When several elements transmit simultaneously, Equation 2 is modified and the expression for the field corresponding to the n'th harmonic then becomes

$$E^{(n)}(\boldsymbol{x}_r, \widetilde{\boldsymbol{x}}_t) = \sum_{m=1}^{M} \alpha_m^{(n)} G(\boldsymbol{x}_r, \boldsymbol{x}_m, n\omega) \left(\sum_{j=1}^{N} b_j G\left(\boldsymbol{x}_m, \boldsymbol{x}_{t,j}, \omega\right) \right)^n$$

where the N-tuple $\widetilde{\boldsymbol{x}}_t = (\boldsymbol{x}_1, \cdots, \boldsymbol{x}_N)$ indicates that all N array elements are in transmission mode and b_j is the amplitude of the signal transmitted by the j'th transmitting element. One can expand the above expression as

$$E^{(n)}(\boldsymbol{x}_r, \widetilde{\boldsymbol{x}}_t) = E_L^{(n)}(\boldsymbol{x}_r, \widetilde{\boldsymbol{x}}_t) + \sum_{m=1}^{M} \alpha_m^{(n)} G(\boldsymbol{x}_r, \boldsymbol{x}_m, n\omega) B(\boldsymbol{x}_m, \widetilde{\boldsymbol{x}}_t)$$

where

$$E_L^{(n)}(\boldsymbol{x}_r, \widetilde{\boldsymbol{x}}_t) = \sum_{m=1}^{M} \alpha_m^{(n)} G(\boldsymbol{x}_r, \boldsymbol{x}_m, n\omega) \sum_{j=1}^{N} G^n\left(\boldsymbol{x}_m, \boldsymbol{x}_{t,j}, \omega\right) b_j^n$$

and $B(\boldsymbol{x}_m, \widetilde{\boldsymbol{x}}_t)$ contains all the remaining cross product terms. Changing the order of summation in the last expression and making use of the definition in Equation 2, one has $E_L^{(n)}(\boldsymbol{x}_r, \widetilde{\boldsymbol{x}}_t) = \sum_{j=1}^{N} E^{(n)}\left(\boldsymbol{x}_r, \boldsymbol{x}_j\right)$ suggesting that $E_L^{(n)}(\boldsymbol{x}_r, \widetilde{\boldsymbol{x}}_t)$ can be obtained as sum of the isolated measurements $E^{(n)}\left(\boldsymbol{x}_r, \boldsymbol{x}_j\right), j = 1, \ldots, N$, i.e. the measurement made when only the array element at $\boldsymbol{x}_j$ is in transmission. Collecting the results of all N receivers in a vector $\boldsymbol{E}_L^{(n)} = \left[E_L^{(n)}(\boldsymbol{x}_1, \widetilde{\boldsymbol{x}}_t), \cdots, E_L^{(n)}(\boldsymbol{x}_N, \widetilde{\boldsymbol{x}}_t) \right]^T$ where the superscript 'T' denotes the transpose, one has the matrix expression

$$E_L^{(n)} = K^{(n)} b^{(n)} \tag{3}$$

where $b^{(n)} = [b_1^n, \cdots, b_N^n]^T$ and

$$K^{(n)} = \sum_{m=1}^{M} K_m^{(n)} \tag{4}$$

is the multistatic response matrix corresponding to the n'th harmonic, that maps the N dimensional complex space to itself i.e. $K^{(n)} : C^N \rightarrow C^N$. Similarly, $K_m^{(n)}$ is the multistatic response matrix for the m'th scatterer, corresponding to the n'th harmonic. The elements of $K_m^{(n)}$ are given as

$$\left[K_m^{(n)} \right]_{ij} = \alpha_m^{(n)} G(x_i, x_m, n\omega) G^n(x_m, x_j, \omega). \tag{5}$$

Further defining the vector quantities

$$g_{r,m}^{(n)} = [G(x_1, x_m, n\omega), \cdots, G(x_N, x_m, n\omega)]^T \tag{6}$$

and

$$g_{t,m}^{(n)} = [G^n(x_1, x_m, \omega), \cdots, G^n(x_N, x_m, \omega)]^T, \tag{7}$$

the multistatic response matrix can alternatively be expressed as:

$$K_m^{(n)} = \alpha_m^{(n)} g_{r,m}^{(n)} \left[g_{t,m}^{(n)} \right]^T. \tag{8}$$

Note that for the fundamental harmonic i.e. $n = 1$, $g_{r,m}^{(1)} = g_{t,m}^{(1)}$, so that the above expressions readily reduce to those given in literature (e.g. [14]) for collocated transmitters and receivers. For the fundamental harmonic, whenever $\left[g_{r,k}^{(1)} \right]^T g_{t,m}^{(1)*} = \left[g_{t,k}^{(1)} \right]^T g_{t,m}^{(1)*} = \delta_{k,m}$ where $\delta_{k,m}$ is the Kronecker delta, the scatterers k and m are said to be resolved [14]. This notion may be generalized to nonlinear scatterers such that nonlinear scatterers k and m are said to be resolved at the n'th harmonic whenever $\left[g_{r,k}^{(n)} \right]^T g_{t,m}^{(n)*} = \delta_{k,m}$. Hence, scatterers that are not resolved at the fundamental harmonic may be resolved at a higher order harmonic. If all scatterers are resolvable at the n'th harmonic then the explicit expression of Equation 4, given as (using Equation 8)

$$K^{(n)} = \sum_{m=1}^{M} \alpha_m^{(n)} g_{r,m}^{(n)} \left[g_{t,m}^{(n)} \right]^T, \tag{9}$$

becomes the singular value decomposition (SVD) of $K^{(n)}$ where $\alpha_m^{(n)}$ corresponds to the singular value with left and right singular vectors $g_{r,m}^{(n)}$ and $g_{t,m}^{(n)*}$, respectively. For particles that are non-resolvable at the n'th harmonic, the multistatic response matrix bears an SVD as $K^{(n)} = U^{(n)} \Lambda^{(n)} \left[V^{(n)} \right]^H$ where the superscript 'H' denotes the Hermitian, $\Lambda^{(n)}$ is an $N \times N$ diagonal matrix of singular values $\sigma_1^{(n)} \geq \cdots \geq \sigma_M^{(n)} > \sigma_{M+1}^{(n)} = \cdots = \sigma_N^{(n)} = 0$ and $U^{(n)} = \left[u_1^{(n)}, \ldots, u_N^{(n)} \right]$ and $V^{(n)} = \left[v_1^{(n)}, \ldots, v_N^{(n)} \right]$ are $N \times N$ orthonormal matrices with columns corresponding to the left and right singular vectors, respectively. In this case however, the left and right singular vectors do not

coincide with the vectors $\boldsymbol{g}_{r,m}^{(n)}$ and $\boldsymbol{g}_{t,m}^{(n)*}$, respectively. Yet, one observes that the matrix $\boldsymbol{g}_{r,m}^{(n)}\left[\boldsymbol{g}_{t,m}^{(n)}\right]^{T}$ of rank 1, maps the one dimensional subspace (a line) spanned by the vector $\boldsymbol{g}_{t,m}^{(n)*}$ into the one dimensional subspace spanned by the vector $\boldsymbol{g}_{r,m}^{(n)}$ so that $\boldsymbol{K}^{(n)}$ is a one to one mapping from $span\left\{\boldsymbol{g}_{t,1}^{(n)}, \dots, \boldsymbol{g}_{t,M}^{(n)}\right\}$ to $span\left\{\boldsymbol{g}_{r,1}^{(n)}, \dots, \boldsymbol{g}_{r,M}^{(n)}\right\}$. As a result, one has $span\left\{\boldsymbol{g}_{t,1}^{(n)}, \dots, \boldsymbol{g}_{t,M}^{(n)}\right\} \subseteq span\left\{\boldsymbol{v}_{1}^{(n)}, \dots, \boldsymbol{v}_{M}^{(n)}\right\}$ and $span\left\{\boldsymbol{g}_{r,1}^{(n)}, \dots, \boldsymbol{g}_{r,M}^{(n)}\right\} \subseteq span\left\{\boldsymbol{u}_{1}^{(n)}, \dots, \boldsymbol{u}_{M}^{(n)}\right\}$. Since $\boldsymbol{V}^{(n)}$ is an orthogonal matrix, it follows that $\left[\boldsymbol{v}_{i}^{(n)}\right]^{H}\boldsymbol{g}_{t,m}^{(n)*} = 0$ for $i = M+1, \dots, N$ i.e. the null space of $\boldsymbol{K}^{(n)}$, determined as $span\left\{\boldsymbol{v}_{M+1}^{(n)}, \dots, \boldsymbol{v}_{N}^{(n)}\right\}$, is orthogonal to $span\left\{\boldsymbol{g}_{t,1}^{(n)}, \dots, \boldsymbol{g}_{t,M}^{(n)}\right\}$. Following [14], the location of the nonlinear scatterers may now be determined by employing the MUSIC algorithm, implemented by defining the steering vector $\boldsymbol{g}_{t}^{(n)}(\boldsymbol{x}) = [G^{n}(\boldsymbol{x}_{1}, \boldsymbol{x}, \omega), \cdots, G^{n}(\boldsymbol{x}_{N}, \boldsymbol{x}, \omega)]^{T}$ and the pseudo-spectrum for the n'th harmonic

$$p^{(n)}(\boldsymbol{x}) = \frac{1}{\sum_{i=M+1}^{N}\left|\left[\boldsymbol{v}_{i}^{(n)}\right]^{H}\boldsymbol{g}_{t}^{(n)*}(\boldsymbol{x})\right|}. \tag{10}$$

On a finite grid, the pseudo-spectrum is a false image of the scattering potential over the grid (ROI) and its value will peak at a pixel containing the scatterer since $p^{(n)}(\boldsymbol{x} = \boldsymbol{x}_{m}) = \infty$ for $m = 1, \dots, M$. Note that alternative pseudo spectra can also be defined using the left singular vectors as in [15,17,18] or using both left and right singular vectors but these alternatives are not pursued in this study for conciseness.

2.1 Effect of Noise in Measurements

The effect of measurement noise has been neglected in the preceeding discussion. In reality, the multistatic response matrix is constructed from noisy measurements of $\boldsymbol{E}_{L}^{(n)}$. The measurement equation is of the form $\boldsymbol{E}_{L}^{(n)} = \boldsymbol{K}^{(n)}\boldsymbol{b}^{(n)} + \boldsymbol{n}$ where $\boldsymbol{n}$ is a measurement noise vector of length N added to the relation in Equation 3. With noise present, the noisy multistatic response matrix $\widetilde{\boldsymbol{K}}^{(n)}$ is in general of full rank implying that $\tilde{\sigma}_{i} > 0, \forall i = 1, \dots, N$. The addition of noise will perturb the singular system $(\boldsymbol{u}_{i}, \sigma_{i}, \boldsymbol{v}_{i}), i = 1, \dots, N$, of $\boldsymbol{K}^{(n)}$ resulting in the new singular system $(\widetilde{\boldsymbol{u}}_{i}, \tilde{\sigma}_{i}, \widetilde{\boldsymbol{v}}_{i})$ for $\widetilde{\boldsymbol{K}}^{(n)}$. In the nomenclature of MUSIC, $\mathcal{S} = span\{\widetilde{\boldsymbol{v}}_{1}, \dots, \widetilde{\boldsymbol{v}}_{M}\}$ is known as the *signal* subspace and $\mathcal{N} = span\{\widetilde{\boldsymbol{v}}_{M+1}, \dots, \widetilde{\boldsymbol{v}}_{N}\}$ is known as the *noise* subspace. The signal and noise subspaces are again orthogonal to each other but because the singular system $(\widetilde{\boldsymbol{u}}_{i}, \tilde{\sigma}_{i}, \widetilde{\boldsymbol{v}}_{i})$ is perturbed from the original noise-free $(\boldsymbol{u}_{i}, \sigma_{i}, \boldsymbol{v}_{i})$ system, the vectors $\boldsymbol{g}_{t,m}^{(n)}$, $m = 1, \dots, M$, will have non-zero projections onto both subspaces. Moreover, because M is not known a priori, the signal and noise subspaces must be identified by some appropriate means. Such a distinction between signal and noise subspaces may be not even be possible if the signal to noise ratio (SNR) is close to or less than unity. A common method for signal and noise subspace identification is to use a threshold $\epsilon_{th}^{(n)}$ such that singular vectors corresponding $\tilde{\sigma}_{i}^{(n)} \geq \epsilon_{th}^{(n)}$ are designated the signal subspace and singular vectors corresponding $\tilde{\sigma}_{i}^{(n)} < \epsilon_{th}^{(n)}$ are designated the noise subspace [14]. Formally, one has $\mathcal{S} = \left\{\widetilde{\boldsymbol{v}}_{i} \mid \tilde{\sigma}_{i}^{(n)} \geq \epsilon_{th}^{(n)}\right\}$ and $\mathcal{N} = \left\{\widetilde{\boldsymbol{v}}_{i} \mid \tilde{\sigma}_{i}^{(n)} < \epsilon_{th}^{(n)}\right\}$. With the proviso that the signal and noise subspaces can be identified, a false image of the scattering potential is constructed using the pseudo-spectrum

$$\tilde{p}^{(n)}(\boldsymbol{x}) = \frac{1}{\sum_{\widetilde{\boldsymbol{v}}_{i}^{(n)} \in \mathcal{N}}\left|\left[\widetilde{\boldsymbol{v}}_{i}^{(n)}\right]^{T}\boldsymbol{g}_{t}^{(n)*}(\boldsymbol{x})\right|}. \tag{11}$$

This pseudo-spectrum will peak at $x = x_m, k = 1, \cdots, M$, yielding the locations of isolated point-like nonlinear scatterers. In the following, the quantity defined as $I^{(n)}(i,j) = 10 \log \left(\tilde{p}^{(n)}(x_i, y_j) \right)$ will be designated as the image corresponding to the n'th harmonic.

3. Numerical Simulations

In this section, the pseudo-spectrum defined in Equation 11, is applied to several imaging scenarios using numerical simulations. Simulation geometry is depicted in Figure 1 with free space as the background medium ($\varepsilon_{rb} = 1$). Throughout, the fundamental frequency is $f = 2.4$ GHz and only the first three harmonics, namely $f, 2f$ and $3f$, are considered. A grid spacing of $\Delta_x = \Delta_y = \lambda_3/10$ and an array inter-element distance of $d = \lambda_3/2$ is assumed where $\lambda_n = c/nf$ is the wavelength of the n'th harmonic. This choice of d is made to prevent spatial aliasing for all three harmonics. The array is also located at $y = -d$. Furthermore, additive Gaussian noise is assumed for the simulations and SNR is defined with respect to the mean magnitude of the multistatic matrix elements. For simplicity, the signal and noise subspaces will be determined directly by M.

In the first set of simulations, the number of scatterers $M = 6$ and the number of array elements $N = 21$. The scattering potentials for the scatterers are selected conveniently as $\alpha_m^{(n)} = 1$ for $m = 1, \ldots, M$ and $n = 1,2,3$. In Figure 2, the image $I^{(1)}$, for the first (fundamental) harmonic is shown on the left for $SNR = 10$ dB (Figure 2a) and on the right for $SNR = 20$ dB (Figure2b). These images are constructed assuming that M is known. The black crosses in the images indicate the actual locations of the scatterers. It is seen in Figure 2a that long bright streaks exist for 10 dB SNR. Although the streaks contain the scatterers, it is not possible to determine the actual number and the locations of the scatterers. For the higher SNR of 20 dB, it is observed in Figure 2b that the bright streaks have contracted considerably. The bright regions in the improved image facilitates identification of at least five scatterers. The size of the bright regions also grows with distance from the array indicating increase in localization uncertainty further away from the array.

The image $I^{(2)}$, corresponding to the second harmonic, is shown in Figure 3a for $SNR = 10$ dB and in Figure 3b for $SNR = 20$ dB. In both figures, all six scatterers can be distinguished from $I^{(2)}$. Compared to Figure 2a of $I^{(1)}$ with 10 dB SNR, $I^{(2)}$ with an SNR of 10 dB appears to have smaller uncertainty in locations of the three scatterers the closest to the array. However, compared to Figure 2, the background intensity has increased toward
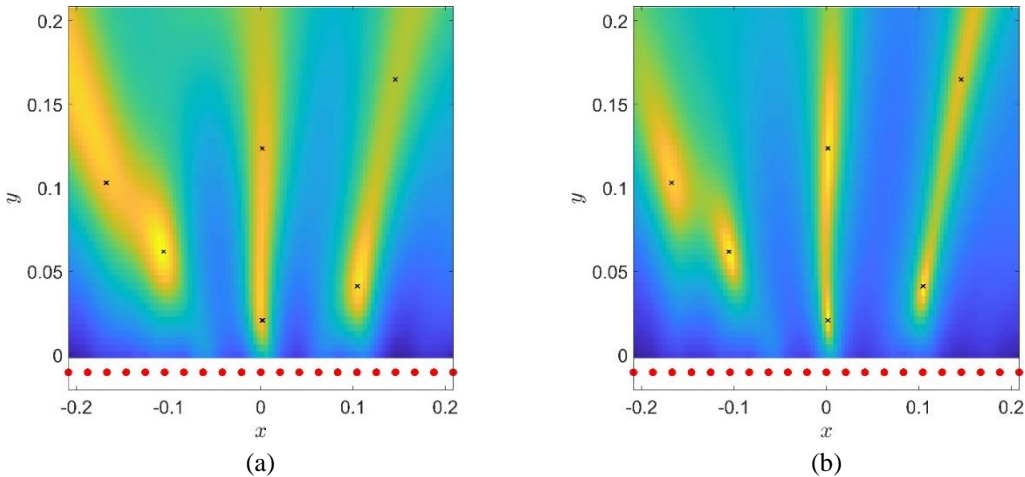
Figure 2. First (fundamental) harmonic image (MUSIC pseudo-spectrum) of $M = 6$ nonlinear point-like scatterers with $N = 21$ array elements for (a) $SNR = 10$ dB and (b) $SNR = 20$ dB.
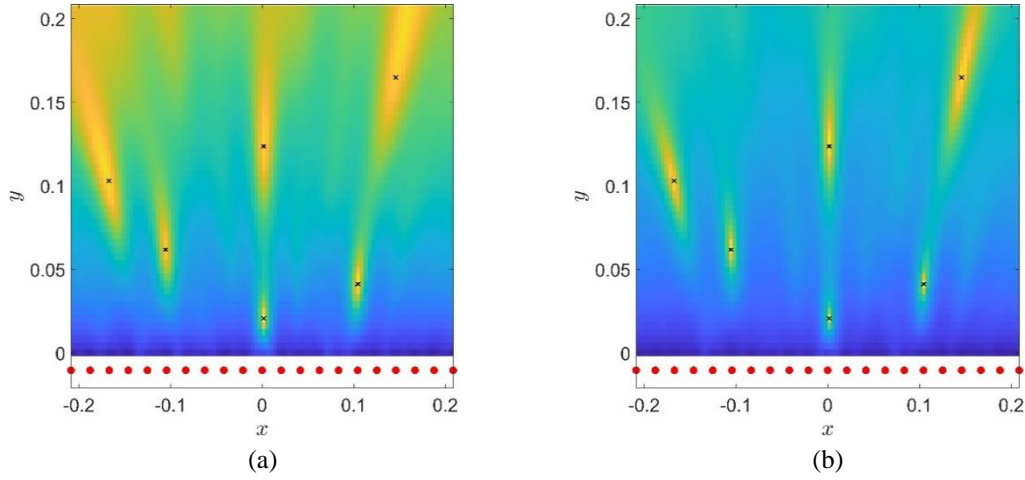
Figure 3. Second harmonic image of $M = 6$ nonlinear point-like scatterers with $N = 21$ array elements for (a) $SNR = 10$ dB and (b) $SNR = 20$ dB.
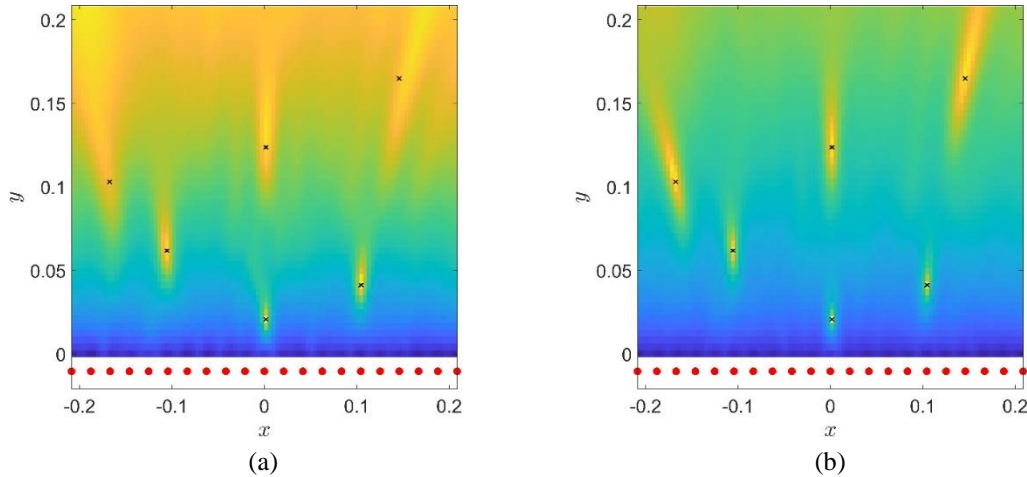
Figure 4. Third harmonic image of $M = 6$ nonlinear point-like scatterers with $N = 21$ array elements for (a) $SNR = 10$ dB and (b) $SNR = 20$ dB.

the top (far) end of the image, causing a decrease in contrast specially to the left of the image. The image $I^{(2)}$ in Figure 3b corresponding the 20 dB SNR shows further improvement such that uncertainty has decreased considerably for all scatterer locations. These two figures suggest that the second harmonic is more robust to measurement noise compared to the fundamental harmonic.

The final image $I^{(3)}$, corresponding to the third harmonic is shown in Figure 4a for $SNR = 10$ dB and in Figure 4b for $SNR = 20$ dB. The most striking feature in the image of Figure 4a is the high background intensity of the image and although the presence of the bright streaks near the top end of the image suggest the presence of at least the three existing scatterers, it is not possible the determine the actual number of scatterers. Nevertheless, the closest three scatterers to the array are clearly resolved with little uncertainty. This is an improvement compared

to $I^{(1)}$ for the same SNR. For $SNR = 20$ dB, it appears in Figure 4b that the third harmonic provides no further improvement over $I^{(2)}$ shown in Figure 3b.

The preceeding analysis instigates further investigation into the relation between resolution, noise and harmonic order. Here, resolution is defined as the minimum distance between two scatterers such that the scatterers are distinguishable. Resolution is related to the spread of the peaks (poles) of the pseudo-spectrum $\tilde{p}^{(n)}(x)$ which is regulated by the level of noise (SNR), the number of array elements N, and the wavelength of the harmonic. As seen from the above figures (Figure 2 – Figure 4), resolution is also expected to be a function of distance from the array degrading with increasing distance. Furthermore, it is also evident from the orientations of the streaks in the figures (extending away from the array and almost normal to the array near the center) that resolutions along the x- and y-axis are very different. To substantiate some of these arguments, consider the two scenarios with $N = 21$, where in the first scenario two scatterers are separated along the x-axis to investigate resolution along array axis and in the second scenario two scatterers are separated along the y-axis to investigate resolution along the normal to array axis. Specifically, in the first scenario the two scatterer locations coordinates are $(-\delta_s/2, h)$ and $(\delta_s/2, h)$, respectively, where $\delta_s = \lambda_1/10$ and $h = \lambda_1/4$. In the second scenario, the two scatterer location coordinates are $(0, h - \delta_s/2)$ and $(0, h + \delta_s/2)$, respectively. For the first scenario, the normalized (relative to its maximum value) sample pseudo-spectrums $\tilde{p}^{(n)}(x)$ for $n = 1,2,3$, are plotted in Figure 5a along the line $y = h$. Similarly, for the second scenario, the normalized sample $\tilde{p}^{(n)}(x)$ for $n = 1,2,3$, are plotted in Figure 5b along the line $x = 0$. In both figures, an SNR of 20 dB is assumed for all harmonics. In Figure 5a, $\tilde{p}^{(1)}$ for the fundamental harmonic (red line) cannot resolve the two scatterers while both $\tilde{p}^{(2)}$ for the second harmonic (green line) and $\tilde{p}^{(3)}$ for the third harmonic (blue line) can distinguish the two scatterers very close to their correct locations. Note also that $\tilde{p}^{(3)}$ is sharper than $\tilde{p}^{(2)}$ suggesting that higher harmonics have better resolution for $h = \lambda_1/4$. In the second scenario on the other hand, it is observed from Figure 5b that the pseudo-spectrums for the first two harmonics cannot resolve the scatterers while the third harmonic can resolve the two scatterers near their correct locations. Also, the curves in the latter figure are not symmetric about the point $y/\lambda_1 = 0.25$, because the left end of the plots is closer to the array. Near the right end of the plots (further to the array), $\tilde{p}^{(2)}$ and $\tilde{p}^{(3)}$ are higher than $\tilde{p}^{(1)}$ likely due to the relative decrease in the magnitude of the steering vector $g_t^{(n)}(x)$, appearing denominator in Equation 11, with increasing distance away from the array. This phenomenon was observed in Figure 3b and Figure 4b as the high background intensity in the images. The pseudo-spectrums in the second scenario are broader than those of in first scenario, causing loss of resolution. This concludes that resolution is better along array axis.
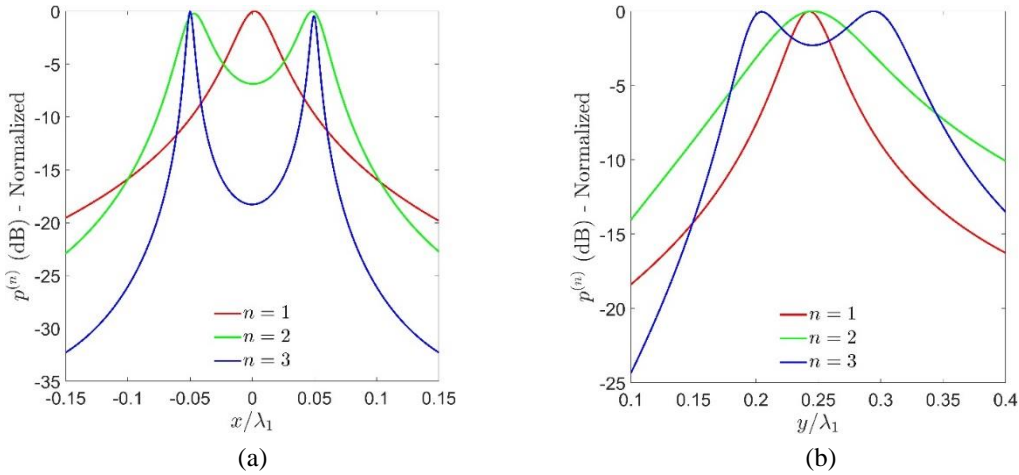
Figure 5. Normalized pseudo-spectrum for two nonlinear point-like scatterers along x-axis (a) and along y-axis (b) for $SNR = 20$ dB and with $N = 21$ array elements.

To further observe the effect of noise on resolution, the above two scenarios are repeated with an SNR of 10 dB. The pseudo-spectrums for the first scenario are plotted in Figure 6a and those for the second scenario are plotted in Figure 6b. In contrast to Figure 5a, the green curve corresponding to $\tilde{p}^{(2)}$ in Figure 6a can no longer resolve the two scatterers along the x-axis. The blue curve corresponding to $\tilde{p}^{(3)}$ can still resolve the two scatterers near their correct locations but the spread of peaks is now broader due to the adverse effect of noise. For the second scenario, the plots in Figure 6b show that none of the harmonics can now resolve the two scatterers. The higher values for the second and third harmonics near the right end of the plots are again indicative of the higher intensities near the top end of the images in Figure 3a and Figure 4a. The conclusion is that noise causes broadening of the peaks in the pseudo-spectrums. As can be observed in the behavior of $\tilde{p}^{(3)}$ in Figure 5b and Figure 6b, this broadening causes the peaks corresponding to two close scatterers to progressively overlap as SNR decreases. Eventually, these peaks will merge into a single peak resulting in a decline in resolution.

For an array with fixed inter-element distance d, resolution for a given SNR can be improved by increasing the number of array elements N, as a result of sharpening of the peaks with increased array length. This is demonstrated using the normalized $\tilde{p}^{(3)}$ (third harmonic) with $SNR = 10$ dB in Figure 7a for the first scenario and in Figure 7b for the second scenario. In both figures, solid curves correspond to the case with $N = 21$ elements and dashed curves correspond to the case with $N = 101$ elements. In Figure 7a, comparison of the two curves clearly shows that the array with $N = 101$ elements produces a much sharper pseudo-spectrum at the scatterer locations (poles) than the pseudo-spectrum with $N = 21$ elements. Similarly, it is seen in Figure 7b that while the array with $N = 21$ elements is unable to resolve the two scatterers, the array with $= 101$ elements can resolve the scatterers. The conclusion is that longer arrays with more elements can result in better resolution.

The effects of the SNR and the number of elements on resolution are summarized in Figure 8 for the first scenario and in Figure 9 for the second scenario. Each curve in the figures corresponds to a single harmonic and provides a relation between the SNR and the number of array elements N, required to resolve the two scatterers with roughly 50% probability. The curves are generated by Monte-Carlo (MC) simulations with a total of $N_{MC} = 1000$ realizations for each harmonic. In each realization of a MC simulation corresponding to the n'th harmonic,
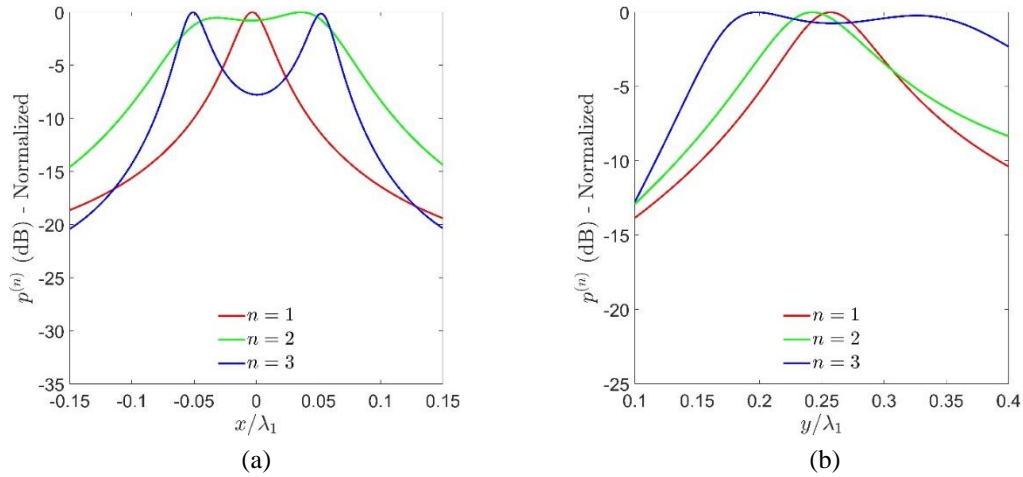
Figure 6. Normalized pseudo-spectrum for two nonlinear point-like scatterers along x-axis (a) and along y-axis (b) for $SNR = 10$ dB and with $N = 21$ array elements.

(a)   (b)
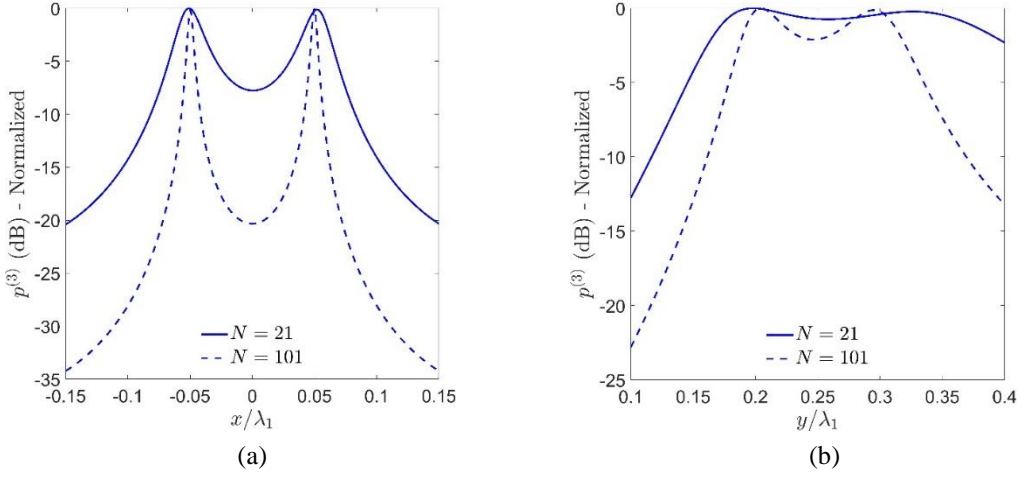
Figure 7. Normalized pseudo-spectrum (3rd harmonic) for two nonlinear point-like scatterers along x-axis (a) and along y-axis (b) for $SNR = 10$ dB with $N = 21$ (solid line) and $N = 101$ (dashed line) array elements.

a noisy sample of the multistatic response matrix $\widetilde{\boldsymbol{K}}^{(n)}$, is generated. The pseudo-spectrum $\tilde{p}_k^{(n)}$, for the k'th sample ($k = 1, \ldots, N_{MC}$) is then computed and the number of peaks $N_{peak,k}^{(n)}$, for the sample is estimated from $\tilde{p}_k^{(n)}$. The expected number of scatterers is obtained by averaging $N_{peak,k}^{(n)}$ over all samples as $\widehat{N}_{peak}^{(n)} = (1/N_{MC}) \sum_{k=1}^{N_{MC}} N_{peak,k}^{(n)}$. Note that $1 \leq \widehat{N}_{peak}^{(n)} \leq 2$ and when $\widehat{N}_{peak}^{(n)} \approx 1$, the two scatterers are not resolved in majority of the samples. In contrast, when $\widehat{N}_p^{(n)} \approx 2$, the two scatterers are resolved in majority of the samples. The curves in the figures correspond to $\widehat{N}_{peak}^{(n)} = 1.5$, which indicates that the two targets are resolved in half of the samples. Hence, further to the right of the curve for the n'th harmonic, it is very likely that the two scatterers
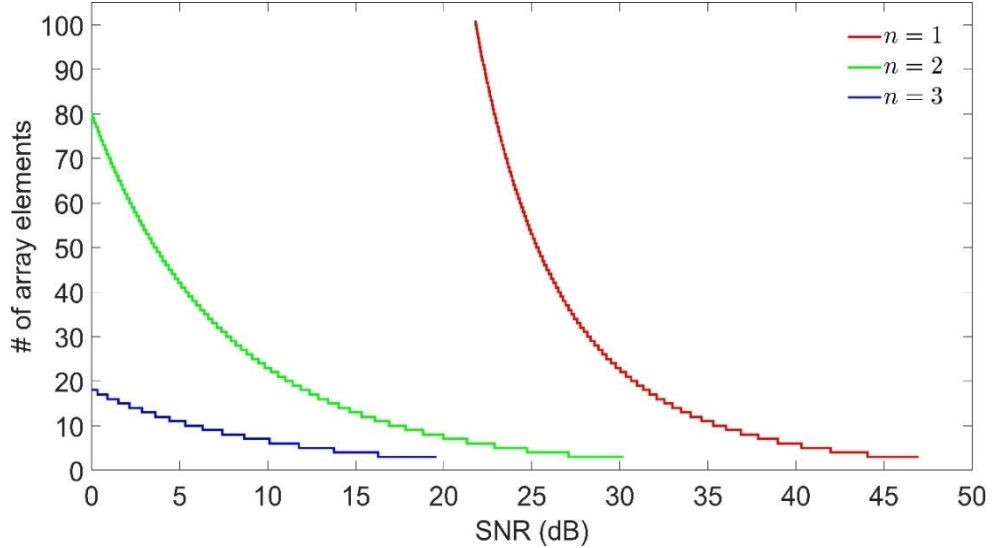
Figure 8. Number of array elements required to resolve two scatterers (with 50% probability) displaced by $\lambda_1/10$ along x-axis vs SNR.
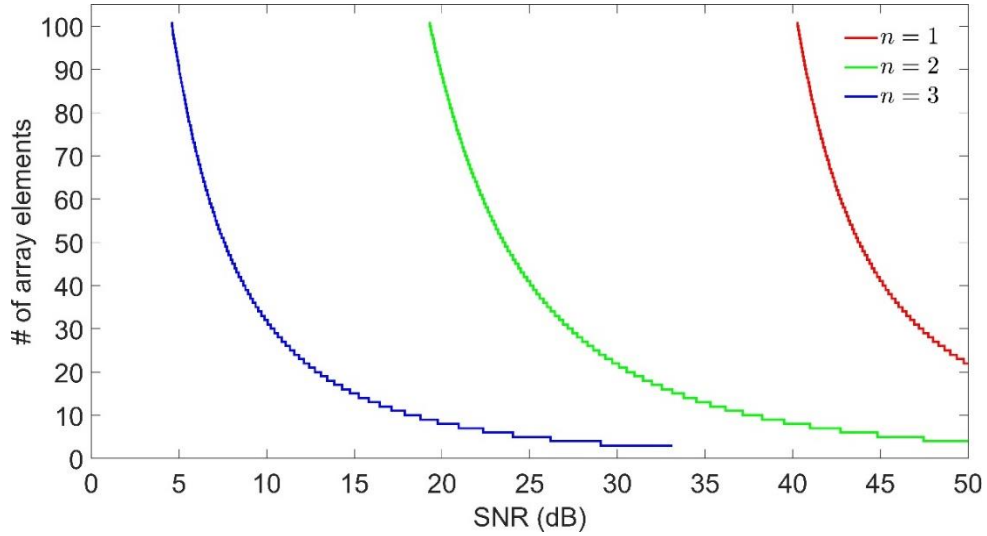
Figure 9. Number of array elements required to resolve two scatterers (with 50% probability) displaced by $\lambda_1/10$ along y-axis vs SNR.

are resolved and further to the left of the curve, it is very unlikely that the two scatterers are resolved by the n'th harmonic.

In both figures, it is observed that irrespective of the harmonic order, more array elements are required to resolve the two scatterers for lower SNR. However, the improvement from additional elements decreases with increasing N as observed by the steep increase in the curves with decreasing SNR. Moreover, curves corresponding to higher order harmonics are shifted further to the left indicating that higher order harmonics require fewer array elements to resolve the scatterers for the same SNR. Finally, comparison of Figure 8 and Figure 9 shows that for each harmonic, fewer number of array elements are required to resolve the two scatterers along the array axis. In fact, it is seen in Figure 9 that below about 5 dB SNR, further increase in N has no effect on the resolution of the third harmonic along the y-axis whereas $N < 20$ is sufficient for the third harmonic to resolve the two scatterers along the x-axis even with SNRs as low as 0 dB. These observations indicate that the resolution along the array axis is superior to that along the array normal.

4. Conclusions

A MUSIC based imaging, previously proposed for improving time-reversal imaging of point-like linear scatterers, is adopted here for imaging of point-like nonlinear scatterers. Unlike previous broadband approaches to localization of nonlinear scatterers, MUSIC based imaging offers a narrowband approach and is better suited for near-field applications. The proposed imaging approach is formulated and simulated in two dimensions for a homogeneous medium. The effect of multiple scattering is neglected which is a reasonable assumption when the point-like scatterers are sufficiently separated. The effect is likely to be stronger in the simulations performed for resolution analysis as the particles were in close proximity of one another. Nevertheless, the results are correct to first order of scattering which accounts for the major effect.

Numerical results show that higher order harmonics can better identify the presence of scatterers and estimate their locations. Higher order harmonics are also more robust to noise near the array of sensors. This is important since the returned signals from the scatterers may be weaker for higher order harmonics. Resolution degrades with distance from the array and also with decrease in SNR. On the other hand, resolution improves with harmonic

order (demonstrated for the first three harmonics) and is also superior along the array axis. The number of array elements plays an important role in resolving of the scatterers so that an array with few elements requires a large SNR to resolve close scatterers whereas an array with many elements can resolve close scatterers with smaller SNR. However, increasing array elements has the cost of dealing with larger multistatic response matrices requiring more field measurements (increasing as N^2). Beyond some trade-off value, increasing the number of elements has a decreasing benefit not justifying the further increase in element number.

The narrowband nature of the of the proposed imaging method is an apparent advantage over the broadband frequency sweeping systems used in [10-12]. But this advantage comes with the cost of increased system complexity due to use all array elements in both transmit and receive modes as opposed to the single transmitting element present in the previous studies. In spite of this drawback, the findings are promising for narrowband, near field imaging of nonlinear scatterers. The current study will be extended to three-dimensional layered media in the future along with experimental work to validate the results. An analysis along the lines of the work done by Ciuonzo et al. [18] for the proposed imaging method is also essential to better gauge its noise performance.

References

[1] Colpitts B.G., Boiteau G., "Harmonic radar transceiver design: Miniature tags for insect tracking," IEEE Antennas and Propagat., vol. 52, no. 11, pp. 2825-2832, 2004.

[2] Jau P.H., Tsai Z.M., Kuo N.C., Kao J.C., Lin K.Y., Chang F.R., Yang E.C., Wang H., "Signal processing for harmonic pulse radar based on spread spectrum technology," IET Radar Sonar Navig., vol. 8, no. 3, pp. 242–250, 2014.

[3] Singh A., Lubecke V.M., "Respiratory monitoring and clutter rejection using a CW Doppler radar with passive RF tags," IEEE Sensors Journal, vol. 12, no. 3, pp. 558-565, 2012.

[4] Granhed M., Forssen K.G., "Sensor-activated transponder," US Patent 20130194100A1, 1 August 2013.

[5] Harzheim T., Muhmel M., Heuermann H., "A SFCW harmonic radar system for maritime search and rescue using passive and active tags,". International Journal of Microwave and Wireless Technologies, vol. 13, pp. 691–707, 2021.

[6] Kubina B., Romeu J., Mandel C., Schussler M., Jakoby R., "Quasi-chipless wireless temperature sensor based on harmonic radar," Electronic Letters, vol. 50, no. 2, pp. 86-88, 2014.

[7] Mondal S., Kumar D., Chahal P., "Recent advances and applications of passive harmonic RFID systems: A review," Micromachines, vol. 12, no. 420, pp. 1-22, 2021.

[8] Lehtola G.E., "RF receiver sensing by harmonic generation," US Patent 7864107B1, 4 January 2011.

[9] Mazzaro G.J., Martone A.F., McNamara D.M., "Detection of RF electronics by multitone harmonic radar" IEEE Trans. On Aerospace and Electronic Sys., vol. 50, no., pp. 477-490, 2014.

[10] Gallagher K.A., "Harmonic Radar: Theory and Applications to Nonlinear Target Detection, Tracking, Imaging and Classification," Ph.D. Dissertation, The Pennsylvania State University, University Park, PA, USA, December 2015.

[11] Gallagher K.A., Narayanan R.M., Mazzaro G.J., Martone A.F., Sherbondy K.D., "Static and moving target imaging using harmonic radar," Electronics, vol. 6, no. 30, pp. 1-20, 2017.

[12] Bischeltsrieder F., Schreiber E., Peichl M., Heinzel A., Jirousek M., "High resolution harmonic radar imaging for safety and security applications," Proceedings of SPIE Conference on Radar Sensor Technology XXIII, vol. 11003, pp. 1-18, Baltimore, MD, May 2019.

[13] Lev-Ari H., Devaney A.J., "The time reversal techniques re-interpreted: Subspace-based signal processing for multistatic target location," Proc. IEEE Sensor Array and Multichannel Signal Processing Workshop, pp. 509-513, Cambridge, MA, March 2000.

[14] Devaney A.J., "Time reversal imaging of obscured targets from multistatic data," IEEE Trans. Antennas Propag., vol. 53, no. 5, pp. 1600-1610, 2005.

[15] Devaney A.J., Marengo E.A., Gruber F.K., "Time-reversal-based imaging and inverse scattering of multiple scattering points," J. Acoust. Soc. Am., vol. 118, no. 5, pp. 3129-3138, 2005.

[16] Prada C., Manneville S., Spoliansky D., Fink M., "Decomposition of the time reversal operator: Detection and selective focusing on two scatterers," J. Acoust. Soc. Am., vol. 99, no. 4, pt. 1, pp. 2067-2076, 1996.

[17] Marengo E.A., Gruber F.K., "Subspace-based localization and inverse scattering of multiply scattering point targets," EURASIP Journal on Advances in Signal Processing, vol. 2007, article ID 17342, 2007, DOI: 10.1155/2007/17342.

[18] Cuionzo D., Romano G., Solimene R., "Performance analysis of time-reversal MUSIC," IEEE Trans. Signal Process., vol. 63, no. 10, pp. 2650-2662, 2015.

[19] Gallagher K.A., Mazzaro G.J., Martone A.F., Sherbondy K.D., Narayanan R.M., "Derivation and validation of the nonlinear radar range equation," Proceedings of SPIE Conference on Radar Sensor Technology Radar Sensor Technology XX, vol. 9829, Baltimore, MD, April 2016.

A Lung Sound Classification System Based on Data Augmenting Using ELM-Wavelet-AE

Berna ARI[1*], Ömer Faruk ALÇİN[2], Abdulkadir ŞENGÜR[1]

[1] Department of Electrical and Electronics Engineering, Firat University, Elazig, Turkey
[2] Department of Electrical and Electronics Engineering, Malatya Turgut Ozal University, Malatya, Turkey
[*1] bernagurler.a@gmail.com, [1] ksengur@firat.edu.tr, [2] omer.alcin@ozal.edu.tr

Abstract: The method is of great importance in systems that include machine learning and classification steps. As a result, academics are constantly working to improve the process. However, the data pertaining to the methodology's performance is equally as valuable as the methodology's creation. While the data is utilized to show the result of the modeling process, it is critical to consider the proper labeling of the data, the technique of acquisition, and the volume. Obtaining data in certain sectors, particularly medical fields, can be costly and time consuming. Thus, data augmenting via classical and synthetic methods has recently gained popularity. Our study uses synthetic data augmentation since it is newer, more efficient, and produces the desired effect. Our study's goal is to classify a data collection of lung sounds into four groups using data augmenting. Obtaining and standardizing the wavelet scatter transformation of each cycle of lung sounds, splitting the transformed data into test and training, augmenting and classifying the training data. In the augmenting stage, we utilized ELM-AE, then ELM-W-AE, with six wavelet functions (Gaussian, Morlet, Mexican, Shannon, Meyer, Ggw) added. The SVM and EBT classifiers improved performance by 4% and 3% in ELM-W-AE compared to the original structure.

Key words: Lung sound, wavelet scatter, data augmentation, ELM-Auto Encoder.

ELM- Dalgacık-AE Kullanılarak Veri Çoğullama Tabanlı Bir Akciğer Sesleri Sınıflama Sistemi

Öz: Makine öğrenmesi ve sınıflandırma adımlarını içeren sistemlerde yöntem büyük önem arz etmektedir. Bu sebeple araştırmacılar genellikle yöntemin iyileştirilmesi üzerinde çalışmalar yapmaktadır. Ancak metodolojinin geliştirilmesi kadar performansını etkileyen veri de bir o kadar değerlidir. Veri, modelleme sürecinde sonucu gözler önüne serebilmek için kullanılırken; verinin doğru etiketlenmesi, elde edilme yöntemi ve hacmi dikkat edilmesi gereken diğer önemli noktalardır. Medikal alanlar başta olmak üzere bazı alanlarda veri elde etmek maliyetli ve zor olabilmektedir. Bu sebeple klasik ve sentetik yöntemlerle veri çoğullama yaklaşımları son zamanlarda popüler olmaya başlamıştır. Sentetik veri çoğullama teknikleri daha yeni, verimli ve istenebilen sonuca yönelik olduğundan çalışmamızda tercih edilmiştir. Çalışmamızın amacı akciğer seslerine ait veri setini dört kategoride sınıflandırırken seçtiğimiz veri çoğullama yönteminin başarımını göstermektedir. Önerdiğimiz yöntemin adımları şu şekildedir: akciğer seslerine ait her bir saykılın Dalgacık saçılım dönüşümünü elde edilmesi ve normalizasyonu, dönüşümden elde edilen verinin test ve eğitim olarak bölünmesi, eğitim için ayrılan verinin çoğullanması ve sınıflandırılmasıdır. Veri çoğullama aşamasında Aşırı Öğrenme Makinesi Oto Kodlayıcı (ELM-AE) ve sonrasında bu modele altı farklı dalgacık fonksiyonun (Gaussian, Morlet, Mexican, Shannon, Meyer, Ggw) eklenmesiyle ELM-W-AE yapısını kullandık. Orijinal yapıya kıyasla sınıflandırmada kullanılan SVM ve EBT sınıflandırıcıları için ELM-W-AE'de sırasıyla yaklaşık %4 ve %3 oranında başarım artışı gözlemledik.

Anahtar kelimeler: Akciğer sesleri, dalgacık saçılımı, veri çoğullama, ELM-Oto Kodlayıcı

1. Introduction

Data is a critical structure that plays a critical part in the modelling phase and enables us to monitor the outcome through system testing. While the volume and consistency of data collected throughout the process of artificial intelligence impact the end, it also results in noticeable variances in the result step. However, approaches such as Convolutional Neural Network (CNN) and (Long Short-term Memory) LSTM, which have lately gained popularity, have been shown to improve performance as the amount of huge data in the system increases. When the studies are examined, it is clear that the approaches prioritize modeling over data-driven approaches, and that when the anticipated performance response is not obtained, the modeling is revised [1]. Data collection procedures in a variety of fields, including engineering, medicine, and education, can be time consuming and costly. Recent studies on data augmenting technologies come to mind at this time. Along with traditional data augmentation techniques, new study topics have been identified for synthetic data augmentation techniques such as (Generative Adversarial Network (GAN), AE (Auto Encoder) and Variational Auto Encoder (VAE) [2-5]. It has been

---

demonstrated that better performance may be obtained by augmenting medical images and sounds when creating decision support systems for time and cost savings [6-9].

Synthetic data augmenting is a more sophisticated and recent technique than traditional data augmenting. There is research on the synthesis of AE using the Extreme Learning Machine (ELM) approach, one of the favored methods for producing synthetic data [3, 7]. AE has become popular due to its efficiency compared to other data duplication methods [2, 10]. On the other hand, the ELM paired with AE called ELM-AE is a single hidden layer feedforward neural network and has been shown to be a high-performing model in numerous investigations. The ELM-AE structure can be modified by altering the number of cells and activation functions in the hidden layer. The issue of data quantity, which is particularly acute in deep architectures, was attempted to be investigated in the categorization of lung disorders, the focus of this work.

Since lung disorders are the third leading cause of death worldwide, identification and follow-up are critical [11]. Following the Covid-19 outbreak, a rise in lung illnesses has been observed [12]. As a result, professionals should develop new approaches for characterizing these disorders. It is well established that lung sounds and their features significantly influence the development of pulmonary disease [13]. Auscultation can be used to discern between these sounds, which are roughly classified as normal and pathological [14]. However, classical auscultation is not without faults, since it is highly dependent on the physician's skill, hearing capacity, expertise, and experience [14, 15, 16].

The non-stationarity of lung sound waves is the primary element that challenges classic technique analysis [17]. Lung sounds are deemed normal when they range between 100 and 1000Hz and lack prominent peaks on the signal [18]. However, in the case of unusual (adventitious) breath sounds, the situation is reversed. These noises contain additional sounds in addition to the typical sounds, and they are classified as continuous-discrete [19]. Wheeze refers to continuous sounds produced by the lungs; crackle refers to isolated sounds produced by the lungs. Wheeze sounds, which contain a tonal structure, feature periodic waveforms with a frequency more than or equal to 100Hz and duration greater than or equal to 100ms [18, 20]. Crackle, on the other hand, has a more complex structure in terms of frequency content, although it runs in less than 20ms [21]. The diagnosis of asthma, pneumonia, and bronchitis is guided by wheeze sounds, whereas crackling sounds are usually encountered in cardiovascular illnesses [22]. Automatic recognition studies have risen to prominence in expert systems assessing the amounts mentioned above, assisting in disease diagnosis and guiding disease interpretation.

When studies were analyzed, it was discovered that lung sounds were classified and substantial results were discovered [23, 24, 25]. The time-frequency domain features of normal and abnormal sounds have been the focus of studies analyzing normal and abnormal noises [26]. In numerous research, Mel frequency cepstral coefficients (MFCC) and estimated entropy have been used [27]. Additionally, recent research using empirical mode decomposition (EMD) and intrinsic mode functions (IMFs) demonstrate these methods' superior efficacy in classifying lung sounds as normal-adventive [23, 25].

As indicated previously, another critical part of methodological preparation for lung sound analysis was the data set. In terms of the debatability of the investigations, the ICHBI 2017 dataset was assessed, which included studies with dual and multiple classifications [28]. When we consider the research that comprises various classes of normal, wheeze, crackle, and both wheeze and crackle, we see that in the study [29], the objective was to convert lung sound data into images using the short-term Fourier transform (STFT). Classification of signals extracted from spectrogram images was performed using a pre-trained CNN. The study [13] began by converting the audio signals in the dataset to spectrograms. Following that, a CNN model is suggested that tries to improve performance by parallelizing the average pooling and maximum pooling layers. Linear Discriminant Analysis (LDA) and Random Subspace Ensembles (RSE) were used to classify the deep features produced in this manner (71.15%). In [22], lung sound signals were transformed to spectrogram pictures and five-fold augmentation was achieved synthetically. It is stressed that the images fed into the multi-layered CNN model and the enhanced data have a beneficial effect on performance. The study [30] used MFCC coefficients as features and tested binary and multi-class classification using Artificial Neural Network (ANN), Random Forest (RF) and Support Vector Machine (SVM). The study [20] feeds the radial-based SVM classifier with the features acquired using wavelet decomposition and STFT.

This study aimed to investigate multi-class discrimination using lung sound signals. The following are the study's contributions to the literature:

- In the feature extraction stage of lung sound analysis, the wavelet scatters transform method was used.
- The ICHBI data set is augmented with the ELM-AE.
- Comparison is accomplished through the use of numerous wavelet functions during augmenting.

2. Categories of Lung Sounds

Fig. 1 shows the methodology that was developed. In begin, lung sound files were extracted from the 2017 ICBHI Respiratory Sound Database [28]. Table 1 contains the cycle details for this dataset, which contains 6898 cycles in total. These breath sounds were collected from various locations on the chest using various instruments.

Table 1. Class and cycle knowledge regarding the dataset

Class	Cycles
Crackles	1864
Wheezes	886
Crackles+ wheezes	506
Normal	3642
Number of all	6898
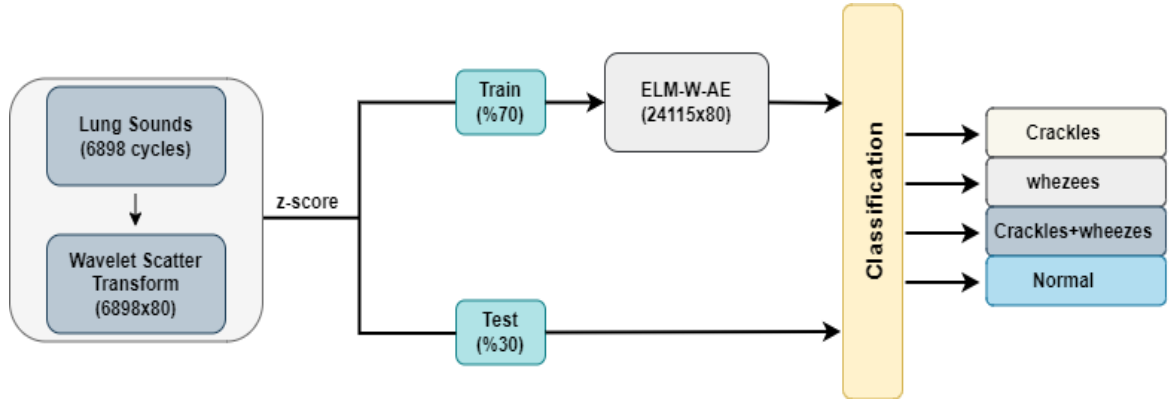
Fig.1. Flowchart of Methodology

2.1. Transform for Wavelet Scattering

Wavelet techniques, which are preferred for data representation and feature extraction, are advantageous because they can be used in conjunction with a wide variety of classification algorithms [31]. Additionally, it is one of the mathematical methods used when time-frequency domain feature extraction is insufficient for more complex signal feature extraction [32]. The Wavelet Scattering Transform (WST) is a structure proposed by Mallat that enables the generation of reliable features and their use in conjunction with a deep neural network structure [31, 33]. The convolution, nonlinearity, and averaging steps illustrated in Fig. 2 describe the primary steps involved in producing the wavelet scattering transform of the time series input signal. In this case, Ψ_1 denotes the wavelet function and φ_J denotes an average low-pass filter.
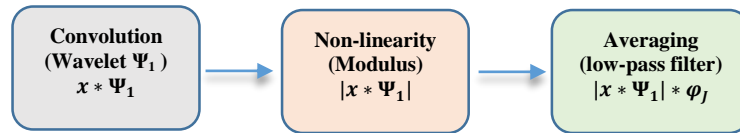
Fig.2. Representation of the wavelet scattering transform process with an x input.

WST defines a deformation-resistant representation. WST has been demonstrated to be capable of extending MFCC by processing modulation spectrum coefficients via wavelet convolutions and module operators [34]. Additionally, it has been demonstrated that WST outperforms MFCC for classification solutions with time scales greater than 25ms in audio representations. Using a set of wavelet decomposition and modulus operators, the scattering transform recovers information lost during Mel-frequency averaging. A wavelet transform is computed using constant-Q filter banks. A wavelet φ_J is a low-pass filter with $\breve{\varphi}(0)$ equal to zero and is denoted by the center frequency ω in equation (1):

$$\varphi_\omega(j) = \omega \cdot \varphi(\omega\, j), \; \breve{\varphi}_\omega(s) = \breve{\varphi}\left(\frac{s}{\omega}\right) \tag{1}$$

The frequency of $\breve{\varphi}$'s center has been normalized to 1 in this case. $\omega = 2^{k/Q}$. Q denotes the octave wavelets. $\breve{\varphi}$ is on a Q^{-1}-scale.

2.2. Synthetic data augmentation

In the study, WST was used to extract the features of the data in the ICHBI 2017 dataset. We applied data augmentation to these image representations containing information from four classes in the training process. Before we proceed with the steps, we utilized the z-score normalization (ZN), a straightforward feature-level transformation that can provide an effective solution for normalization. More precisely, when we speak of ZN, we subtract the mean of all components from each component and then divide by the standard deviation of all components [35]. The ELM-AE structure was investigated in the first model. The wavelet functions were then integrated into the designed structure to reveal the change. The abbreviation ELM-W-AE will be used to refer to wavelet functions. This section will detail each stage.

ELM: Huang's ELM is described as a simple one-hidden-layer neural network model [36]. Due to the random initialization of the input weights and single hidden layer thresholds, and the analytical calculation of the output weights, the ELM has a high learning rate. $\{(x_i, y_i)| x_i = [x_{j1}, x_{j2}, \ldots, x_{jn}]^T \in R^n$ is the representation of the $y_i = [y_{j1}, y_{j2}, \ldots, y_{jm}]^T \in R^m\}_{j=1}^N$ input-output structure for training pairs when the size of the training dataset is N, the number of input attributes is n, and the number of class labels is m.

$$\sum_{i=1}^{L} \beta_i f(w_i \cdot x_j + b_i) = o_j, \; j = 1, \ldots, N \tag{2}$$

In equation (2), L denotes the number of hidden layer neurons, $\beta_i = [\beta_{i1}, \beta_{i2}, \ldots, \beta_{im}]^T$ denotes the weight vector connecting the *ith* hidden node to the output node, f(·) indicates the activation function, $w_i = [\omega_{i1}, \omega_{i2}, \ldots, \omega_{in}]^T$ denotes the weight vector of the input layer, b_i denotes the hidden layer thresholds, and $w_i \cdot x_j$ denotes the values of w_i and x_j. It is used to denote the inner product of the output vector o_j. Equation (2) may not always produce the desired output o_j, and this new output may produce the desired output y_j , as illustrated in (3).

$$\sum_{i=1}^{L} \beta_i f(w_i \cdot x_j + b_i) = y_j, \; j = 1, \ldots, N \tag{3}$$

To optimize the performance of the Single Layer Feedforward Network (SLFN), the error should be $\sum_{j=1}^{N} \|o_j - y_j\| = 0$ or less. Equation (3) can be expressed straightforwardly in the matrix form specified in equation (4) [1].

$$Y = H\beta \tag{4}$$

$$Y = \begin{bmatrix} y_1^T \\ \vdots \\ y_N^T \end{bmatrix}_{N \times m}, \; \beta = \begin{bmatrix} \beta_1^T \\ \vdots \\ \beta_L^T \end{bmatrix}_{L \times m} \tag{5}$$

where Y denotes the output vector, W denotes the weights of the output layer, and H represents the output layer matrix in the equation (6). Calculate the output weights by solving the equation in (7).

$$H = \begin{bmatrix} f(w_1 \cdot x_1 + b_1) & \cdots & f(w_L \cdot x_1 + b_L) \\ \vdots & \cdots & \vdots \\ f(w_1 \cdot x_N + b_1) & \cdots & f(w_L \cdot x_N + b_L) \end{bmatrix}_{N \times L} \tag{6}$$

Here, H is the H matrix's generalized Moore-Penrose inverse.

$$\beta = H^\dagger Y \tag{7}$$

ELM-AE: The ELM-based Auto-Encoder (ELM-AE) is used to build an ELM-based multi-layer perceptron that is capable of learning new data representations. In contrast to ELM, which is used for classification, ELM-AE aims to minimize the reconstruction error associated with the input X. In other words, ELM-input AE's and output are both X. As a result, the objective function of ELM-AE with *L2* norm is as follows [37]:

$$\text{min:} \frac{1}{2}\|\beta\|^2 + C\frac{1}{2}\|X - H\beta\|^2 \tag{8}$$

where *C* is the factor of regularization. Then the gradient of Eq. 9 in terms of β is,

$$\beta = \left(\frac{1}{c} + H^T H\right)^{-1} H^T X \tag{9}$$

We obtain the optimal output weight β by setting the gradient to zero. The representation of the new data obtained is shown as in the Eq. (10).

$$X_{new} = G(X\beta^T) \tag{10}$$

where *G* is the function of activation. Notably, if the total number of hidden nodes in an ELM-based MLP is equal, *G* should be a linear activation function [37].

ELM-W-AE: Wavelet theory is a field of study that includes critical and constructive, including mathematics, physics, and engineering. The term "wavelet theory" translates as "little wave." In continuous form, the wavelet transform behaves similarly to a spanning elastic time-frequency window. It is classified into two types: continuous and discrete wavelet transforms. ELM is well-established as a superior method for learning Single Layer Feed-Forward Networks when compared to traditional methods. However, with careful consideration of parameter initialization and function selection, it is possible to achieve superior performance [38]. As stated in Eq.10, *G,* Table 2 contains six kernel types suitable for use as wavelet activation functions.

Table 2. Wavelet activation functions and mathematical representations used in the study

Wavelet Kernel Type	Function
Morlet	$\psi(t) = \cos(1.75t)e^{(-\frac{t^2}{2})}$
Gaussian	$\psi(t) = \frac{1}{\sqrt{2\pi}} exp^{(-\frac{t^2}{2})}$
Mexican	$c = \frac{2}{\sqrt{3}}\pi^{(-\frac{1}{4})} \quad \psi(t) = c(1 - t^2)exp\left(\frac{t^2}{2}\right)$
Shannon	$\psi(t) = \frac{sin\pi(t - 1/2) - sin2\pi(t - 1/2)}{\pi(t - 1/2)}$
Meyer	$\psi(t) = 35t^4 - 84t^5 + 70t^6 - 20t^7$
GGW	$\psi(t) = \sin(3t) + \sin(0.3t) + \sin(0.03t)$

2.3. Classifiers

The original and augmented data sets were evaluated on classifiers, and this part explains the two classifiers that produced the best results.

SVM: Support Vector Machine (SVM) is a powerful technique for classifying data that works by creating a line in the plane between the members of two groups. It is favorable in that it applies to both linear and nonlinear data, has a high degree of precision, is capable of modeling complex decision boundaries, and works with many independent variables.

Decision-making function for SVM; x_i i is the data point, x_* a test vector, a_i is the Lagrangian multiplier associated with the training example x_i, y_i is the class of data point i (-1 or +1), and with b being the bias value, they are defined as[39,40]:

$$f(x_*) = sign\left[\sum_{i=1}^{N} a_i\, y_i\, \varphi\left(x_*, x_i\right) + b\right] \tag{11}$$

In the expression of the Quadratic (2nd order) optimization problem, ρ is the width of the separator between the support vector classes, w is the normal of the multi-plane (weight vector), $\| w \|$ w is the Euclidean representation of w for each $\{(x_i, y_i)\}$:

It is maximized with $\rho=2/(\|w\|)$. If $y_i = 1$ then; $w^T x_i + b \geq 1$. If $y_i = -1$ is equal to $w^T x_i + b \geq -1$.

EBT: The Ensemble Bagging Tree (EBT) classifier, which is a form of community learning, is intended to boost success rates through collaborative classification techniques. Rather than using a single learner, a decision tree is constructed using many copies of the primary learner's output, and the classifier output is coupled with the voting method [41]. Bagging is a term that refers to a group of decision trees that is utilized in regression. Community techniques employ numerous models to improve prediction performance by bagging together many lousy learner results into a high-quality community predictor. Bagging a community of decision trees is a variance reduction approach used to enhance decision trees' prediction performance. The bagged community power is calculated by estimating out-of-bag observations for each tree and averaging them across the entire community. Each observation's estimated out-of-bag response is compared to its actual value. The average out-of-bag error is computed by comparing expected to actual responses for all observations utilized in education. The average error extracted from this bag is a non-negative estimator of the genuine union error [42].

3. Experiments and Results

We present a series of experimental results relating to multi-class discrimination using lung sound signals in this study. The classification results were validated using the architectures described in Section 2.3. The effects of data augmentation were then analyzed using synthetic data augmentation methods. Synthetic data were generated using the methods described in Section 2.2. Because the Mexican kernel type performed better in the ELM-W-AE method during the experiments, the results were heavily weighted toward this section.

Table 3 compares the original, ELM-AE and ELM-W-AE results according to accuracy, specificity, sensitivity, precision, F1, MCC, Kappa [43]. Using the WST method, features were extracted from lung sounds (Crackle/ Whezees /Crackle+ Whezees / Normal) taken as 6898 cycles in four classes. 6898×80 features were extracted as a result of feature extraction. After normalization with ZN, the obtained features were divided into 70% training and 30% testing using hold-out cross-validation. A feature vector from the training set was augmented four times and formed into 5×80 dimensions using ELM-AE. A 24145×80 dimensional feature matrix was created using this approach for training features. The test data was not intended to be included in the augmented process, preventing memorization and ensuring the study's reliability. By testing synthetic lung data for three distinct phases, we examined the effects of data augmentation. We first evaluated the classifiers on the original images for the three major stages mentioned previously. In the second step, we created and analyzed synthetic images with the specified ELM-AE structure. The final stage involved integrating the six wavelet kernel listed in Table 2 into the ELM-W-AE structure and evaluating those using classifiers.

SVM and EBT methods were used to classify augmented training data and non-augmented test data, and the results are summarized in Table 3. The study's summary diagram is shown in Fig. 1. When Table 3 is examined, it is clear that the Mexican wavelet function provides the best performance. According to the classification of the original data, it was observed that EBT improved performance by approximately 3% and SVM improved performance by approximately 4.5 %. The complexity matrices for the original and Mexican wavelet functions are shown in Figures 3-6 in light of these data. When wavelet functions are viewed in general, it is clear that they perform better than the results obtained with the original data. Given the prevalence of lung diseases, it is clear that this percentage increase is significant. The authors concluded that wavelet kernel functions are worth experimenting with for this and similar classifications.

Table 3. Performance comparison of wavelet functions on original, ELM-AE and ELM-W-AE structure

Category		Method	Accuracy	Sensitivity	Specificity	Precision	F1	MCC	Kappa
Original		EBT	69.599	52.446	85.947	68.675	0.565	0.462	0.189
		DVM	56.404	31.284	78.440	57.059	0.291	0.157	0.140
ELM-AE		EBT	69.212	51.318	86.324	64.475	0.544	0.439	0.179
		DVM	59.981	37.673	81.214	52.318	0.382	0.247	0.063
ELM-W-AE	**Gaussian**	EBT	70.130	54.357	86.514	67.645	0.581	0.474	0.203
		DVM	59.884	37.400	80.966	51.589	0.381	0.245	0.065
	Morlet	EBT	71.242	54.828	86.884	68.990	0.587	0.488	0.233
		DVM	59.836	37.306	80.940	51.414	0.380	0.243	0.066
	Mexican	EBT	72.692	56.318	87.617	71.514	0.605	0.513	0.272
		DVM	60.609	38.969	81.200	56.848	0.407	0.277	0.048
	Shannon	EBT	69.357	50.862	85.915	65.721	0.544	0.441	0.183
		DVM	55.582	30.319	78.003	47.320	0.280	0.137	0.156
	Meyer	EBT	70.420	53.705	86.807	65.667	0.569	0.465	0.211
		DVM	59.401	36.948	80.721	50.565	0.376	0.236	0.076
	Ggw	EBT	70.904	55.978	87.052	68.783	0.597	0.493	0.224
		DVM	60.029	37.652	81.267	50.712	0.381	0.244	0.062
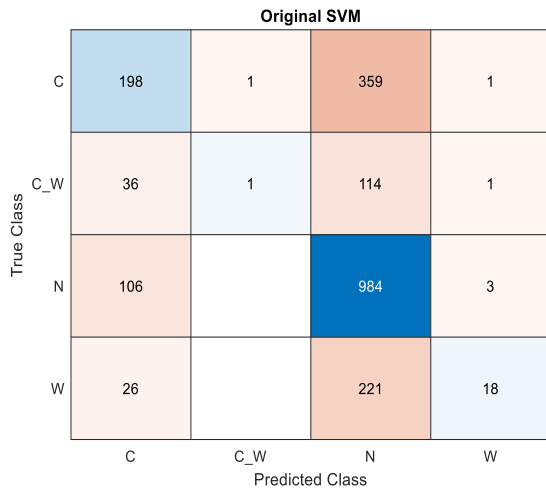
Fig.3. The complexity matrix of classification with SVM for the original data
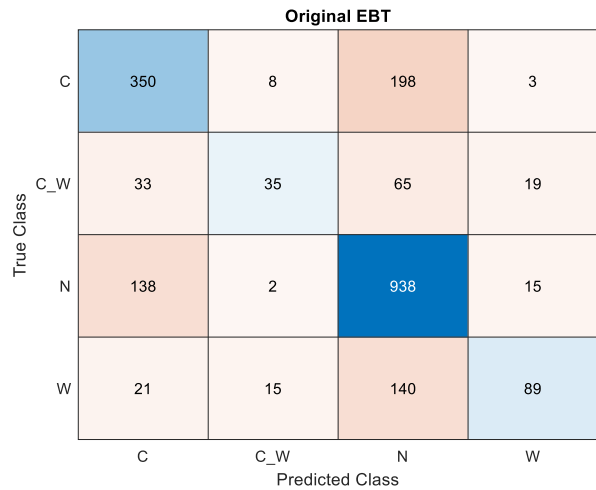
Fig.4. The complexity matrix of classification with EBT for the original data

Fig.5. The complexity matrix of classification with SVM for data multiplexed with Mexican structure

Fig.6. Complexity matrix of classification with SVM for multiplexed with Mexican structure

3.1. Comparison with other studies

As mentioned previously, we performed classification using synthetic amplification. The ELM-W-AE construct outperformed synthetic augmentation with ELM-AE alone. We compared our classification results for synthetic augmentation to the state-of-the-art studies using our best result, ELM-Mexican-AE. We chose it as a comparison because the studies we chose used the same dataset and classes. Table 4 compares the performance of the aforementioned studies in terms of preprocessing, feature extraction, classification, and classification accuracy.

Table 4. Comparison of lung sounds with four classes (Normal, crackles, wheezes, crackles+wheezes) with other studies

Reference	Pre-process	Feature Extraction and Method	Classification	Acc.
Ref[19]	resample to 4 KHz for standardization of all signals, 12th order Butterworth band pass filter	STFT, Q-factor wavelet	SVM	%54.15
Ref[22]	Band-pass filter in the frequency range 150-250 Hz, FFT	Spectrogram	CNN	%64.50
Ref[29]	-	Deep Feature with CNN model	SVM	%65.50
Ref[44]	Butterworth band pass filter, a non-linear resonance based wavelet decomposition	13 first mel-frequency cepstral coefficients	SVM	%49.86
Ref[45]	resample to 4 KHz for standarization of all signals	13 MFCCs coefficients STF and LTF parametres	SVM ANN RF	%72.1 %68.7 %68.7
The first proposed method	ZN	WST, ELM-AE	SVM EBT	%69.21 %59.98
The second proposed method	ZN	WST, ELM-W-AE	SVM EBT	%72.69 %60.61

4. Conclusion

The purpose of this study was to distinguish four classes based on voice recordings from the ICBHI 2017 respiratory dataset: normal, wheezing, wheezing, wheezing, and wheezing. Experiments were conducted in stages

to evaluate the proposed method's classification performance. To begin, in contrast to previous research, audio signals are subjected to the wavelet scatter process for feature extraction. To offer a suitable classification approach, we first calculated and compared the classification accuracies of the original and augmented data. The train feature parts were augmented fivefold, including the original images with ELM-W-AE. SVM and EBT were used to classify the test features that were not included in the augmenting process and the augmented train features. Simultaneously, this classification process has been validated without the use of augmenting. The system was first compared to other architectures in terms of incremental and non-incremental classifiers. Both cases demonstrated unequivocally that the proposed incremental method performed better. The proposed architecture indicates that it is capable of providing a solution for disease detection while introducing a novel feature and experimental stage for the analysis of multi-class lung sounds.

References

[1] Sambasivan, N., Kapania, S., Highfill, H., Akrong, D., Paritosh, P., & Aroyo, L. M. (2021, May). "Everyone wants to do the model work, not the data work": Data Cascades in High-Stakes AI. In proceedings of the 2021 CHI Conference on Human Factors in Computing Systems (pp. 1-15).

[2] Altan, G., & Kutlu, Y. (2018). Generative autoencoder kernels on deep learning for brain activity analysis. Natural and Engineering Sciences, 3(3), 311-322.

[3] Ferreira, J., Ferro, M., Fernandes, B., Valenca, M., Bastos-Filho, C., & Barros, P. (2017, November). Extreme learning machine autoencoder for data augmentation. In 2017 IEEE Latin American Conference on Computational Intelligence (LA-CCI)(pp. 1-6). IEEE.

[4] Nishizaki, H. (2017, December). Data augmentation and feature extraction using variational autoencoder for acoustic modeling. In 2017 Asia-Pacific Signal and Information Processing Association Annual Summit and Conference (APSIPA ASC) (pp. 1222-1227). IEEE.

[5] Cao, G., & Kamata, S. I. (2019, September). Data augmentation for historical documents via cascade variational auto-encoder. In 2019 IEEE International Conference on Signal and Image Processing Applications (ICSIPA) (pp. 340-345). IEEE.

[6] Hussain, Z., Gimenez, F., Yi, D., & Rubin, D. (2017). Differential data augmentation techniques for medical imaging classification tasks. In AMIA annual symposium proceedings (Vol. 2017, p. 979). American Medical Informatics Association.

[7] Frid-Adar, M., Klang, E., Amitai, M., Goldberger, J., & Greenspan, H. (2018, April). Synthetic data augmentation using GAN for improved liver lesion classification. In 2018 IEEE 15th international symposium on biomedical imaging (ISBI 2018) (pp. 289-293). IEEE.

[8] Zhao, A., Balakrishnan, G., Durand, F., Guttag, J. V., & Dalca, A. V. (2019). Data augmentation using learned transformations for one-shot medical image segmentation. In Proceedings of the IEEE/CVF Conference on Computer Vision and Pattern Recognition (pp. 8543-8553).

[9] Eaton-Rosen, Z., Bragman, F., Ourselin, S., & Cardoso, M. J. (2018). Improving data augmentation for medical image segmentation.

[10] ŞENGÜR, D. EEG, EMG and ECG based Determination of Psychosocial Risk Levels in Teachers based on Wavelet Extreme Learning Machine Autoencoders. Politeknik Dergisi, 1-1.

[11] Shuvo, S. B., Ali, S. N., Swapnil, S. I., Hasan, T., & Bhuiyan, M. I. H. (2020). A lightweight cnn model for detecting respiratory diseases from lung auscultation sounds using emd-cwt-based hybrid scalogram. IEEE Journal of Biomedical and Health Informatics.

[12] ÇOLAK, M., BENLİ, Ş. G., & Müge, D. O. L. U. Akciğer Hastalıklarının Dalgacık Katsayıları Kullanılarak Karar Ağaçlarına Dayalı Sınıflandırılması. Avrupa Bilim ve Teknoloji Dergisi, (24), 463-468.

[13] Demir, F., Ismael, A. M., & Sengur, A. (2020). Classification of lung sounds with cnn model using parallel pooling structure. IEEE Access, 8, 105376-105383.

[14] N. Sengupta, M. Sahidullah and G. Saha, "Lung sound classification using cepstral-based statistical features", Comput. Biol. Med., vol. 75, pp. 118-129, Aug. 2016.

[15] G.-C. Chang and Y.-F. Lai, "Performance evaluation and enhancement of lung sound recognition system in two real noisy environments", Comput. Methods Programs Biomed., vol. 97, pp. 141-150, Feb. 2010.

[16] S. Reichert, R. Gass, C. Brandt and E. Andrès, "Analysis of respiratory sounds: State of the art", Clin. medicine. Circulatory Respiratory Pulmonary Med., vol. 2, pp. 1-14, Jan. 2008.

[17] S. İçer and Ş. Gengeç, "Classification and analysis of non-stationary characteristics of crackle and rhonchus lung adventitious sounds," Digit. Signal Process., vol. 28, pp. 18–27, 2014, doi: 10.1016/j.dsp.2014.02.001.

[18] A. Kandaswamy, C. S. Kumar, R. P. Ramanathan, S. Jayaraman, and N. Malmurugan, "Neural classification of lung sounds using wavelet coefficients," Comput. Biol. Med., vol. 34, no. 6, pp. 523–537, 2004, doi: https://doi.org/10.1016/S0010-4825(03)00092-1.

[19] S. ULUKAYA, G. SERBES, İ. ŞEN, and Y. P. KAHYA, "Akciğer Solunum Seslerinin Spektral Öznitelikler ile Sınıflandırılması," Süleyman Demirel Üniversitesi Fen Bilim. Enstitüsü Derg., vol. 22, no. 2, p. 711, 2017, doi: 10.19113/sdufbed.84471.

[20] A. Sovijärvi et al., "Characteristic of breath sounds and adventitious respiratory sounds," Charact. Breath Sounds Adventitious Respir. Sounds, vol. 10, pp. 591–596, Jan. 2000.

[21] Rocha, B. M., Pessoa, D., Marques, A., Carvalho, P., & Paiva, R. P. (2021, January). Influence of Event Duration on Automatic Wheeze Classification. In 2020 25th International Conference on Pattern Recognition (ICPR) (pp. 7462-7469). IEEE.

[22] ER, M. B. (2020). Akciğer Seslerinin Derin Öğrenme ile Sınıflandırılması. Gazi Üniversitesi Fen Bilimleri Dergisi Part C: Tasarım ve Teknoloji, 8(4), 830-844.

[23] Khan, S. I., Palodiya, V., & Poluboyina, L. (2021). Automated classification of human lung sound signals using phase space representation of intrinsic mode function.

[24] Nguyen, T., & Pernkopf, F. (2021). Crackle Detection In Lung Sounds Using Transfer Learning And Multi-Input Convolitional Neural Networks. arXiv preprint arXiv:2104.14921.

[25] Khan, S. I., & Pachori, R. B. (2021). Automated classification of lung sound signals based on empirical mode decomposition. Expert Systems with Applications, 184, 115456.

[26] Murphy, Raymond & Vyshedskiy, Andrey & Power-Charnitsky, Verna-Ann & Bana, Dhirendra & Marinelli, Patricia & Wong-Tse, Anna & Paciej, Rozanne. (2005). Automated Lung Sound Analysis in Patients With Pneumonia. Respiratory care. 49. 1490-7. 10.1378/chest.124.4_MeetingAbstracts.190S-b.

[27] Aras, S., & Gangal, A. (2017, July). Comparison of different features derived from mel frequency cepstrum coefficients for classification of single channel lung sounds. In 2017 40th International Conference on Telecommunications and Signal Processing (TSP) (pp. 346-349). IEEE.

[28] "Challenge", 2017, [online] Available: https://bhichallenge.med.auth.gr/.

[29] Demir, F., Sengur, A., & Bajaj, V. (2020). Convolutional neural networks based efficient approach for classification of lung diseases. Health information science and systems, 8(1), 1-8.

[30] Serbes, G., Ulukaya, S., & Kahya, Y. P. (2017, November). An automated lung sound preprocessing and classification system based onspectral analysis methods. In International Conference on Biomedical and Health Informatics (pp. 45-49). Springer, Singapore.

[31] Soro, B., & Lee, C. (2019). A wavelet scattering feature extraction approach for deep neural network based indoor fingerprinting localization. Sensors, 19(8), 1790.

[32] Sepúlveda, A., Castillo, F., Palma, C., & Rodriguez-Fernandez, M. (2021). Emotion Recognition from ECG Signals Using Wavelet Scattering and Machine Learning. Applied Sciences, 11(11), 4945.

[33] Mallat, S. Group invariant scattering. Commun. Pure Appl. Math. **2012**, 65, 1331–1398.

[34] Lauraitis, A., Maskeliūnas, R., Damaševičius, R., & Krilavičius, T. (2020). Detection of speech impairments using cepstrum, auditory spectrogram and wavelet time scattering domain features. IEEE Access, 8, 96162-96172.Zscore

[35] Fei, N., Gao, Y., Lu, Z., & Xiang, T. (2021). Z-Score Normalization, Hubness, and Few-Shot Learning. In Proceedings of the IEEE/CVF International Conference on Computer Vision (pp. 142-151).

[36] Huang, G. B., Zhu, Q. Y., & Siew, C. K. (2006). Extreme learning machine: theory and applications. Neurocomputing, 70(1-3), 489-501.

[37] Uzair, M., & Mian, A. (2016). Blind domain adaptation with augmented extreme learning machine features. IEEE transactions on cybernetics, 47(3), 651-660.

[38] Javed, K., Gouriveau, R., & Zerhouni, N. (2014). SW-ELM: A summation wavelet extreme learning machine algorithm with a priori parameter initialization. Neurocomputing, 123, 299-307.

[39] Cherkassky, V., & Ma, Y. (2004). Practical selection of SVM parameters and noise estimation for SVM regression. Neural networks, 17(1), 113-126.

[40] Ucuz, I., Ciçek, A. U., Ari, A., Ozcan, O. O., & Sari, S. A. (2020). Determining the probability of juvenile delinquency by using support vector machines and designing a clinical decision support system. Medical hypotheses, 143, 110118.

[41] Breiman, L. (1996). Bagging predictors. Machine learning, 24(2), 123-140.

[42] Berna, A. R. I., Ali, A. R. I., & ŞENGÜR, A. (2020). Suicide Prediction from Hemogram with Machine Learning. Avrupa Bilim ve Teknoloji Dergisi, 364-369.

[43] Berna, A. R. I., İlknur, U. C. U. Z., Ali, A. R. I., Özdemir, F., & SENGUR, A. (2020). Grafik Tablet Kullanılarak Makine Öğrenmesi Yardımı ile El Yazısından Cinsiyet Tespiti. Fırat Üniversitesi Mühendislik Bilimleri Dergisi, 32(1), 243-252.

[44] Chambres, G., Hanna, P., & Desainte-Catherine, M. (2018, September). Automatic detection of patient with respiratory diseases using lung sound analysis. In 2018 International Conference on Content-Based Multimedia Indexing (CBMI) (pp. 1-6). IEEE.

[45] Gómez, A. F. R., & Orjuela-Cañón, A. D. (2021, May). Respiratory Sounds classification employing a Multi-label Approach. In 2021 IEEE Colombian Conference on Applications of Computational Intelligence (ColCACI) (pp. 1-5). IEEE

Efficient Text Classification with Deep Learning on Imbalanced Data Improved with Better Distribution

Beytullah YILDIZ[1*]

[1] Department of Software Engineering, School of Engineering, Atilim University, Ankara, Turkey
[*1] beytullah.yildiz@atilim.edu.tr

Abstract: Technological developments and the widespread use of the internet cause the data produced on a daily basis to increase exponentially. An important part of this deluge of data is text data from applications such as social media, communication tools, customer service. The processing of this large amount of text data needs automation. Significant successes have been achieved in text processing recently. Especially with deep learning applications, text classification performance has become quite satisfactory. In this study, we proposed an innovative data distribution algorithm that reduces the data imbalance problem to further increase the text classification success. Experiment results show that there is an improvement of approximately 3.5% in classification accuracy and over 3 in F1 score with the algorithm that optimizes the data distribution.

Key words: Text classification, Data Imbalance, Data Distribution, Deep learning, Word Embedding.

Daha İyi Dağıtımla İyileştirilmiş Dengesiz Veriler Üzerinde Derin Öğrenme ile Verimli Metin Sınıflandırması

Öz: Teknolojik gelişmeler ve internetin yaygınlaşması, günlük olarak üretilen verilerin katlanarak artmasına neden olmaktadır. Bu veri tufanının önemli bir kısmı sosyal medya, iletişim araçları, müşteri hizmetleri gibi uygulamalardan gelen metin verilerinden kaynaklanmaktadır. Bu büyük miktarda metin verisinin işlenmesi otomasyona ihtiyaç duymaktadır. Son zamanlarda metin işlemede önemli başarılar elde edilmiştir. Özellikle derin öğrenme uygulamaları ile metin sınıflandırma performansı oldukça tatmin edici hale gelmiştir. Bu çalışmada, metin sınıflandırma başarısını daha da artırmak için veri dengesizliği sorununu azaltan yenilikçi bir veri dağıtım algoritması önerdik. Deney sonuçları, veri dağılımını optimize eden algoritma ile sınıflandırma doğruluğunda yaklaşık %3,5 ve F1 puanında 3'ün üzerinde bir iyileşme olduğunu göstermektedir.

Anahtar kelimeler: Metin sınıflandırma, Veri Dengesizliği, Veri Dağıtımı, Derin öğrenme, Kelime Gömme.

1. Introduction

With the widespread use of the Internet, data production speed, volume, and variety of data have increased significantly. Text data has a significant share in the produced data. Many applications such as social media, customer service, and communication tools are increasingly generating huge text data. The processing and analysis of these data become very important. Institutions and organizations hire employees and experts who will carry out the tasks of reading, classifying, evaluating, and responding to texts. The correct and fast processing and the response of the text are extremely important in terms of quality and satisfaction. However, the current business model has some drawbacks that need improvement. When the workload increases, either the number of employees or the working hours of the employees must be increased in order to provide the necessary service. This results in compromising the quality of the work. In addition, increasing the number of employees or working hours is a costly solution. Therefore, Automation has become necessary for the processing of increasing text data.

Classification is one of the main tasks for text processing. We see its application in many natural language processing (NLP) tasks. Recently, very successful classification results have been obtained with the prominent deep learning models [1-3]. Well-known deep learning networks such as Convolutional Neural Network (CNN), Recurrent Neural Network (RNN), and recently networks with Attention layer, especially Transformer, have been used text classification [4, 5]. In order to better classify the text with these networks, data preparation is important; it is vital that the data is appropriately represented and well distributed among the training batches. In addition to simple word representation methods such as one-hot encoding, bag-of-words, and term frequency-inverse document frequency (TF-IDF), advanced methods that take into account semantic and syntactic information such as Word2Vec [6], FastText [7], Glove [8], BERT [9] can be used. To improve performance and success, it is

---

[*] Corresponding author: beytullah.yildiz@atilim.edu.tr. ORCID Number of authors: [1] 0000-0001-7664-5145

advantageous to use features that best describe the text in terms of classification, rather than using the entire text. The correct representation of the text and the selection of the correct features are processes that require expertise depending on the data and method to be used. With the use of deep learning and word representation methods, there have been important conveniences and gains in this regard.

Deep learning models are trained with batches of data. The data distribution in these batches should ideally be homogeneous so that the models can learn the patterns efficiently. However, it is not always possible to have ideal data and it is difficult to eliminate this deficiency, which we can define as imbalanced data[10]. One way to do this is to use shuffle to randomly distribute data. However, this may not eliminate the imbalanced data problem. Another way is to use data augmentation. Text data augmentation has some problems. It is difficult to create new text data that contains the original information and properties of the data. Therefore, in this study, we introduce an algorithm to create better distribution to mitigate imbalanced data problems. We classified 263168 documents containing 15 classes using deep learning models. Word2Vec word vectors were created using 2803125 documents of approximately 203 million words. Long short-term memory (LSTM) based deep learning models were created for classification tasks. We proposed an innovative algorithm for better distribution of the training dataset to increase classification success. Experimental results show an increase of about 3.5% in classification accuracy and an improvement of over 3 in F1 score with the proposed data distribution.

In the second section of this article, related works are presented. In the third section, we describe the methodology of our research. Results and evaluations are given in the fourth section. In the last section, we provide the conclusion of our research.

2. Related Work

A brief overview of text classification algorithms was provided by Kowsari et al. in [11]. In the article, existing algorithms and techniques, text feature extraction methods, and dimensionality reduction methods were discussed. The authors also explored the limitations of each technique in real-world problems. An effective text classification requires good word representation and data distribution, in addition to other requirements. The importance of word representation was discussed in [12, 13]. The authors examined the effect of better word representation on classification success. On the other hand, the problem of data imbalance, which hinders classification success, has also attracted the attention of many studies.

Sun et al. studied imbalanced data where the number of text data in some classes was relatively small [14]. The authors provided some conclusions as a result of the experiments. They stated that when the number of texts in the classes is the same, the difference in the number of words in the texts is a factor affecting the success of classification. They also claimed that if the number of texts in the classes is different, increasing the number of texts in the class with a small number of texts does not affect the success much. However, we think that the reason for this claim is due to the difficulty of producing texts representing the class. In [15], the authors presented an approach to measure and reduce unwanted bias in machine learning models. In this context, it was shown how models with imbalances in the training dataset can lead to undesirable bias and thus potentially unfair practices. To provide a solution, a reduction method, which is an unsupervised approach based on balancing the training dataset, was proposed. The approach was claimed to reduce unwanted bias without sacrificing overall model quality. [16] presented a KNN-based method for unevenly distributed large sets of documents. Experimental results showed that the approach provides better text classification.

Imbalance in classes is often come across in real applications of text classifications, especially one-vs-all methods. Therefore, it is quite important to address the issue for reasonable performance. To mitigate the problem, Ogura et al. focused their attention on a feature selection scheme and explored various criteria for feature selection [17]. They examined three different types of metrics and showed that feature selections using the appropriate metrics in the unbalanced dataset yield satisfactory classification success. The problem of underrepresentation of categories with fewer examples was attempted to be solved by Liu et al. using a simple probability-based term weighting scheme [18]. This scheme directly used two critical information ratios, namely, relevance indicators. Using Support Vector Machines and Naïve Bayes classifiers on two benchmark datasets, including Reuters-21578, the proposed work was compared with other classical weighting schemes and showed significant improvement for categories with fewer examples. [10] presented an experimental analysis using various text data representations and data balancing schemes to obtain a classification model with the highest success. The authors' proposed schemes to deal with data imbalance and to analyze it with a numerical optimization problem in which the costs are derived by a Differential Evolution algorithm. In the book chapter, Liu et al. explained the approaches adopted to resolve data imbalance in text classification and group them according to their primary focus [19]. The authors

showed the effects of class imbalance on classification models in [20]. They conduct extensive experiments to highlight the nature of the relationship between the degree of class imbalance and classifier performance.

3. Methodology

In many real-world applications, some classes in training datasets have less representation than others. This imbalanced data structure causes problems in Machine Learning classification and results in poor classification success as there is not enough data to learn. Therefore, we presented an algorithm that optimizes the data distribution as a solution to the data imbalance. We studied this algorithm in an LSTM-based deep learning model. We made text classification on 263168 Turkish documents labeled in 15 categories. The same text data and the same word representations were used when evaluating the model. Since deep learning methods use numbers instead of text, we drew attention to the vectorization of texts using a word representation. Python programming language was used in the development of the application. Word vectors were created using Gensim [21] library and the TensorFlow library was used for deep learning model development.

We performed the steps in Figure 1 to train and test the classification model. We trained and tested our model on the normal dataset containing Turkish documents and the dataset with the removed data imbalance in which we applied our algorithm. The algorithm was applied while generating batches for training. The deep learning model was trained with batches of text documents because the data size was huge. In the remainder of this section, we'll explain our solution to the data imbalance. We will provide detailed information about the classification model, the dataset we used, and the Word2vec model we used to create the word representations.
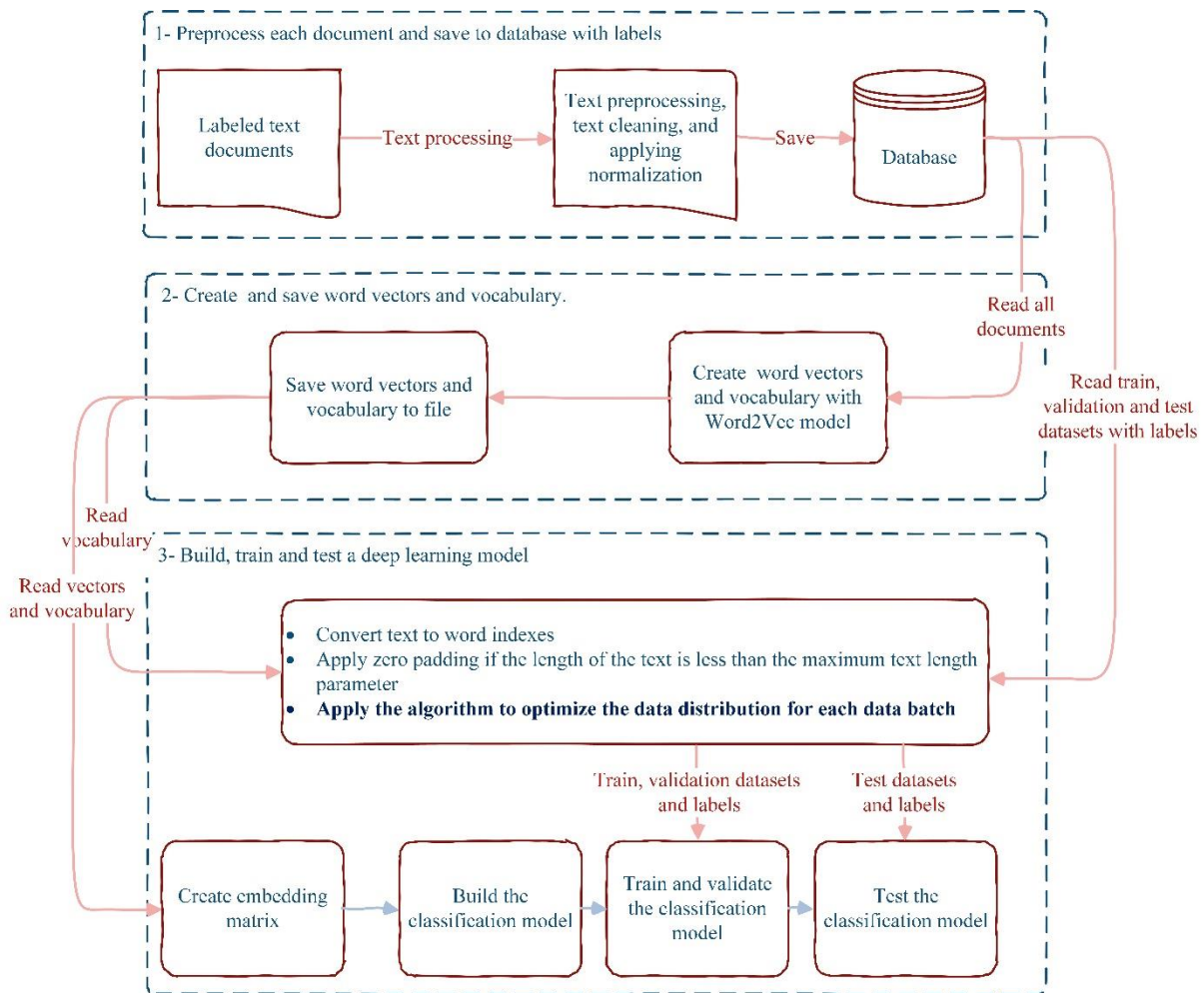
Figure 1. Training and testing the classification model and applying algorithms that resolve data imbalances.

3.1. Solving Data Imbalance

In many real-life application datasets, some classes are less represented than others. In other words, the data is skewed. When the number of texts in some classes is less than in others, the training process is negatively affected. This problem is called imbalanced data. There are solutions to mitigate this problem, such as data augmentation and deleting data from classes with more data. Data deletion is generally not a good choice as it can remove some necessary information. On the other hand, data augmentation is difficult for text data as opposed to image data. For this reason, we prefer to distribute the data optimally into the training batches, considering the number of documents in the classes. Hence, we created the following algorithm that optimally performs the data distribution in the datasets. Algorithm 1 creates ideal batches, while Algorithm 2 performs optimal data distribution in each training batch.

Algorithm 1: Distribute Data

1: **procedure** GetBatches()
2:      Number of classes is m
3:      **for** i ← 1, m **do**
4:          classes(i) ← getClasses()
5:          batches← CreateWellDistributedBatches (classes)
6:       **end for**
7: **end procedure**

Algorithm 2: Create Well-distributed Batches

1: **procedure** CreateWellDistributedBatches (classes)
2:      normIndex is a two dimentional array
3:      **for** i ← 1, m **do**
4:          class ← classes(i)
5:          max ← len(class), min ← 1, row ← 1
6:          **while** class is not empty **do**
7:              index (row) ← an incremental value starting from 1 to max for each row
8:              normIndex (i ,row) ← (index(row) – min)/ (max – min)
9:              row ← row+ 1
10:         **end while**
11:     **end for**
12:     classesWithNormIndex ← join classes with normalized indexes
13:     range ← 1/numberOfBatch
14:     r ← 0
15:     **for** i ← 1, numberOfBatch **do**
16:         **while** data in classes **do**
17:             **if** r < normIndex for the data < r+range **then**
18:                 selectToBatch(classesWithNormIndex)
19:             **end if**
20:         **end while**
21:         r ← r + range
22:     **end for**
23: **end procedure**

We will give an example shown in Table 1 to explain how the algorithm works. Let's say we have a dataset with categories A, B, and C. Category A consists of 10 texts, Category B consists of 5 texts, and Category C consists of 3 texts. There are 18 texts in total in the dataset. It is aimed to divide the dataset into 3 optimal batches of text. When the data is divided into three equal parts without any mixing or distribution as shown in Table 1 (Left-Original), it is seen that the classes are stacked in certain parts. The first part consists of A class texts, the second part consists of A and B class texts. The third part consists of B and C class texts. Generally, classes are randomly distributed using shuffle. However, this method does not guarantee that the categories are optimally distributed in the batches for classification training. The texts in Table 1 (right) were distributed according to the text frequency in the classes using the algorithm we suggested. When the data is divided into batches, it is seen

that the texts in each class are distributed as evenly as possible. Data that is not evenly distributed across 3 batches is placed in an appropriate batch. As the number of data increases, this small error will decrease and the data distribution will approach the ideal.

Table 1. A sample distribution of data.

Original						Distributed				
Indices	**Class**	**Min**	**Max**	**Normalized Indices**	**Part**	**Indices**	**Class**	**Min**	**Max**	**Normalized Indices**
1	A	1	10	0.00	1	1	A	1	10	0.00
2	A	1	10	0.11	2	1	B	1	5	0.00
3	A	1	10	0.22	3	1	C	1	3	0.00
4	A	1	10	0.33	4	2	A	1	10	0.11
5	A	1	10	0.44	5	3	A	1	10	0.22
6	A	1	10	0.56	6	2	B	1	5	0.25
7	A	1	10	0.67	1	4	A	1	10	0.33
8	A	1	10	0.78	2	5	A	1	10	0.44
9	A	1	10	0.89	3	3	B	1	5	0.50
10	A	1	10	1.00	4	2	C	1	3	0.50
1	B	1	5	0.00	5	6	A	1	10	0.56
2	B	1	5	0.25	6	7	A	1	10	0.67
3	B	1	5	0.50	1	4	B	1	5	0.75
4	B	1	5	0.75	2	8	A	1	10	0.78
5	B	1	5	1.00	3	9	A	1	10	0.89
1	C	1	3	0.00	4	10	A	1	10	1.00
2	C	1	3	0.50	5	5	B	1	5	1.00
3	C	1	3	1.00	6	3	C	1	3	1.00

3.2. Word Representation

We used the Word2Vec model, an unsupervised method proposed by Mikolov et al. [6, 22], for representing words in texts. Word2Vec takes a corpus and creates word vectors of several hundred dimensions. It creates numerical vectors to represent words by trying to position similar syntactic and semantic words close to each other in vector space. There are two different methods for creating word vectors. The first of these is CBOW (Continuous Bag of Words) and the second is SG (Skip-Gram). While the CBOW method tries to guess the word from the words in a particular window to the right and left of the word, the SG method tries to guess the words to the right and left of the word from the word itself. Besides word vectors, we also come across researches that create vectors for documents, patterns, users, and classes [23, 24].

We created the word vectors using the SG model. The SG model has an input layer, a hidden layer, and an output layer. The input vector $x = \{x_1, \ldots, x_v\}$ is one-hot encoded. The weights between the input layer and the hidden layer can be represented by the V x N matrix W shown in formula 1, where V is the vocabulary size and N is the unit size in the hidden layer. Between the output layer and the hidden layer, there is another V x N weight matrix W' shown in formula 2.

$$W_{VxN} = \begin{bmatrix} v_{11} & \cdots & v_{1N} \\ \vdots & \vdots & \vdots \\ v_{V1} & \cdots & v_{VN} \end{bmatrix} \tag{1}$$

$$W'_{VxN} = \begin{bmatrix} v'_{11} & \cdots & v'_{1N} \\ \vdots & \vdots & \vdots \\ v'_{V1} & \cdots & v'_{VN} \end{bmatrix} \tag{2}$$

Given a single word x_k, and assuming $x_k = 1$ and $x_{k'} = 0$ for $k \neq k'$, we obtain the formula 3 for the hidden-layer outputs, where v_{w_I} denotes the input vector of the associated word w of the input layer.

$$h = x^T W = W_{(k,)} := v_{w_I} \tag{3}$$

The output utilizing the Softmax function can be calculated by using $v'_w \cdot h$. Applying Formula 3, we get the following formula:

$$p(w_O|w_I) = \frac{\exp(v'_{w_O} .v_{w_I})}{\sum_{j'=1}^{V} \exp(v'_{w_{j'}} .v_{w_I})} \tag{4}$$

Thus, the loss function is formula 5 where c is the number of context words.

$$E = -\log p\left(w_{O,1}, w_{O,2}, \dots w_{O,C}|w_I\right) \tag{5}$$

After providing the mathematical background information, we explain how we generate the word vectors. A collection of 2.8 million Turkish texts was used to create the Word2Vec model. The corpus has a total of 243 million words and 2.6 million unique words, including misspellings words. All uppercase letters have been converted to lowercase to avoid creating a new token for the same word. While Word2vec training, windows size, negative sample, minimum word count, and vector size were set to 20, 5, 5 250, respectively, in the SG method. When the minimum word count parameter was set to 5, the number of unique words decreased from 2.6 million to 603 thousand words. This is because there are many misspelled words in the corpus. Therefore, the minimum word count parameter was chosen as 5.

3.3. Deep Learning Model

For the experiments, we used an LSTM-based deep learning model, which is known to classify well on text data. With the algorithm we proposed, the dataset that solved the problem of data imbalance and the regular dataset, in which this algorithm was not applied, were trained using the same model. In other words, two datasets were tested on the same deep learning model. In the deep learning model, 1 Embedding layer, 2 bidirectional LSTM layers of 128 units, 2 Dense layers of 500 and 300 units, and 1 output layer of 15 units were used. A 160 x 250 matrix was created for each text, with the embedding layer set to a maximum text length of 160 and using Word2Vec vectors of size 250. Zero padding was applied to texts less than 160 words. 0.2 Dropout was utilized in layers containing LSTM and Dense. Softmax activation function was applied to the output layer. "Adam" was preferred as the optimization function and "sparse_categorical_crossentropy" was used as the loss function.

3.4. Dataset

Statistics of the text dataset used for classification are given in Table 2. The dataset contains a total of 263168 labeled documents with 15 classes. Of these documents, approximately 70% corresponding to 185344 documents were used for training, approximately 15% corresponding to 38912 documents were used for verification, and approximately 15% corresponding to 38912 documents were used for testing.

Table 2. Dataset used for classification.

Class Name	Total	Train	Validation	Test
1.Class	12055	8490	1782	1783
2.Class	18150	12782	2684	2684
3.Class	14405	10145	2130	2130
4.Class	26086	18372	3857	3857
5.Class	9550	6726	1412	1412
6.Class	20945	14751	3097	3097
7.Class	37180	26186	5497	5497
8.Class	11280	7944	1668	1668
9.Class	15505	10919	2293	2293
10.Class	15435	10871	2282	2282
11.Class	10768	7584	1592	1592
12.Class	30312	21348	4482	4482
13.Class	11795	8307	1744	1744
14.Class	12109	8528	1791	1790
15.Class	17593	12391	2601	2601
Total	**263168**	**185344**	**38912**	**38912**
Ratio (~%)	**100**	**70**	**15**	**15**

4. Benchmark and Evaluation

We used the documents whose statistics are given in Table 2 in the experiments. We first trained the dataset as it provided. We collected the experimental metrics. We then optimally redistribute documents from datasets to batches to find the improvement our algorithm provides to mitigate the data imbalance issue. Although the train, validation, and test datasets contain the same number of documents, we rearrange the documents in the batches by class types so that the distribution is optimal. Then, we collected experimental results. We did not make use of the "EarlyStopping" callback to see the experimental behaviors and used 20 epochs for model training. However, we save the best models for both experiments. A batch size of 1024 was used for each experiment. Precision, recall, F1-score metrics, and model accuracies were used to evaluate approaches.

4.1. Classification Model with Regular Dataset

The loss and accuracy graphs of the train and validation datasets are given in Figure 2 and Figure 3. The model starts overfitting from Epoch 14. After this point, the validation loss and accuracy are not improving even though training loss and accuracy values are getting better. Hence, we save the model at this point to measure precision, recall, and F1 scores and accuracy on test datasets.
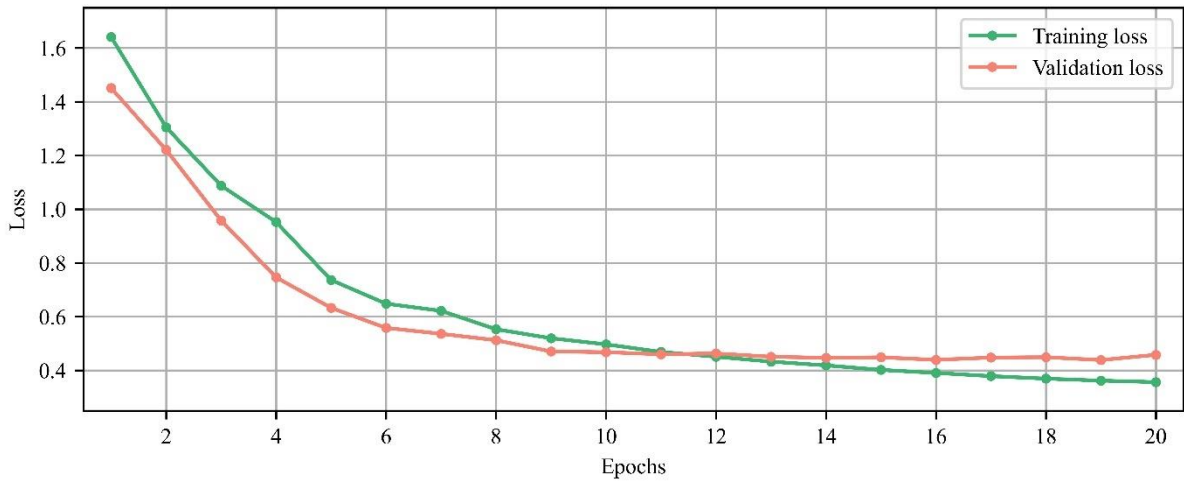
Figure 2. The loss results obtained during the training with the dataset in which the proposed distribution algorithm is not applied.
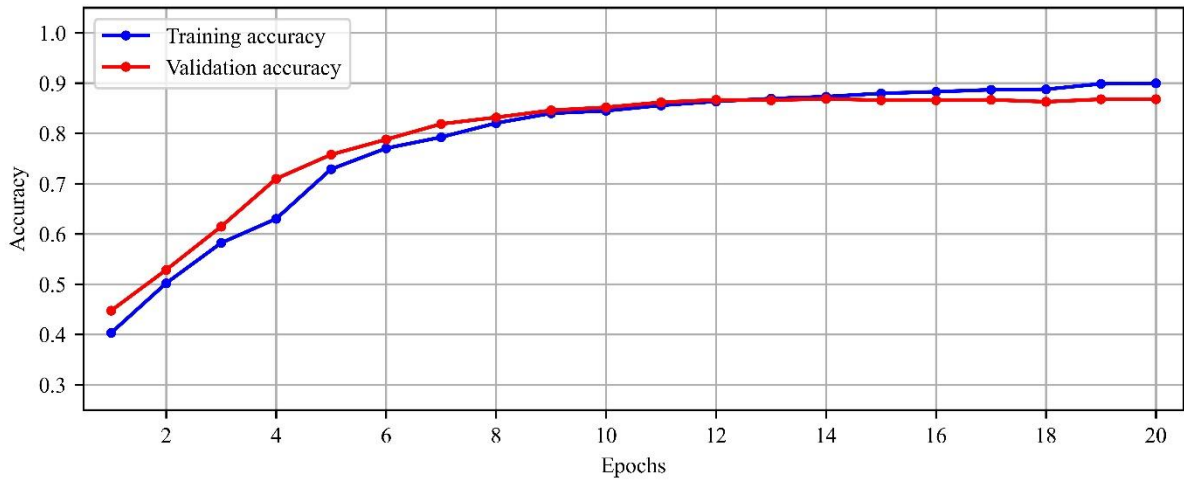
Figure 3. The accuracy results obtained during the training with the dataset in which the proposed distribution algorithm is not applied.

The saved model was used to collect benchmarks. The accuracy of the test dataset is 87.96%. The precision, recall, and F1-score values for each class are given in Table 3. The model's F1 score is 87.84. The other metrics are also reasonable. Class transitivity seems to have caused bad results in some classes. Since the dataset we use was obtained from a real-life application, some classes such as economics and education have similar content with other classes. Therefore, metrics are worse in these classes.

Table 1. Precision, recall, and F1-score metrics obtained with the test dataset in the model trained with the dataset to which the distribution algorithm is not applied.

Class Name	1	2	3	4	5	6	7	8	9	10	11	12	13	14	15	All
Support	1783	2684	2130	3857	1412	3097	5497	1668	2293	2282	1592	4482	1744	1790	2533	**38912**
Precision	90.63	83.15	83.33	89.77	91.18	90.65	89.53	83.84	85.1	89.65	83.43	89.27	91.94	87.28	86.38	**87.99**
Recall	92.5	90.29	64.1	88.74	92.76	88.41	92.51	94.28	73.67	85.03	87.51	96.15	83.26	86.44	90.16	**88**
F1-Score	91.56	86.57	72.46	89.25	91.96	89.52	91	88.75	78.97	87.28	85.42	92.58	87.38	86.86	88.23	**87.84**

4.2. Classification Model with Well-distributed Dataset

For the optimally distributed dataset to the batches, loss and accuracy plots of the train and validation datasets are given in Figure 4 and Figure 5. The model started to encounter the overfitting problem after Epoch 11. Therefore, we save the model at this point to measure precision, recall, F1 score, and the accuracy value on the test dataset. Compared to the model described in the previous section, the model is trained faster with the optimally distributed dataset using our proposed algorithm. In addition, it is observed that the training and validation accuracy values are much higher.
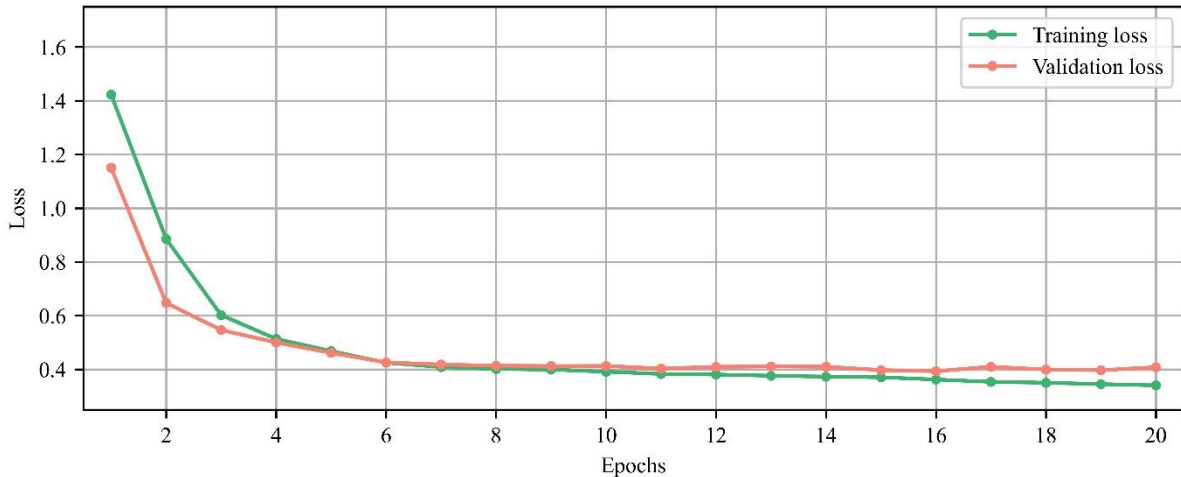
Figure 4. The loss results obtained in the model trained with the dataset created with the proposed distribution algorithm.

Table 2. Precision, recall, and F1-score metrics obtained with the test dataset using the model trained with the dataset created with the distribution algorithm.

Class Name	1	2	3	4	5	6	7	8	9	10	11	12	13	14	15	All
Support	1783	2684	2130	3857	1412	3097	5497	1668	2293	2282	1592	4482	1744	1790	2533	**38912**
Precision	94	86.25	86.23	93.67	95.51	92.78	92.72	88.16	90.91	92.63	87.85	91.79	92.31	89.76	91.11	**91.3**
Recall	95.79	93.22	70.28	91.73	94.83	91.22	94.78	96.88	76.8	88.65	90.83	98.55	92.2	91.12	92.62	**91.31**
F1-Score	94.89	89.6	77.44	92.69	95.17	91.99	93.74	92.31	83.26	90.6	89.32	95.05	92.25	90.43	91.86	**91.19**
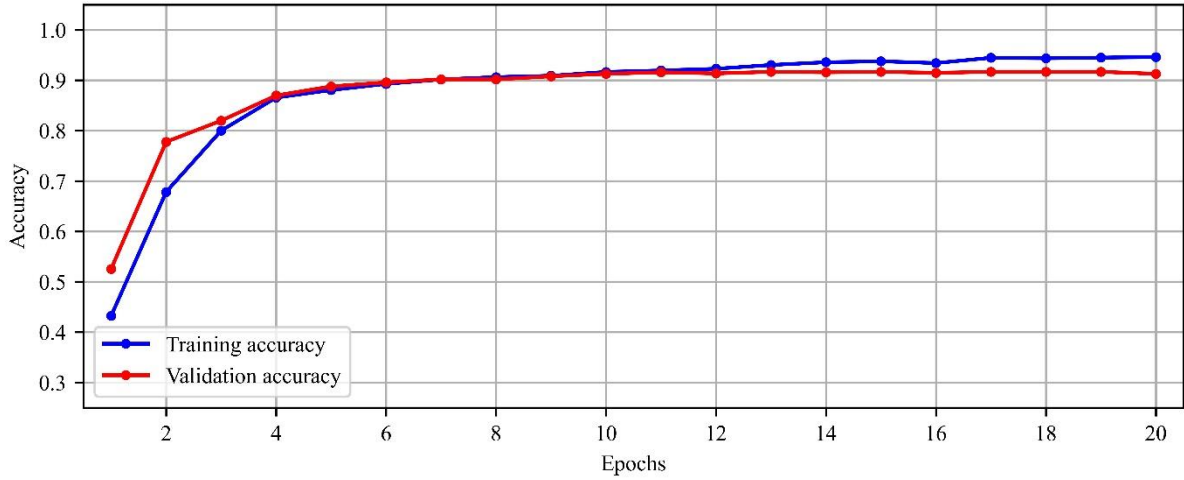
Figure 5. The accuracy results obtained in the model trained with the dataset created with the proposed distribution algorithm.

When we look at the metrics collected for the test dataset. The accuracy of the test dataset was measured as 91.45%. Precision, recall, and F1 score values are given in Table 4. For the entire dataset, they are 91.3, 91.31, and 91.19, respectively. It is clearly seen that these metrics are also better than the results we obtained in the previous experiment.

4.3 Comparison

In terms of accuracy, we observe that our algorithm to distribute data into batches optimally provides 3.46% better output. In addition, the average F1 score improved by 3.35. We see similar advances in recall and precision measures. When we look at each of the classes, we witness improvement in almost every metric. In particular, it appears that improvement is higher in classes with the worst metrics of previous experiments. This shows that our proposed algorithm contributes better to solve the problem of data imbalance in underrepresented or transitive classes. In addition, training takes less time as the model trained with the data set with the improved distribution is optimized faster.

5. Conclusion

Nowadays, huge amounts of text data are produced from many sources. This excessive amount of text data creates more workload. Dealing with this workload with new employees or more working hours is an expensive method. Therefore, document classification, which is an important task for text data, requires atomization. Deep learning, which has achieved significant success recently, offers an ideal solution. However, real-life application datasets often do not have balanced datasets. Data imbalance is ubiquitous in real-life applications. This problem leads to poor classification success.

In order to reduce the data imbalance problem, we proposed an algorithm that can better distribute the data to the batches. We analyzed our proposed method using a very large Turkish dataset containing 263168 documents with 15 classes. We conducted our experiments using an LSTM-based deep learning model. First, we trained the deep learning model and collected the experimental metrics without using the proposed method on the data set we collected. Then, we trained the same model using the dataset improved with our proposed distribution algorithm. We compared the metrics we gathered from both experiments. Our proposed solution yielded approximately 3.5% better accuracy than the experiment using a regular approach. It also shows an increase of more than 3 in the F1 score. Similar improvements are seen in other metrics. These results clearly demonstrate the importance of better data distribution to training batches in text classification. Our proposed algorithm, which mitigates the data imbalance problem, offers an important solution in this regard.

References

[1] Lai S, Xu L, Liu K, Zhao J. Recurrent convolutional neural networks for text classification. In: 29th AAAI conference on artificial intelligence, Austin, Texas USA, January 25–30, 2015 2015.

[2] Minaee S, Kalchbrenner N, Cambria E, Nikzad N, Chenaghlu M, Gao J. Deep Learning-based Text Classification: A Comprehensive Review. ACM Computing Surveys (CSUR), vol. 54, no. 3, pp. 1-40, 2021.

[3] Tufek A, Aktas M S. On the provenance extraction techniques from large scale log files: a case study for the numerical weather prediction models. In: European Conference on Parallel Processing, 2020: Springer, pp. 249-260.

[4] Tezgider M, Yildiz B, Aydin G. Text classification using improved bidirectional transformer. Concurrency and Computation: Practice and Experience, p. e6486.

[5] Soyalp G, Alar A, Ozkanli K, Yildiz B. Improving Text Classification with Transformer. In: 2021 6th International Conference on Computer Science and Engineering (UBMK), 2021; Ankara, Turkey, IEEE pp. 707-712.

[6] Mikolov T, Sutskever I, Chen K, Corrado G, Dean J. Distributed representations of words and phrases and their compositionality. In: 26th International Conference on Neural Information Processing Systems, 2013, Lake Tahoe, Nevada, pp. 3111-3119.

[7] Joulin A, Grave E, Bojanowski P, Mikolov T. Bag of Tricks for Efficient Text Classification. In: 15th Conference of the European Chapter of the Association for Computational Linguistics, April 2017, Valencia, Spain: Association for Computational Linguistics, in Proceedings of the 15th Conference of the European Chapter of the Association for Computational Linguistics: Volume 2, Short Papers, pp. 427-431.

[8] Pennington J, Socher R, Manning C. Glove: Global Vectors for Word Representation. In: The Conference on Empirical Methods in Natural Language Processing (EMNLP). October 2014 Doha, Qatar: Association for Computational Linguistics, pp. 1532-1543.

[9] Devlin J. Chang M W, Lee K, Toutanova K. BERT: pre-training of deep bidirectional transformers for language understanding. In: 2019 Conference of the North American Chapter of the Association for Computational Linguistics: Human Language Technologies, 2019, Minneapolis, MN, USA.

[10] Padurariu C, Breaban M E. Dealing with data imbalance in text classification. Procedia Computer Science, 2019, vol. 159, pp. 736-745.

[11] Kowsari K, Jafari Meimandi K, Heidarysafa M, Mendu S, Barnes L, Brown D. Text Classification Algorithms: A Survey. Information, 2019, vol. 10, no. 4, p. 150.

[12] Yildiz B, Tezgider M. Improving word embedding quality with innovative automated approaches to hyperparameters. Concurrency and Computation: Practice and Experience, 2021 p. e6091.

[13] Yildiz B, Tezgider M. Learning Quality Improved Word Embedding with Assessment of Hyperparameters. In European Conference on Parallel Processing, 2019: Springer, pp. 506-518.

[14] Li Y, Sun G, Zhu Y. Data imbalance problem in text classification. In: 2010 Third International Symposium on Information Processing, 2010: IEEE, pp. 301-305.

[15] Dixon L, Li J, Sorensen J, Thain N, Vasserman L. Measuring and mitigating unintended bias in text classification. In: Proceedings of the 2018 AAAI/ACM Conference on AI, Ethics, and Society, 2018, pp. 67-73.

[16] Shi K, Li L, Liu H, He J, Zhang N, Song W. An improved KNN text classification algorithm based on density. In: 2011 IEEE International Conference on Cloud Computing and Intelligence Systems, 2011: IEEE, pp. 113-117.

[17] Ogura H, Amano H, Kondo M. Comparison of metrics for feature selection in imbalanced text classification. Expert Systems with Applications, 2011, vol. 38, no. 5, pp. 4978-4989.

[18] Liu Y, Loh H T, Sun A. Imbalanced text classification: A term weighting approach. Expert systems with Applications, 2009, vol. 36, no. 1, pp. 690-701.

[19] Liu Y, Loh H T, Kamal Y T, Tor and S B. Handling of imbalanced data in text classification: Category-based term weights. In: Natural language processing and text mining: Springer, 2007, pp. 171-192.

[20] Thabtah F, Hammoud S, Kamalov F, Gonsalves A. Data imbalance in classification: Experimental evaluation. Information Sciences, 2020, vol. 513, pp. 429-441.

[21] Rehurek R, Sojka P. Software framework for topic modelling with large corpora. In: Proceedings of the LREC 2010 Workshop on New Challenges for NLP Frameworks, 2010: Citeseer.

[22] Mikolov T, Chen K, Corrado G, Dean J. Efficient estimation of word representations in vector space. arXiv preprint, 2013, arXiv:1301.3781.

[23] Olmezogullari E, Aktas M S. Pattern2Vec: Representation of clickstream data sequences for learning user navigational behavior. Concurrency and Computation: Practice and Experience, 2021, p. e6546.

[24] Hallac I R, Makinist S, Ay B, and Aydin G. user2vec: Social media user representation based on distributed document embeddings. In: 2019 International Artificial Intelligence and Data Processing Symposium (IDAP), 2019: IEEE, pp. 1-5.

Multiplicative Conformable Fractional Differential Equations

Sertaç GÖKTAŞ[1*]

[1] Department of Mathematics, Faculty of Science and Letters, Mersin University, Mersin, Turkey
[*1]srtcgoktas@gmail.com

Abstract: In this study, multiplicative conformable fractional differential equations are presented. Wronskian concept, linear dependence-independence concepts are defined on multiplicative conformable fractional calculus and some theorems and results are given among them. Finally, some examples are solved by giving some methods for finding general solutions of multiplicative conformable fractional differential equations.

Key words: Conformable fractional derivative, multiplicative conformable fractional derivative, non-Newtonian calculus, variation of parameters.

Çarpımsal Uyumlu Kesirli Diferansiyel Denklemler

Öz: Bu çalışmada, çarpımsal uyumlu kesirli diferansiyel denklemler sunulmuştur. Çarpımsal uyumlu kesirli analiz üzerinde Wronskian kavramı, lineer bağımlılık-bağımsızlık kavramları tanımlanarak bunlar arasında bazı teoremler ve sonuçlar verilmiştir. Son olarak, çarpımsal uyumlu kesirli diferansiyel denklemlerin genel çözümlerinin bulunması üzerine bazı metotlar verilerek bazı örnekler çözülmüştür.

Anahtar kelimeler: Uyumlu kesirli türev, çarpımsal uyumlu kesirli türev, non-Newtonian analiz, parametrelerin değişimi.

1. Introduction

In 1970's, non-Newtonian calculus with infinite sub-branches was firstly presented as an alternative to usual calculus in [1,2]. The sub-branches such as geometric, anageometric, bigeometric, quadratic and harmonic calculus, etc. can be given as examples. The geometric calculus, which is one of these, is also defined as multiplicative calculus by some authors [3-9]. In this calculus, changes of arguments and values of a function are measured by differences and ratios, respectively. On the other hand, they are measured by differences in the classical case.

Many events such as the levels of sound signals, the acidities of chemicals and the magnitudes of earthquakes change exponentially. For this reason, examining these problems in nature using multiplicative calculus offers great convenience and benefits. In the study of these physical properties, it would be more accurate to prefer the multiplicative differential equations. In numerous fields as biology, chaos theory, demography, earthquakes, engineering, economics, business and medicine [5,10-15], this calculus yields better outcomes than the classical case.

Fractional calculus, which is frequently encountered with various applications [16-20] in different fields of engineering and science, is defined as a generalization of classical calculus. We prefer the conformable fractional (CF) calculus in the present study. Because the other fractional derivatives used in the literature fail to satisfy some basic properties. Thus, it can be found basic properties and main results of CF calculus in [21,22]. Some applications of fractional derivatives are given in [23-27].

Multiplicative fractional calculus theory is a combination of both fractional calculus theory and multiplicative calculus theory. We refer to the paper [28] that encourages us and from which the main concepts of the multiplicative fractional calculus are set. Here, it has been defined conformable multiplicative fractional derivative and multiplicative fractional integral and has been studied some of their properties.

In [29-30], the constructs and methods on CF calculus guided us in the preparation of this study.

2. Preliminaries

In this section, some basic definitions and properties of CF calculus, the multiplicative calculus and the multiplicative CF calculus theories will be given.

---

[*] Corresponding author: srtcgoktas@gmail.com. ORCID Number of authors: [1] 0000-0001-7842-6309

Definition 2.1. [21,22] Consider the function $f:[a,\infty) \to \mathbb{R}$. Then, CF derivative and CF integral of f order $\alpha \in (0,1]$ are defined by:

$$T_\alpha^a f(x) := \lim_{h \to 0} \frac{f(x + h(x-a)^{1-\alpha}) - f(x)}{h},$$

$$I_\alpha^a f(x) := \int_a^x f(t) d_\alpha(t,a) = \int_a^x (t-a)^{\alpha-1} f(t) dt, \qquad \text{for } x > 0,$$

respectively. Here, the last integral to the right of this equality is the usual Riemann integral. Moreover, when $a = 0$, the CF derivative be written T_α and the CF integral be written I_α and $d_\alpha(t,a) = d_\alpha t$. In addition, if f is usual differentiable, then $T_\alpha f(x) = x^{1-\alpha} f'(x)$.

Definition 2.2. [28] Consider the function $f: \mathbb{R} \to \mathbb{R}^+$. Then, the forward multiplicative and the backward multiplicative derivative of f are defined by:

$$\frac{d^*}{dx^*} f(x) = f^*(x) := \lim_{h \to 0} \left(\frac{f(x+h)}{f(x)} \right)^{\frac{1}{h}},$$

$$\frac{d_*}{dx_*} f(x) = f_*(x) := \lim_{h \to 0} \left(\frac{f(x)}{f(x-h)} \right)^{\frac{1}{h}},$$

respectively. It can easily be shown that

$$f^{*(n)}(x) = f_*^{(n)}(x) = \exp\left(\frac{d^n}{dx^n} \ln f(x) \right).$$

Definition 2.3. [28] Consider the function $f: [a,b] \to \mathbb{R}^+$. Then, the forward or the backward multiplicative integrals of $f(x)$ are defined by:

$$\int_a^b f(x)^{dx} = \int_a^b f(x)_{dx} = \exp\left(\int_a^b \ln f(x) \, dx \right).$$

Definition 2.4. [28] Consider the function $f: [a,b] \to \mathbb{R}^+$. Then, the multiplicative CF derivative and the multiplicative CF integral of f order $\alpha \epsilon (0,1]$ are defined by:

$$^*T_\alpha^a f(x) := \lim_{h \to 0} \left(\frac{f(x + h(x-a)^{1-\alpha})}{f(x)} \right)^{\frac{1}{h}}.$$

$$(^*I_\alpha^a f)(x) := \int_a^x f(t)_{d_\alpha^*(t,a)} = \exp\left\{ \int_a^x \ln f(t) d_\alpha(t,a) \right\}$$

$$= \int_a^x f(t)_{dt}^{(t-a)^{\alpha-1}} = \exp\left\{ \int_a^x (t-a)^{\alpha-1} \ln f(t) dt \right\}, \qquad \text{for } x > 0$$

respectively. Hence, the last integral to the right of this equality is the usual Riemann integral.
When $a = 0$, the multiplicative CF derivative be written $^*T_\alpha$ and the multiplicative CF integral be written $^*I_\alpha$, and $d_\alpha^*(t,a) = d_\alpha^* t$.

Now, let $\alpha \epsilon (0,1]$ and $n \in \mathbb{Z}^+$. The sequential multiplicative CF derivatives of order n is defined by
$$^{*(n)}T_\alpha f(x) = \underbrace{^*T_\alpha \, ^*T_\alpha \cdots \, ^*T_\alpha}_{n-times} f(x).$$

Proposition 2.1. [28] Consider the function $f: [0,b] \to \mathbb{R}^+$ and $\alpha \epsilon (0,1]$. Then,

   i) $^*T_\alpha f(x) = \exp\{T_\alpha \ln f(x)\} = \exp\left\{ \frac{T_\alpha f(x)}{f(x)} \right\}$,

   ii) $(^*I_\alpha f)(x) = \exp\{I_\alpha \ln f(x)\}$.

Proposition 2.2. [28] Consider the function $f: [0,b] \to \mathbb{R}^+$ and $\alpha \epsilon (0,1]$. Then,
   i) $(^*T_\alpha \, ^*I_\alpha f)(x) = f(x)$,   for f is continuous,

ii) $({}^*I_\alpha \, {}^*T_\alpha f)(x) = \dfrac{f(x)}{f(a)}.$

Theorem 2.1. [31] Let $f, g : [0, b] \to \mathbb{R}^+$ be multiplicative CF differentiable of order $\alpha \epsilon (0,1]$ and h be CF differentiable $\alpha \epsilon (0,1]$ at x. Then,

i) $\tau(cf)(x) = \tau f(x),$

ii) $\tau(fg)(x) = \tau f(x)\tau g(x),$

iii) $\tau\left(\dfrac{f}{g}\right)(x) = \dfrac{\tau f(x)}{\tau g(x)},$

iv) $\tau(f^h)(x) = \{\tau f(x)\}^{h(x)} f(x)^{T_\alpha h(x)},$

v) $\tau(f \circ h)(x) = \left\{(\tau f)\big(h(x)\big)\right\}^{T_\alpha h(x) h(x)^{\alpha-1}},$

vi) $\tau(f + g)(x) = [\tau f(x)]^{\frac{f(x)}{f(x)+g(x)}} [\tau g(x)]^{\frac{g(x)}{f(x)+g(x)}},$

where c is a positive constant and $\tau y = {}^*T_\alpha y.$

Theorem 2.2. [31] Let $f, g : [0, b] \to \mathbb{R}^+$ be multiplicative CF integrable of order $\alpha \epsilon (0,1]$ at x. Then,

i) $\displaystyle\int_0^b [f(x)]^k_{d_\alpha^* x} = \left[\int_0^b f(x)_{d_\alpha^* x}\right]^k,$

ii) $\displaystyle\int_0^b [f(x)g(x)]_{d_\alpha^* x} = \int_0^b f(x)_{d_\alpha^* x} \int_0^b g(x)_{d_\alpha^* x},$

iii) $\displaystyle\int_0^b \left[\dfrac{f(x)}{g(x)}\right]_{d_\alpha^* x} = \dfrac{\int_0^b f(x)_{d_\alpha^* x}}{\int_0^b g(x)_{d_\alpha^* x}},$

iv) $\displaystyle\int_0^b f(x)_{d_\alpha^* x} = \int_0^c f(x)_{d_\alpha^* x} \int_c^b f(x)_{d_\alpha^* x},$

v) $\displaystyle\int_0^b [\tau f(x)]^{g(x)}_{d_\alpha^* x} = \dfrac{f(b)^{g(b)}}{f(0)^{g(0)}} \left\{\int_0^b f(x)^{T_\alpha g(x)}_{d_\alpha^* x}\right\}^{-1},$

where $k \in \mathbb{R}$ and $c \in [0, b]$ is a positive constant. The last formula is called $\alpha - {}^*$integration by parts.

3. Multiplicative Conformable Fractional Differential Equations

It is aimed to apply conformable fractional differential equations to multiplicative calculus with a method similar to the application of classical differential equations to multiplicative calculus such as in [10].

Definition 3.1. The multiplicative differential equation

$$(\tau^n y)^{a_0(x)}(\tau^{n-1}y)^{a_1(x)} \cdots (\tau y)^{a_{n-1}(x)} y^{a_n(x)} = b(x) \tag{3.1}$$

is defined as *multiplicative CF differential equation of n order*, where $b(x)$ is a positive valued function. Here,

$$\tau y = {}^*T_\alpha y, \quad \tau^2 y = {}^{*(2)}T_\alpha y = {}^*T_\alpha \, {}^*T_\alpha y, \quad \ldots \quad \tau^n y = {}^{*(n)}T_\alpha y = \underbrace{{}^*T_\alpha \, {}^*T_\alpha \ldots {}^*T_\alpha}_{n-times} y.$$

If the exponents $a_0(x) \neq 0$, $a_k(x)$, $k = \overline{1,n}$ are constants, Eq.(3.1) is called *linear multiplicative CF differential equation with constant exponents*; otherwise *linear multiplicative CF differential equation with variable exponents*. Moreover, if $b(x) = 1$, Eq.(3.1) is called *homogeneous multiplicative CF differential equation*, that is

$$(\tau^n y)^{a_0(x)}(\tau^{n-1}y)^{a_1(x)} \cdots (\tau y)^{a_{n-1}(x)} y^{a_n(x)} = 1, \tag{3.2}$$

otherwise *nonhomogeneous multiplicative CF differential equation*.

Theorem 3.1. Let $y_h(x)$ be the general solution of Eq.(3.2) and $y_p(x)$ be any particular solution of Eq.(3.1). Then, $y_h(x)y_p(x)$ is a general solution of Eq.(3.1).

Proof. Let $y(x)$ be a solution of Eq.(3.1). Since $y_p(x)$ be any solution of Eq.(3.1), it must be shown that $\frac{y(x)}{y_p(x)}$ is also the solution of Eq.(3.2) to complete the proof. Indeed, considering the properties on theorem 2.1 of the multiplicative CF derivative, we obtain

$$\left(\tau^n\left(\frac{y}{y_p}\right)\right)^{a_0(x)}\left(\tau^{n-1}\left(\frac{y}{y_p}\right)\right)^{a_1(x)}\cdots\left(\tau\left(\frac{y}{y_p}\right)\right)^{a_{n-1}(x)}y^{a_n(x)} =$$

$$= \frac{(\tau^n y)^{a_0(x)}(\tau^{n-1}y)^{a_1(x)}\cdots(\tau y)^{a_{n-1}(x)}y^{a_n(x)}}{(\tau^n y_p)^{a_0(x)}(\tau^{n-1}y_p)^{a_1(x)}\cdots(\tau y_p)^{a_{n-1}(x)}y_p^{a_n(x)}} = \frac{b(x)}{b(x)} = 1.$$

Hereby, $y_h(x)$ being the general solution of Eq.(3.2) causes $\frac{y(x)}{y_p(x)}$ to be the general solution of Eq.(3.2) too. Consequently, we reach $y(x) = y_h(x)y_p(x).$ □

Theorem 3.2. Let the functions $y_1(x)$, $y_2(x), \ldots, y_m(x)$ be any solutions of Eq.(3.2) on an interval I. Then, the function $y(x) = y_1^{c_1}(x)y_2^{c_2}(x)\ldots y_m^{c_m}(x)$ is also a solution of Eq.(3.2) for any real constants c_k, $k = \overline{1,m}$.

Proof. The theorem is easily proved if the properties on theorem 2.1 of the multiplicative CF derivative, we obtain are taken into account.□

Definition 3.2. Consider the positive functions $y_1(x)$, $y_2(x), \ldots, y_n(x)$ on an interval I. If c_k, $k = \overline{1,n}$ are scalars, then the *multiplicative linear combination* of the functions $y_1(x)$, $y_2(x), \ldots, y_n(x)$ is

$y_1^{c_1}(x)\, y_2^{c_2}(x)\ldots y_n^{c_n}(x).$

Definition 3.3. Consider the positive functions $y_1(x)$, $y_2(x), \ldots, y_n(x)$ on an interval I. If a sequence of the functions $y_1(x)$, $y_2(x), \ldots, y_n(x)$ is said to be *multiplicative linearly independent* if it is not *multiplicative linearly dependent*, that is, if the equation

$y_1^{c_1}(x)\, y_2^{c_2}(x)\ldots y_n^{c_n}(x) = 1, \quad \forall x \in I$ (3.3)

can only be satisfied by $c_k = 0$, $k = \overline{1,n}$.

Definition 3.4. Consider the positive functions $y_1(x)$, $y_2(x), \ldots, y_n(x)$ which are $(n-1)-$times multiplicative CF differentiable on an interval I. The determinant

$$^*W_\alpha(y_1, y_2, \ldots, y_n)(x) = \begin{vmatrix} y_1 & y_2 & \cdots & y_n \\ \tau y_1 & \tau y_2 & \cdots & \tau y_n \\ \vdots & \vdots & \ddots & \cdots \\ \tau^{n-1}y_1 & \tau^{n-1}y_2 & \cdots & \tau^{n-1}y_n \end{vmatrix}^*$$

is called *multiplicative CF Wronskian* ($\alpha -{}^*Wronskıanı$) of the functions $y_1(x)$, $y_2(x), \ldots, y_n(x)$, where $|\cdot|^*$ is multiplicative determinant and the abbreviation $^*W_\alpha(x)$ will be used instead of $^*W_\alpha(y_1, y_2, \ldots, y_n)(x)$ [32]. For example, when $n = 2$,

$$^*W_\alpha(y_1, y_2)(x) = \begin{vmatrix} y_1 & y_2 \\ \tau y_1 & \tau y_2 \end{vmatrix}^* = \frac{y_1^{\ln \tau y_2}}{y_2^{\ln \tau y_1}}$$ (3.4)

Theorem 3.3.($\alpha -{}^*$Abel Formula) Consider the continuous functions $a_k(x)$, $k = \overline{0,n}$ and $a_0(x) \neq 0$ on an interval I. If the positive functions $y_1(x)$, $y_2(x), \ldots, y_n(x)$ are multiplicative linearly independent solutions of Eq.(3.2) on an interval I, then the formula

$$^*W_\alpha(x) = \{^*W_\alpha(x_0)\}^{^*I_\alpha^{x_0}\left(e^{-\frac{a_1(x)}{a_0(x)}}\right)}$$

holds for $\forall x \in I$, where $^*I_\alpha^{x_0}(\cdot)$ will symbolize the multiplicative CF integral from definition 2.4..

Proof. For the sake of clarity, the proof in the case $n = 2$ will be given instead of the proof of the general case. Let y_1 and y_2 be the continuous functions on an interval I and be multiplicative linearly independent solutions of Eq.(3.2) for $\forall x \in I$. Then, we can write the following

$$(\tau^2 y_1) = (\tau y_1)^{-\frac{a_1(x)}{a_0(x)}} y_1^{-\frac{a_2(x)}{a_0(x)}} \qquad \text{and} \qquad (\tau^2 y_2) = (\tau y_2)^{-\frac{a_1(x)}{a_0(x)}} y_2^{-\frac{a_2(x)}{a_0(x)}}. \tag{3.5}$$

On the other hand, taking the multiplicative CF derivative of both sides of (3.4) with respect to x when $n = 2$, we obtain

$$\tau\left(^*W_\alpha(y_1, y_2)\right) = \tau\left(\frac{\{\tau y_2\}^{\ln y_1}}{\{\tau y_1\}^{\ln y_2}}\right) = \frac{\{\tau^2 y_2\}^{\ln y_1}}{\{\tau^2 y_1\}^{\ln y_2}}. \tag{3.6}$$

Substituting Eqs. (3.5) into (3.6) yields to

$$\tau\left(^*W_\alpha(y_1, y_2)\right)\{^*W_\alpha(y_1, y_2)\}^{\frac{a_1(x)}{a_0(x)}} = 1. \tag{3.7}$$

If the algebraic operations on the multiplicative calculus are taken into account in Eq.(3.7), this equation is written in the following form:

$$\tau\left(\ln ^*W_\alpha(y_1, y_2)\right) = e^{-\frac{a_1(x)}{a_0(x)}}.$$

Taking the multiplicative CF integral of both sides of the last equality with respect to x, the proof is completed.□

Corollary 3.1. Consider the continuous functions $a_k(x)$, $k = \overline{0, n}$ and $a_0(x) \neq 0$ on an interval I. If the positive function $y_1, y_2, \ldots, y_n$ are the solutions of Eq.(3.2) on an interval I, then for $\forall x \in I$ either $^*W_\alpha(y_1, y_2, \ldots, y_n)(x) = 1$ or $^*W_\alpha(y_1, y_2, \ldots, y_n)(x) \neq 1$ is provided.

Proof. From the $\alpha - ^*$Abel formula, for $\forall x \in I$, $^*I_\alpha^{x_0}\left(e^{-\frac{a_1(x)}{a_0(x)}}\right) \neq 0$ dir. If $^*W_\alpha(x_0) = 1$ is provided at a point $x_0 \in I$, then $^*W_\alpha(x) = 1$ is provided for $\forall x \in I$; if $^*W_\alpha(x_0) \neq 1$ is provided at a point $x_0 \in I$, then $^*W_\alpha(x) \neq 1$ is provided for $\forall x \in I$. This completes the proof. □

Theorem 3.4. Let the positive function $y_1, y_2, \ldots, y_n$ be the solutions of Eq.(3.2) on an interval I. The functions $y_1, y_2, \ldots, y_n$ are multiplicative linearly dependent solutions of Eq.(3.2) on an interval I if and only if $^*W_\alpha(y_1, y_2, \ldots, y_n)(x) = 1$.

Proof. For the sake of clarity, the proof in the case $n = 2$ will be given instead of the proof of the general case. Suppose that the functions y_1 and y_2 are multiplicative linearly dependent solutions of Eq.(3.2) on an interval I. Then, there is a constant C such that $y_2(x) = y_1^C(x)$. From the properties of multiplicative CF derivative, we get $\tau y_2(x) = \{\tau y_1(x)\}^C$. If the constant C is eliminated in this last equalities, the equality

$$\{\tau y_2(x)\}^{\ln y_1(x)}\{\tau y_1(x)\}^{-\ln y_2(x)} = 1 \tag{3.8}$$

is obtained, that is, $^*W_\alpha(y_1, y_2)(x) = 1$.

On the other hand, Let $^*W_\alpha(y_1, y_2)(x) = 1$, that is, let the equality (3.8) be provided. If $y_1(x) = 1$ on an interval I, then the function y_2 becomes multiplicative linearly dependent on y_1. Now, let's assume $y_1(x) \neq 1$ on a subinterval of the interval I. Then, taking the power $\{\ln y_1(x)\}^{-2}$ of both sides of the equality (3.8) gives

$\tau\left(\ln\{y_2(x)\}^{\{\ln y_1(x)\}^{-1}}\right) = 1$. From here and the properties of multiplicative CF derivative, we get $\ln\{y_2(x)\}^{\{\ln y_1(x)\}^{-1}} = C$ or $y_2(x) = y_1^C(x)$. This completes the proof. □

Theorem 3.5. Let the functions $y_1, y_2, \ldots, y_n$ be multiplicative linearly independent solutions of Eq.(3.2) on an interval I. Then, a $y(x)$ solution of Eq.(3.2) in the same interval, that is, the general solution, is in the form below:

$$y(x) = y_1^{c_1}(x)\, y_2^{c_2}(x) \ldots y_n^{c_n}(x). \tag{3.9}$$

Proof. Let the functions $y(x)$ be a solution of Eq.(3.2) on an interval I. Since the functions $y_1^{c_1}(x)\, y_2^{c_2}(x) \ldots y_n^{c_n}(x)$ ve $y(x)$ are solutions of Eq.(3.2) on an interval I, at some x_0 of the interval, the arbitrary constants c_k, $k = \overline{1,n}$ must to be found such that the following system is provided:

$$y_1^{c_1}(x_0)\, y_2^{c_2}(x_0) \ldots y_n^{c_n}(x_0) = y(x_0\,),$$
$$\tau y_1^{c_1}(x_0)\, \tau y_2^{c_2}(x_0) \ldots \tau y_n^{c_n}(x_0) = \tau y(x_0\,),$$
$$\vdots$$
$$\tau^{n-1} y_1^{c_1}(x_0)\, \tau^{n-1} y_2^{c_2}(x_0) \ldots \tau^{n-1} y_n^{c_n}(x_0) = \tau^{n-1} y(x_0\,).$$

In order for this system to be solvable according to the arbitrary constants, the coefficients matrix of this system must be ${}^{*}W_{\alpha}(y_1, y_2, \ldots, y_n)(x_0) \neq 1$. Consequently, from theorem 3.3, it is obtained that ${}^{*}W_{\alpha}(y_1, y_2, \ldots, y_n)(x) \neq 1$ for $\forall x \in I$. This completes the proof. □

4. Some Methods for General Solution of Multiplicative CF Differential Equations

In this section, for the sake of clarity, some methods for finding the general solution of the homogeneous multiplicative CF differential equation (3.2) for $n = 2$ will be given. When $n = 2$, let's rearrange Eq.(3.2) as follows:

$$(\tau^2 y)(\tau y)^{p(x)} y^{q(x)} = 1, \tag{4.1}$$

where $p(x) = \dfrac{a_1(x)}{a_0(x)}$, $q(x) = \dfrac{a_2(x)}{a_0(x)}$ and $a_0(x) \neq 0$

4.1. The Solution of Type $y_2(x) = \{y_1(x)\}^{\ln u(x)}$

For brevity's sake, let's use these abbreviations $y_1 = y_1(x)$, $y_2 = y_2(x)$ and $u = u(x)$. Suppose that the function $y_1 \neq 1$ which known and $y_2 = y_1^{\ln u}$ functions are solutions of Eq.(4.1), where $u(x)$ is an unknown positive function. Thus, the following system is obtained:

$$\tau y_2 = \{\tau y_1\}^{\ln u} y_1^{T_\alpha(\ln u)}$$

$$\tau^2 y_2 = \{\tau^2 y_1\}^{\ln u} \{\tau y_1\}^{2 T_\alpha(\ln u)} y_1^{{}^{(2)}T_\alpha(\ln u)}.$$

After these equalities are written in Eq.(4.1), considering that $y_1(x)$ is a solution to Eq.(4.1), we get

$$\left\{\{\tau y_1\}^2 y_1^{p(x)}\right\}^{T_\alpha(\ln u)} y_1^{{}^{(2)}T_\alpha(\ln u)} = 1$$

or

$$\frac{{}^{(2)}T_\alpha(\ln u)}{T_\alpha(\ln u)} = -2\frac{T_\alpha(\ln y_1)}{\ln y_1} - p(x).$$

CF integrating both sides of last equality, we get

$$T_\alpha(\ln u) = \ln^{-2} y_1\, e^{-I_\alpha p(x)} \qquad \Rightarrow \qquad u = e^{I_\alpha\left(\ln^{-2} y_1 e^{-I_\alpha p(x)}\right)}, \tag{4.2}$$

or

$$\tau u = e^{\ln^{-2} y_1\, {}^{*}I_\alpha e^{-p(x)}} \qquad \Rightarrow \qquad u = {}^{*}I_\alpha\left(e^{\ln^{-2} y_1\, {}^{*}I_\alpha e^{-p(x)}}\right), \tag{4.3}$$

where $I_\alpha \cdot$ is CF integral from definition 2.1 and ${}^{*}I_\alpha \cdot$ is multiplicative CF integral from definition 2.4. Consequently, the general solution of Eq.(4.1) is as follows

$$y(x) = y_1^{c_1}(x)\{y_1(x)\}^{c_2 \ln u(x)}, \tag{4.4}$$

where $u(x)$ is defined by (4.2) or (4.3).

Example 4.1. Consider the following multiplicative CF equation for which $y_1(x) = e^x$ has a known solution:

$$(\tau^2 y)(\tau y)^{\frac{1}{2\sqrt{x}}} y^{-\frac{1}{x}} = 1, \tag{4.5}$$

where $\tau y = {}^* T_{\frac{1}{2}} y$ and $\tau^2 y = {}^* T_{\frac{1}{2}} {}^* T_{\frac{1}{2}} y$.

Then considering the formula (4.2), we have $u(x) = e^{-\frac{x^{-2}}{2}}$. Consequently, from (4.4), the general solution of Eq.(4.5) is as follows:

$$y(x) = e^{c_1 x + c_2 x^{-1}}.$$

4.2. The Solution When the Coefficients are Constant

In Eq.(4.1), let $p(x)$ and $q(x)$ be constants. So let's look for the solutions of Eq.(4.1) in type $y(x) = e^{e^{k\left(\frac{1}{\alpha}x^\alpha\right)}}$. If the first and second multiplicative CF derivatives of this function are taken, it is obtained as follows, respectively:

$$\tau y(x) = e^{k e^{k\left(\frac{1}{\alpha}x^\alpha\right)}} \quad \text{and} \quad \tau^2 y(x) = e^{k^2 e^{k\left(\frac{1}{\alpha}x^\alpha\right)}}.$$

If these derivatives are substituted in (4.1), we have

$$e^{(k^2 + pk + q) e^{k\left(\frac{1}{\alpha}x^\alpha\right)}} = 1,$$

or

$$k^2 + pk + q = 0. \tag{4.6}$$

The following three cases exist for the roots k_1 and k_2 of Eq.(4.6).

i) If $k_1 \neq k_2 \in \mathbb{R}$, the general solution of Eq.(4.1) is as follows

$$y(x) = e^{c_1 e^{k_1\left(\frac{1}{\alpha}x^\alpha\right)} + c_2 e^{k_2\left(\frac{1}{\alpha}x^\alpha\right)}} \quad \text{or} \quad y(x) = a^{e^{k_1\left(\frac{1}{\alpha}x^\alpha\right)}} b^{e^{k_2\left(\frac{1}{\alpha}x^\alpha\right)}} \qquad (a = e^{c_1}, \ b = e^{c_2}). \tag{4.7}$$

ii) If $k_1 = k_2 \in \mathbb{R}$, the general solution of Eq.(4.1) is as follows

$$y(x) = e^{\left(c_1 + c_2\left(\frac{1}{\alpha}x^\alpha\right)\right) e^{k_1\left(\frac{1}{\alpha}x^\alpha\right)}} \quad \text{or} \quad y(x) = a^{e^{k_1\left(\frac{1}{\alpha}x^\alpha\right)}} b^{\left(\frac{1}{\alpha}x^\alpha\right) e^{k_1\left(\frac{1}{\alpha}x^\alpha\right)}} \qquad (a = e^{c_1}, \ b = e^{c_2}). \tag{4.8}$$

iii) If $k_1 = \sigma - i\tau$, $k_2 = \sigma + i\tau$ the general solution of Eq.(4.1) is as follows

$$y(x) = e^{e^{\sigma\left(\frac{1}{\alpha}x^\alpha\right)}\left(c_1 \cos \tau\left(\frac{1}{\alpha}x^\alpha\right) + c_2 \sin \tau\left(\frac{1}{\alpha}x^\alpha\right)\right)}. \tag{4.9}$$

Example 4.2. Consider the following multiplicative CF equation

$$(\tau^2 y)(\tau y) y^{-3} = 1. \tag{4.10}$$

Then, from (4.7), the general solution of Eq.(4.10) is as follows:

$$y(x) = e^{c_1 e^{\left(\frac{1}{\alpha}x^\alpha\right)} + c_2 e^{-2\left(\frac{1}{\alpha}x^\alpha\right)}} \quad \text{or} \quad y(x) = a^{e^{\left(\frac{1}{\alpha}x^\alpha\right)}} b^{e^{-2\left(\frac{1}{\alpha}x^\alpha\right)}} \qquad (a = e^{c_1}, \ b = e^{c_2}).$$

Example 4.3. Consider the following multiplicative CF equation

$$(\tau^2 y)(\tau y)^{-2} y^2 = 1. \tag{4.11}$$

Then, from (4.9), the general solution of Eq.(4.11) is as follows:

$$y(x) = e^{e^{\left(\frac{1}{\alpha}x^\alpha\right)}\left(c_1 \cos 2\left(\frac{1}{\alpha}x^\alpha\right) + c_2 \sin 2\left(\frac{1}{\alpha}x^\alpha\right)\right)}.$$

4.3. Variation of Parameters

Suppose that $y_1 = y_1(x)$ and $y_2 = y_2(x)$ be two multiplicative linearly independent solutions for Eq.(4.1). The aim is to find the particular solution $y_p = y_p(x)$ for

$$(\tau^2 y)(\tau y)^{p(x)} y^{q(x)} = b(x). \tag{4.12}$$

Let

$$y_p = y_1^{c_1} y_2^{c_2}, \tag{4.13}$$

where the functions $c_1 = c_1(x)$ and $c_2 = c_2(x)$ are two unknown functions.
By taking the multiplicative CF derivative of Eq.(4.13) with respect to x, we get

$$\tau y_p = (\tau y_1)^{c_1} y_1^{T_\alpha c_1} (\tau y_2)^{c_2} y_2^{T_\alpha c_2}. \tag{4.14}$$

If the equality

$$y_1^{T_\alpha c_1} y_2^{T_\alpha c_2} = 1 \tag{4.15}$$

is assumed in Eq.(4.14), we get

$$\tau y_p = (\tau y_1)^{c_1} (\tau y_2)^{c_2}. \tag{4.16}$$

Later, taking the multiplicative CF derivative of Eq.(4.16) with respect to x, we obtain

$$\tau^2 y_p = (\tau^2 y_1)^{c_1} (\tau y_1)^{T_\alpha c_1} (\tau^2 y_2)^{c_2} (\tau y_2)^{T_\alpha c_2}. \tag{4.17}$$

Considering that the functions y_1 and y_2 are the solution of Eq.(4.1), substituting Eqs.(4.13), (4.14), and (4.17) into (4.12) yields to

$$(\tau y_1)^{T_\alpha c_1} (\tau y_2)^{T_\alpha c_2} = b(x). \tag{4.18}$$

Now, solving the system of the Eqs.(4.15) and (4.18), we get

$$T_\alpha c_1 = \frac{-\ln b(x) \ln y_2(x)}{\ln({}^*W_\alpha(y_1, y_2)(x))} \qquad \text{and} \qquad T_\alpha c_2 = \frac{\ln b(x) \ln y_1(x)}{\ln({}^*W_\alpha(y_1, y_2)(x))},$$

or

$$c_1 = I_\alpha\left(\frac{-\ln b(x) \ln y_2(x)}{\ln({}^*W_\alpha(y_1, y_2)(x))}\right) \qquad \text{and} \qquad c_2 = I_\alpha\left(\frac{\ln b(x) \ln y_1(x)}{\ln({}^*W_\alpha(y_1, y_2)(x))}\right).$$

Consequently, the particular solution is as follows:

$$y_p = y_1^{I_\alpha\left(\frac{-\ln b(x) \ln y_2(x)}{\ln({}^*W_\alpha(y_1,y_2)(x))}\right)} y_2^{I_\alpha\left(\frac{\ln b(x) \ln y_1(x)}{\ln({}^*W_\alpha(y_1,y_2)(x))}\right)}. \tag{4.19}$$

Corollary 4.1. Let the functions $y_1, y_2, \dots, y_n$ be multiplicative linearly independent solutions of Eq.(3.2) on an interval I. If the above method is applied for these functions, it can be easily shown that

$$c_n = I_\alpha\left(\frac{\ln\left({}^*_n W_\alpha(y_1, y_2, \dots, y_n)(x)\right)}{\ln({}^*W_\alpha(y_1, y_2, \dots, y_n)(x))}\right),$$

where ${}^*_n W_\alpha(y_1, y_2, \dots, y_n)(x)$ is the determinant obtained by replacing the nth column on ${}^*W_\alpha(y_1, y_2, \dots, y_n)(x)$ by the column $[0\ 0\ \cdots 0\ \ln b(x)]_{1 \times n}$. Consequently, the particular solution is as follows:

$$y_p = \prod_{k=1}^n y_k^{I_\alpha\left(\frac{\ln\left({}^*_k W_\alpha(y_1,y_2,\dots,y_n)(x)\right)}{\ln({}^*W_\alpha(y_1,y_2,\dots,y_n)(x))}\right)}.$$

Example 4.4. Consider the following multiplicative CF equation

$$(\tau^2 y)(\tau y)^6 y^9 = e^{e^{-6\sqrt{x}}}, \tag{4.20}$$

where $\tau y = {}^*T_{\frac{1}{2}} y$ and $\tau^2 y = {}^*T_{\frac{1}{2}} {}^*T_{\frac{1}{2}} y$.
Then, from (4.8), the homogeneous solution of Eq.(4.20) is as follows:

$$y_h(x) = e^{\left(c_1 + c_2(2\sqrt{x})\right)e^{-6\sqrt{x}}}.$$

Namely, $y_1(x) = e^{e^{-6\sqrt{x}}}$ and $y_2(x) = e^{2\sqrt{x} e^{-6\sqrt{x}}}$. Therefore,

$$c_1 = I_\alpha\left(-2\sqrt{x}\right) = -2x \qquad \text{and} \qquad c_2 = I_\alpha(1) = 2\sqrt{x}$$

holds and from (4.19),

$$y_p = \left(e^{e^{-6\sqrt{x}}}\right)^{-2x}\left(e^{2\sqrt{x}e^{-6\sqrt{x}}}\right)^{2\sqrt{x}} = e^{2xe^{-6\sqrt{x}}}. \qquad (4.21)$$

is a particular solution of Eq.(4.21). Consequently, from Theorem 3.1 with (4.21) , the general solution of Eq.(4.20) is as follows:

$$y(x) = y_h(x)y_p(x) = e^{\left(c_1+c_2(2\sqrt{x})\right)e^{-6\sqrt{x}}}e^{2xe^{-6\sqrt{x}}} = e^{\left(c_1+c_2(2\sqrt{x})\right)e^{-6\sqrt{x}}+2xe^{-6\sqrt{x}}}.$$

5. Conclusion

In multiplicative conformable fractional calculus which brings together multiplicative calculus and conformable fractional calculus, the concept of differential equations is presented. The basic definitions, properties, and results of this concept are given. Some solution methods of this equation are explained. A few examples have been solved for clarity.

References

[1]   Grossman M. An introduction to non-Newtonian calculus. Int J Math Educ Sci Technol 1979; 10(4): 525–528.
[2]   Grossman M, Katz R. Non-Newtonian calculus, Pigeon Cove, MA: Lee Press, 1972.
[3]   Bashirov AE, Kurpınar EM, Özyapıcı A. Multiplicative calculus and its applications. J Math Anal Appl 2008; 337(1): 36-48.
[4]   Stanley D. A multiplicative calculus. Primus 1999; IX (4): 310-326.
[5]   Bashirov AE, Misirli E, Tandoğdu Y, Özyapıcı, A. On modeling with multiplicative differential equations. Appl Math J Chinese Univ Ser A 2011; 26(4): 425-438.
[6]   Bashirov AE, Riza M. On complex multiplicative differentiation. TWMS J of Apl & Eng Math 2011; 1(1): 75-85.
[7]   Gurefe Y, Kadak U, Misirli E, Kurdi A. A new look at the classical sequence spaces by using multiplicative calculus. UPB Sci Bul Ser A. 2016; 78(2): 9-20.
[8]   Kadak U, Gurefe Y. A generalization on weighted means and convex functions with respect to the Non-Newtonian calculus. Int J Anal 2016; 5416751: 1-10.
[9]   Uzer A. Multiplicative type complex calculus as an alternative to the classical calculus. Comput Math Appl 2010; 60(10): 2725-2737.
[10] Yalcin N, Celik E. Solution of multiplicative homogeneous linear differential equations with constant exponentials. New Trend Math Sci 2018; 6(2): 58–67.
[11] Yalcin N, Dedeturk M. Solutions of multiplicative ordinary differential equations via the multiplicative differential transform method. AIMS Mathematics 2021; 6(4): 3393-3409.
[12] Yilmaz E. Multiplicative Bessel equation and its spectral properties, Ric. Mat. 2021; 1-17. https://doi.org/10.1007/s11587-021-00674-1.
[13] Bashirov AE, Bashirova G. Dynamics of literary texts and diffusion. OJCMT 2011; 1(3): 60-82.
[14] Filip D, Piatecki C, A non-newtonian examination of the theory of exogenous economic growth. Math. AEterna 2014; 4(2): 101–117.
[15] Florack L, Assen Hv. Multiplicative calculus in biomedical image analysis. J Math Imaging Vis 2012; 42(1): 64–75.
[16] Baleanu D, Guvenc ZB, Machado JAT. New Trends in Nanotechnology and Fractional Calculus Applications. New York (NY): Springer; 2010.
[17] Kilbas AA, Srivastava HM, Trujillo JJ. Theory and Applications of Fractional Differential Equations (Vol. 204) Elsevier, 2006.
[18] Miller KS, An Introduction to Fractional Calculus and Fractional Differential Equations. New York (NY): J Wiley and Sons; 1993.
[19] Oldham KB, Spanier J. The Fractional Calculus. New York (NY): Academic Press; 1974.
[20] Podlubny I. Fractional Differential Equations, New York: Academic Press; 1999.
[21] Abdeljawad T. On conformable fractional calculus. J Comput Appl Math 2015; 279: 57-66.
[22] Khalil R, Al Horani M, Yousef A, Sababheh M. A new definition of fractional derivative. J Comput Appl Math 2014; 264: 65–70.
[23] Atangana A, Baleanu D, Alsaedi A. New properties of conformable derivative. Open Math 2015; 13(1): 889-898.
[24] Benkhettou N, da Cruz AMB, Torres DFM, A fractional calculus on arbitrary time scales: fractional differentiation and fractional integration. Signal Processing 2015, 107: 230–237.
[25] Miller KS. An Introduction to Fractional Calculus and Fractional Differential Equations. NewYork (NY): J Wiley and Sons; 1993.
[26] Gulsen T, Yilmaz E, Goktas S. Conformable fractional Dirac system on time scales. J Inequal Appl 2017; 2017(1): 1-10.

[27] Gulsen T, Yilmaz E, Kemaloglu H. Conformable fractional Sturm-Liouville equation and some existence results on time scales. Turk J Math 2018; 42(3): 1348- 1360.

[28] Abdeljawad T, Grossman M. On geometric fractional calculus. J. Semigroup Theory Appl. 2016; 2016(2): 1-14.

[29] Ilie M, Biazar J, Ayati Z. General solution of second order fractional differential equations. Int J Appl Math Research 2018; 7(2): 56-61.

[30] Al Horani M, Hammad MA, Khalil R. Variation of parameters for local fractional nonhomogenous linear differential equations. J. Math. Computer Sci 2016;16: 147-153.

[31] Goktas S, Kemaloglu H, Yilmaz E. Multiplicative conformable fractional Dirac system. Turk J Math 2022; doi:10.3906/mat-2112-55.

[32] Gurefe Y. Multiplicative differential equations and its applications. Ph.D. Thesis, 2013; Ege University, pp.91.

Production and Characterization of Al/NiO:ZnO/p-Si/Al Composite Photodiodes for Solar Energy Tracking Systems

Ezgi GÜRGENÇ[1*], Aydın DİKİCİ[2], Fehmi ASLAN[3]

[1] Energy Systems Engineering, Faculty of Technology, Firat University, Elazig, Turkey
[2] Energy Systems Engineering, Faculty of Technology, Firat University, Elazig, Turkey
[3] Rail Systems Machinery Technology, Yeşilyurt Vocational School, Turgut Özal University, Malatya, Turkey
[*1] ezgigurgenc89@gmail.com, [2] adikici1@firat.edu.tr, [3] faslan558@gmail.com

Abstract: In present study, NiO:ZnO thin films in molar ratios of 1:0, 0:1, 3:1, 1:1 and 1:3 were formed on p-Si layers with Aluminium (Al) bottom contact. The dynamic sol-gel spin coating method was used as coating method. The Al top contacts were deposited on thin films and Al/NiO:ZnO/p-Si/Al photodiodes were fabricated. The structural and morphological properties of the photodiodes were determined by X-ray diffraction (XRD), emission scanning electron microscopy (FE-SEM), and energy dispersive X-ray spectroscopy (EDX). The photoresponse and electrical properties of the produced photodiodes were investigated by current–voltage (I–V) and capacitance-voltage (C-V) measurements. The Al/NiO:ZnO/p-Si/Al photodiodes were successfully fabricated. It was determined that the thin films were composed of nanostructures. All photodiodes are sensitive to light. It was seen that the photosensitivity of composite photodiodes was higher than the pure photodiodes and photosensitivity decreased as the ZnO ratio increased. It was determined that the most sensitive photodiode to light was the composite photodiode with a NiO:ZnO ratio of 3:1, and the highest photosensitivity was measured as 3.12 x 10^3 at 100 mW/cm^2 light intensity in this photodiode. In all photodiodes, the capacitance values decreased as the frequency increased. The results show that by changing the NiO:ZnO ratio, the photoresponse and electrical parameters of the photodiodes can be controlled and the produced photodiodes can be used as a photosensor in solar tracking systems and optoelectronic applications.

Key words: Semiconductor metal oxide, Sol-gel, Composite photodiode, Nanomaterial, Solar irradiation.

Güneş Enerjisi Takip Sistemleri için Al/NiO:ZnO/p-Si/Al Kompozit Fotodiyotların Üretimi ve Karakterizasyonu

Öz: Mevcut çalışmada, 1:0, 0:1, 3:1, 1:1 ve 1:3 molar oranlarında NiO:ZnO ince filmler Alüminyum (Al) alt kontaklı p-Si tabakalar üzerinde oluşturuldu. Kaplama yöntemi olarak dinamik döndürerek kaplama metodu kullanıldı. Al üst kontaklar ince filmler üzerinde biriktirildi ve Al/NiO:ZnO/p-Si/Al fotodiyotlar üretilmiş oldu. Fotodiyotların yapısal ve morfolojik özellikleri X-ışını kırınımı (XRD), emisyon taramalı elektron mikroskobu (FE-SEM) ve enerji dağıtıcı X-ışını spektroskopisi (EDX) ile belirlendi. Üretilen fotodiyotların fototepki ve elektriksel özellikleri akım–voltaj (I–V) ve kapasite-gerilim (C-V) ölçümleri ile araştırıldı. Al/NiO:ZnO/p-Si/Al fotodiyotlar başarılı bir şekilde üretildi. İnce filmlerin nanoyapılardan meydana geldiği tespit edildi. Tüm fotodiyotlar ışığa karşı duyarlıdır. Kompozit fotodiyotların ışığa karşı duyarlılıklarının saf fotodiyotlara göre daha yüksek olduğu ve ZnO oranı arttıkça azaldığı belirlendi. Işığa karşı en duyarlı olan fotodiyotun NiO:ZnO oranı 3:1 olan kompozit fotodiyot olduğu tespit edildi ve en yüksek fotosensitivite bu fotodiyotta 100 mW/cm^2 ışık şiddetinde 3.12 x 10^3 olarak ölçüldü. Tüm fotodiyotlarda frekans arttıkça kapasite değerleri düşmüştür. Sonuçlar, NiO:ZnO oranının değiştirilerek fotodiyotların fototepki ve elektriksel parametrelerinin kontrol edilebileceğini ve üretilen fotodiyotların güneş takip sistemlerinde ve optoelektronik uygulamalarda fotosensör olarak kullanılabileceğini göstermektedir

Anahtar kelimeler: Yarı iletken metal oksit, Sol-jel, Kompozit fotodiyot, Nanomalzeme, Güneş ışınımı.

1. Introduction

In recent years, advanced and functional materials are needed in photovoltaic applications [1]. Solar tracking systems are one of the most important systems used in recent years to increase the gathering efficiency of solar energy [2, 3]. In these systems, photodiodes are generally preferred sensors for direct detection of light [4, 5]. The researches on metal oxide semiconductors are increasing day by day in many fields. This is because metal oxide semiconductors such as ZnO, TiO$_2$, SnO$_2$, NiO and CdO have unique physical and chemical properties. Therefore,

---

[*] Corresponding author: ezgigurgenc89@gmail.com. ORCID Number of authors: [1] 0000-0002-0653-4041, [2] 0000-0003-4892-2277, [3] 0000-0002-5304-0503

these oxides have become very interesting materials in electronic and optoelectronic applications [6-8]. Among these metal oxide semiconductors, ZnO (n-type) is very interesting because of its properties such as, has a direct and wide (~3.3 eV) energy band gap, can be directed optical and electrical properties by doping, high exciton binding energy, relatively low toxicity and relatively low processing temperature. Due to these properties, it finds use in many electrical and optoelectronic applications [9, 10]. NiO is another promising p-type metal oxide semiconductor in electronic and optoelectronic devices due to its excellent optoelectronic properties, wide band gap (3.6-4.0 eV), low cost, high chemical and thermal stability [11-14]. The properties of photodiodes can be modified and improved by doping with a different element. One of the methods used to change and improve the properties of photodiodes is to obtain a new composite structure by mixing various semiconductor metal oxides in different ratios, in addition to doping [15-18]. The devices consisting of (p-n) NiO:ZnO heterojunction thin films are one of the promising alternatives for optoelectronic and photovoltaic applications [19].

ZnO and NiO thin films can be produced by methods such as (Direct Current) DC and RF (Radio frequency) sputtering, sol–gel, chemical vapour deposition (CVD), pulsed laser deposition and spray pyrolysis [20]. Among these methods, the sol-gel spin coating method has advantages such as allowing a large area to be coating, simplicity of the process, controllable thickness, low temperature and low cost [12, 19, 20].

Park et al., have performed gradual ZnO and NiO composite coatings on ITO glass using the sol-gel spin coating method. They performed the structural characterization of the thin films they produced and investigated the photodiode properties [19]. Again, Tyagi et al., first coated ZnO thin film with RF magnetron sputtering technique on ITO glass, and then formed a composite structure by coating NiO on ZnO with the same method. They investigated the structural, electrical and photoresponse properties of the photodiode they produced [21]. Demirezen et al., obtained ZnO:NiO thin film on the p-Si layer by spin coating method by mixing 2%, 10% and 20% NiO with ZnO and PCBM was coated on this layer. Thus, composite Al/(PCBM/NiO ZnO)/p-Si photodiodes were produced. They investigated the electrical and photo-sensing properties of the photodiodes they produced [22]. As seen in the literature, there is not much work on the coating of NiO:ZnO on p-Si by dynamic spin coating method and investigating its electrical and photoresponse properties. Therefore, in this study, NiO:ZnO/p-Si composite photodiodes were produced to obtain photodiodes with different properties and their photodiode properties were investigated.

In this study, NiO:ZnO/p-Si composite photodiodes were fabricated by dynamic sol-gel spin coating. The structural and morphological properties of the thin films coatings were characterized by XRD, FE-SEM and EDX. The photoresponse and electrical properties were investigated by I-V and C-V analyses.

2. Experimental Details

In this study, NiO:ZnO thin films were formed on p-Si layers by dynamic sol-gel spin coating method. The $\langle 100 \rangle$ orientation, 600 µm thickness and 1-10 cm-Ω resistance p-Si layers were first cleaned in acetone in an ultrasonic bath for 5 minutes. After this process, it was rinsed in an ultrasonic bath in deionized water at the same amount of time. The same procedures were repeated with ethanol and distilled water, and finally, p-Si plates were immersed in HF:H_2O solution mixed at a ratio of 1:10 for 30 seconds and then rinsed in deionized water in an ultrasonic bath for 5 minutes. The opaque sides of the plates dried with nitrogen gas were coated with 150 nm thick Al (99.99% purity) by Nanovak brand vacuum thermal evaporation device. Then, the plates were annealed under nitrogen gas in an oven at 570 °C for 5 minutes. To produce pure NiO thin films, 0.5 M Carlo Erba brand Nickel (II) acetate tetrahydrate (Ni($OCOCH_3$)$_2$ · $4H_2O$) was poured into 10 ml of Chemsolute brand 2-methoxyethanol ($CH_3OCH_2CH_2OH$) and mixed with a magnetic stirrer. After all the powders were dissolved, Chemsolute brand monoethanolamine ($NH_2CH_2CH_2OH$) was added to this mixture in the same molar ratio while the mixing process was continuing, and the sol-gel was obtained by mixing together at 80 °C for 2 h. After resting for one day, this sol-gel was coated on p-Si plates cut into certain sizes at 3000 rpm for 30 seconds. The coating process was performed on the FYTRONIX spin coating device in dynamic mode. The coated samples were dried at 150 °C for 10 minutes, and after this process, they were allowed to cool at room temperature for 10 minutes. By repeating the same processes, one more layer of coating was formed. The produced thin films were annealed at 450 °C for 1 h. The coated surfaces were covered with 99.99% pure Al using a Nanovak brand vacuum thermal evaporator with a physical mask, and thus top contacts were obtained on thin films. The same procedures were repeated to produce pure ZnO photodiodes, with the only difference being that Sigma Aldrich brand Zinc acetate dihydrate (Zn(CH_3COO)$_2$ · $2H_2O$) was used instead of Ni($OCOCH_3$)$_2$ · $4H_2O$. In composite NiO:ZnO photodiodes, on the other hand, Ni($OCOCH_3$)$_2$ · $4H_2O$/ (CH_3COO)$_2$Zn · $2H_2O$ was used in molar ratios of 3:1, 1:1 and 1:3 with a total of 0.5 M. XRD analyses of thin films were performed in PANalytical Empyrean brand XRD device at 45

kV/40 mA, CuKα (λ = 1.5406 ˚A) radiation and 2θ = 20 - 80°. Surface properties and compositions of thin films were determined with Zeiss Crossbeam 540 brand FE-SEM device and EDX. The photoresponse and electrical characterizations were performed using KEITHLEY 4200 semiconductor analysis system and FYTRONIX brand solar simulator.

3. Results and Discussion

3.1. Structural and Morphological Properties of NiO:ZnO/p-Si Thin Films

The XRD analysis results of the produced NiO:ZnO thin films are shown in Figure 1. As can be seen, intense peaks occurred at 37.26°, 43.30°, 62.92°, 75.48° and 79.44° 2θ degrees in pure NiO. These peaks are consistent with JCPDS card no. 47–1049 [23-25] and correspond to planes (111), (200), (220), (311) and (222), respectively. The peaks in (100), (002), (101), (102), (110), (103), (200), (112), (201), (004) and (202) planes in pure ZnO observed at 31.85°, 34.50°, 36.32°, 47.63°, 56.67°, 62.94°, 66.46°, 68.01°, 69.14°, 72.63° and 77.07° 2θ degrees, respectively. The peaks are in agreement with the JCPDS card no. 36-1451 and literature studies and show that the produced ZnO films are in hexagonal wurtzite structure [26-29]. The (111) and (200) planes seen in high density in pure NiO are attributed to the crystalline nature of NiO [23-25] and different peaks in pure ZnO indicate that ZnO is polycrystalline [30]. On the other hand, characteristic peaks of both oxides were found in composite thin films. Although the intensities and positions of the peaks change, they are in agreement with the XRD patterns of pure NiO and pure ZnO. The intensities of characteristic peaks of NiO and ZnO increased as their ratio in the composite increased. No impurities or peaks of a different phase were found in pure and composite thin films. This indicates that the NiO:ZnO films were successfully formed and high purity.
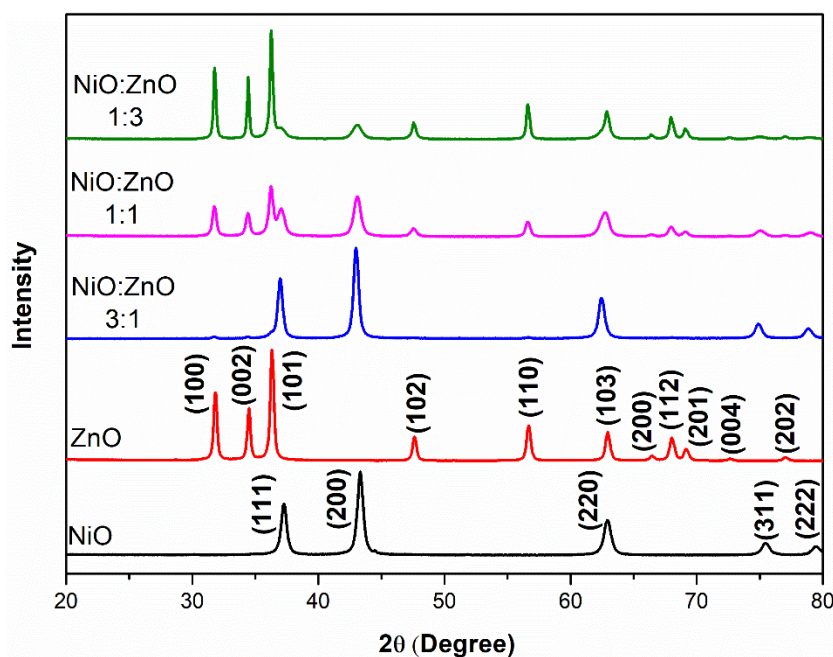
Figure 1. The XRD patterns of NiO:ZnO thin films.

Figure 2 shows FE-SEM images and EDX analysis results of NiO:ZnO thin films. All thin films were successfully coated on p-Si in a crack-free and homogeneously. Thin films are composed of nanostructures. These structures are in the form of aggregated fine-grained nanoparticles in NiO. In ZnO, on the other hand, it is composed of fiber-like structures in addition to the same structures [31]. The composite thin films are composed of aggregated fine-grained nanoparticles that are somewhat larger than pure NiO and ZnO. When the EDX analysis results were examined, it was seen that they were in agreement with the XRD analysis results and the doping ratio.

These results show that NiO:ZnO thin films were successfully formed on p-Si by dynamic sol-gel spin coating method.
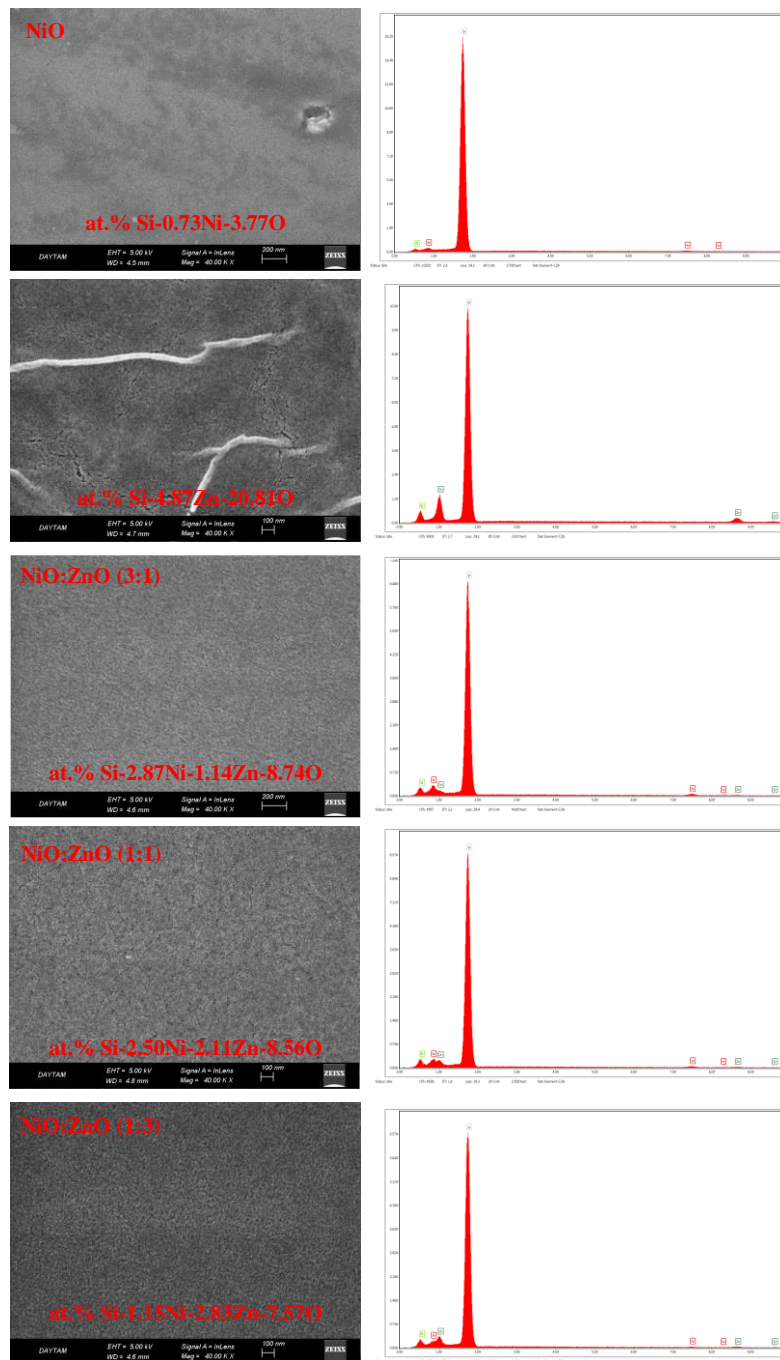
Figure 2. The FE-SEM images and EDX analysis results of NiO:ZnO thin films.

3.2. I-V Characteristics of Prepared Photodiodes

The I-V characteristics of the produced NiO:ZnO/p-Si photodiodes in the dark and at light intensities varying between 20 and 100 mW/cm^2 are shown in Figure 3. All samples showed rectifying properties. Except for the photodiode with a NiO:ZnO ratio of 3:1, it was observed that the current in the forward region was not affected

much by the light intensity in other photodiodes. In this sample, on the other hand, variations in current values were observed in the range of approximately 2.5-3.5 V. In the reverse region, the current was affected by the light intensity and as the light intensity increased, the current increased. This shows that the produced devices exhibit photodiode behaviour and it is thought that this is due to the spread of the electron-hole pair over a wider area in the reverse bias region [17, 27]. The results indicate that photodiodes exhibit photoconductive behaviour and the photoconductive behaviour can be controlled by changing the NiO:ZnO ratio. The photosensitivity values of the photodiodes were found at -5V using the Equation 1 given below [5].

$$PS = \frac{I_{ph} - I_{dark}}{I_{dark}} \tag{1}$$

In this equation, I_{ph} represents the photocurrent and I_{dark} represents the current in the dark. The photosensitivity values of the produced photodiodes are shown in Figure 4. The photosensitivity of photodiodes under illumination was higher than in the dark state and increased with increasing illumination intensity. The composite photodiodes are more sensitive to light than pure ones and decrease as the ZnO ratio increased. The photodiode with the highest sensitivity to light is the NiO:ZnO ratio of 3:1 and the highest photosensitivity is 3.12×10^3 at 100 mW/cm^2 light intensity in this device. The results show that photoresponse can be controlled by changing the NiO:ZnO ratio and the produced photodiodes can be used as photodiodes in solar tracking systems [1]. The photoresponsivity (P_R) of the produced photodiodes was determined using Equation 2 given below [12].

$$P_R = \frac{I_{ph} - I_{dark}}{PA} \tag{2}$$

where P is the light intensity and A is the surface area of the photodiode. The P_R values of the devices under 100 mW/cm^2 light intensity are 4.83×10^{-4} A/W, 1.49×10^{-3} A/W, 2.46×10^{-4} A/W, 1.54×10^{-4} A/W and 2.12×10^{-4} A/W for 1:0, 0:1, 3:1, 1:1 and 1:3 respectively according to the NiO:ZnO ratio. All photodiodes are sensitive to light. The P_R values of photodiodes can be varied by changing the NiO:ZnO ratio.

The I-t characterizations of photodiodes have an important place in understanding their photoconductive behaviour. The I-t graphs of the produced NiO:ZnO/p-Si photodiodes at light intensities varying between 20 and 100 mW/cm^2 and at -5V are shown in Figure 5. As can be seen, the photocurrents increased as the light intensity increased. This proves that the photodiodes show photoconductive behaviour [27, 32]. When the devices were illuminated, the photocurrent suddenly increased to a certain level and fell back to its previous level after the lighting was turned off. When the illumination is first turned on, there is an increase in free charge carriers and in this case photogenerated electrons contribute to the photocurrent. When the illumination is turned off, the charge carriers are trapped in the lower levels, thus reducing the photocurrent [17, 27, 32]. The highest photoconductivity value was obtained in pure ZnO photodiode and the photoconductivity of composite photodiodes is lower. The results show that the photoconductivity properties of the photodiodes can be controlled by the NiO:ZnO ratio.
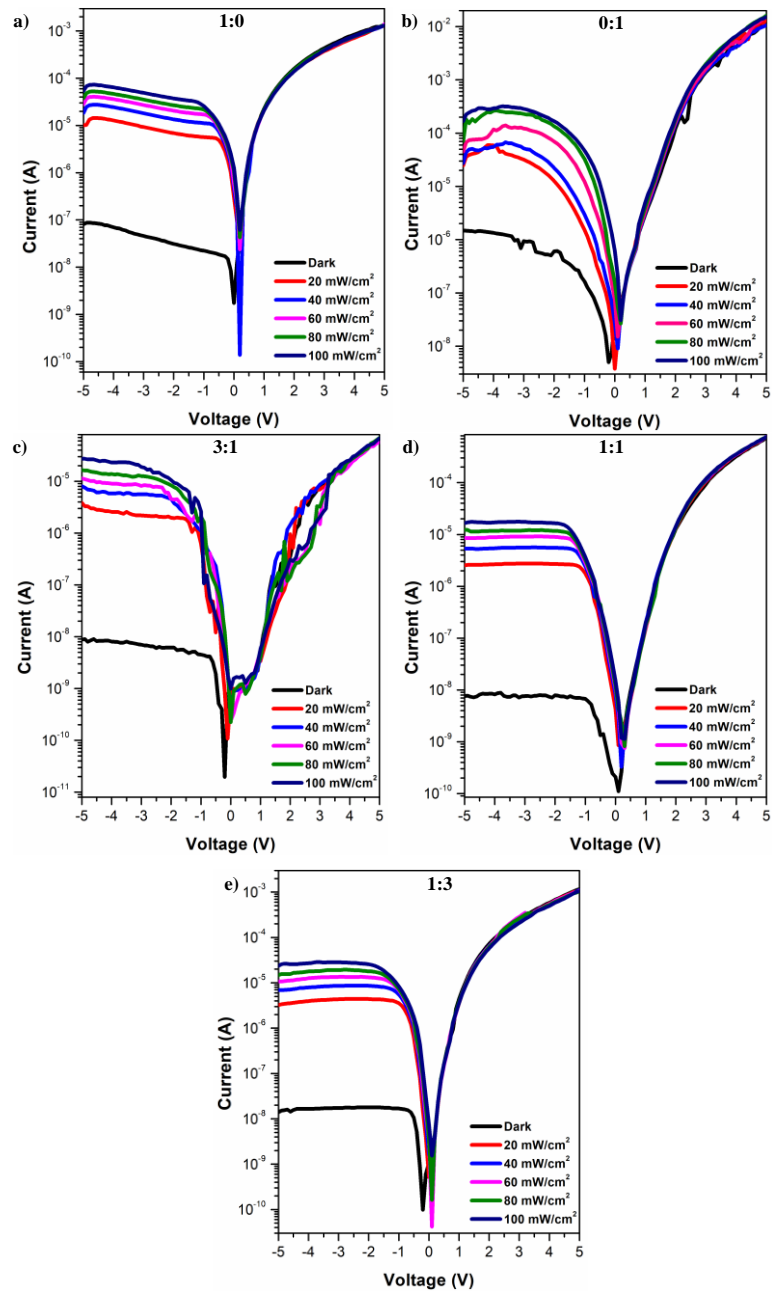
Figure 3. I-V graphs of NiO:ZnO/p-Si photodiodes under dark and various illuminations.
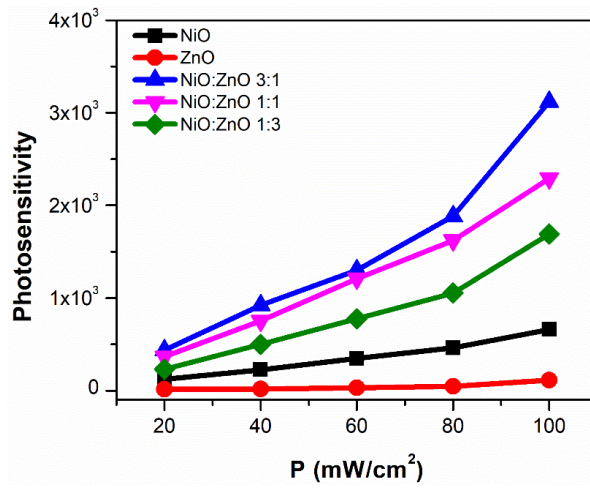
Figure 4. The photosensitivity values of NiO:ZnO/p-Si photodiodes.
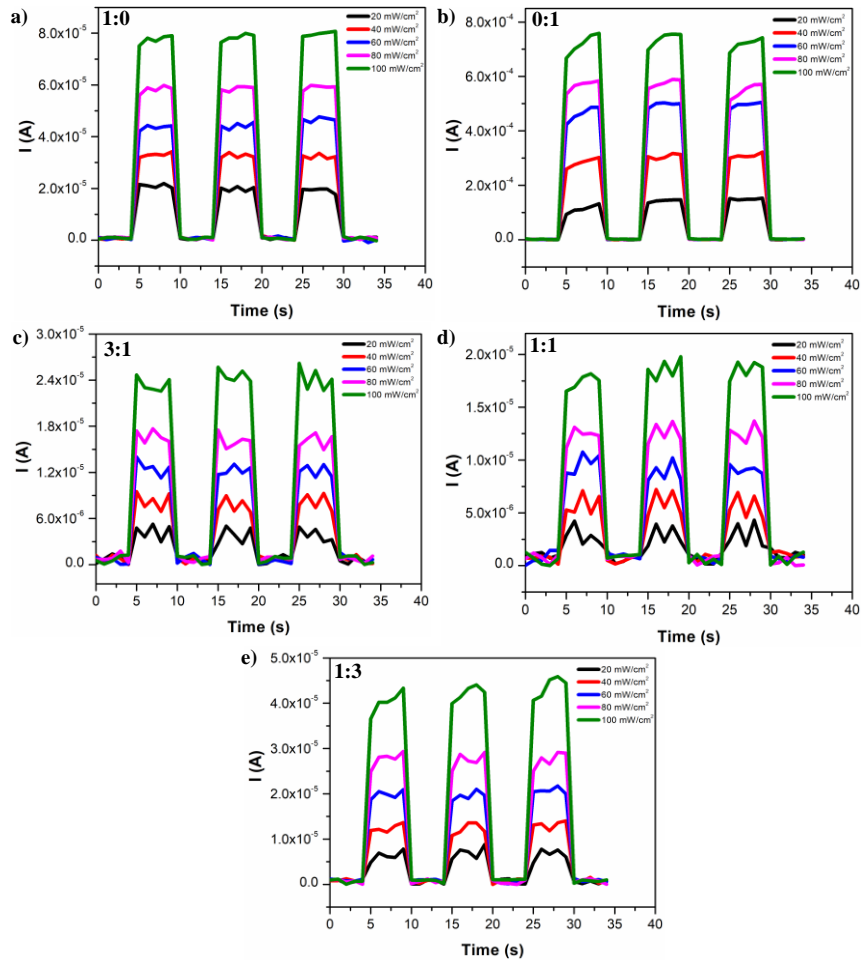
Figure 5. I-t graphs of NiO:ZnO/p-Si photodiodes.

115

3.3. C-V Characteristics of Prepared Photodiodes

The C-V characteristics of photodiodes are used to better characterize their electrical behaviour. The C-V characteristics of the produced photodiodes at frequencies ranging from 10 kHz to 1MHz are shown in Figure 6. As can be seen, the capacitance decreased as the frequency increased in all photodiodes. In the NiO photodiode, a peak occurred in the reverse bias region at a frequency of 10 kHz. At frequencies higher than this, the peaks occurred in the forward bias. It is thought that the peaks in the C-V graphs occur due to the presence of interfacial charge carriers and series resistance. In ZnO and composite photodiodes, while the photodiode capacitance changes with frequency in the reverse bias region, the capacitance in the forward bias region generally does not change with frequency. It is thought that the change in the negative region is due to the change of the depletion region of the device depending on the applied voltage and the response of the interface states in different frequency and electric fields [1, 33].
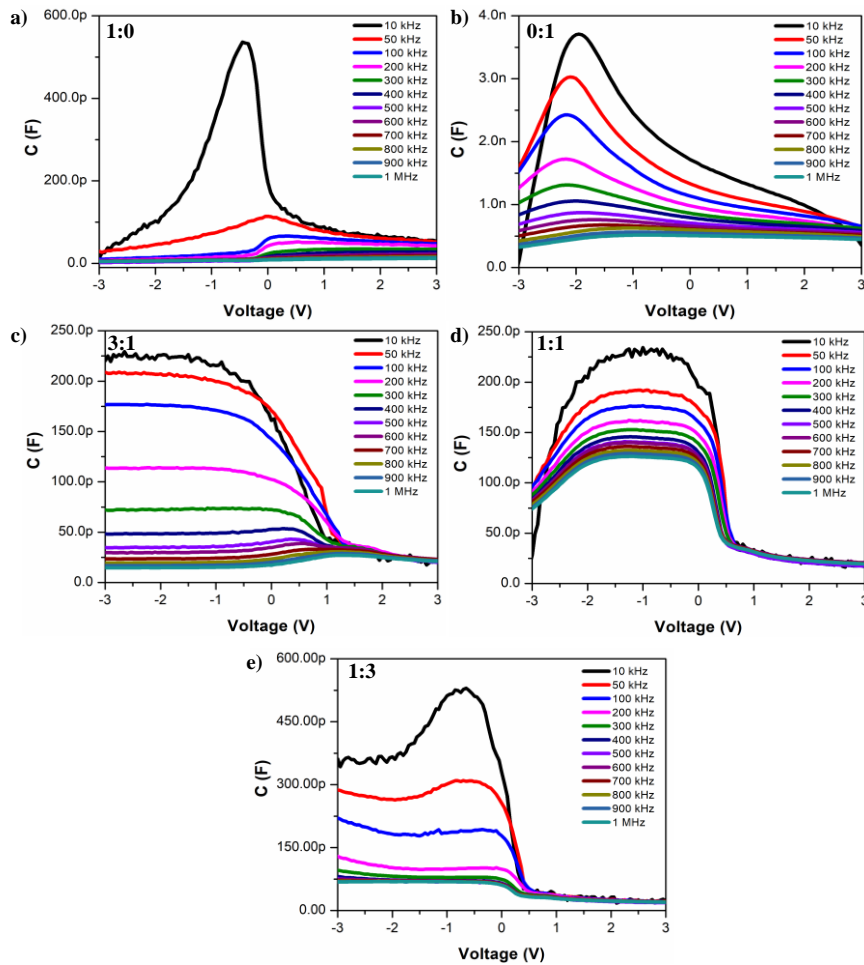
Figure 6. C-V characteristics of NiO:ZnO/p-Si photodiodes.

Series resistance (R_S)-V curves are shown in Figure 7. The R_S values decreased as the frequency increased in the accumulation and depletion region and was especially high at low frequency. In the non-ideal behaviour of diodes and deviations have an important place, and therefore R_S has a great importance. The peak values of the R_S-V curves also decreased as the frequency increased, and the peak positions changed depending on the Voltage and the NiO:ZnO ratio. It is thought that this situation is caused by the interface conditions that follow the AC signal more easily at low frequencies and the relaxation time of the charges [22].
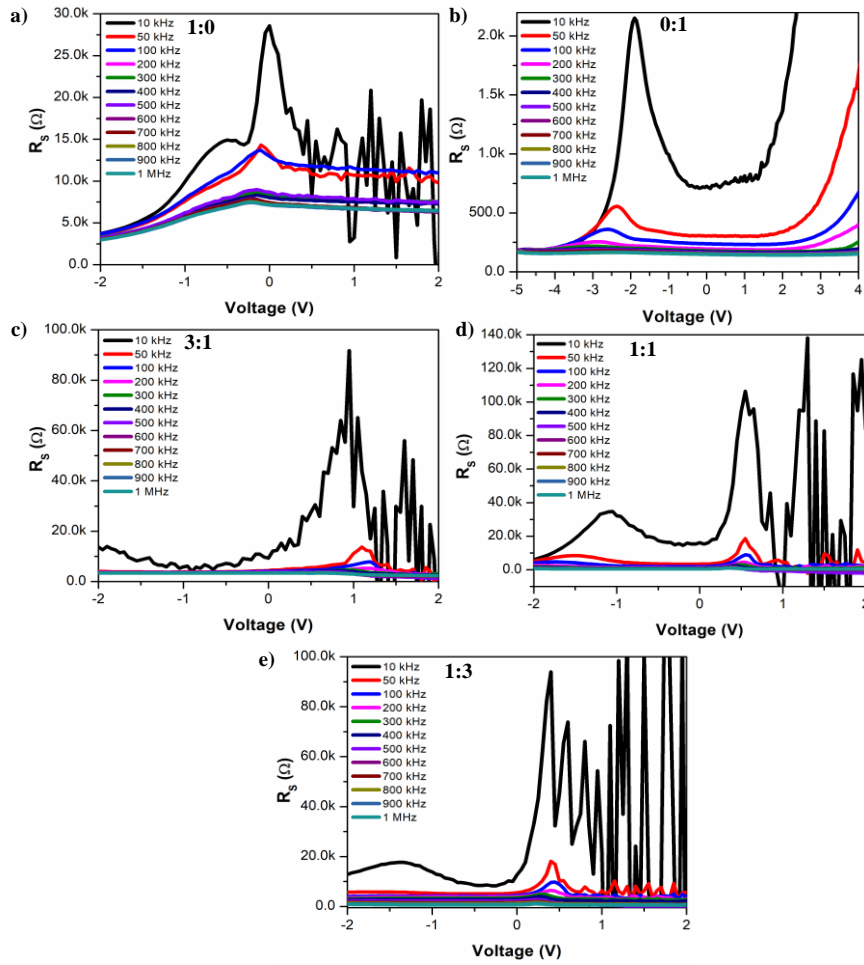
Figure 7. R_S-V characteristics of NiO:ZnO/p-Si photodiodes.

4. Conclusions

The NiO:ZnO/p-Si composite photodiodes were successfully fabricated using the dynamic sol-gel spin coating method. Characteristic peaks of NiO and ZnO were found in the composite thin films and it was observed that their intensity increased as their ratio in the composite increased. It was determined that NiO:ZnO thin films consisted of aggregated fine-grained nanoparticles. It was concluded that NiO:ZnO/p-Si composite Photodiodes are light sensitive. It has been seen that the photoresponse, photocurrent and capacitance properties of photodiodes can be controlled by light. The highest photosensitivity value was measured as 3.12×10^3 in the photodiode with a NiO:ZnO ratio of 3:1. It was seen that NiO:ZnO/p-Si composite photodiodes showed rectifying property and it was concluded that they exhibited photoconductive behaviour. It was observed that the voltage and frequency affected the electrical properties of the photodiodes. It was concluded that photodiodes with different properties can be obtained according to the NiO:ZnO ratio. The results show that, NiO:ZnO/p-Si composite photodiodes can find use in solar energy tracking systems and optoelectronic applications.

Acknowledgment

References

[1] Dere A. Al/P-Si/Zn:CuO/Al photodiodes for solar tracking systems. Phys Sci 2018; 13(4): 64-75.

[2] Yang C-K, Cheng T-C, Cheng C-H, Wang C-C, Lee C-C. Open-loop altitude-azimuth concentrated solar tracking system for solar-thermal applications. Sol Energy 2017; 147: 52-60.

[3] Nsengiyumva W, Chen S G, Hu L, Chen X. Recent advancements and challenges in Solar Tracking Systems (STS): A review. Renew Sust Energ Rev 2018; 81(1): 250-279.

[4] Chen C-P, Lin P-H, Chen L-Y, Ke M-Y, Cheng Y-W, Huang J. Nanoparticle-coated n-ZnO/p-Si photodiodes with improved photoresponsivities and acceptance angles for potential solar cell applications. Nanotechnology 2009; 20(24): 245204.

[5] Aslan F, Esen H, Yakuphanoglu F. The effect of coumarin addition on the electrical characteristics of Al/Coumarin: CdO/p-Si/Al photodiode prepared by drop casting technique. Optik 2019; 197: 163203.

[6] Kavuran G, Gurgenç T, Özkaynak F. On the modeling of the multi-segment capacitance: a fractional-order model and Ag-doped SnO_2 electrode fabrication. J Mater Sci 2022; 57: 2775–2793.

[7] Afzal A M, Bae I-G, Aggarwal Y, Park J, Jeong H-R, Choi E H, Park B. Highly efficient self-powered perovskite photodiode with an electron-blocking hole-transport NiO_x layer. Sci Rep 2021; 11(169): 1-14.

[8] Gozeh B A, Karabulut A, Ismael C B, Saleh S I, Yakuphanoglu F. Zn-doped CdO effects on the optical, electrical and photoresponse properties of heterojunctions-based photodiodes. J Alloys Compd 2021; 872: 159624.

[9] Liu H-Y, Huang Z-Y. Investigation of p-NiO/N-$Ga_{0.3}Zn_{0.7}O$ Heterojunction Photodiodes for Ultraviolet-B Detection. IEEE Sens J 2021; 21(19): 21486-21493.

[10] Abbasi M A, Ibupoto Z H, Khan A, Nur O, Willander M. Fabrication of UV photo-detector based on coral reef like p-NiO/n-ZnO nanocomposite structures. Mater Lett 2013; 108: 149-152.

[11] Tataroğlu A, Al-Sehemi A G, Ilhan M, Al-Ghamdi A A,Yakuphanoglu F. Optical, electrical and photoresponse properties of Si-based diodes with NiO-doped TiO_2 film prepared by sol-gel method. Silicon 2018; 10(3): 913-920.

[12] Pehlivanoglu S A. Fabrication of p-Si/n-NiO: Zn photodiodes and current/capacitance-voltage characterizations. Phys B: Condens Matter 2021; 603: 412482.

[13] Parida B, Kim S, Oh M, Jung S, Baek M, Ryou J-H, Kim H. Nanostructured-NiO/Si heterojunction photodetector. Mater Sci Semicond Process 2017; 71: 29-34.

[14] Choi J-M, Im S. Ultraviolet enhanced Si-photodetector using p-NiO films. Appl Surf Sci 2005; 244(1-4): 435-438.

[15] Yakuphanoglu F. Transparent metal oxide films based sensors for solar tracking applications. Compos B Eng 2016; 92: 151-159.

[16] Ameen B A H, Yildiz A, Farooq W, Yakuphanoglu F. Solar light photodetectors based on nanocrystalline zinc oxide cadmium doped/p-Si heterojunctions. Silicon 2019; 11(1): 563-571.

[17] Khusayfan N M. Electrical and photoresponse properties of Al/graphene oxide doped NiO nanocomposite/p-Si/Al photodiodes. J Alloys Compd 2016; 666: 501-506.

[18] Sevik A, Coskun B, Soylu M. The effect of molar ratio on the photo-generated charge activity of ZnO–CdO composites. Eur Phys J Plus 2020; 135(65): 1-16.

[19] Park N, Sun K, Sun Z, Jing Y, Wang D. High efficiency NiO/ZnO heterojunction UV photodiode by sol–gel processing. J Mater Chem C 2013; 1(44): 7333-7338.

[20] Gupta R, Hendi A, Cavas M, Al-Ghamdi A A, Al-Hartomy O A, Aloraini R, El-Tantawy F, Yakuphanoglu F. Improvement of photoresponse properties of NiO/p-Si photodiodes by copper dopant. Phys E: Low-Dimens Syst Nan 2014; 56: 288-295.

[21] Tyagi M, Tomar M, Gupta V. Fabrication of an efficient GLAD-assisted p-NiO nanorod/n-ZnO thin film heterojunction UV photodiode. J Mater Chem C 2014; 2(13): 2387-2393.

[22] Demirezen S, Çetinkaya H, Kara M, Yakuphanoğlu F, Altındal Ş. Synthesis, electrical and photo-sensing characteristics of the Al/(PCBM/NiO: ZnO)/p-Si nanocomposite structures. Sens Actuator A Phys 2021; 317: 112449.

[23] Soylu M, Dere A, Al-Sehemi A G, Al-Ghamdi A A, Yakuphanoglu F. Effect of calcination and carbon incorporation on NiO nanowires for photodiode performance. Microelectron Eng 2018; 202: 51-59.

[24] Al-Ghamdi A, Mahmoud W E, Yaghmour S J, Al-Marzouki F. Structure and optical properties of nanocrystalline NiO thin film synthesized by sol–gel spin-coating method. J Alloys Compd 2009; 486(1-2): 9-13.

[25] Zhao S, Shen Y, Zhou P, Zhang J, Zhang W, Chen X, Wei D, Fang P,Shen Y. Highly selective NO_2 sensor based on p-type nanocrystalline NiO thin films prepared by sol–gel dip coating. Ceram Int 2018; 44(1): 753-759.

[26] Rasool A, Kumar S, Mamat M, Gopalakrishnan C, Amiruddin R. Analysis on different detection mechanisms involved in ZnO-based photodetector and photodiodes. J Mater Sci: Mater Electron 2020; 31(9): 7100-7113.

[27] Aslan F, Esen H, Yakuphanoglu F. Electrical and fotoconducting characterization of Al/coumarin: ZnO/Al novel organic-inorganic hybrid photodiodes. J Alloys Compd 2019; 789: 595-606.

[28] Karthick K, Kathirvel P, Marnadu R, Chakravarty S, Shkir M. Ultrafast one step direct injection flame synthesis of zinc oxide nanoparticles and fabrication of p-Si/n-ZnO photodiode and characterization. Phys B: Condens Matter 2021; 612: 412971.

[29] Samavati A, Samavati Z, Ismail A, Othman M, Rahman M A, Zulhairun A, Amiri I. Structural, optical and electrical evolution of Al and Ga co-doped ZnO/SiO 2/glass thin film: role of laser power density. RSC Adv 2017; 7(57): 35858-35868.

[30] Islam M R, Rahman M, Farhad S, Podder J. Structural, optical and photocatalysis properties of sol–gel deposited Al-doped ZnO thin films. Surf Interfaces 2019; 16: 120-126.

[31] Fazmir H, Wahab Y, Saadon S, Anuar A, Zainol M, Johari S, Mazalan M, Arshad M M. Study of ideal piezoelectric sandwich structure based on foot plantar pressure applications. J Teknol Sci Eng 2015; 72: 1-6.

[32] Tataroğlu A, Aydın H, Al-Ghamdi A A, El-Tantawy F, Farooq W, Yakuphanoglu F. Photoconducting properties of Cd 0.4 ZnO 0.6/p-Si photodiode by sol gel method. J. Electroceramics 2014; 32(4): 369-375.

[33] Al-Sehemi A G, Mensah-Darkwa K, Al-Ghamdi A A, Soylu M, Gupta R, Yakuphanoglu F. Composite CuFe1−xSnxO2/p-type silicon photodiodes. Spectrochim Acta A Mol Biomol Spectrosc 2017; 180: 110-118.

Vegetable and Fruit Image Classification with SqueezeNet based Deep Feature Generator

Mehmet BAYGIN[1*]

[1] Bilgisayar Mühendisliği Bölümü, Mühendislik Fakültesi, Ardahan Üniversitesi, Ardahan, Türkiye
[*1] mehmetbaygin@ardahan.edu.tr

Abstract: Automatic classification of food products according to their types is one of the most common problems in computer vision. In this paper, automatic classification was performed using two different vegetable and fruit datasets. A deep learning-based transfer learning approach is used for the automatic fruit and vegetable classification problem. The first dataset (DB1) used in the study consists of 21000 images and the second dataset (DB2) consists of 980 images. In addition, the first dataset contains 15 classes and the second dataset contains 20 classes. SqueezeNet architecture is used for feature extraction in the developed deep learning-based machine learning model. In addition, the ReliefF method was used for feature selection and the most significant features were determined by eliminating negative features. In the classification phase of the developed application, Linear Discriminant Analysis (LDA) method was preferred. In this study, hold-out and 10-fold cross validation techniques were used for DB1. Also, 10-fold cross validation was used for DB2. An accuracy value of over 99% was obtained for both DB1 and DB2. The obtained results of the study show that the proposed method can be used successfully in automatic vegetable and fruit classification.

Key words: Vegetable and fruit classification, SqueezeNet, ReliefF, Linear Discriminant Analysis.

SqueezeNet tabanlı Derin Öznitelik Oluşturucu ile Sebze ve Meyve Görüntü Sınıflandırması

Öz: Gıda ürünlerinin türlerine göre otomatik sınıflandırılması bilgisayarlı görme alanında sıklıkla karşılaşılan problemlerden biridir. Bu çalışmada, iki farklı sebze ve meyve veri seti kullanılarak otomatik sınıflandırma yapılmıştır. Otomatik meyve ve sebze sınıflandırma problemi için derin öğrenme tabanlı öğrenme aktarımı yaklaşımı kullanılmıştır. Çalışmada kullanılan birinci veri seti (DB1) 21000 görüntüden oluşmaktadır ve ikinci veriseti (DB2) 980 görüntüden meydana gelmektedir. Ayrıca, ilk veri seti 15 sınıftan ve ikinci veri seti 20 sınıftan oluşmaktadır. Geliştirilen derin öğrenme tabanlı makine öğrenmesi modelinde özellik çıkarımı için SqueezeNet mimarisi kullanılmaktadır. Ayrıca özellik seçimi için ReliefF yöntemi kullanılmış ve bu sayede negatif özellikler elimine edilerek en anlamlı özellikler belirlenmiştir. Geliştirilen uygulamanın sınıflandırma fazında Lineer Diskriminant Analizi (LDA) yöntemi tercih edilmiştir. Bu çalışmada, hold-out ve 10-katlamalı çapraz doğrulama teknikleri DB1 için kullanılmıştır. Ayrıca, 10-kat çapraz doğrulama tekniği DB2 için kullanılmıştır. Hem DB1 hem de DB2 için %99 üzerinde bir doğruluk değeri elde edilmiştir. Çalışma kapsamında elde edilen sonuçlar, önerilen yöntemin otomatik sebze sınıflandırmada başarılı bir şekilde kullanılabileceğini göstermektedir.

Anahtar kelimeler: Sebze ve meyve sınıflandırma, SqueezeNet, ReliefF, Lineer Diskriminant Analizi.

1. Giriş

Vegetable is the name given to the part of the plant that is consumed by humans and animals [1]. Vegetables are produced in almost many parts of the world and these vegetables are consumed by humans and animals. With this type of food in the food pyramid, people can meet their various vitamin and mineral needs [2,3].

Nowadays, computer vision is actively used in many fields [4]. Areas such as mass production sites, automobile factories and textiles are among these sectors [5,6]. Another area where computer technology is actively used is the food industry [7]. Various tasks such as automatic quality control, product counting, product classification can be performed with these approaches [8]. In this way, food products can be evaluated in many ways [9]. At this point, vegetable and fruit classification is seen as a very important issue. Because vegetable and fruit food groups contain some manual processes from the production stage to the delivery stage. The similarities between vegetables and fruits, also various parameters such as color, texture, size can sometimes challenge automatic classification approaches [10]. For this reason, automatic classification of these and similar foods according to their types becomes a very important issue.

The topic of automatic vegetable classification in the literature is a problem that has been studied for a long time and continues to be studied. Some studies on this subject are summarized in Table 1.

---

[*] Corresponding author: mehmetbaygin@ardahan.edu.tr. ORCID Number of authors: [1] 0000-0002-5258-754X

Table 1. Literature review on vegetable and fruit classification

Author(s)	Year	Method	Dataset Information	Type (Vegetable/Fruit)	Result(s)
F. Yuesheng et. al. [11]	2021	GoogleNet based CNN	6 class and 6600 image	Mixed	Accuracy=98.82
J. K. Bhavya et. al. [12]	2021	CNN	24 class and 3924 images	Mixed	Accuracy=95.5
R. S. Latha et. al. [13]	2021	Custom design CNN	12 class and 6783 images	Mixed	Accuracy=97.4
M. I. Ahmed et al. [14]	2021	Custom design CNN	15 class and 21000 images	Vegetable	Accuracy=97.5
O. Patil and V. Gaikwad [15]	2018	Image preprocessing and InceptionV3	4 class and 1200 images	Vegetable	Accuracy=99
H. Kuang et. al. [16]	2018	Fused HOG, Local Binary Pattern (LBP) and GaborLBP	5 class and 20433 images	Fruits	Accuracy=99.5
Z. Yuhui et. al. [17]	2021	Custom designed deep CNN	20 class and 10756 images	Mixed	Accuracy=95.67
J. L. Joseph et. al. [18]	2021	Custom designed CNN	131 class and 90483 images	Mixed	Accuracy=94.35

As can be seen from Table 1, there are various studies in the literature for automatic fruit and vegetable classification. Although recent studies are summarized in Table 1, there are previous studies on this subject. In this table, only fruit and vegetable classification is focused on. Studies carried out for the food industry are not only about classification. There are also studies on various subjects such as sorting vegetables and fruits according to their quality, freshness control, and whether there is a disease in foods.

The automatic classification problem is one of the hot topics studied in many different areas in the literature [19,20]. The approach that is frequently used in this type of problem is deep learning and machine learning methods [21,22]. In this paper, automatic vegetable classification was investigated. In developed model for this purpose, deep feature extraction based on SqueezeNet [23,24], feature selection based on ReliefF [25] method and classification with LDA [26] method were performed. The main motivation of this study is to develop a high-performance, easy-to-use and easy-to-apply model on large datasets. For this purpose, a vegetable and fruit dataset consisting of 21000 and 980 images was used and the developed model was validated on these datasets. In addition, most of the methods developed in the literature use deep learning methods and the designed deep networks are trained end-to-end. In this study, deep network architectures are used as a feature extractor. Transfer learning approach is used for this process and a feature vector is obtained from each image. In the next phase of the model, the feature selection process is applied, and the most significant features are selected and the feature vector is reduced. In this way, it is aimed to reduce computational complexity. In the last phase of the model, the classification process was carried out with the LDA algorithm, which is a well-known and fast-running method in the literature. Some contributions of the proposed method in this study are given below:

- Deep learning approaches are very popular in the literature. Pre-trained deep networks and custom designs are frequently used, especially in image-related fields. Although these approaches produce successful results, they are methods with high computational complexity. In particular, end-to-end training of a deep network architecture consumes a lot of time. In this study, contrary to the literature, pre-trained deep network architectures were used as feature extractors. In this way, a new feature extractor with low computational complexity is provided.
- The proposed model in this study has been tested with a large dataset. Three different cases were created for the test process and all the images in the dataset were used in the test process. In addition, two different validation methods were used in the study. These are hold-out and k-fold cross validation, respectively. The model developed in both validation methods and datasets has achieved 99% and above accuracy. In terms of dataset size (class and number of images), the proposed method produced quite good results compared to the literature.

The remainder of the paper is organized as follows. In the second section, the used datasets to test the developed model are examined. In the third section of the study, the details of the model developed for automatic vegetable and fruit classification are shared. In the fourth section, the obtained results from the proposed method are given. In the fifth and final section, conclusions and future works are given.

2. Material

Two data sets (DB1 and DB2) were used to test the developed model. Details of these datasets are given in the subsection.

2.1. First Dataset (DB1)

In this paper, a new deep learning-based vegetable classification model was developed. In the model developed, an open access dataset was used and this dataset consists of 21,000 images [14,27]. In addition, the dataset contains 1400 images of 15 different vegetable species in total. Some information about the dataset is presented in Table 2.

Table 2. Detailed features of DB1

Features	Values
Number of classes	15
Class names	Bean, Bitter Gourd, Bottle Gourd, Brinjal, Broccoli, Cabbage, Capsicum, Carrot, Cauliflower, Cucumber, Papaya, Potato, Pumpkin, Radish, Tomato
Total number of images	21,000
Number of images in each class	1400
Image type	JPG
Images of size	224x224

This dataset, which is shared as open access, is divided into three as training, testing and validation. The training group contains 15,000 images, the test group contains 3,000 images, and the validation group contains 3,000 images. In this paper, the developed model was tested in two different ways. In the first test phase, all of these groups were combined and classified using the hold-out validation technique. In the second test phase of the developed model, 10-fold cross validation was applied to the test and validation groups, separately. Some sample images used in the testing phase of the study are shown in Figure 1.

(a) Bean   (b) Bitter Gourd   (c) Bottle Gourd   (d) Brinjal   (e) Broccoli

(f) Cabbage   (g) Capsicum   (h) Carrot   (i) Cauliflower   (j) Cucumber

(k) Papaya   (l) Potato   (m) Pumpkin   (n) Radish   (o) Tomato
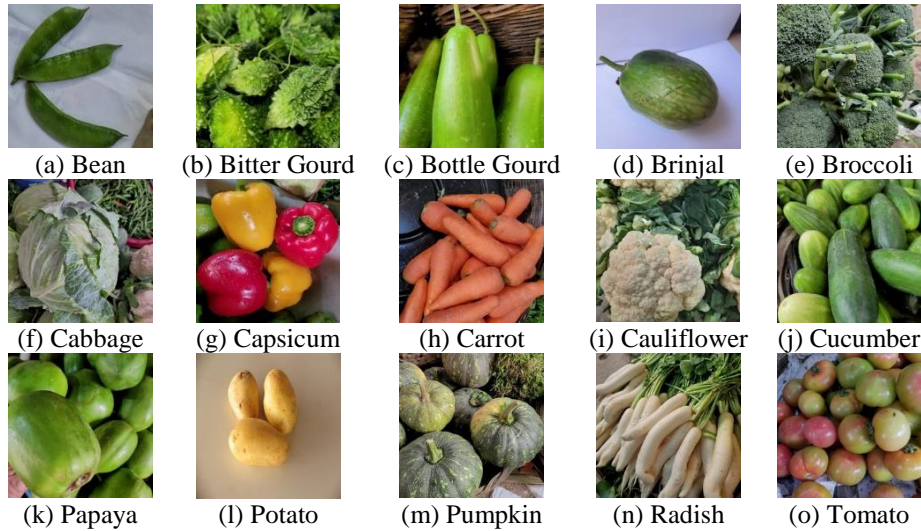
Figure 1. Vegetable images in the DB1

2.2. Second Dataset (DB2)

Another dataset used in the study is named DB2 [28]. This dataset contains various vegetable and fruit images belonging to 20 classes. There are a total of 980 images in the DB2 and available as open access. Details of this dataset are presented in Table 3. Since DB2's data size is small, only 10-fold cross validation technique is used on this dataset in testing phase. Some sample images from this dataset used in the test phase are given in Figure 2.

Table 3. Detailed features of DB2

Features	Values
Number of classes	20
Class names	Apple, Bitter Melon, Brinjal Dotted, Chili, Fig, Green Orange, Green Pepper, Khira, Kiwi, Onion, Red Pepper, Pomegranate, Red Cabbage, Sapodilla, Kundru, Sponge Gourd, Strawberry, Green Tomato, Red Tomato, Watermelon
Total number of images	980
Number of images in each class	50 (Only green orange is 30)
Image type	JPG
Images of size	Various sizes

(a) Apple	(b) Bitter Melon	(c) Brinjal Dotted	(d) Chili	(e) Fig
(f) Green Orange	(g) Green Pepper	(h) Khira	(i) Kiwi	(j) Onion
(k) Red Pepper	(l) Pomegranate	(m) Red Cabbage	(n) Sapodilla	(o) Kundru
(p) Sponge Gourd	(r) Strawberry	(s) Green Tomato	(t) Red Tomato	(u) Watermelon
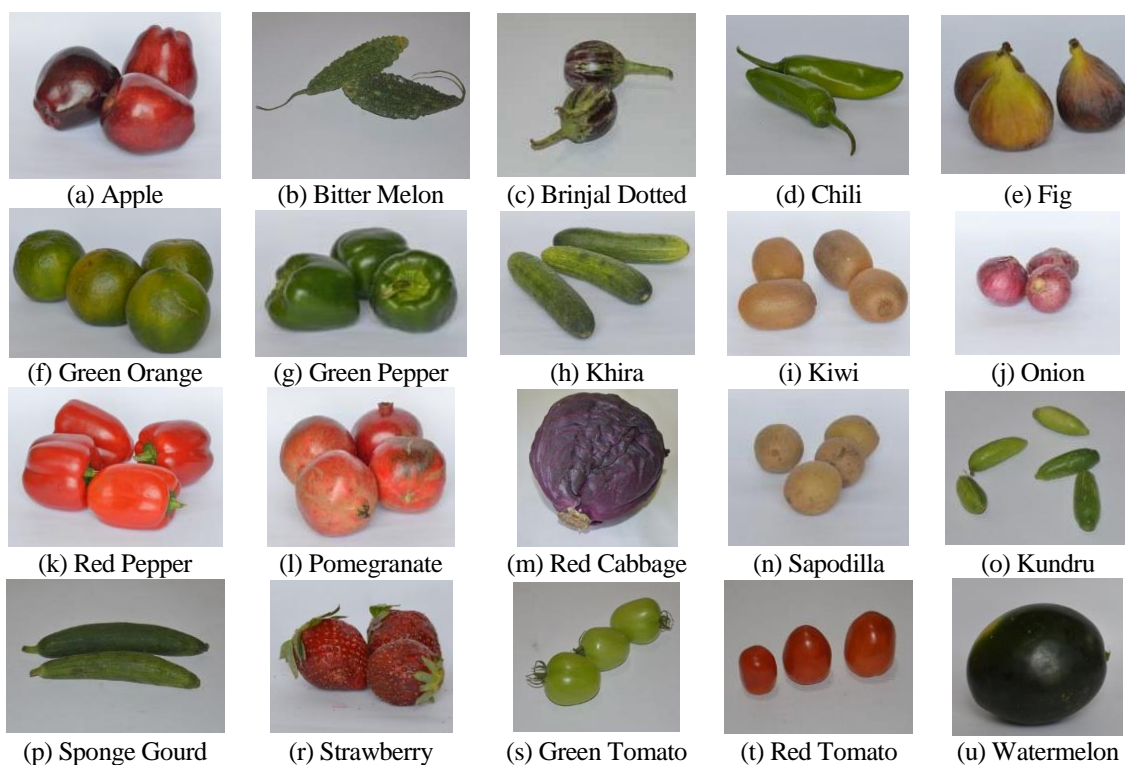
Figure 2. Vegetable and fruit images in the DB2

3. Automatic Vegetable Classification Model based on SqueezeNet

In this study, a deep learning-based automatic vegetable classification model was developed. The developed model basically consists of 3 steps. These steps are feature extraction, feature selection and classification, respectively. In the first step of the developed model, features were extracted from the images using the pre-trained SqueezeNet deep network architecture. In the second phase of the model, the most significant features were selected using the ReliefF approach. In the classification phase of the application, the LDA method was used. The steps of the developed model are shared in the subsections. In addition, the flowchart of the proposed method is presented in Figure 3.
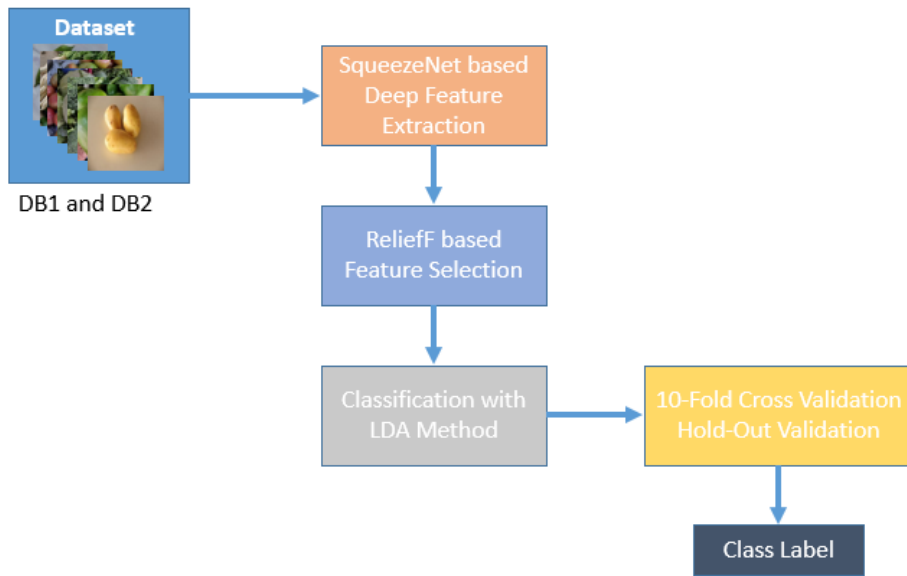
Figure 3. Flowchart of the proposed method

3.1. Deep Feature Extraction with SqueezeNet

In the developed model, feature extraction was carried out with the transfer learning approach. For this purpose, the pre-trained SqueezeNet deep learning model was used and a feature matrix was obtained using this model. For this process, the "GlobalAveragePooling" layer of the SqueezeNet architecture was used, and 1000 features were obtained for each image from this layer. With this approach, features are acquired without the need for retraining the network. A block diagram summarizing the feature extraction step of the developed model is given in Figure 4.

Step 1: Extract deep feature from vegetable images using SqueezeNet architecture
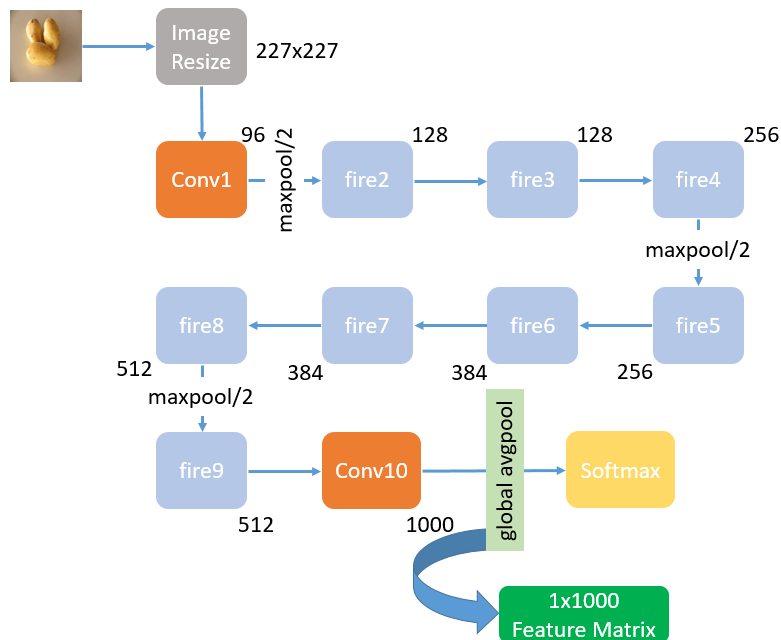
Figure 4. Feature extraction with SqueezeNet architecture

3.2. Feature Selection

The second step of the developed model is feature selection. Feature selection is an approach frequently used in machine learning methods. Thanks to this step, the performance of the classification process is increased by selecting the most meaningful features. In addition, as meaningless features are eliminated, computational complexity is reduced. ReliefF feature selection method is utilized in this step of the developed model. In this method, a weight value is calculated for each feature in the feature vector. Calculated weight values can be positive or negative. Positive weight value represents the most significant feature, while negative values represent meaningless features. For this reason, a threshold value was set in order to eliminate features with negative weight in the study and this threshold value was determined as 0.01. In other words, the features with a weight of 0.01 and above, which were calculated during the feature selection stage, were taken into account. A pseudocode for the ReliefF algorithm used in the developed model is given in Algorithm 1.

Step 2: Select feature with ReliefF algorithm using Algorithm 1

Algorithm 1. ReliefF algorithm based feature selection

Input: Feature vector (fv) with size of 1000 and labels (lbl)
Output: Selected features (sf) with the size of L
1:   *[idx,weights]=relieff(fv, lbl, 10);*
2:   count = 1;
3:   **for** i=1 to 1000 **do**
4:     **if** weights(i) > 0.01
5:       *sf (:,count) = fv (:,i);*
6:       *count = count + 1;*
7:     **end if**
8:   *i=i+1;*
9:   **end for i**

3.3. Classification

The last step of the automatic vegetable and fruit classification model implemented in this study is classification. LDA algorithm was utilized in the classification phase of the model. LDA algorithm is a very simple, fast and a classification method that produces good results. MATLAB Classification Learner Toolbox (MCLT) was used in the classification phase. In addition, hold-out and k-fold cross validation methods were used as validation techniques for DB1. In the hold-out validation technique, the train/test ratio was determined as 80:20. In the k-fold cross validation method, the k value was determined as 10. In the test process for DB2, only the 10-fold cross validation technique was applied.

Step 3: Classify selected features using the LDA method

4. Performance Analysis

In this study, an automated deep learning approach is developed to distinguish vegetables and fruits. The developed model uses the SqueezeNet deep network architecture and extracts deep features with this network. In addition, the most significant features were selected using the ReliefF algorithm and these features were classified with the LDA algorithm. Hold-Out (80:20) and 10-fold cross validation methods were used to validate the developed model on DB1 and DB2. The model was coded on the MATLAB 2021b platform and features were classified using MCLT. The features of the computer used in the development and testing phases of the model are given in Table 4.

Table 4. PC features used in the study

Features	Values
CPU	Intel Xeon 2.70GHz
RAM	256 GB
Harddisk	512 GB SSD
Operating System	Windows Server 2019
Platform	Matlab 2021b

4.1. Results

In this paper, the two open access vegetable and fruit dataset was used. The first dataset, DB1 contains 21,000 images of 15 different species. This dataset is basically divided into three groups. These are training, testing and validation, respectively. Three different tests were performed on this dataset. First, all groups are combined and a single test set with 21000 images is obtained. The model developed for this group was tested with the hold-out (80:20) method. In the second test phase, the test set in the dataset was used and test process was carried out with 10-fold cross validation method. In the third test performed in the study, the validation set was used and the 10-fold cross validation method was preferred. Another dataset used in the study is DB2 and contains 980 images. This dataset has 20 classes. 10-fold cross validation technique has been applied for DB2. As a result of each test process, a confusion matrix was obtained and performance metrics were calculated using this matrix. These calculated metric values are accuracy, recall, precision and f-measure, respectively. The mathematical equivalent of these performance metric values are given in Equation (1)-(4) [29].

$$Accuracy = \frac{TP + TN}{TP + TN + FP + FN} \tag{1}$$

$$Recall = \frac{TP}{TP + FN} \tag{2}$$

$$Precision = \frac{TP}{TP + FP} \tag{3}$$

$$F_{Measure} = \frac{2 * precision * recall}{precision + recall} \tag{4}$$

In this paper, three test cases for DB1 and one test case for DB2 were created. Detailed explanation of these tests and the results obtained from the test procedures are given in the subsections.

4.1.1. Case 1: Hold-Out (80:20) validation by using all images in DB1

Three different test procedures for DB1 were applied in the test phase of the developed model. The first of these tests was carried out using the hold-out (80:20) technique. In this test process, images divided into three groups (training, testing and validation) in the dataset were collected in a single group and all 21000 images were taken into account in the test process. In this test approach, 80:20 hold-out validation was utilized and the obtained confusion matrix is given in Figure 4. The calculated performance metric values are presented in Table 4.
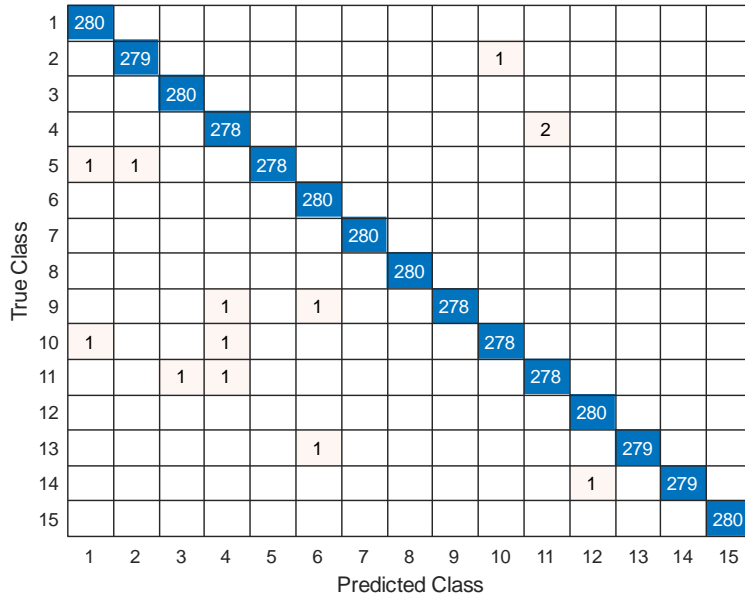
Figure 4. Confusion matrix for hold-out (80:20) validation on DB1

Table 4. Performance metric results for hold-out validation on DB1

Class No	Class Label	Recall	Precision	F-Measure	Avg. Accuracy
1	Bean	1	0.9929	0.9964	
2	Bitter Gourd	0.9964	0.9964	0.9964	
3	Bottle Gourd	1	0.9964	0.9982	
4	Brinjal	0.9929	0.9893	0.9911	
5	Broccoli	0.9929	1	0.9964	
6	Cabbage	1	0.9929	0.9964	
7	Capsicum	1	1	1	
8	Carrot	1	1	1	0.9969
9	Cauliflower	0.9929	1	0.9964	
10	Cucumber	0.9929	0.9964	0.9946	
11	Papaya	0.9929	0.9929	0.9929	
12	Potato	1	0.9964	0.9982	
13	Pumpkin	0.9964	1	0.9982	
14	Radish	0.9964	1	0.9982	
15	Tomato	1	1	1	
	Avg.	0.9969	0.9969	0.9969	

4.1.2. Case 2: 10-fold cross validation for "test" set in DB1 dataset

In the second test of the developed model, the test set in the dataset was used. The test set in the dataset contains 200 images for each label. This set consists of a total of 3000 images. In this test phase, 10-fold cross validation technique was utilized and obtained confusion matrix is given in Figure 5. The performance metric values calculated for this test process are shared in Table 5.

Figure 5. Confusion matrix for 10-fold cross validation (test set in DB1)

Table 5. Performance metric results for 10-fold cross validation (test set in DB1)

Class No	Class Label	Recall	Precision	F-Measure	Avg. Accuracy
1	Bean	1	0.9804	0.9901	
2	Bitter Gourd	0.9800	1	0.9899	
3	Bottle Gourd	1	1	1	
4	Brinjal	1	0.9852	0.9926	0.9940
5	Broccoli	0.9950	1	0.9975	
6	Cabbage	0.9900	0.9950	0.9925	
7	Capsicum	0.9950	1	0.9975	

8	Carrot	1	1	1
9	Cauliflower	0.9950	0.9900	0.9925
10	Cucumber	0.9850	0.9752	0.9801
11	Papaya	0.9800	0.9949	0.9874
12	Potato	1	1	1
13	Pumpkin	0.9900	1	0.9950
14	Radish	1	1	1
15	Tomato	1	0.9901	0.9950
	Avg.	0.9940	0.9941	0.9940

4.1.3. Case 3: 10-fold cross validation for "validation" set in DB1 dataset

In the third test of the model, the validation set in the dataset was used. This group contains 200 images for each vegetable type and a total of 3000 images. As in Case 2, the 10-fold cross validation method was used in this test phase as well. The confusion matrix obtained as a result of test is given in Figure 6 and the performance metric values are given in Table 6.
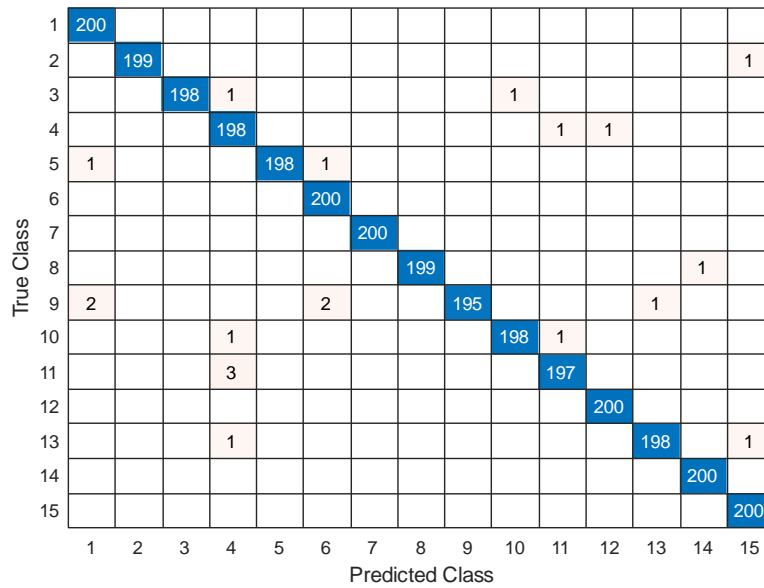
Figure 6. Confusion matrix for 10-fold cross validation (validation set in DB1)

Table 6. Performance metric results for 10-fold cross validation (validation set in DB1)

Class No	Class Label	Recall	Precision	F-Measure	Avg. Accuracy
1	Bean	1	0.9852	0.9926	
2	Bitter Gourd	0.9950	1	0.9975	
3	Bottle Gourd	0.9900	1	0.9950	
4	Brinjal	0.9900	0.9706	0.9802	
5	Broccoli	0.9900	1	0.9950	
6	Cabbage	1	0.9852	0.9926	
7	Capsicum	1	1	1	
8	Carrot	0.9950	1	0.9975	0.9933
9	Cauliflower	0.9750	1	0.9873	
10	Cucumber	0.9900	0.9950	0.9925	
11	Papaya	0.9850	0.9899	0.9875	
12	Potato	1	0.9950	0.9975	
13	Pumpkin	0.9900	0.9950	0.9925	
14	Radish	1	0.9950	0.9975	
15	Tomato	1	0.9901	0.9950	
	Avg.	0.9933	0.9934	0.9933	

4.2.1. Case 1: 10-fold cross validation for DB2 dataset

The developed model was validated using 2 different datasets. The second dataset used in the study is named DB2 and contains 980 images and 20 classes. Since the size of this dataset is small, validation was performed using the 10-fold cross validation technique. The confusion matrix obtained using this dataset is given in Figure 7. In addition, the calculated performance metric values using the confusion matrix are presented in Table 7.
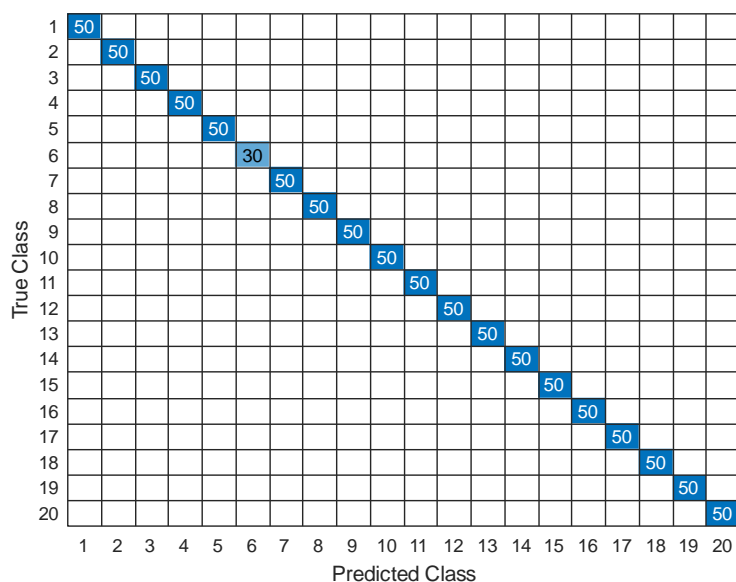
Figure 6. Confusion matrix for 10-fold cross validation (DB2)

Table 6. Performance metric results for 10-fold cross validation

Class No	Class Label	Recall	Precision	F-Measure	Avg. Accuracy
1	Apple	1	1	1	
2	Bitter Melon	1	1	1	
3	Brinjal Dotted	1	1	1	
4	Chili	1	1	1	
5	Fig	1	1	1	
6	Green Orange	1	1	1	
7	Green Pepper	1	1	1	
8	Khira	1	1	1	
9	Kiwi	1	1	1	
10	Onion	1	1	1	
11	Red Pepper	1	1	1	1
12	Pomegranate	1	1	1	
13	Red Cabbage	1	1	1	
14	Sapodilla	1	1	1	
15	Kundru	1	1	1	
16	Sponge Gourd	1	1	1	
17	Strawberry	1	1	1	
18	Green Tomato	1	1	1	
19	Red Tomato	1	1	1	
20	Watermelon	1	1	1	
	Avg.	1	1	1	

4. Discussion

Nowadays, computer-based automatic classification is actively used in many different fields. In this study, two different datasets were used for automatic classification of vegetables. In addition, a new machine learning model based on deep learning has been developed. In the first stage of the developed model, deep feature extraction was applied. At this stage, SqueezeNet architecture is used. Before choosing this architecture, other pre-trained

deep network architectures were also tested on DB1. In the test process, the feature vector obtained from each deep network was tested with SVM and the highest accuracy was achieved with the SqueezeNet architecture. The tested other deep network architectures and the obtained accuracies are shown in Figure 7.
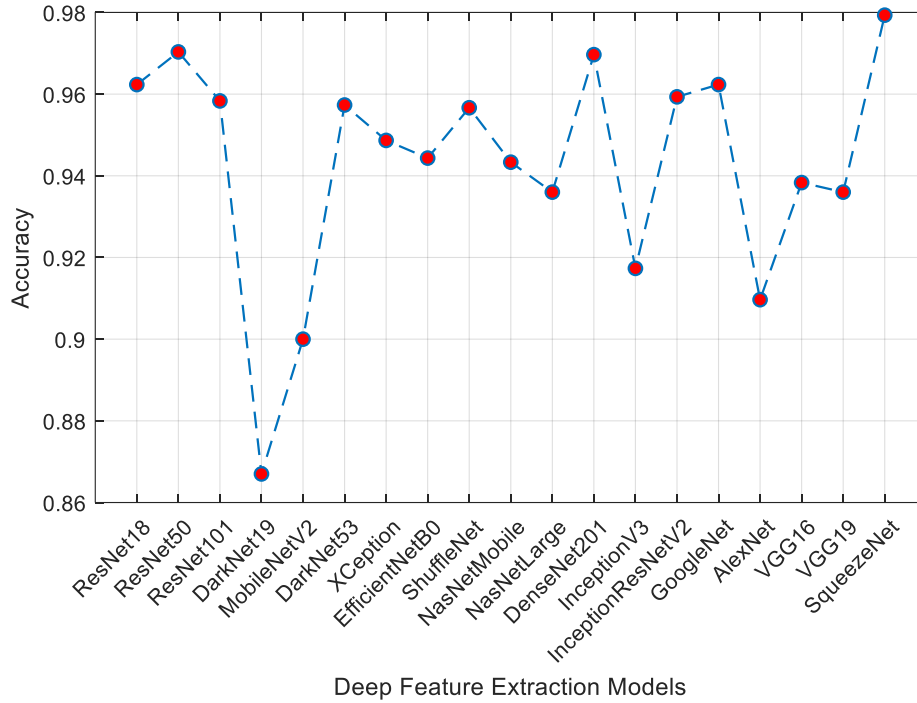
Figure 7. Performances of deep feature extractors

As can be seen from Figure 7, the best accuracy value was obtained with the SqueezeNet architecture. For this reason, this architecture was preferred in the study and the application was developed using this architecture. In addition, 5 different classification algorithms were tested to determine the best classifier in the developed model. These are Tree, LDA, Support Vector Machine (SVM), k-Nearest Neighbor (kNN) and Neural Network (NN), respectively. The accuracy values obtained using these methods are shown in Figure 8.
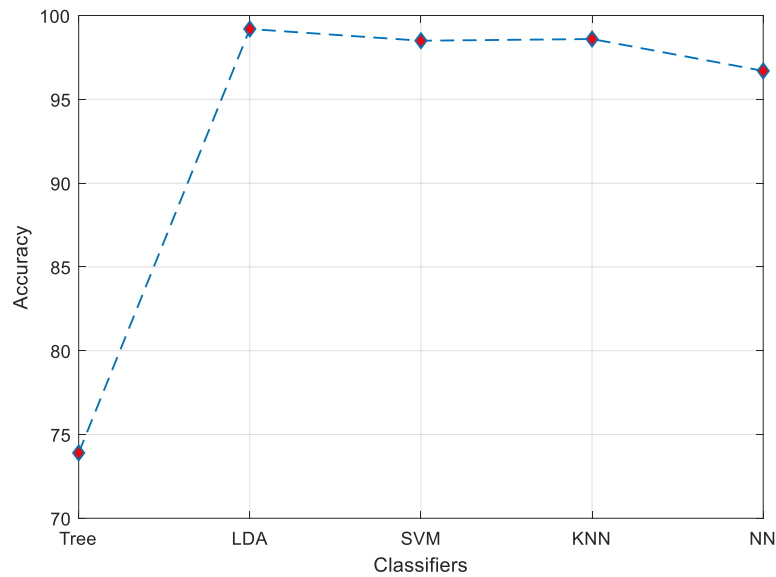
Figure 8. Performances of classifiers

As can be seen from Figure 8, the best accuracy was obtained with the LDA algorithm. After all the methods were determined in this way, the test phase of the developed model was started. Two different datasets were used in the test phase. These are DB1 and DB2 respectively. Two different validation techniques have been used for DB1, these methods are hold-out and 10-fold cross validation, respectively. Three cases have been created for DB1. In the first case, all images were used and validation was made with the hold-out method. In the second and third cases, test and validation sets were used, respectively, and classification was made with the 10-fold cross validation method. Accuracy of 99.69%, 99.4% and 99.33% was achieved for Case 1, Case 2 and Case 3, respectively. In addition, another dataset named DB2 was used in the study. In this dataset, classification was made with 10-fold cross validation method and 100% accuracy value was obtained. The obtained results reveal the success of the proposed method. A comparison of the studies performed for automatic vegetable and fruit classification is given in Table 7.

**Table 7.** Comparisons of state-of-the art on automatic vegetable and fruit classification

Author(s)	Year	Method	Validation(s)	Result(s)
M. I. Ahmed et. al. [14]	2021	Custom CNN	Hold-out (70:15:15)	Accuracy=97.5%
H. Kuang et. al. [16]	2018	Fused HOG, Local Binary Pattern (LBP), GaborLBP	5-fold cross validation	Accuracy=%98.5
Z. M. Khaing et. al. [30]	2018	Custom CNN	---	Accuracy=%94
M. S. Hossain et. al. [31]	2019	VGG-16 Fine tuning	Hold-out (85:15)	Accuracy=%99.75
S. Jana et. al. [32]	2020	Otsu threshold, fractal dimension calculation, gray-level co-occurrence matrix and Naïve bayes	---	Accuracy=%98.33
S. W. SideHabi et. al. [33]	2018	K-Means clustering, RGB and A features and artificial neural network	5-fold cross validation	Accuracy=%90
D. Hussain et. al. [34]	2022	Deep CNN	---	Accuracy=%96
R. S. Latha et. al. [13]	2021	Custom CNN	---	Accuracy=%98
L. Rajasekar and D. Sharmila [35]	2019	Color, shape and texture features, k-Nearest Neighbor	10-fold cross validation	Accuracy=%97.5
O. I. Alvarez-Canchila et. al. [36]	2020	Data augmentation, AlexNet based custom CNN	Hold-out (80:20)	Accuracy=%98.12
This study		Deep feature extraction (SqueezeNet), ReliefF and LDA	Case 1: Hold-Out (80:20) Case 2: 10-fold cross validation Case 3: 10-fold cross validation	DB1-Case 1: 21000 image Accuracy: 99.69 Recall: 99.69 Precision: 99.69 F-Measure: 99.69 DB1-Case 2: 3000 image Accuracy: 99.40 Recall: 99.40 Precision: 99.41 F-Measure: 99.40 DB1-Case 3: 3000 image Accuracy: 99.33 Recall: 99.33 Precision: 99.34 F-Measure: 99.33
			Case 1: 10-fold cross validation	DB2-Case 1: 980 image Accuracy: 100 Recall: 100 Precision: 100 F-Measure: 100

As given in Table 7, the proposed method produced better results than other studies in automatic fruit and vegetable classification. Studies carried out in the literature have been tested on different datasets. In many studies, the dataset was collected by the authors. In this study, two different datasets shared as open access were used. The developed model is easy to implement and has low computational complexity. In addition, the obtained accuracy value shows the usability of the proposed method. The developed model has been tested with two different validation techniques and datasets. The results obtained for all cases are over 99%, proving the performance of the developed model.

5. Conclusions

This study proposes a new deep feature extraction model for vegetable and fruit classification using vegetable images. In this paper, the performance of deep feature extraction in classifying vegetable images was investigated. For this purpose, different deep network architectures have been tested on the dataset. In addition, feature selection was made with the ReliefF algorithm and the selected features were classified by the LDA method. Two datasets were used in the study. DB1 contains 21000 images and 15 classes. In addition, DB2 includes 980 images and 20 classes. Three cases were created in the study for DB1 and tests were carried out on these cases. For DB1-Case 1, which has the largest data, 99.69% accuracy was achieved. When compared with the studies [14] using the same dataset in the literature, the proposed method has achieved a very high success rate. Another dataset used to verify the success of the proposed method, DB2, has reached 100% accuracy. The most important advantage of the proposed method is that it is simple, applicable and fast. In this study, deep features are obtained by using pre-trained networks instead of end-to-end training of deep network architecture. In addition to this approach, feature selection and classification methods, which are well known and frequently used in the literature, are used. Considering all these methods, the proposed approach in this study has very low computational complexity. In order for the proposed method to be used in real time, it should be tested on datasets with larger size and higher number of classes. This situation constitutes the limitation of the study.

The results show that the proposed method is very successful in automatic vegetable and fruit classification and produces satisfactory results. With future studies, it is planned to increase the number of classes and to achieve similar results in higher class numbers.

References

[1]   G.J.H. Grubben, Vegetables, Prota, 2004.

[2]   J.L. Slavin, B. Lloyd, Health benefits of fruits and vegetables, Adv. Nutr. 3 (2012) 506–516.

[3]   J.C. Rickman, C.M. Bruhn, D.M. Barrett, Nutritional comparison of fresh, frozen, and canned fruits and vegetables II. Vitamin A and carotenoids, vitamin E, minerals and fiber, J. Sci. Food Agric. 87 (2007) 1185–1196.

[4]   K. Ikeuchi, Computer vision: A reference guide, Springer, 2021.

[5]   A.I. Khan, S. Al-Habsi, Machine learning in computer vision, Procedia Comput. Sci. 167 (2020) 1444–1451.

[6]   M. Hassaballah, K.M. Hosny, Recent advances in computer vision, Stud. Comput. Intell. 804 (2019).

[7]   J.F.S. Gomes, F.R. Leta, Applications of computer vision techniques in the agriculture and food industry: a review, Eur. Food Res. Technol. 235 (2012) 989–1000.

[8]   D. Wu, D.-W. Sun, Colour measurements by computer vision for food quality control–A review, Trends Food Sci. Technol. 29 (2013) 5–20.

[9]   S. Li, Y. Tian, P. Jiang, Y. Lin, X. Liu, H. Yang, Recent advances in the application of metabolomics for food safety control and food quality analyses, Crit. Rev. Food Sci. Nutr. 61 (2021) 1448–1469.

[10]   S. Gaikwad, Literature Review on Multi-Spectral Imaging for Fruits and Vegetable, Available SSRN 3905180. (2021).

[11]   F. Yuesheng, S. Jian, X. Fuxiang, B. Yang, Z. Xiang, G. Peng, W. Zhengtao, X. Shengqiao, Circular fruit and vegetable classification based on optimized GoogLeNet, IEEE Access. 9 (2021) 113599–113611.

[12]   J.K. Bhavya, B.S. AC, K. Gayithri, B.L. Keerthi, M.Y. MG, The Literature Survey On Intra Class Fruits And Vegetable Recognition System Using Deep Learning, (n.d.).

[13]   R.S. Latha, G.R. Sreekanth, R.C. Suganthe, M. Geetha, N. Swathi, S. Vaishnavi, P. Sonasri, Automatic Fruit Detection System using Multilayer Deep Convolution Neural Network, in: 2021 Int. Conf. Comput. Commun. Informatics, IEEE, 2021: pp. 1–5.

[14]   M.I. Ahmed, S.M. Mamun, A.U.Z. Asif, DCNN-Based Vegetable Image Classification Using Transfer Learning: A Comparative Study, in: 2021 5th Int. Conf. Comput. Commun. Signal Process., IEEE, 2021: pp. 235–243.

[15]   O. Patil, Classification of Vegetables using TensorFlow, Int. J. Res. Appl. Sci. Eng. Technol. 6 (2018) 2926–2934. https://doi.org/10.22214/ijraset.2018.4488.

[16]   H. Kuang, C. Liu, L.L.H. Chan, H. Yan, Multi-class fruit detection based on image region selection and improved object proposals, Neurocomputing. 283 (2018) 241–255.

[17]   Z. Yuhui, C. Mengyao, C. Yuefen, L. Zhaoqian, L. Yao, L. Kedi, An Automatic Recognition Method of Fruits and Vegetables Based on Depthwise Separable Convolution Neural Network, J. Phys. Conf. Ser. 1871 (2021). https://doi.org/10.1088/1742-6596/1871/1/012075.

[18]   J.L. Joseph, V.A. Kumar, S.P. Mathew, Fruit Classification Using Deep Learning, in: Innov. Electr. Electron. Eng., Springer, 2021: pp. 807–817.

[19]   H. Bingol, B. Alatas, Classification of Brain Tumor Images using Deep Learning Methods, Turkish J. Sci. Technol. 16 (2021) 137–143.

[20]   S. Metin, One-dimensional Center Symmetric Local Binary Pattern Based Epilepsy Detection Method, Turkish J. Sci. Technol. 16 (2021) 155–162.

[21]   Y. Akbulut, R. Khalaf, Smart Arms Detection System Using YOLO Algorithm and OpenCV Libraries, Turkish J. Sci. Technol. 16 (n.d.) 129–136.

[22]   S. Metin, S. Dogan, Novel Fuzzy Kernels Based Local Binary Pattern And Local Graph Structure Methods, Turkish J. Sci. Technol. 16 (2021) 163–177.

[23]   F.N. Iandola, S. Han, M.W. Moskewicz, K. Ashraf, W.J. Dally, K. Keutzer, SqueezeNet: AlexNet-level accuracy with 50x fewer parameters and< 0.5 MB model size, ArXiv Prepr. ArXiv1602.07360. (2016).

[24]   B. Koonce, SqueezeNet, in: Convolutional Neural Networks with Swift Tensorflow, Springer, 2021: pp. 73–85.

[25]   T. Tuncer, E. Akbal, S. Dogan, Multileveled ternary pattern and iterative ReliefF based bird sound classification, Appl. Acoust. 176 (2021) 107866. https://doi.org/10.1016/j.apacoust.2020.107866.

[26]   P. Xanthopoulos, P.M. Pardalos, T.B. Trafalis, Linear discriminant analysis, in: Robust Data Min., Springer, 2013: pp. 27–33.

[27]   M.I. Ahmed, Vegetable Image Dataset, (2022). https://www.kaggle.com/misrakahmed/vegetable-image-dataset.

[28]   D.D. Tripathi, Mukesh; D.Maktedar, Fruits and Vegetables, Mendeley Data, V2. (2020). https://doi.org/10.17632/73kpfrbcck.2.

[29]   D.M.W. Powers, Evaluation: from precision, recall and F-measure to ROC, informedness, markedness and correlation, (2020). https://arxiv.org/abs/2010.16061 (accessed November 15, 2021).

[30]   Z.M. Khaing, Y. Naung, P.H. Htut, Development of control system for fruit classification based on convolutional neural network, in: 2018 IEEE Conf. Russ. Young Res. Electr. Electron. Eng., IEEE, 2018: pp. 1805–1807.

[31]   M.S. Hossain, M. Al-Hammadi, G. Muhammad, Automatic fruit classification using deep learning for industrial applications, IEEE Trans. Ind. Informatics. 15 (2018) 1027–1034.

[32]   S. Jana, R. Parekh, B. Sarkar, Automatic classification of fruits and vegetables: a texture-based approach, in: Algorithms Mach. Learn. Paradig., Springer, 2020: pp. 71–89.

[33]   S.W. Sidehabi, A. Suyuti, I.S. Areni, I. Nurtanio, Classification on passion fruit's ripeness using K-means clustering and artificial neural network, in: 2018 Int. Conf. Inf. Commun. Technol., IEEE, 2018: pp. 304–309.

[34]   D. Hussain, I. Hussain, M. Ismail, A. Alabrah, S.S. Ullah, H.M. Alaghbari, A Simple and Efficient Deep Learning-Based Framework for Automatic Fruit Recognition, Comput. Intell. Neurosci. 2022 (2022).

[35]   L. Rajasekar, D. Sharmila, Performance analysis of soft computing techniques for the automatic classification of fruits dataset, Soft Comput. 23 (2019) 2773–2788.

[36]   O.I. Álvarez-Canchila, D.E. Arroyo-Pérez, A. Patiňo-Saucedo, H.R. González, A. Patino-Vanegas, Colombian fruit and vegetables recognition using convolutional neural networks and transfer learning, in: J. Phys. Conf. Ser., IOP Publishing, 2020: p. 12020.

A new dataset for EEG abnormality detection: MTOUH

İrem TAŞCI[1], Burak TAŞCI[2*], Şengül DOĞAN[3], Türker TUNCER[4]

[1] Department of Neurology, School of Medicine, Malatya Turgut Ozal University, Malatya, Turkey
[2] Vocational School of Technical Sciences, Firat University, Elazig 23119, Turkey
[3,4] Department of Digital Forensics Engineering, Technology Faculty, Firat University, Elazig, Turkey
[1] irem.tasci@ozal.edu.tr, *[2] btasci@firat.edu.tr, [3] sdogan@firat.edu.tr, [4] turkertuncer @firat.edu.tr

Abstract: Electroencephalogram (EEG) is widely used for monitoring electrical activity in the brain. Analyzing EEG signals by physicians is tiring and time-consuming. Therefore, machine learning techniques can be used to improve detection accuracy. This study created a 2-class data set consisting of 35 channels, 10575x15 seconds of normal and 11240x15 seconds of abnormal EEG signals. This data set was obtained by examining the EEG signals of the patients who applied to Malatya Turgut Ozal University Malatya Research and Training Hospital in 2021. In the study, a statistical feature extraction-based model is proposed. After the feature vector reduction was performed using the neighboring component analysis to the proposed model, the classification was made using the support vector machines. The highest accuracy out of 35 channels was obtained in the P4O2 channel. Accuracy, sensitivity, specificity, precision and f-score for the P4O2 channel were 81.3%, 78.9%, 83.7%, 82.0% and 80.4%, respectively.

Key words: Electroencephalography signals classification, SVM, Machine Learning.

EEG anormallik tespiti için yeni bir veri seti: MTOUH

Öz: Elektroensefalogram (EEG), beyindeki elektriksel aktivitenin izlenmesi için yaygın olarak kullanılmaktadır. EEG sinyallerinin hekimler tarafından incelenmesi yorucu ve zaman alıcıdır. Bu nedenle, algılama doğruluğunu artırmak için makine öğrenme teknikleri kullanılabilir. Bu çalışmada 35 kanal, 10575x15 saniye normal ve 11240x15 saniye anormal EEG sinyalinden oluşan 2 sınıflı veri seti oluşturulmuştur. Bu veri seti Turgut Özal Üniversitesi Malatya Eğitim Araştırma Hastanesi'ne 2021 yılında başvuran hastaların EEG sinyalleri incelenerek elde edilmiştir. Çalışmada istatistiksel özellik çıkarımı tabanlı bir model önerilmiştir. Önerilen modele komşu bileşen analizi kullanılarak öznitelik vektörü indirgemesi yapıldıktan sonra destek vektör makineleri kullanılarak sınıflandırma yapılmıştır. 35 kanaldan en yüksek doğruluk P4O2 kanalında elde edilmiştir. P4O2 kanalı için doğruluk, duyarlılık, özgüllük, kesinlik ve f-skoru sırasıyla %81.3,%78.9, %83.7, %82.0 ve %80.4 olarak elde edilmiştir.

Anahtar kelimeler: Elektroensefalografi sinyal sınıflandırması, DVM, Makine Öğrenmesi.

1. Introduction

Electroencephalography (EEG) is the process of recording the brain's electrical activity through electrodes placed on the scalp [1]. The German neuropsychiatrist Hans Berger used the term EEG and performed the first human EEG recording [2]. EEG has been utilized in the diagnosis and differential diagnosis of various neurological illnesses since the turn of the twentieth century. It has been used to diagnose epilepsy, non-epileptic psychogenic seizures, hypoxia, and intracranial space-occupying lesions [3]. Postsynaptic electrical potentials of pyramidal neurons in the cortex play a role in the formation of EEG activity. Five different brain waves have been defined according to their frequency ranges. Delta rhythm is 0.5-3.5 Hz, theta rhythm is 4-7.5 Hz, the alpha rhythm is 8-14 Hz, the beta rhythm is 15-30 Hz, gamma rhythm is 30-48 Hz. In a healthy person, the dominant rhythm is alpha in the parietooccipital regions with eyes closed and at rest. Beta rhythm is observed while awake and eyes open. Theta is the dominant rhythm in shallow sleep and delta in deep sleep and anesthesia [4]. The electrodes are attached to the scalp during EEG recording according to the 10-20 system accepted by the international federation. Recordings can be performed with unipolar or bipolar montage. The most commonly used is the bipolar mount. In this technique, electrodes are attached to the right and left prefrontal (Fp), frontal (F), central (C), temporal (T), parietal (P), occipital (O), auricular (A) regions. Odd-numbered electrodes indicate the left hemisphere, and even-numbered electrodes indicate right hemisphere localizations [5]. There are many clinical and engineering studies on the use of EEG signals to detect neurological diseases. Some studies on EEG signals in the literature are presented below.

---

* Corresponding author: btasci@firat.edu.tr. ORCID Number of authors: [1] 0000-0001-7069-769X, *[2] 0000-0002-4490-0946, [3] 0000-0001-9677-5684, [4] 0000-0002-1425-4664

Zhao et al. [6] classified the EEG signals using the 1D CNN deep learning structure. The accuracy rates obtained in their study were 99.52% in the two-class classification problem, 98.06% in the three-class EEG classification problem, and 93.55% in the five-class classification problem, respectively. Khan et al. [7] classified the features selected by correlation-based Q-score using an LSTM-based deep learning model after extracting the features of the EEG signal using HVD (Hilbert Vibration Decomposition). Their studies were conducted with two different data sets. An accuracy of 96.00% was achieved for the Bonn dataset and 83.30% for the Sensor Networks Research Lab data. Wang et al. [8] performed feature extraction from EEG signals using EMD and DWT (Discrete Wavelet Transform) methods. Their study obtained 92.07% accuracy, 91.13% sensitivity, and 92.96% specificity for the Bonn data set. Rashid et al. [9] obtained accuracy values (99.21%, 93.19%, 93.57%, and 90.32%) for CI Competition III, IVA, and BCI Competition IV datasets, respectively, using the kNN technique. Kumar et al. [10] transformed the real value mode into an analytical signal with frequency spectrum by VMD (Variable Mode Decomposition) method. Then, semantic feature extraction was applied to generate the features. A Random Forest classifier was used in the study, and a success rate of 94.1% was achieved. Sheoran et al. [11] obtained scalogram images by transitioning EEG signals from the time domain to frequency domain with CWT (Continuous Wavelet Transform). Feature extraction was performed by calculating the potential feature values of the instantaneous frequency components, LBP (Local Binary Patterns), and HOG (Oriented Gradient Histograms) from the obtained scalogram images. They obtained an accuracy value of 99.08% with the SVM classifier. Bera et al. [12] achieved a success rate of 98% for binary class and 84% for multiclass classification with the error correction exit codes (ECOC) approach using the BCI Competition-IV dataset. Ha et al [13] firstly, the motor image EEG signals in the BCI Competition-IV dataset were converted into 2D images using the short-term Fourier transform (STFT) algorithm. The converted signals were then used for training and testing the capsule network. In this study, 78.44% accuracy was obtained.

2. Material and Method

2.1. Dataset

Ethical approval of the study was given by the Malatya Turgut Ozal University Medical Faculty Ethics Committee (2022/01), following the principles of the Declaration of Helsinki. Awake EEG images of patients over 18 who applied to the electroneurophysiology laboratory were scanned retrospectively. EEG recordings were made in the awake state with bipolar mounting according to the 10-20 system accepted by the International Federation. In this technique, electrodes are attached to the right and left prefrontal (Fp), frontal (F), central (C), temporal (T), parietal (P), occipital (O), auricular (A) regions. Electrodes indicated with odd numbers indicate their localizations in the left hemisphere, and even numbers indicate their localizations in the right hemisphere. EEG signal recordings of the patients were recorded in 500Hz EDF format. These signals were labeled as normal and abnormal after being reconstructed as 15-second data packets with the help of the Matlab program for 35 channels. Patients under 18, patients who had sleep EEG recordings, and those with intense artifacts were excluded from the study. Patient information and details are given in Table 1.

Table 1. Dataset information

Classes	Male	Female	Age	Number of Channels	Number of Data Packs
Normal	20	24	32.4±11.28	35	10575x15sec
Abnormal	113	127	38.4±18.8	35	11240x15sec

Furthermore, this database was published publicly and the users/researcher can download this database from https://www.kaggle.com/buraktaci/mtouh (accessed on 3 March 2022).

2.2. Method

In this work, a statistical feature extraction-based model has been presented. The presented model has been applied to the Collected EEG signal dataset. This model contains three primary phases: statistical feature extraction, feature vector reduction using neighborhood component analysis, and classification with support vector machine classifier. To better explain the presented model, a graph of this model is given in Figure 1.
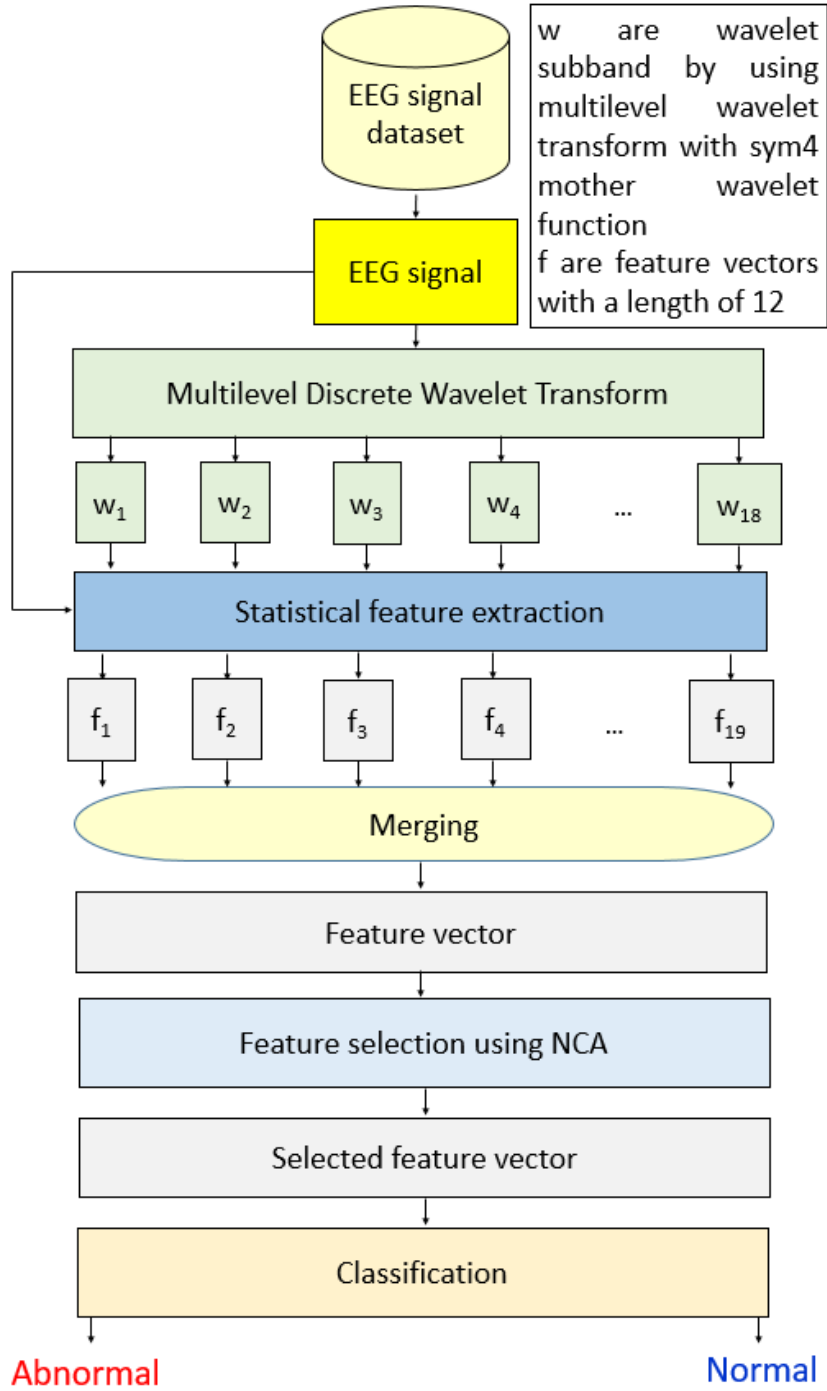
Figure 1. Graph of the presented EEG signal classification model using a statistical model.

The steps of the presented model are given below.

Step 0: Read each EEG signal from the dataset.

Step 1: Apply multilevel DWT to EEG signal to generate subbands.

$$[low^1, high^1] = DWT(signal,' sym4') \tag{1}$$

$$[low^{t+1}, high^{t+1}] = DWT(low^t,' sym4'), t \in \{1,2,\dots,8\} \tag{2}$$

$$w^{2h-1} = low^h, h \in \{1,2,...,9\} \tag{3}$$

$$w^{2h} = high^h \tag{4}$$

Herein, low and $high$ denote low-pass and high-pass filter subbands of the DWT ($DWT(.,.)$), w contains wavelet subbands. We generated 18 wavelet subbands using multilevel DWT, and both low and high subbands have been utilized to extract features in this work.

Step 2: Generated statistical features from EEG signal and wavelet subbands (w) to create a feature vector.

$$f^1 = sfg(signal) \tag{5}$$

$$f^t = sfg(w^{t-1}), t \in \{2,3,...,19\} \tag{6}$$

Herein, f are generated feature vectors, and the length of each feature vector is 12. To extract statistical features, maximum, minimum, average, median, mode, standard deviation, information entropy, root mean square error, range, mean absolute deviation, variance, skewness, and kurtosis moments have been used. By applying these moments, 12 statistical features have been extracted from each generated one-dimensional signal. Briefly, sfg(.) extracts 12 features from a signal. In this step, 19 feature vectors have been generated.

Step 3: Merge the extracted feature vectors to obtain the final feature vector.

$$fv(i + 12 \times (j - 1)) = f^j(i), i \in \{1,2,...,12\}, j \in \{1,2,...,19\} \tag{7}$$

Herein, fv is a feature vector with a length of 228 (=12×19).

Step 3: Normalize fv applying minimum-maximum normalization.

Step 4: Choose the most informative/distinctive 60 features employing NCA [14] feature selection model. NCA is the feature selection version of the k nearest neighbors (kNN) [15] method and uses distances to assign weights to each feature. We have selected 60 of 228 features.

Step 5: Classify the chosen feature using the Fine Gaussian Support Vector Machine (FG-SVM) [16] [17] classifier with an 80:20 split ratio.

3. Performance Analysis

3.1. Experimental setup and Results

All coding in this study was carried out with a simulation program called Matlab, which is based on the Windows 10 operating system. 80% of the data set used to evaluate the performance of the proposed method is randomly allocated for training and 20% for testing.

Precision, sensitivity, specificity, F1-score, and accuracy metrics were used to obtain results [18, 19]. These metrics are generally used in machine learning. Therefore, we considered these metrics to evaluate our proposed method. The mathematical definition of these performance metrics is given in Equations 8-12. Also, true positive (TP), true negative (TN), false positive (FP), and false-negative (FN) values are used to calculate these performance metrics. In the study, classification was made with Fine Gaussian SVM. Classification has been performed for 35 different channels. The confusion matrices of the first 6 channels with the best results are given in Figure 1.

$$Accuracy = \frac{TP + TN}{TP + TN + FP + FN} \tag{8}$$

$$Sensitivity = \frac{TP}{TP + FN} \tag{9}$$

$$Specificity = \frac{TN}{TN + FP} \tag{10}$$

$$Precision = \frac{TP}{TP + FP} \tag{11}$$

$$F - score = 2 \times \frac{Precision \times Sensitivity}{Precision + Sensitivity} \tag{12}$$

Table 2. Channel-based results of the proposed method (%)

Channel	Accuracy(%)	Sensitivity(%)	Specificity(%)	Precision(%)	F-Score(%)
P4O2	**81.3**	**78.9**	83.7	82.0	**80.4**
C3P3	81.1	74.7	**87.1**	**84.5**	79.3
P3O1	80.9	78.3	83.3	81.5	79.9
C4P4	80.3	76.6	83.8	81.7	79.1
F3C3	79.7	73.1	85.8	82.9	77.7
F4C4	79.4	76.6	82.1	80.1	78.3
P3A1	79.3	75.9	82.4	80.2	78.0
C4A2	78.8	75.0	82.3	79.9	77.4
T6A2	78.7	70.5	86.4	83.0	76.3
T4T6	78.4	70.7	85.8	82.6	76.2
F7A1	78.2	75.2	81.0	78.8	77.0
F8T4	78.1	71.8	84.0	80.9	76.1
F3A1	78.1	73.8	82.2	79.6	76.5
T3T5	78.0	71.8	83.9	80.8	76.0
T6O2	77.6	70.2	84.5	81.0	75.2
C3A1	77.5	73.2	81.5	78.9	75.9
O2A2	77.1	70.9	82.8	79.5	75.0
F4A2	76.8	74.0	79.4	77.1	75.5
P1F3	76.6	70.5	82.2	78.9	74.5
O1A1	76.4	72.4	80.1	77.4	74.8
P4A2	76.4	72.2	80.2	77.5	74.8
T5O1	76.1	72.8	79.3	76.8	74.7
P1F7	75.8	71.4	80.0	77.0	74.1
P1A1	75.6	67.8	82.9	78.9	72.9
T4A2	75.5	66.1	84.3	79.9	72.4
F7A1	75.5	68.1	82.4	78.4	72.9
CZA1	75.2	65.6	84.3	79.7	72.0
T5A1	75.1	67.5	82.3	78.2	72.5
P2F4	75.0	66.1	83.3	78.8	71.9
P2F8	75.0	66.1	83.3	78.8	71.9
PZA2	74.9	74.6	75.3	73.9	74.2
P2A2	74.9	66.8	82.5	78.2	72.1
F8A2	74.7	66.0	82.8	78.3	71.6
T3A1	74.4	68.6	79.9	76.2	72.2
FZA2	74.2	67.4	80.6	76.6	71.7

The highest results for accuracy sensitivity and F-Score, with 78.9% and 80.4%, respectively, were obtained at the P4O2 channel. The highest results for specificity and precision, 87.1% and 84.5%, respectively, were obtained in the C3P3 channel. Lowest accuracy at 74.2% at FZA2 channel, lowest sensitivity at 66.0% at F8A2 channel, lowest specificity at 79.3% at T5O1 channel, lowest precision at 73.9% at PZA2 channel, and lowest F-score(%) at FZA2 channel at 71.7% has been obtained.

Figure 2. Confusion matrices of 6 channels.

Performance metrics are calculated using these confusion matrices. The performance ratios calculated for 35 channels are tabulated in Table 2.

4. Conclusions

In this study, a feature selection-based decision support system was proposed to detect abnormal EEG signals. In the study, feature extraction was performed for each channel difference of the EEG. The highest classification accuracy was obtained with the P4O2 channel. In the process, it is aimed to increase the classification performance and accuracy and reduce the cost. It is expected that the study will help physicians in diagnosis.

The primary purpose of this article is to classify abnormal EEG signals in the newly created data set. In future studies, the number of data and classes in the dataset will be increased.

References

[1] Kocaaslan A., Bayazıt O., Kahya M., Elektroensefalografinin Biyofiziksel Temelleri, Turkiye Klinikleri J Neurol 2017: 10(2); 110-114.

[2] Biasiucci A., Franceschiello B., Murray M.M., Electroencephalography, Current Biology 2019: 29; 80-85.

[3] Millett D., Hans Berger: From psychic energy to the EEG, Perspectives in biology and medicine 2001: 44; 522-542.

[4] Galip A., Sabiha T., Elektroensefalografinin Tarihçesi, Turkiye Klinikleri J Neurol 2017: 10(2); 105-109.

[5] Süleyman K., Nihat Ş., Rutin Elektroensefalografi Kayıtlaması ve Aktivasyon Yöntemleri, Turkiye Klinikleri J Neurol, 2017: 10(2); 115-119.

[6] Zhao W., Zhao W., Wang W., Jiang X., Zhang X., Peng Y., Zhang B., Zhang G., A novel deep neural network for robust detection of seizures using EEG signals, Computational and mathematical methods in medicine: 2020;1-9.

[7] Khan P., Khan Y., Kumar S., Khan M.S., Gandomi A.H., HVD-LSTM based recognition of epileptic seizures and normal human activity, Computers in Biology and Medicine 2021: 136; 104684.

[8] Wang Y., Dai Y., Liu Z., Guo J., Cao G., Ouyang M., Liu D., Shan Y., Kang G., Zhao G., Computer-Aided Intracranial EEG Signal Identification Method Based on a Multi-Branch Deep Learning Fusion Model and Clinical Validation, Brain Sciences 2021; 11; 615.

[9] Rashid M., Bari B.S., Hasan M.J., Razman M.A.M., Musa R.M., Ab Nasir A.F., Majeed A.P.A., The classification of motor imagery response: an accuracy enhancement through the ensemble of random subspace k-NN, PeerJ Computer Science 2021; 7; e374.

[10] Ravi Kumar M., Srinivasa Rao Y., Epileptic seizures classification in EEG signal based on semantic features and variational mode decomposition, Cluster Computing 2019: 22; 13521-13531.

[11] Sheoran P., Rathee N., Saini J., Epileptic seizure detection using bidimensional empirical mode decomposition and distance metric learning on scalogram, in: 2020 7th International Conference on Signal Processing and Integrated Networks (SPIN), IEEE, 2020, pp. 675-680.

[12] Bera S., Roy R., Sikdar D., Kar A., Mukhopadhyay R., Mahadevappal M., A randomised ensemble learning approach for multiclass motor imagery classification using error correcting output coding, in: 2018 40th Annual International Conference of the IEEE Engineering in Medicine and Biology Society (EMBC), IEEE, 2018; 5081-5084.

[13] Ha K.-W., Jeong J.-W., Motor imagery EEG classification using capsule networks, Sensors, 2019: 19; 2854.

[14] Goldberger J., Roweis S., Hinton G., Salakhutdinov R., Neighbourhood components analysis, in: Proceedings of the 17th International Conference on Neural Information Processing Systems, MIT Press, Vancouver, British Columbia, Canada, 2004: 513–520.

[15] Peterson L.E., K-nearest neighbor, Scholarpedia 2009: 4; 1883.

[16] Vapnik V., The Support Vector Method of Function Estimation, in: J.A.K. Suykens, J. Vandewalle (Eds.) Nonlinear Modeling: Advanced Black-Box Techniques, Springer US, Boston, MA 1998: 55-85.

[17] Vapnik V., The nature of statistical learning theory, Springer science & business media, 1999.

[18] Warrens M.J., On the equivalence of Cohen's kappa and the Hubert-Arabie adjusted Rand index, Journal of classification 2008: 25; 177-183.

[19] Chicco D., Jurman G., The advantages of the Matthews correlation coefficient (MCC) over F1 score and accuracy in binary classification evaluation, BMC genomics 2020: 21; 6.

A Substitution-Box Structure Based on Solar Panel Data

Esin TURAN[1*], Mustafa Kemal ÖZDEMİR[2], Barış KARAKAYA[3], Fatih ÖZKAYNAK[4]

[1, 2]Department of Mathematics, Faculty of Arts and Sciences, University of Inonu, Malatya, Turkey
[3]Department of Electrical and Electronics Engineering, Faculty of Engineering, University of Firat, Elazığ, Turkey
[4]Software Engineering Department, Faculty of Technology, University of Firat, Elazığ, Turkey
[*1]esingoger@gmail.com, [2]kozdemir73@gmail.com, [3]bkarakaya@firat.edu.tr, [4]ozkaynak@firat.edu.tr

Abstract: The demonstration that the nonlinearity criterion of substitution box (s-box) structures based on the random selection principle can be improved through post-processing techniques has created a new research area. The necessity of obtaining sbox structures that can be given as input to these post-processing algorithms has emerged. In this study, a study was carried out on how to obtain sbox structures based on solar panel data. The cryptological properties of the obtained sbox structures were tested using five basic evaluation metrics and compared with similar studies in the literature. The successful results indicated that these outputs may have various practical applications in the future.

Key words: Substitution box, block cipher, chaos, random selection.

Güneş Paneli Verilerine Dayalı İkame Kutusu Yapısı

Öz: Rasgele seçim prensibine dayalı ikame kutusu yapılarının doğrusal olmama ölçütünün son işlem teknikleri aracılığı ile iyileştirilebileceğinin gösterilmesi yeni bir araştırma alanı doğurmuştur. Bu son işlem algoritmalarına giriş olarak verilebilecek ikame kutusu yapılarının elde edilmesi gerekliliği ortaya çıkmıştır. Bu çalışmada güneş paneli verileri temel alınarak ikame kutusu yapılarının nasıl elde edilebileceğine ilişkin bir çalışma gerçekleştirilmiştir. Elde edilen ikame kutusu yapılarının kriptolojik özellikleri beş temel değerlendirme metriği kullanılarak test edilmiş ve literatürdeki benzer çalışmalar ile kıyaslanmıştır. Elde edilen başarılı sonuçlar bu çıktıların ileride çeşitli pratik uygulamalara sahip olabileceğine işaret etmiştir.

Anahtar kelimeler: İkame kutusu, blok şifreleme, kaos, rastgele seçim.

1. Introduction

In the last two decades, chaos-based encryption has been one of the most striking topics among the practical applications of chaotic systems. There are thousands of studies in the literature. However, when these studies are examined, two main categories come to the fore. The studies in the first category propose new encryption protocols that use the rich randomness dynamics of chaotic systems, while the studies in the second category analyze the security weaknesses of the proposals in this first category [1]. These two opposite situations cause many researchers to approach chaos-based cryptology with suspicion. Recently, in order to address these problems, researchers have carried out various studies to improve the cryptographic characteristics of chaotic systems with the help of optimization algorithms, to transform the outputs obtained by physical unclonable functions and various post-processing techniques into practical applications in cryptography [2]. These studies have been shown that cryptographically more successful designs can be obtained using post-processing algorithms [3].

A remarkable study among these post-processing algorithms aims to improve the nonlinearity value of substitution-box (s-box) structures [4, 5] as much as possible. The design logic of the post-processing algorithm is based on the principle of obtaining a new s-box table by swapping two selected cell values each time. If the nonlinearity value of the new s-box whose cell positions are changed is higher than the nonlinearity value of the previous s-box, the new s-box structure is used in the next step. Otherwise, two different cells are selected and their values are changed. In optimization algorithms, nature is generally imitated in the selection process. In the proposed post-processing algorithm, cells are selected sequentially. This selection logic makes the process much easier than optimization algorithms. Since the proposed algorithm is based on the principle of applying a post-processing technique to a random selection-based s-box structure with low nonlinearity value, instead of focusing on complex optimization processes, it both improves the nonlinearity value and gives fast results [3]. After the successful results of the post-processing technique, a new field of study has emerged. S-box datasets with average nonlinearity value produced according to the random selection principle to be given as input to the post-processing

algorithm are needed. This study aims to produce a dataset that can serve this purpose. Original aspect of the study is that a photovoltaic (PV) solar panel energy generation data is used as the randomness source.

2. Random Selection Based S-box Generator Program

There are many studies published based on the random selection principle. Ref. [6] study can be examined for the basic design approaches used in the literature and the metrics that are the evaluation criteria in these studies. Since the aim of this study is to generate s-box structures with nonlinearity values close to the mean (103-106), a program was used. This program uses chaotic systems as entropy sources. In this study, PV data is taken as the basis as the entropy source. In Figure 1, various visuals of the interfaces of this program are presented. The program has a simple use. In addition to a promotional video.
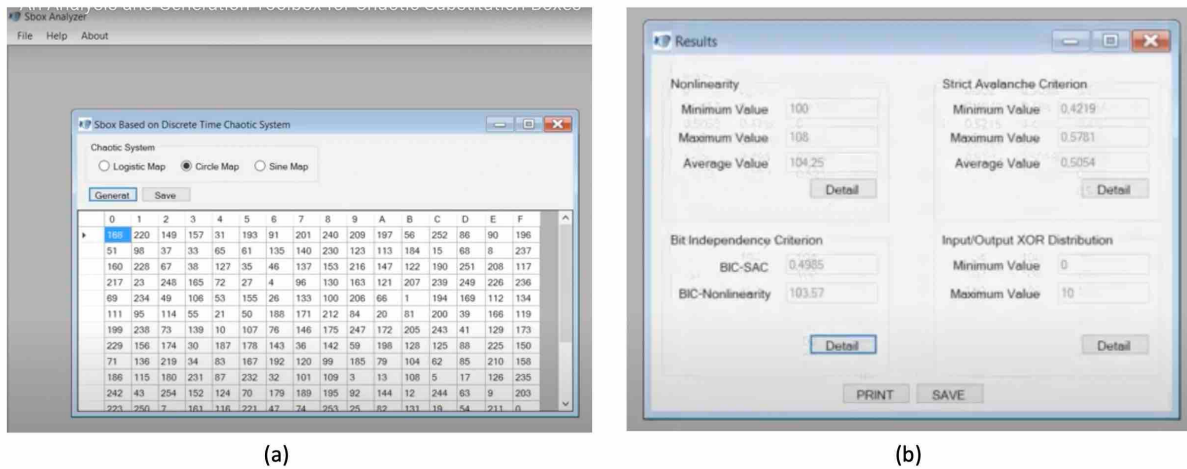
Figure 1. Screenshots for the s-box generator and analysis parts of the program

The link in Ref. [7], there is a dataset that has been shared publicly. A cryptographic protocol will be developed based on the file named "EXPORT TenMinData - Substation Voltages". The suitability of the data we examined as an entropy source will be analyzed in this study. For example, aim of study is that to generate the s-box using the "Substation_VA_Filtered" data in the 11th column of the file. S-box is a transform table that replaces the original data with encrypted data that the attacker cannot understand. If the data has a high entropy, a strong transformation table will be obtained. In other words, we will use the data itself to encrypt the data. In this way, we will be able to address the problems related to General Data Protection Regulation (GDPR). Only the person or persons with the original data will be able to open the encrypted data. The general view of file is shown in Figure 2.

Figure 2. The general view of "Substation_VA_Filtered" file

3. Generated S-box Structure

A simple mod operation is used to generate sbox structures from the dataset. Since the mod function is a one-way function, it will have several advantages in the process of hashing the data. The 11th column of the dataset is named Substation_VA_Filtered. The last three digits of the data in this column are used. To produce a 16x16 s-box, values are mapped between 0 and 255 by applying mod 256 to the last three digits. For example, the last three digits of the first value of this column have the value 975. Since 976%256=208, this value is assigned to the first cell of the s-box structure. This process is continued by selecting a new value until the entire table is full, and the data producing the same values are ignored. In this way, the bijective feature, which is the most basic requirement for s-box structures, is guaranteed [8, 9]. The first s-box structure obtained from the dataset and the output of the analysis program are shown in Figure 3.
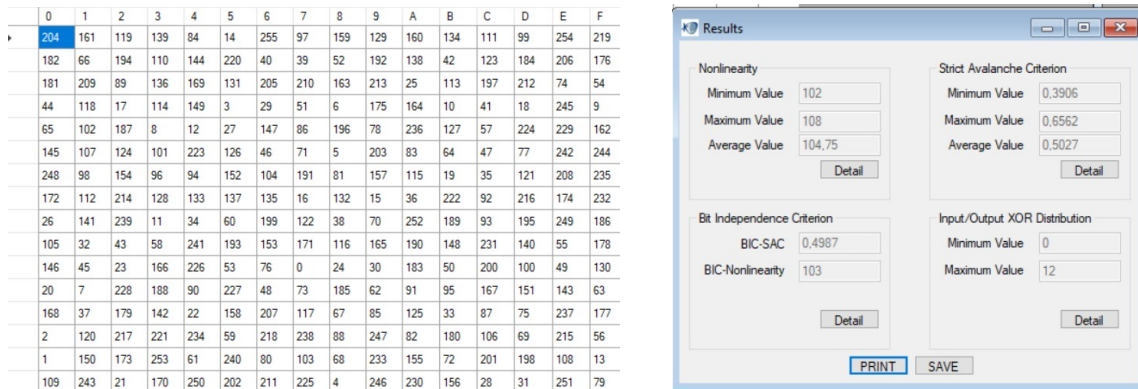
Figure 3. Generated s-box and analysis results

The other four generally accepted properties for s-box structures are the strict avalanche criterion, independence of input and output bits, nonlinearity, and XOR distribution table showing resistance to differential attacks, respectively. For more details on these criteria and their mathematical expression, see Ref. [4, 5, 8] can be examined. More detailed reports can be generated for these four evaluation criteria using the analysis program. The general view of the detailed analysis report for the s-box structure produced in Figure 3 is given in Figure 4.

Figure 4. The general view of the detailed analysis report

Acceptable values for other analysis metrics shown in Figure 4 are summarized below.
- A value of 0.5 is accepted as the ideal value for the strict avalanche criterion (SAC).
- For nonlinearity measurement, the value 112 is the highest value that can be reached.
- The BIC (independence of input and output bits) value is reconsidering the input-output relationship for the SAC and nonlinearity criteria.
- In the XOR distribution table, the highest value among the calculated values is desired to be as small as possible.

4. Performance Comparisons

Performance comparisons of s-box structure in Figure 3 with some studies previously published in the literature are given in Table 1. When compared to chaos-based s-box structures, two criteria come to the fore. these are nonlinearity and XOR distributions. The other two criteria are very close to acceptable values. It is an advantage that it has a higher nonlinearity value compared to many studies and is smaller in XOR value than many other structures.

Table 1. Performance comparisons

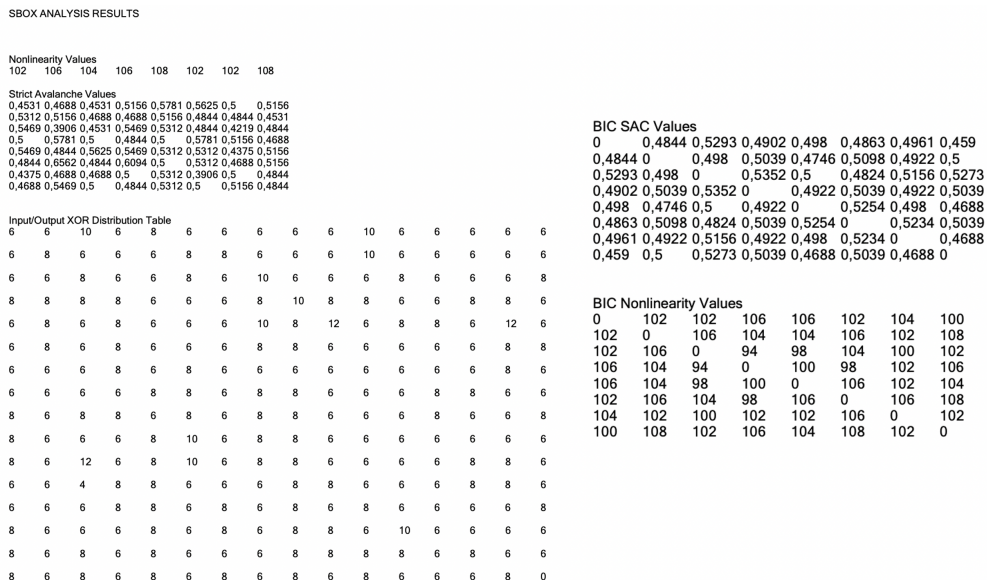| S-box	Strict Avalanche Criterion			Nonlinearity (NL)			Maximum I/O XOR	Bit Independence Criterion	
	avg	max	min	min	max	avg		SAC	NL
Ref. [10]	0.5022	0.5781	0.4063	100	110	105.5	32	0.4983	107
Ref. [11]	0.4926	0.5937	0.4062	98	110	105.5	32	0.4994	105.7
Ref. [12]	0.5010	0.6094	0.4063	102	110	105.5	12	0.4988	104.3
Ref. [13]	0.5056	0.5781	0.4375	102	108	105.3	10	0.4971	104
Ref. [14]	0.5059	0.5781	0.4063	102	108	105.2	12	0.5013	104.3
Ref. [15]	0.4987	0.5469	0.4531	104	108	105.25	10	0.4990	102.6
Ref. [16]	0.5037	0.5625	0.4375	102	108	105.25	10	0.4994	102.6
Ref. [17]	0.5073	0.6094	0.4062	98	108	105.25	10	0.4986	103,86
Ref. [18]	0.5012	0.5938	0.4063	104	106	105	10	0.4994	103.4
Ref. [19]	0.5046	0.6093	0.4750	102	106	105	10	0.5004	103.6
Ref. [20]	0.4990	0.5850	0.4290	100	107	104.8	12	0.4890	104.7
Proposed	**0.5027**	**0.6562**	**0.3906**	**102**	**108**	**104.7**	**12**	**0.4987**	**103**
Ref. [21]	0.4037	0.5938	0.3906	100	108	104.7	32	0.4965	105
Ref. [22]	0.5056	0.5937	0.3906	102	108	104.7	12	0.5021	104.1
Ref. [23]	0.4978	0.6093	0.4218	100	108	104.75	12	0.5009	103,6
Ref. [24]	0.4982	0.5781	0.4218	100	108	104.7	10	0.4942	103.1
Ref. [25]	0.5034	0.5938	0.3906	102	108	104.7	10	0.4972	103.3
Ref. [26]	0.498	0.6406	0.4219	102	108	104.5	12	0.5013	104.6
Ref. [27]	0.4980	0.6093	0.3750	102	106	104	10	0.4971	103.2
Ref. [28]	0.5026	0.5781	0.3906	100	106	104	10	0.5033	103.2
Ref. [29]	0.5	-	-	-	-	104	10	0.498	102.8
Ref. [30]	0.4954	0.6094	0.2813	98	108	104	12	0.4967	102
Ref. [31]	0.4946	0.6250	0.3750	100	106	104	10	0.4990	102.5
Ref. [32]	0.5018	0.5175	0.4825	102	106	104	10	0.5019	103.5
Ref. [33]	0.5039	0.6093	0.4218	98	108	104	12	0.5078	104
Ref. [34]	0.5058	0.5781	0.3906	101	108	103.8	14	0.4958	102.6
Ref. [35]	0.5036	0.6328	0.4140	101	106	103.8	10	0.5037	103.4
Ref. [36]	0.4987	0.6015	0.4140	99	106	103.3	10	0.4995	103.3
Ref. [37]	0.5058	0.625	0.4062	99	106	103.3	12	0.5037	103.6
Ref. [38]	0.5058	0.5975	0.3671	98	108	103.2	12	0.5031	104.2
Ref. [39]	0.5048	0.5937	0.4218	100	106	103.2	10	0.5009	103.7
Ref. [40]	0.5039	0.625	0.3906	96	106	103	12	0.5010	100.3
Ref. [41]	0.5	0.6093	0.4218	100	106	103	14	0.5024	103.1
Ref. [42]	0.5012	0.5937	0.4062	98	108	103	12	0.4988	104.1
Ref. [43]	0.5178	0.6719	0.3906	96	106	102.5	54	0.4026	102.5
Ref. [44]	0.4836	0.6016	0.3281	98	108	102.3	14	0.4992	100
Ref. [45]	0.5059	0.6094	0.4219	96	108	102.25	16	0.5050	103.5
Ref. [46]	-	-	-	-	-	102	8	-	-
Ref. [47]	0.4812	0.625	0.125	84	106	100	16	0.4962	101.9
Ref. [48]	0.4812	0.625	0.125	84	106	100	16	0.4962	101.9

5. Conclusions

S-box structures are a critical component in the design of cryptological algorithms. Therefore, new s-box designs should be researched in order to address developing and diversifying attack scenarios and to best meet user requirements (speed, low memory requirement, simplicity and ease of use). It is known that chaotic s-box structures have advantages against algebraic and application attacks. However, the low nonlinearity value of these designs is a problem. Recently, several studies using post-processing algorithms have attempted to address this problem. The simple structure, fast results and easy implementation of the techniques based on post-processing method provide a great advantage especially against optimization-based designs [3, 49]. The post-processing method has been shown to improve the nonlinearity value of an s-box structure with a nonlinearity value of 106.75 to 110 at the end of 12*255*255 processing steps in the worst-case scenario. The success of the proposed method becomes more evident when compared to a solution proposal that can be found with optimization algorithms within a wide search space with a wide range of possibilities.

Initial s-box structure populations are needed to increase the variety of s-box numbers with the proposed post-processing techniques. In this study, it has been investigated whether solar panel data can be used as an entropy source in order to meet this need. This dataset contains voltage, current, power, energy, and weather data from low-voltage substations and domestic premises with high uptake of solar photovoltaic (PV) embedded generation. Data collected as part of the project run by UK Power Networks. The results obtained on a sample dataset supported the proposed hypothesis. In the future, it is planned to analyze these results in more detail and to analyze their success in practical applications.

Acknowledgment

References

[1]. Z. M. Z. Muhammad and F. Özkaynak, "Security Problems of Chaotic Image Encryption Algorithms Based on Cryptanalysis Driven Design Technique," in IEEE Access, vol. 7, pp. 99945-99953, 2019, doi: 10.1109/ACCESS.2019.2930606.

[2]. V Dudykevych, I Garasym, Survivable security Systems Analysis, 2010, Computer science and information technologies: Materials of the VIth International scientific and technical conference CSIT, 108-110

[3]. F. Artuğer, F. Özkaynak, "An effective method to improve nonlinearity value of substitution boxes based on random selection", Information Sciences 576, 577-588, 2021, doi: 10.1016/j.ins.2021.07.036

[4]. T. Cusick and P. Stanica, Cryptographic Boolean Functions and Applica- tions. Amsterdam, The Netherlands: Elsevier, 2009.

[5]. C. Wu and D. Feng, Boolean Functions and Their Applications in Cryp- tography. Berlin, Germany: Springer, 2016.

[6]. F Artuğer, F Özkaynak, A method for generation of substitution box based on random selection, Egyptian Informatics, https://doi.org/10.1016/j.eij.2021.08.002

[7]. London Datastore, Solar Panel Energy Generation data, https://data.london.gov.uk/dataset/photovoltaic--pv--solar-panel-energy-generation-data

[8]. K. Nyberg, "Differentially uniform mappings for cryptography," inProc. Eurocrypt, in Lecture Notes in Computer Science, vol. 765. Berlin, Germany: Springer, 1994, pp. 55–64.

[9]. M. S. Acikkapi, F. Ozkaynak, and A. B. Ozer, "Side-channel analy- sis of chaos-based substitution box structures," IEEE Access, vol. 7, pp. 79030–79043, 2019, doi: 10.1109/ACCESS.2019.2921708.

[10]. I. Hussain, T. Shah, H. Mahmood, and M. Gondal, ''A projective general linear group based algorithm for the construction of substitution box for block ciphers,'' Neural Comput. Appl., vol. 22, no. 6, pp. 1085–1093, 2013.

[11]. M. Khan and T. Shah, ''A novel image encryption technique based on Hénon chaotic map and S8 symmetric group,'' Neural Comput. Appl., vol. 25, nos. 7–8, pp. 1717–1722, 2014.

[12]. A. Belazi and A. A. A. El-Latif, ''A simple yet efficient S-box method based on chaotic sine map,'' Optik, vol. 130, pp. 1438–1444, Feb. 2017.

[13]. A. Belazi, A. Khan, A. Latif, and S. Belghith, ''Efficient cryptosys- tem approaches: S-boxes and permutation–substitution-based encryption,'' Nonlinear Dyn., vol. 87, no. 1, pp. 337–361, 2017.

[14]. I. Hussain, T. Shah, M. Gondal, and H. Mahmood, ''A novel method for designing nonlinear component for block cipher based on TD-ERCS chaotic sequence,'' Nonlinear Dyn., vol. 73, no. 1, pp. 633–637, 2013.

[15]. K. K. Butt, G. Li, F. Masood, S. Khan, "A Digital Image Confidentiality Scheme Based on Pseudo-Quantum Chaos and Lucas Sequence", Entropy 2020, 22(11), 1276; https://doi.org/10.3390/e22111276

[16]. F. Özkaynak, "On the effect of chaotic system in performance character- istics of chaos based S-box designs," Phys. A, Stat. Mech. Appl., vol. 550, Jul. 2020, Art. no. 124072, doi: 10.1016/j.physa.2019.124072.

[17]. M. Ş. Açikkapi and F. Özkaynak, "A Method to Determine the Most Suitable Initial Conditions of Chaotic Map in Statistical Randomness Applications," in IEEE Access, vol. 9, pp. 1482-1494, 2021, doi: 10.1109/ACCESS.2020.3046470.

[18]. F. Özkaynak, "From biometric data to cryptographic primitives: A new method for generation of substitution boxes," in Proc. ACM Int. Conf. Biomed. Eng. Bioinformat., Bangkok, Thailand, Sep. 2017, pp. 27–33. doi: 10.1145/3143344.3143355.

[19]. F. Artuğer and F. Özkaynak, "A novel method for performance improvement of chaos-based substitution boxes," Symmetry, vol. 12, no. 4, p. 571, Apr. 2020.

[20]. I. Hussain, T. Shah, H. Mahmood, and M. Gondal, "Construction of S8 Liu J S-boxes and their applications," Comput. Math. Appl., vol. 64, no. 8, pp. 2450–2458, 2012.

[21]. I. Hussain, T. Shah, M. Gondal, W. Khan, and H. Mahmood, "A group theoretic approach to construct cryptographically strong substitution boxes," Neural Comput. Appl., vol. 23, no. 1, pp. 97–104, 2013.

[22]. I. Hussain, T. Shah, and M. Gondal, "A novel approach for designing substitution-boxes based on nonlinear chaotic algorithm," Nonlinear Dyn., vol. 70, no. 3, pp. 1791–1794, 2012.

[23]. M. Khanand, and T. Shah, "An efficient construction of substitution box with fractional chaotic system," Signal, Image Video Process., vol. 9, no. 6, pp. 1335–1338, 2015.

[24]. F. Özkaynak, V. Çelik, and A. B. Özer, "A new S-box construction method based on the fractional-order chaotic Chen system," Signal, Image Video Process., vol. 11, no. 4, pp. 659–664, 2017.

[25]. F. Özkaynak, "An analysis and generation toolbox for chaotic substitu- tion boxes: A case study based on chaotic labyrinth rene thomas sys- tem," Iranian J. Sci. Technol.-Trans. Elect. Eng., pp. 1–10, 2019. doi: 10.1007/s40998-019-00230-6.

[26]. L.Liu, Y.Zhang, and X.Wang, "AnovelmethodforconstructingtheS- box based on spatiotemporal chaotic dynamics," Appl. Sci., vol. 8, no. 12, p. 2650, 2018. doi: 10.3390/app8122650.

[27]. G. Chen, "A novel heuristic method for obtaining S-boxes," Chaos, Soli- tons Fractals, vol. 36, no. 4, pp. 1028–1036, 2008.

[28]. X. Wang, J. Yang, "A novel image encryption scheme of dynamic S-boxes and random blocks based on spatiotemporal chaotic system", Optik - International Journal for Light and Electron Optics 217 (2020) 164884

[29]. N. A. Khan, M. Altaf, F. A. Khan, "Selective encryption of JPEG images with chaotic based novel S-box". Multimed Tools Appl (2020). https://doi.org/10.1007/s11042-020-10110-5

[30]. M. Khan, T. Shah, and M. Gondal, "An efficient technique for the construction of substitution box with chaotic partial differential equation," Nonlinear Dyn., vol. 73, no. 3, pp. 1795–1801, 2013.

[31]. M. Khan and T. Shah, "A construction of novel chaos base nonlinear component of block cipher," Nonlinear Dyn., vol. 76, no. 1, pp. 377–382, 2014.

[32]. H. Liu, A. Kadir, and Y. Niu, "Chaos-based color image block encryption scheme using S-box," AEU-Int. J. Electron. Commun., vol. 68, no. 7, pp. 676–686, Jul. 2014.

[33]. M. Khan, T. Shah, and S. Batool, "A new implementation of chaotic S-boxes in CAPTCHA, "Signal, Image Video Process., vol. 10, no. 2, pp. 293–300, 2016.

[34]. G. Tang and X. Liao, "A method for designing dynamical S-boxes based on discretized chaotic map," Chaos Solitons Fractals, vol. 23, no. 5, pp. 1901–1909, 2005.

[35]. F. Özkaynak and S. Yavuz, "Designing chaotic S-boxes based on time- delay chaotic system", Nonlinear Dyn., vol. 74, no. 3, pp. 551–557, Nov. 2013.

[36]. G. Tang, X. Liao, and Y. Chen, "A novel method for designing S-boxes based on chaotic maps" Chaos Solitons Fractals, vol. 23, no. 2, pp. 413–419, 2005.

[37]. N. Hematpour and S. Ahadpour, "Execution examination of chaotic S- box dependent on improved PSO algorithm," Neural Comput. Appl., Aug. 2020, doi: 10.1007/s00521-020-05304-9.

[38]. G. Jakimoski and L. Kocarev, "Chaos and cryptography: Block encryption ciphers based on chaotic maps," IEEE Trans. Circuits Syst. I. Fundam. Theory Appl., vol. 48, no. 2, pp. 163–169, Feb. 2011.

[39]. F. Özkaynak and A. B. Özer, "A method for designing strong S-boxes based on chaotic Lorenz system," Phys. Lett. A, vol. 374, no. 36, pp. 3733–3738, 2010.

[40]. M. Khan, T. Shah, H. Mahmood, M. Gondal, and I. Hussain, "A novel technique for the construction of strong S-boxes based on chaotic Lorenz systems," Nonlinear Dyn., vol. 70, no. 3, pp. 2303–2311, 2012.

[41]. G. Chen, Y. Chen, and X. Liao, "An extended method for obtaining S-boxes based on three-dimensional chaotic Baker maps", Chaos Solitons Fractals, vol. 31, no. 3, pp. 571–579, 2007.

[42]. M. Khan, T. Shah, H. Mahmood, and M. Gondal, "An efficient method for the construction of block cipher with multi-chaotic systems," Nonlinear Dyn., vol. 71, no. 3, pp. 489–492, 2013.

[43]. M. Khan and Z. Asghar, "A novel construction of substitution box for image encryption applications with Gingerbreadman chaotic map and S8 permutation," Neural Comput. Appl., vol. 29, no. 4, pp. 993–999, Feb. 2018. doi: 10.1007/s00521-016-2511-5.

[44]. S. Jamal, M. Khan, and T. Shah, "A watermarking technique with chaotic fractional S-box transformation," Wireless Pers. Commun., vol. 90, no. 4, pp. 2033–2049, 2016.

[45]. B. B. Cassal-Quiroga and E. Campos-Canton, "Generation of Dynamical S-Boxes for Block Ciphers via Extended Logistic Map," Mathematical Problems in Engineering Volume 2020, https://doi.org/10.1155/2020/2702653

[46]. A. Freyre-Echevarria, I. Martinez-Diaz, C. M. L. Perez, G. Sosa-Gomez, and O. Rojas, "Evolving nonlinear S-boxes with improved theoretical resilience to power attacks," IEEE Access, vol. 8, pp. 202728–202737, 2020, doi: 10.1109/ACCESS.2020.3035163.

[47]. M. Khan, "A novel image encryption scheme based on multiple chaotic S-boxes," Nonlinear Dyn., vol. 82, no. 1, pp. 527–533, 2015.

[48]. M. Khan, T. Shah, and S. Batool, "Construction of S-box based on chaotic Boolean functions and its application in image encryption," Neural Com- put. Appl., vol. 27, no. 3, pp. 677–685, 2016.

[49]. F. Artuğer, F. Özkaynak, "A method for generation of substitution box based on random selection", Egyptian Informatics Journal 23 (1), 127-135 2022, doi: 10.1016/j.eij.2021.08.002

C O P Y R I G H T   R E L E A S E   F O R M

TURKISH JOURNAL OF SCIENCE AND TECHNOLOGY (TJST)
Published by Firat University

Firat University, Fen Bilimleri Enstitüsü Müdürlüğü
Turkish Journal of Science & Technology Editörlüğü
Elazığ-TURKEY,
Manuscript title: ....
....
....
Full names of all authors (in order to appear on manuscript): ....
....
Name, address etc. of corresponding author: ....
....
....
ID Number: .... Telephone: ....
E-mail: .... Mobile phone: ....

The author(s) warrant(s) that:
a) the manuscript submitted is his/her/their own original work;
b) all authors participated in the work in a substantive way and are prepared to take public responsibility for the work;
c) all authors have seen and approved the manuscript as submitted;
d) the manuscript has not been published and is not being submitted or considered for publication elsewhere;
e) the text, illustrations, and any other materials included in the manuscript do not infringe upon any existing copyright or other rights of anyone. Notwithstanding the above, the Contributor(s) or, if applicable the Contributor's Employer, retain(s) all proprietary rights other than copyright, such as
a) patent rights;
b) to use, free of charge, all parts of this article for the author's future works in books, lectures, classroom teaching or oral presentations;
c) the right to reproduce the article for their own purposes provided the copies are not offered for sale.
However, reproduction, posting, transmission or other distribution or use of the article or any material contained therein, in any medium as permitted hereunder, requires a citation to the Journal and appropriate credit to Firat University as publisher, suitable in form and content as follows:
Title of article, author(s), journal title and volume/issue, Copyright© year.
All materials related to manuscripts, accepted or rejected, including photographs, original figures etc., will be kept by Turkish Journal of Science and Technology editority for one year following the editor's decision. These materials will then be destroyed.
I/We indemnify Firat University and the Editors of the Journals, and hold them harmless from any loss, expense or damage occasioned by a claim or suit by a third party for copyright infringement, or any suit arising out of any breach of the foregoing warranties as a result of publication of my/our article. I/We also warrant that the article contains no libelous or unlawful statements and does not contain material or instructions that might cause harm or injury.
This copyright form must be signed by all authors. Separate copies of the form (completed in full) may be submitted by authors located at different institutions; however, all signatures must be original.

ID number: ....….........…….......................... ID number: …….......……….................................……..
Full name (block letters) …..........…......…...……....... Full name (block letters) ….........……......……......……......
Signature …………....…......…… Date ……....…… Signature ……....……....…… Date ....
ID number: ....….…....…….......................... ID number: …….......….……................................…….
Full name (block letters) …..........…......…...……....... Full name (block letters) ….........……......……......……......
Signature …………....…......…… Date ……....…… Signature ……....……....…… Date ....
ID number: ....….......…….......................... ID number: …….......…..……...............................…….

Turkish authors must supply their ID card number; foreign authors must supply their passport number (if possible)